Dynamical and Radiative Modeling of Sagittarius A*

A dissertation presented
by

Roman V. Shcherbakov

to
The Department of Astronomy
in partial fulfillment of the requirements
for the degree of
Doctor of Philosophy
in the subject of

Astronomy

Harvard University
Cambridge, Massachusetts
May 2011

Thesis advisor

Ramesh Narayan

Author

Roman V. Shcherbakov

Dynamical and Radiative Modeling of Sagittarius A*

Abstract

Sgr A* in our Galactic Center is the closest supermassive black hole (SMBH) with the largest event horizon angular size. Most other SMBHs are likely in the same dormant low-luminosity accretion state as Sgr A*. Thus, the important physical effects in lives of BHs can be best observed and studied in our Galactic Center. One of these effects is electron heat conduction. Conduction may be the main reason why Sgr A* is so dramatically underluminous: it transfers heat outwards from the inner flow and unbinds the outer flow, quenching the accretion. In Chapter 3 I build a realistic model of accretion with conduction, which incorporates feeding by stellar winds. In a model with accretion rate $< 1\%$ of the naive Bondi estimate I achieve agreement of the X-ray surface brightness profile and Faraday rotation measure to observations. An earlier model proposed in Chapter 2 with adiabatic accretion of turbulent magnetized medium cannot be tweaked to match the observations. Its accretion rate appears too large, so turbulent magnetic field cannot stop gas from falling in.

Low accretion rate leads to a peculiar radiation pattern from near the BH: cyclo-synchrotron polarized radiation is observed in radio/sub-mm. Since it comes from several Schwarzschild radii, the BH spin can be determined, when we overcome all modeling challenges. I fit the average observed radiation spectrum with a theoretical spectrum, which is computed by radiative transfer over a simulation-based model. Relevant plasma effects responsible for the observed polarization state are accurately computed for thermal

plasma in Chapter 4. The prescription of how to perform the correct general relativistic polarized radiative transfer is elaborated in Chapter 5. Application of this technique to three-dimensional general relativistic magneto hydrodynamic numerical simulations is reported in Chapter 6. The main results of analysis are that the spin inclination angle is estimated to lie within a narrow range $\theta_{\rm est} = 50^\circ - 59^\circ$, and most probable value of BH spin is $a_* = 0.9$.

I believe the researched topics will play a central role in future modeling of typical SMBH accretion and will lead to effective ways to determine the spins of these starving eaters. Computations of plasma effects reported here will also find applications when comparing models of jets to observations.

Contents

Citations to Previously Published Work

The results reported in Chapter 2 were published as

> "Spherically Symmetric Accretion Flows: Minimal Model with Magnetohydrodynamic Turbulence," Roman V. Shcherbakov,
> 2008, ApJS, **177**, 493 [arXiv:0803.3909 [astro-ph]].

Chapter 3 appears in its entirety in the paper

> "Inflow-Outflow Model with Conduction and Self-consistent Feeding for Sgr A*," Roman V. Shcherbakov and Frederick K. Baganoff,
> 2010, ApJ, **716**, 504 [arXiv:1004.0702 [astro-ph]].

The investigation of plasma effects described in Chapter 4 is published as

> "Propagation Effects in Magnetized Transrelativistic Plasmas," Roman V. Shcherbakov,
> 2008, ApJ, **688**, 695 [arXiv:0809.0012 [astro-ph]].

The formalism of ray tracing through plasma near black hole elaborated in Chapter 5 is published as

> "General Relativistic Polarized Radiative Transfer: Building a Dynamics - Observations Interface," Roman V. Shcherbakov and Lei Huang,
> 2011, MNRAS, **410**, 1052 [arXiv:1007.4831 [astro-ph]].

The culmination of the thesis, sub-millimeter modeling of Sgr A* written in Chapter 6, is currently under the second round of review in Astrophysical Journal

> "Constraining the Accretion Flow in Sgr A* by General Relativistic Dynamical and Polarized Radiative Modeling," Roman V. Shcherbakov, Robert F. Penna, and Jonathan C. McKinney
> arXiv:1007.4832 [astro-ph].

In the interest of brevity, I have omitted from my thesis a relevant paper published in 2009 that I was a single author on.

Electronic preprints (shown in `typewriter font`) are available on the Internet at the following URL:

> `http://arXiv.org`

Acknowledgments

I am grateful to my thesis advisor Ramesh Narayan (Harvard) for subtle guidance over the course of my PhD. Not only Ramesh was eager to discuss with me every my project, but also I have learnt from him to choose the projects wisely and to effectively interact with other researchers. The group meetings of Ramesh's group revealed to me the joy of scientific brainstorming and productive discussion. I am thankful to my Thesis Advisory Committee (TAC) consisting of Steven Cranmer (SAO), Avi Loeb (Harvard), Jim Moran (Harvard), and Ramesh Narayan. They gave me the essential feedback on science and general directions of my research endeavors.

I thank my direct collaborators and co-authors for shaping me into a better researcher: Lei Huang (ASIAA, SHAO) for help in developing the long-term research program and maintaining the rigorous system of cross-checks; Frederick Baganoff (MIT) for the incessant desire to collaborate and to refine the presentation and for giving me the opportunity to present at the press conference at AAS; Robert Penna (Harvard) for patience in running and re-running the numerical simulations, for useful comments, and for help with writing; Jonathan McKinney (Harvard, Stanford) for improving my standards of writing and formatting and the desire to give the immediate feedback 24 hours a day 7 days a week.

I'm grateful to Andreas Eckart (Cologne), Christopher Reynolds and Coleman Miller (UMD), Julian Krolik (JHU), Charles Gammie, Monika Moscibrodzka, and Po Kin Leung (UIUC), Avery Broderick (Harvard, CITA), Eliot Quataert (Berkeley), Andrey Beresnyak (LANL), Alexander Tchekhovskoy (Harvard, Princeton), Chi-Kwan Chan (Harvard, NORDITA), Vincent Fish and Shepherd Doeleman (MIT Haystack) for essential comments, which improved science and presentation of this work.

I am especially indebted to my wife Sreedhari Desai for moral support, help with writing, and continuous interest in the field of Astronomy.

I acknowledge NASA's award of Earth and Space Science Fellowship. The award was motivating me during the graduated career and helped me to shape an original program of research.

I also acknowledge the help of symbolic computation environment *Mathematica*, which hugely accelerated computations and creation of plots for all presented projects. Closer interactions with future versions of *Mathematica* and other means of computer-assisted research will lead to ever-increasing productivity of scientists.

Chapter 1

Introduction

1.1 Place of Sgr A* in the Cosmos

1.1.1 Formation Scenarios of Seed Black Holes

Supermassive black holes (SMBH) are the most extreme objects found in the Universe. They possess an event horizon, from underneath which nothing can escape. The horizon is often larger in size than the radius of Earth's orbit around the Sun. The centers of Galaxies are proven to host these supermassive objects (e.g. Begelman & Rees 2010). How did they get there and why are they so big?

The life of a SMBH starts with its birth. Several mechanisms were proposed for that without definite conclusions about how SMBHs are actually born. Figure 1.1 reviews a list of possible ways. SMBHs may start their lives as relatively tiny objects formed via the collapse of Population III stars that are dominated by radiation pressure. These stars may develop pair instability, runaway generation of electron-positron pairs, and collapse into a

$\sim 100 M_\odot$ BH (e.g. Bond et al. 1984; Fryer et al. 2001). Here $M_\odot = 2 \cdot 10^{33}$g is a solar mass.

Another mechanism of seed BH formation is through the collapse of the nucleus of a stellar cluster (Begelman & Rees, 1978; Miller & Hamilton, 2002; Devecchi & Volonteri, 2009). Compact protogalaxies in the early Universe can undergo massive star-formation episodes in their centers. The newly formed stars start a chain of runaway star-star collisions, which culminate with the formation of a huge several thousand $M_\odot$ star. This star collapses into $\sim 1000 - 2000 M_\odot$ seed BH.

The initial BHs do not have to be small. A different mechanism was proposed, which can lead to formation of BHs with masses up to $10^4 - 10^6 M_\odot$. The primordial high-density clumps of gas can effectively lose angular momentum and quickly collapse as a whole (Haehnelt & Rees, 1993; Loeb & Rasio, 1994; Eisenstein & Loeb, 1995; Begelman et al., 2006). Such a process also requires low metallicity of the early Universe to avoid active cooling and fragmentation of the cloud into small stars.

1.1.2 Mergers and Accretion over Hubble Time

Let us examine the destiny of seed BHs. Once they are formed, BHs may either already be at the centers of protogalaxies or may drift to the centers due to dynamical friction (Chandrasekhar, 1943). However, the life of a BH is not so simple. Over the age of the Universe galaxies undergo substantial interactions with their neighbors. Galaxy merger (Toomre & Toomre, 1972; Toomre, 1977; Barnes & Hernquist, 1992; Barnes, 1998; Schweizer, 1998; Hopkins et al., 2006) involves coalescence of two central BHs (e.g. Volonteri et al. 2003). The resultant bigger BH gets kicked from the center (Buonanno et

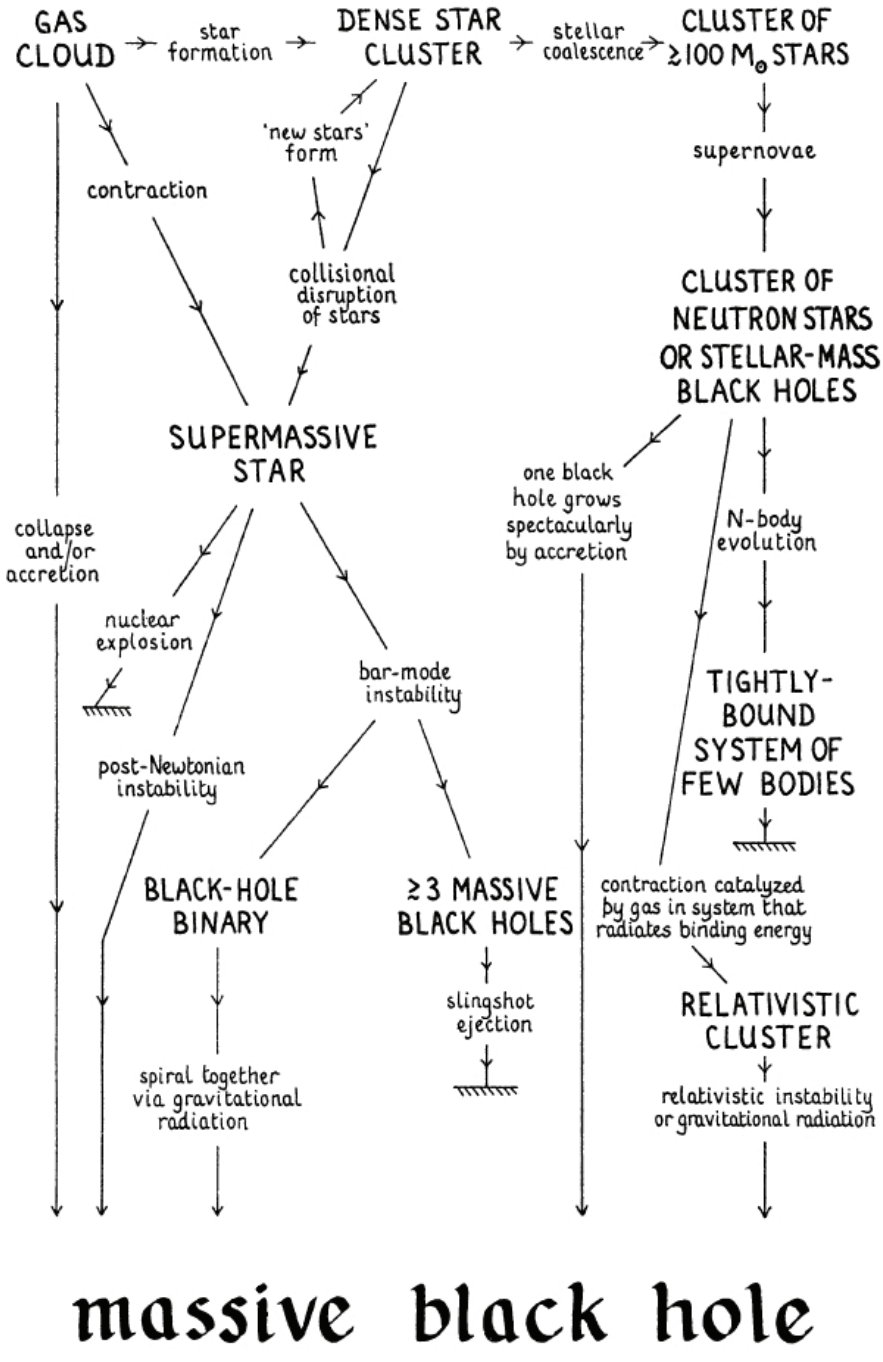

Figure 1.1.— Formation scenario of seed BHs. Adopted from Rees (1984).

al., 2007; Campanelli et al., 2007; Gonzalez et al., 2007), but is likely to stay bound and sink back to the center, as the recoil velocity is normally smaller than the galaxy velocity dispersion σ. Thus, SMBHs grow through a series of coalescence events.

Another frequent activity of BHs is accretion. Substantial amounts of gas can cool and fall onto the BH during and after the galaxy merger phase (e.g. Hopkins et al. 2006). At this time the accretion flow often radiates at high luminosity or shoots a powerful bright jet, so that the BH and the accretion flow are classified as an active galactic nucleus (AGN) (e.g. Begelman & Rees 2010). The BH mass grows through accretion. Owing to coalescence events and accretion supermassive BHs may end up having masses of $10^9 - 10^{10} M_\odot$ at the present epoch.

However, a survey of nearby galaxies shows that they are generally not very active (see Ho 2008 for the review). The average galaxy is not an active AGN. A typically short period of high luminosity (Hopkins et al., 2005) appears to be followed by a longer phase as a low-luminosity AGN (LLAGN). These are dormant BHs in galactic centers, accreting relatively little gas. Thus, to study a typical SMBH, we need to study it in a low-luminosity phase. Coincidentally, we have such a dormant accretor in the center of our own Galaxy, the Milky Way. This BH is called Sgr A*. Due to its small distance compared to the distances to other galaxies, Sgr A* is relatively easy to study.

1.1.3 Recent and Present-day Activity

Despite the advantage of its nearby location, we have to deal with the disadvantages of low luminosity and high obscuration, when studying Sgr A*. At present, radiation from it is barely detectable. Only in the early 1970-s was an unusual radio source observed in the

very center of our Galaxy (Balick & Brown, 1974). Yet, it is non-trivial to unambiguously associate the observed radio emission with some process near the BH. The convincing proof that our galactic center contains a SMBH came much later from observations of stellar orbits (Schödel et al., 2002; Ghez et al., 2003).

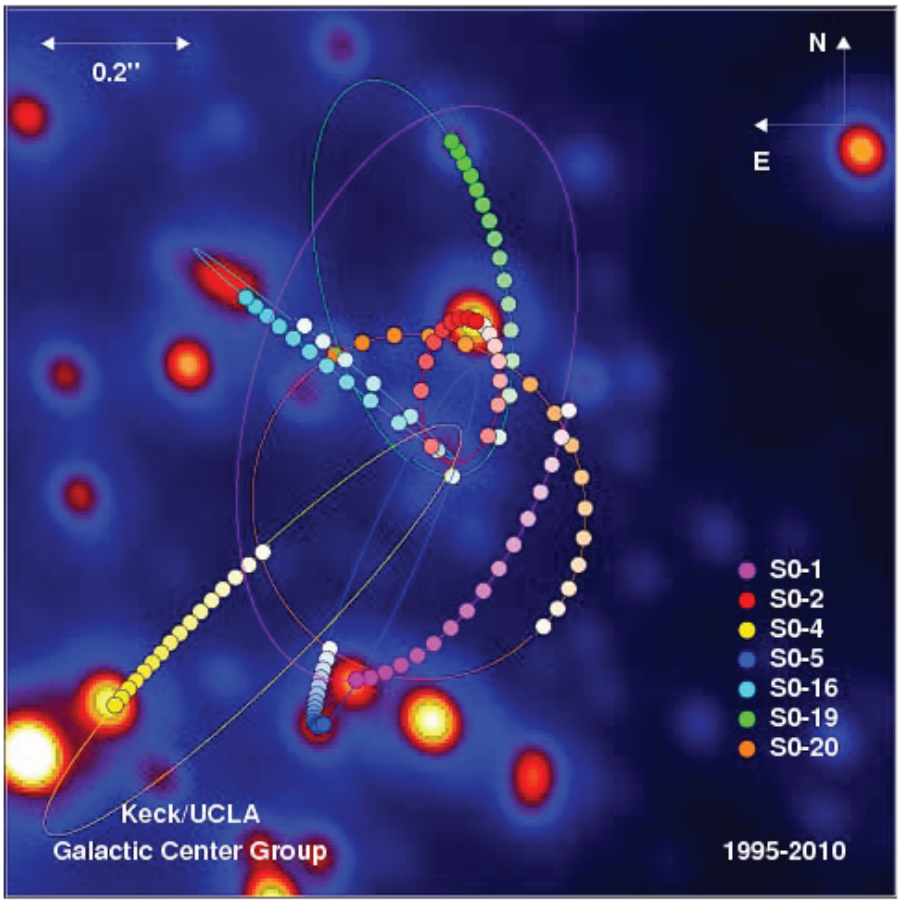

Figure 1.2.— Orbits of stars around Sgr A* BH. Image credit: Keck/UCLA Galactic Center Group.

Some stars were seen blazing at 5000km s^{-1} around the center (see Figure 1.2), whereas the source of radio emission stays in one location to a high precision (Reid et al.,

2008), which proves the object is very massive. The mass of Sgr A* appears to be around $4.3 \cdot 10^6 M_\odot$ (Genzel et al., 1997; Ghez et al., 2003, 2008; Gillessen et al., 2009). Since this estimate became available, theorists were wondering, why the BH is so dramatically underluminous with bolometric luminosity less than 10^{37}erg s^{-1} (e. g. Narayan et al. 1998). A large set of possible explanations was proposed. Some of them are elaborated upon within this thesis. When the density of matter was estimated near Sgr A* (Quataert & Gruzinov, 2000b; Marrone et al., 2007), it became apparent that for a typical accretion scenario the luminosity would be much greater, were the central object to have a solid surface outside of the event horizon (Broderick & Narayan, 2006; Broderick et al., 2009b). This is another proof that a SMBH is present in the center of our Galaxy.

There is some evidence that Sgr A* was not always very underluminous. A fluorescent iron line was discovered to emanate from Sgr B (Koyama et al., 1996). It is most naturally explained by irradiation from Sgr A* some 300 years ago. Another tentative evidence for past bright states of the SMBH in the Galactic center is a jet feature seen by *Chandra* (see Figure 1.4) (Muno et al., 2008). It points exactly in the direction of Sgr A*. A sky projection of the jet feature is perpendicular to the Galactic plane. One more potential evidence of a past jet has recently been discovered. An extended excess of radiation was seen by WMAP and Fermi from near the center of the Galaxy (Su et al., 2010). A possible explanation for this excess is a transient jet (Guo & Mathews, 2011) that radiated about 10^{57-58}erg. Other galaxies sometimes also have bubbles around their centers (Allen et al., 2006). The production of these bubbles is often ascribed to outflows and jets. Thus, it would not be surprising, if Sgr A* had a jet in the recent past.

Figure 1.3.— X-ray view of 10 pc region centered on Sgr A*. Different bands of *Chandra* are color-coded as follows: red corresponds to $2-4$ keV band, green — $4-6$ keV band, blue — $6-8$ keV. Thus, blue dots represent hard point sources, whereas red shows soft emission from diffuse gas. Image credits: NASA/CXC/MIT/F.K. Baganoff et al.

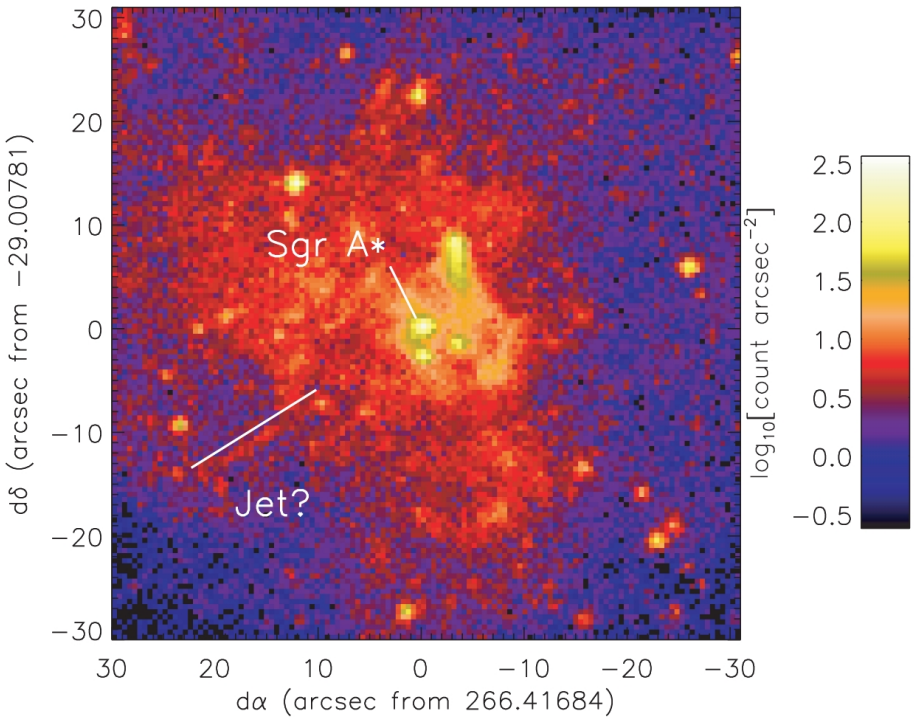

Figure 1.4.— X-ray close-up on Sgr A region (Muno et al., 2008). A jet feature is clearly visible at PA = 120° East of North.

1.2 Summary of Sgr A* Observations

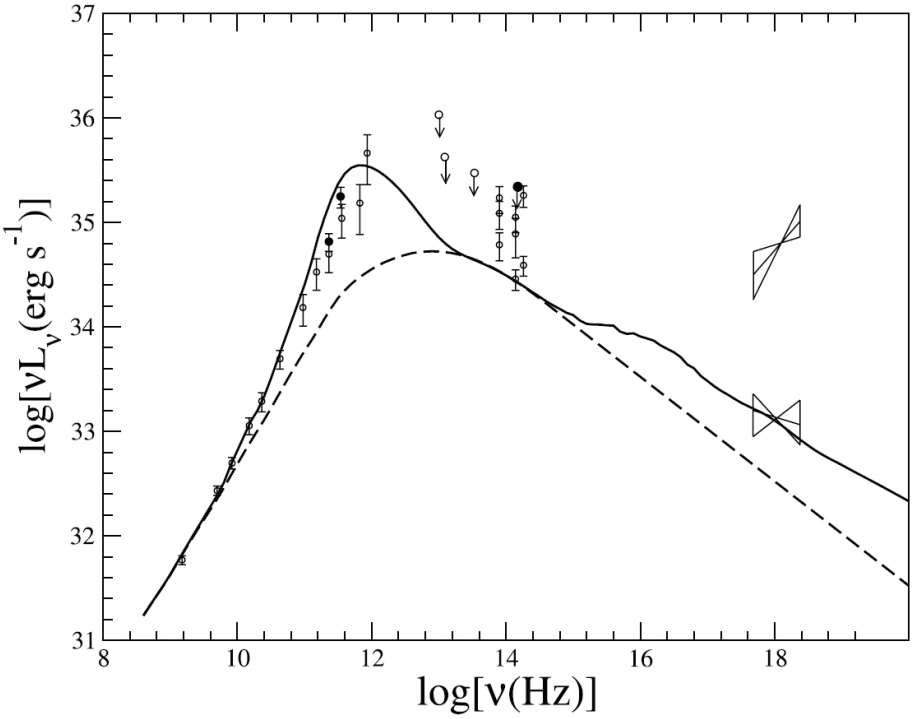

Figure 1.5.— Compilation of Sgr A* spectrum from radio to X-rays adopted from Yuan et al. (2004). Curves represent certain radiation models in Yuan et al. (2004). Two different levels of observed X-rays correspond to a quiescent state and a flaring state.

A typical spectrum of Sgr A* is depicted on Figure 1.5. Emission occurs over a broad frequency range from radio to X-rays with a peak in sub-mm. Let me review the particulars of radiation in different bands.

1.2.1 Sub-mm and Radio Observations

Since the discovery of Sgr A* in radio (Balick & Brown, 1974), various radio and sub-mm observational campaigns were conducted over the subsequent three and

a half decades. Various telescopes and arrays have observed Sgr A*: Berkeley Illinois Maryland Association telescope (BIMA), Combined Array for Research in Millimeter-wave Astronomy (CARMA), Caltech Submillimeter Observatory (CSO), Global Millimeter Very Long Baseline Interferometry (VLBI) Array (GMVA), Institute of Radioastronomy in Millimeter wavelengths telescope (IRAM), James Clerk Maxwell Telescope (JCMT), Max Planck Institute of Radioastrophysics telescope (MPIfR), Nobeyama millimeter array (NMA), Nobeyama single-dish telescope, Owens Valley Radio Observatory (OVRO), Submillimeter Array (SMA), Very Large Array (VLA), Very Large Baseline Array (VLBA). Future telescopes include Atacama Large Millimeter/submillimeter Array (ALMA) and Expanded VLA (EVLA). There is ongoing work to add more VLBI stations in exotic locations to probe new baselines with distinct orientations (Fish et al., 2009).

Reliable radio and sub-mm data were accumulated over decades of frequent monitoring. These data showed variability at each frequency up to a factor of $2-3$, but never more than a factor of ~ 5. Whereas radio emission in AGNs and LLAGNs is thought to be typically produced by a jet (see e.g. Blandford & Konigl 1979; Falcke & Markoff 2000 for models), only indirect evidence of jets/outflows is present for Sgr A*. In addition to evidence for past activity of Sgr A*, some current observations suggest extended structure of radio and sub-mm emission. A time lag was observed between the emission at 43 GHz and 22 GHz with emission at higher frequency coming first (Yusef-Zadeh et al., 2008). This is the signature of the expansion or the outflow. Second, the observed correlated fluxes are inconsistent between different baselines. VLBI correlated flux at 230 GHz for Hawaii-Arizona baseline (Fish et al., 2011) is substantially smaller than 60 m baseline flux. The discrepancy is most likely due to a structure of size $10-10^5 r_{\rm g}$. The mysterious discrepancy of mean levels and variability behavior of VLA and VLBA observations at

43 GHz (Yusef-Zadeh et al., 2009) perfectly conforms to the extended structure idea. Despite these complications, we mostly discuss accretion models without jets in what follows.

Since Sgr A* radio/sub-mm variability levels are small, it makes sense to define the mean spectrum and model it. The detailed definition of mean observed spectrum is deferred till Chapter 6, while here I discuss its general shape. The average Sgr A* spectrum is consistent with self-absorbed cyclo-synchrotron radiation (e.g. Rybicki & Lightman 1979). Flux grows approximately as a power-law till the peak at about 500 GHz. Flux decreases quickly with frequency ν for $\nu > 500$ GHz, yet the rate of this decrease cannot be quantified due to an absence of sub-mm observations above 857 GHz. No noticeable flattening of radio spectrum at $\nu \leq 43$ GHz can be identified.

In addition to the total flux, modern radio/sub-mm telescopes can observe the polarization state of the radiation. Four Stokes parameters I, Q, U, and V integrated over the image or a set of total flux F_ν, linear polarization (LP) fraction, circular polarization (CP) fraction, and electric vector position angle EVPA fully describe the polarization state. If one can observe all Stokes parameters, then the amount of information from a given exposure increases fourfold. Unfortunately, the polarization fractions are much below 100% and are hard to observe (Marrone et al. 2007, Munoz et al.(2011) in prep). Only incomplete polarization data are available. Nevertheless, as I will show, these data are enough to constrain the BH spin, its orientation, and flow properties.

Extra information can be extracted from variable lightcurves. In general, lightcurve variability is ascribed to magneto hydrodynamic turbulence (Chan et al., 2009; Dexter et al., 2009), which is associated with variability of density, magnetic field, and particle

energy. The probability density function (PDF) can be constructed to isolate particular states (Herrnstein et al. 2004; this work, Chapter 6). A Fourier transform at a single frequency can be computed to search for typical variability period, the same search can be done even more effectively with the help of the structure function (Yusef-Zadeh et al., 2011). Even though characteristic periods of ~ 20 min have been seen (Genzel et al., 2003; Yusef-Zadeh et al., 2011), the evidence for quasi-periodic oscillations (QPOs) in Sgr A* remain elusive.

VLBI observations of BH Shadow

A distinct type of sub-mm observations was recently conducted for the first time for Sgr A*. The extreme angular resolution of VLBI technique at 230 GHz allowed the observers to resolve the material plunging onto the BH from within several $r_{\rm g} = GM/c^2$ (Doeleman et al., 2008). Here G is a gravitational constant, M is the BH mass, and c is speed of light. The size and shape of the source image are distinct for different accretion profiles, BH spins, and spin inclination angles. This method offers a way to directly observe the predicted BH shadow and to constrain the flow properties. At present, a simple spherical accretion model can be ruled out, since its emission region would be too large. Models based on three-dimensional (3D) general relativistic MHD (GRMHD) simulations with spin $a = 0.9$ generally predict the correct image size (Moscibrodzka et al., 2009; Dexter et al., 2010; Shcherbakov et al., 2010). Finding correlated fluxes at lower frequencies would provide more observational constraints, but, unfortunately, this technique cannot be reliably extended to low ν because of interstellar scattering (e.g. Shen et al. 2005).

1.2.2 Infrared Observations

Substantial levels of near-infrared (NIR) emission were recently detected from Sgr A* by *Hubble* (Yusef-Zadeh et al., 2009), Keck with adaptive optics (Do et al., 2009), and Very Large Telescope (VLT) (Dodds-Eden et al., 2011). NIR observations are quite hard due to uncertain dust obscuration and frequent source confusion in Sgr A* field. Variability in NIR is more substantial than in radio and sub-mm, routinely reaching 10 times the median level. When flux is substantially above the median, Sgr A* enters the so-called "flaring state". Synchrotron and synchrotron self-Compton (SSC) mechanisms are proposed (e.g. Markoff et al. 2001; Eckart et al. 2006a; Dodds-Eden et al. 2010) to explain the flaring state. In addition to studies of flares, NIR variability of Sgr A* was quantified with probability density function, which resembles a log-normal distribution at high fluxes (Dodds-Eden et al., 2011). Search for periodicity showed that variations are consistent with red noise (Do et al., 2009) with no statistically significant periodicity.

1.2.3 X-ray Observations

The amazing spatial resolution of *Chandra* allowed researchers to study the center of our Galaxy in unprecedented detail. Sgr A* region is very rich. There are several types of sources within 0.2 pc from the BH: a pulsar wind nebula, an accreting variable binary system, and lots of hot gas as can be seen on Figure 1.6 (Muno et al., 2008, 2009). To isolate the emission of diffuse hot gas, one needs to subtract the point sources, which the field is quite contaminated with. This exercise is doable for Sgr A* field (see Chapter 3), since we can resolve all point sources down to a very low luminosity. Then one can quantify the emission from diffuse gas and say how much matter is available for a BH to swallow.

Such an exercise, which gives the necessary input to construct an accretion model, has been for Sgr A* in the present work. Unfortunately, it is not easy to reliably isolate the contribution from diffuse gas in the nuclei of other nearby galaxies such as Andromeda (Garcia et al., 2005) or nearby LLAGNs (Pellegrini, 2005; Soria et al., 2006a,b).

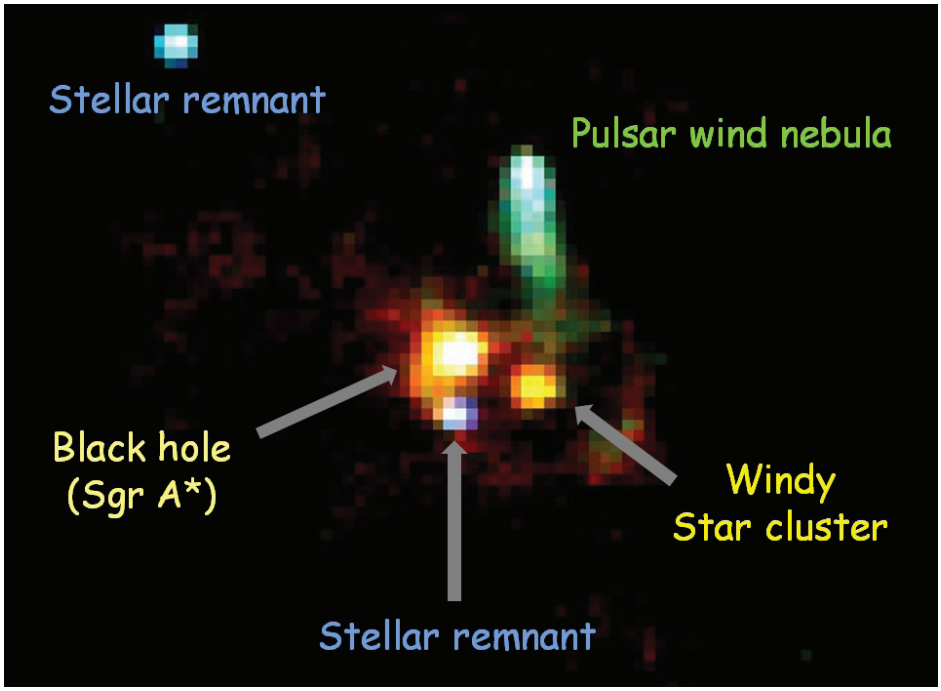

Figure 1.6.— Various sources of X-ray emission from near Sgr A*. Image credits: NASA/CXC/MIT/F.K. Baganoff et al.

Normally, the X-ray flux from Sgr A* is dominated by diffuse gas and is constant. However, flares were observed to reach $10 - 100$ times the median flux from several pixels around Sgr A* position (Baganoff et al., 2001). Synchrotron and SSC models were proposed to simultaneously fit NIR and X-ray observations of flares. Both mechanisms involve acceleration of electrons to ultrarelativistic energies.

1.3 Summary of Sgr A* Modeling

1.3.1 General Flow Structure

Radiation from Sgr A*, which we see with telescopes, is produced in hot gas/plasma. The extreme forces of the BH make the gas move. Motion towards the BH inevitably leads to compression and heating of plasma and to production of a unique emission pattern.

Thus, to understand BHs, researchers study the motion of gas around them. The simplest type of gas motion is spherically symmetric inflow as described by the Bondi solution (Bondi, 1952). It predicts a certain accretion rate for a given gas temperature and density outside the Bondi radius r_B, which is the radius of BH gravitational influence as compared to gas pressure influence. Simple Bondi flow is not very realistic. Virtually all hot astrophysical fluids have embedded magnetic field. A natural extension of the Bondi flow, spherical accretion with random magnetic field, is discussed in Chapter 2.

However, the spherical inflow itself is not realistic (Beskin & Karpov, 2005). As the gas is dragged from about $10^6 r_{\rm g}$ to $1 r_{\rm g}$, even a tiny amount of net angular momentum would lead to circularization of the flow at a radius $\gg 1 r_{\rm g}$. Simulations of Sgr A* region by Cuadra et al. (2008) suggested circularization radius of $\sim 3 \cdot 10^3 r_{\rm g}$. When the flow becomes rotationally supported, even small initial magnetic field gets amplified by magnetorotational instability (MRI) (Balbus & Hawley, 1991) and develops MHD turbulence (Balbus & Hawley, 1998; Hawley & Krolik, 2001). This turbulence helps to transport the angular momentum outside and the matter towards the BH. Various rotationally supported models were invented to quantify this process. Preserving the assumption of energy conservation in the flow, Narayan & Yi (1995) came up with the

advection-dominated accretion flow (ADAF). Being quite an advanced model already, ADAF can still be ruled out for Sgr A*. Energy conservation ensures the steep density profile $\rho \propto r^{-1.5}$. Computing such a flow structure from known density and temperature at Bondi radius, one stumbles into problems: overproduction of Faraday rotation measure (Quataert & Gruzinov, 2000b) or/and the overproduction of sub-mm and X-ray emission from the inner flow (Shcherbakov & Baganoff, 2010).

A number of proposed flow solutions depart from adiabaticity and energy conservation. The generic type of energy exchange between the inner and the outer flow helps to reconcile theory with observations. As Blandford & Begelman (1999) put it: "the binding energy of a gram of gas at a few $r_{\rm g}$ drives off 100 kg of gas from $10^5 r_{\rm g}$." Blandford & Begelman (1999) proposed the name adiabatic inflow-outflow solutions (ADIOS), yet not quantifying the energy exchange mechanism. A year later convection was found to be a suitable mechanism for tapping into the energy of the inner flow. Thus, convection-dominated accretion flow (CDAF) (Narayan et al., 2000; Quataert & Gruzinov, 2000a) was proposed. As I will show in Chapter 3 even stronger effect, conduction, is at play in our Galactic Center. The model will also incorporate Sgr A* feeding by stellar winds. See Cuadra et al. (2008) and Figure 1.7 for the discussion of feeding. Chapter 6 will discuss the steady-state model based on 3D GRMHD simulations.

As noted above, the observed Sgr A* lightcurves show variability in all wavelengths, which cannot be addressed within a steady-state model. A turbulent flow needs to be properly quantified. The best researchers can do now is to conduct direct numerical simulations (DNS). There is no complete theory of the statistical properties of turbulence (Leslie, 1973), so analytical approaches are not reliable. Simulations are hard to perform and have various problems with inclusion of relevant physical effects, correctness of

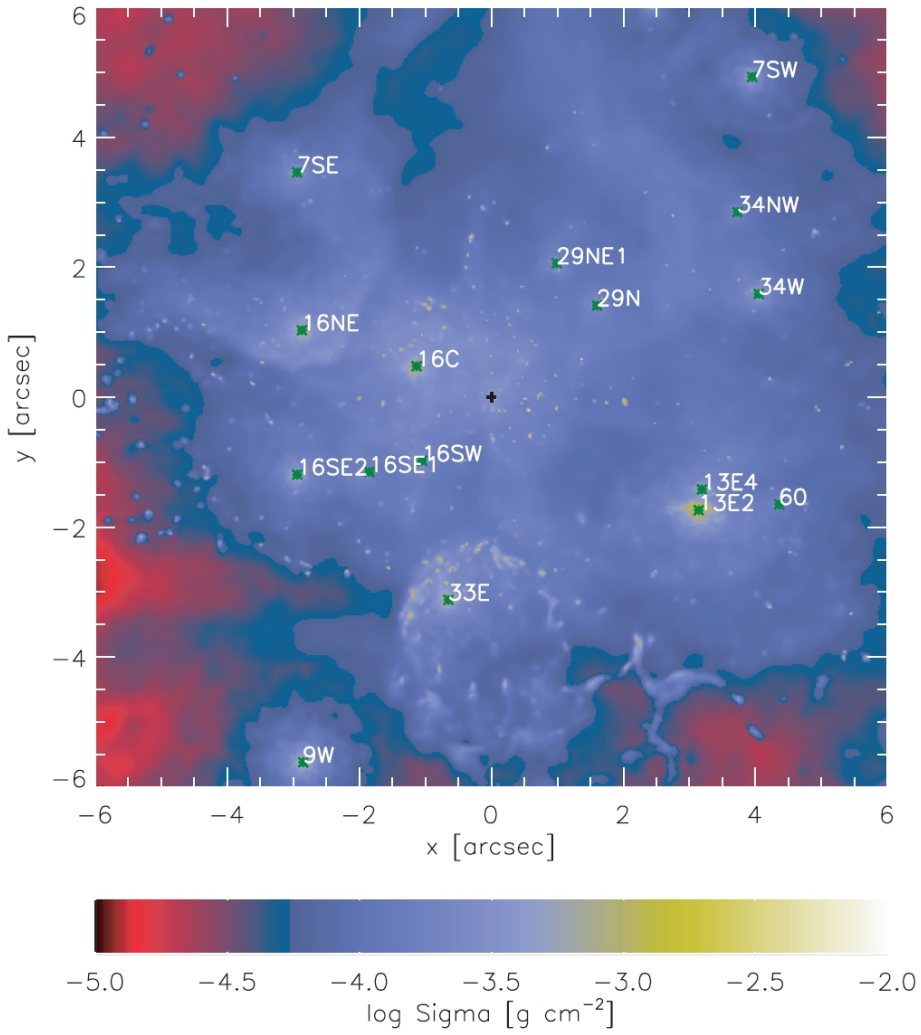

Figure 1.7.— Surface density of gas near Sgr A* Cuadra et al. (2008) as simulated to be ejected by stellar winds. The properties of wind-producing stars can be identified and then the dynamics of gas can be simulated with smoothed-particle hydrodynamics (SPH).

implementation, and convergence (Hawley et al., 2011). Simulations large numbers of CPU-hours to run. Yet, it is essential to do quantitatively correct simulations to accurately estimate the properties of the BH and the accretion flow. It is possible to make order of magnitude estimates for BH mass, electron temperature, and accretion rate within simple models. However, order of magnitude estimates of BH spin and inclination angle are meaningless since they would cover the entire ranges of these quantities.

1.3.2 Collisionless Effects

The plasma in the direct vicinity of Sgr A* is one of the hardest to model environments in the Universe. Besides feeling the extreme gravitational pull of the BH, the gas there is collisionless with collisional mean free path much larger than the distance from the BH. In addition, electrons appear to be transrelativistic with gamma-factors on the order of several: $\gamma \sim 2 - 10$.

The main collisionless effect in the flow is heat conduction. Electrons do not feel the resistance of ions and can travel effectively through tangled magnetic fields (Narayan & Medvedev, 2001), which leads to effective energy exchange between the inner and the outer flow, so that the flow structure changes. I discuss this effect in Chapter 3, but since I do not rigorously determine the conduction strength, the results of that chapter should not be considered as final. When the flow structure is determined, the radiation is still not: one needs to know the typical energy and distribution of the emitting species, electrons. Energy dissipation is one of the main mechanisms for electron heating, but not much is known about it. Heating by Coulomb collisions is weak near Sgr A* (Narayan et al., 1998), but heating by collective effects (Begelman & Chiueh, 1988; Quataert, 1998) may

be more substantial. Promising subfields of gyrokinetics (see (Howes et al., 2006) for a review) and particle-in-cell (PIC) simulations (e.g. Buneman 1993; Sironi & Spitkovsky 2009) may answer the question of electron heating in the future. Chapter 6 adopts thermal energy distribution of electrons and leaves the heating rate as a free parameter, whereas the chapter Chapter 5 discusses some implications of non-thermal electron distributions.

1.3.3 Emissivity and Radiative Transfer

Having discussed observations of Sgr A* and the dynamical models, let us briefly review the link between the two — the radiative transfer. Unlike the problems in dynamical modeling, radiative modeling of the SMBH in Galactic Center is quite easy. The flow onto the BH is truly radiatively inefficient (e.g. Narayan et al. 1998; Sharma et al. 2007a). Only a small fraction of total electron energy gets radiated, so that electrons do not lose their energy. This fact allows researchers to first do the dynamical modeling of the flow and then compute radiation on top of the resultant model. The feedback of radiation on dynamics is negligible.

Given a dynamical model, we need to use the right methods to compute the radiation. We should be especially careful when radiation is coming from near the BH. In this case light travels along null geodesics and the plane of linear polarization rotates. Another concern is that electrons are typically modeled (Sharma et al., 2007a; Dexter et al., 2010; Broderick et al., 2010; Huang et al., 2009a) to have $\gamma \sim 2 - 10$, or temperatures just above the electron rest mass. In this transrelativistic regime LP and CP emissivities, Faraday rotation and Faraday conversion effects all have the same order of magnitude, which complicates the calculations. Despite complications, a precise recipe can be given for

general relativistic polarized radiative transfer in transrelativistic plasmas. I summarize the formalism in Chapter 5. Precise polarized radiative transfer requires correct Faraday rotation and Faraday conversion coefficients, which are accurately computed for the first time in this thesis. The technique and the results are elaborated upon in Chapter 4 for thermal particle distributions. Non-thermal particle distributions are considered in ongoing work (Huang, Shcherbakov 2011, in prep). The application of radiative transfer for Sgr A* is described in Chapter 6.

1.4 Thesis Outline

Despite all the aforementioned complications, this thesis leads to some definite conclusions about the gas and the BH in the Galactic Center. I also provide some pieces of original plasma physics research, e.g. lay the foundation of precise general relativistic polarized radiative transfer in transrelativistic plasmas.

Chapter 2: Spherically Symmetric Accretion Flows: Minimal Model with MHD Turbulence. This chapter considers spherical Bondi accretion with random magnetic field. Magnetic field, if not dissipated, could effectively stop the accretion (Shvartsman, 1971). However, the accretion rate is found to drop by only a factor of $2-5$ times compared to the Bondi rate, if realistic turbulence dissipation rates are taken from simulations of hydro/MHD turbulence. The proposed model cannot provide an explanation for the observed low accretion rate onto Sgr A*.

Chapter 3: Inflow-Outflow Model with Conduction and Self-consistent Feeding for Sgr A*. An elaborate model of realistic accretion onto our Galactic Center is devised. We incorporate feeding from stellar winds averaged over the actual massive

stars in Sgr A* vicinity. Then we compute a radial model with realistic unsaturated conduction and compare bremsstrahlung X-ray surface brightness profile to that found in 1Ms quiescent *Chandra* observations. We find excellent agreement for an accretion rate $\dot{M} = 6 \cdot 10^{-8} M_{\odot}\text{year}^{-1}$ and a point source with luminosity $L \approx 4 \cdot 10^{32}\text{erg s}^{-1}$. The revealed point source likely corresponds to synchrotron self-Compton emission in quiescence.

Chapter 4: Propagation Effects in Magnetized Transrelativistic Plasmas. This chapter fixes conceptual and arithmetic errors (e.g. Melrose 1997c) and eliminates approximations (e.g. Ballantyne et al. 2007) in previous calculations of Faraday rotation and conversion measures for a thermal particle distribution. Accurate fitting formulae and analytic expansions are computed for Faraday rotation and conversion. The Faraday conversion coefficient is found to peak at a temperature of several electron masses $k_B T_e \sim 3 - 10 m_e c^2$, instead of dramatically increasing with T_e. Here k_B is Boltzmann constant and m_e is the electron mass. The Faraday rotation coefficient is found to decrease more than thought before (Ballantyne et al., 2007) in the intermediate regime $T_e \sim m_e$. This calculation is essential to properly treat linear and circular polarization in hot accretion flows. Work is now underway (Huang, Shcherbakov, 2011, in prep.) to compute Faraday rotation and conversion for arbitrary non-thermal particle distributions.

Chapter 5: General Relativistic Polarized Radiative Transfer: Building a Dynamics-Observations Interface. General relativistic polarized radiative transfer is a necessary tool to convert any reasonable accretion model in the Kerr metric into simulated flux, linear and circular polarization fractions, and electric vector position angle. We compile a step-by-step guide for carrying out such calculations. An original fast method for computing cyclo-synchrotron emissivities, Faraday rotation and conversion is proposed. I developed a numerical C++ code based on the proposed method and employed it in

Shcherbakov et al. (2010). As polarized observations of cyclo-synchrotron emitting sources (LLAGNs, jets) become increasingly common in radio and sub-mm, the technique will be increasingly crucial in modeling these sources, in particular, estimating BH spin.

Chapter 6: Constraining the Accretion Flow in Sgr A* by General Relativistic Dynamical and Polarized Radiative Modeling. We compile from the literature the mean spectrum of Sgr A* and model it. We perform 3D GRMHD simulations, conduct GR polarized radiative transfer calculations, and explore the 3.5D parameter space of electron temperature, accretion rate, inclination angle, and BH spin. We fit the flux spectrum within 86-850 GHz and known linear and circular polarization fractions within the same band. Performing χ^2 analysis of fits, we find that the best-fitting model corresponds to a dimensionless BH spin $a^* = 0.9$ with $\chi^2 = 4.05$. For this solution, the 90% confidence intervals are $\theta = 53^\circ \pm 3^\circ$, PA $= 121^\circ \pm 20^\circ$, $\dot{M} = (1.09 \pm 0.13) \times 10^{-8} M_\odot \mathrm{year}^{-1}$, $T_e = (4.62 \pm 0.56) \cdot 10^{10}$ K at $6M$ for inclination angle, spin position angle, accretion rate, and electron temperature, respectively. The conservative estimates over two models with spin $a_* = 0.9$ are $\theta = 50^\circ - 59^\circ$, PA $= 101^\circ - 143^\circ$, $\dot{M} = (0.9 - 1.7) \times 10^{-8} M_\odot \mathrm{year}^{-1}$, $T_e = (2.7 - 5.2) \cdot 10^{10}$ K at $6M$. The computed constraints on the inclination angle are narrower than reported by other groups. Images of the accretion flow close to the BH are shown in Fig. 6.15. We estimate the power-law index $\beta = 0.8 - 0.9$ for the density profile $n \sim r^{-\beta}$ between the Bondi radius and the inner flow. This index lies in between $\beta = 1.5$ for advection-dominated flow and $\beta = 0.5$ for convection-dominated flow. The PA of spin projection coincides with that of the tentative X-ray jet PA $= 120^\circ$.

Chapter 2

Spherically Symmetric Accretion Flows: Minimal Model with MHD Turbulence

Abstract

The first spherical accretion model was developed 55 years ago, but the theory is yet far from being complete. The real accretion flow was found to be time-dependent and turbulent. This chapter presents the minimal MHD spherical accretion model that separately deals with turbulence. Treatment of turbulence is based on simulations of several regimes of collisional MHD. The effects of freezing-in amplification, dissipation, dynamo action, isotropization, and constant magnetic helicity are self-consistently included. The assumptions of equipartition and magnetic field isotropy are released. Correct dynamics

of magnetized flow is calculated. Diffusion, convection, and radiation are not accounted for. Two different types of Radiatively Inefficient accretion flows are found: a transonic non-rotating flow (I), a flow with effective transport of angular momentum outward (II). Non-rotating flow has an accretion rate several times smaller than Bondi rate, because turbulence inhibits accretion. Flow with angular momentum transport has accretion rate about 10-100 times smaller than Bondi rate. The effects of highly helical turbulence, states of outer magnetization, and different equations of state are discussed. The flows were found to be convectively stable on average, despite gas entropy increases inward. The proposed model has a small number of free parameters and the following attractive property. Inner density in the non-rotating magnetized flow was found to be several times lower than density in a non-magnetized accretion. Still several times lower density is required to explain the observed low IR luminosity and low Faraday rotation measure of accretion onto Sgr A*.

2.1 Introduction

Dynamics of magnetized accretion flows is a major topic of astrophysical research. The problem can be solved with two different approaches: numerical and analytical. Each of them has specific difficulties, so these methods can be applied together for a better result.

Realistic numerical simulations require a lot of computational time to model even the isotropic case (Lazarian, 2006). Convergence of properties of the isotropic turbulence is reached only when computational domain has more than 1024 cells in each dimension (Ladeinde & Gaitonde, 2004; Biskamp, 2003). Non-isotropic simulations of this size were

not performed. It is also very difficult to model the system with large range of scales. The system then possesses vastly different timescales. Existing simulations of accretion flows are either axisymmetric (McKinney, 2006b) or consider a rather small domain close to the object (Hawley & Balbus, 2002; Igumenshchev, 2006). In addition, simulations should be run for sufficiently long time or several runs should be made to obtain average quantities, e.g. accretion rate, power of emitted radiation.

Analytical models do not suffer from a need to average, if they are based on averaged quantities. However, to build a reasonable model is itself difficult. No unified method exists to combine insights in physics and mathematics into a perfect analytical model. That is why the zoo of approximations of astrophysical flows is so huge.

In particular, many analytical treatments were devised for accretion: spherically symmetric treatment (Bondi, 1952; Meszaros, 1975; Coker & Melia, 2000; Beskin & Karpov, 2005), standard disk (Shakura & Sunyaev, 1973), Advection-Dominated Accretion Flow (ADAF) (Narayan & Yi, 1995) with its variation Hot Luminous Accretion Flow (Yuan, 2001), Adiabatic Inflow-Outflow Solutions (ADIOS) (Blandford & Begelman, 1999), Convection Dominated Accretion Flow (CDAF) (Narayan et al., 2000; Quataert & Gruzinov, 2000a), Jet-ADAF (Yuan et al., 2002). They are aimed to describe essentially the same process: axisymmetric plasma inflow onto a compact source. Some models include the effects the others miss. Energy transport in CDAF, outflows in ADIOS are the examples. Some effects are not treated properly in any approximation.

Magnetic field is a main source of uncertainty and mistakes in theory of accretion flows. Two assumptions are usually posed to incorporate it into the model. Firstly, magnetic field is considered to be isotropic (Coker & Melia, 2000; Narayan & Yi, 1995). Then magnetic

pressure and magnetic energy density may be put (Narayan & Yi, 1995) into the dynamical equations. Secondly, the ratio of magnetic field energy density to gas thermal energy density is set to constant. This is called thermal equipartition assumption. These two ideas are at least unproven or may even not work. Magnetic field is predominantly radial in spherical inflow (Shvartsman, 1971) because of freezing-in condition and predominantly toroidal in disk (Hawley & Balbus, 2002) because of magnetorotational instability.

In a good model direction and strength of the magnetic field should be determined self-consistently. Non-isotropy of magnetic field requires special dynamics. Dynamical equations were partially derived more than 20 years ago (Scharlemann, 1983), but did not receive much attention or were even considered erroneous (Beskin & Karpov, 2005).

Such a model may offer a natural explanation of certain accretion patterns. Accretion onto Sgr A* gives an excellent opportunity for testing. Our Galaxy is proven to host a Supermassive Black Hole (SMBH) named Sgr A* in its center (Ghez et al., 2003; Shen, 2006). This black hole accretes matter and emits radiation with characteristic low-luminosity spectrum (Narayan et al., 1998). This spectrum was satisfactory explained with the combination of two models: jet or non-thermal (Yuan et al., 2003) radio-emission and X-Rays with IR radiation coming from conventional ADAF flow. However, the large number of free parameters allows one to fit any spectrum well. Model with no free parameters left is an ultimate goal of the ongoing study.

Partial progress in building a self-consistent accretion model is made in this chapter, which is organized as follows. Averaged spherical MHD model with turbulence is devised in § 2.2. Approximate model employs the characteristic length scale about the size of the region of interest. Coefficients are taken from several hydrodynamic and MHD simulations.

External sources sustain turbulence at large radii, whereas turbulence is self-sustained in the converging flow at small radii. Necessary boundary conditions are discussed in § 2.3 for general flow and for Sgr A*. Results in § 2.4 are followed by the discussion of the model in § 2.5. Observational implications in § 2.6 are supplemented with prospects for future work and Conclusion in § 2.7. Chapter has several appendices.

2.2 Spherical Model

I base all calculations on Magneto Hydrodynamic system of equations (Landau et al. , 1984). The viscous terms are retained where they do not vanish in the limit of vanishing viscosity. The quantities in the following equations are fully dependent on time and coordinates. General mass flux equation reads

$$\frac{\partial \rho}{\partial t} + \nabla \cdot (\rho \mathbf{V}) = 0, \tag{2.1}$$

where $\mathbf{V}$ is fluid velocity. Force balance is described by Navier-Stokes equation

$$\frac{\partial \mathbf{V}}{\partial t} + (\mathbf{V} \cdot \nabla)\mathbf{V} = -\frac{\nabla p}{\rho} - \nabla \phi_{\rm g} - \frac{[\mathbf{B} \times [\nabla \times \mathbf{B}]]}{4\pi\rho} + \nu \triangle \mathbf{V}, \tag{2.2}$$

where $\phi_{\rm g}$ is gravitational potential, ν is kinematic viscosity. The last term is responsible for finite energy dissipation through Kolmogorov cascade (Landau & Lifshitz, 1987). Momentum equation is a combination of equations (2.1) and (2.2)

$$\frac{\partial (\rho V_i)}{\partial t} = -\frac{\partial}{\partial x_k}\left(p\delta_{ik} + \rho V_i V_k + \frac{1}{4\pi}\left(\frac{1}{2}B^2\delta_{ik} - B_i B_k\right)\right) - \frac{\partial \phi_{\rm g}}{\partial x_i} + \nu(\triangle \mathbf{V})_i. \tag{2.3}$$

Energy equation

$$\frac{\partial}{\partial t}\left(\frac{\rho \mathbf{V}^2}{2} + \rho\varepsilon + \frac{\mathbf{B}^2}{8\pi}\right) = -\nabla\left(\rho\mathbf{V}\left(\frac{\mathbf{V}^2}{2} + \phi_{\rm g} + w\right) + \frac{1}{4\pi}[\mathbf{B} \times [\mathbf{V} \times \mathbf{B}]] + \mathbf{viscous}\right) \tag{2.4}$$

includes information about the equation of state. Here ε is gas internal energy density, $w = \varepsilon + \int dp/\rho$ is gas specific enthalpy. Viscous term is responsible for diffusion. Magnetic field evolution is described by induction equation

$$\frac{\partial \mathbf{B}}{\partial t} = \nabla \times [\mathbf{V} \times \mathbf{B}] + \nu_M \triangle \mathbf{B} \tag{2.5}$$

with magnetic diffusivity ν_M. Magnetic field is solenoidal as well as incompressible random velocity field:

$$\nabla \mathbf{B} = 0, \qquad \nabla \mathbf{u} = 0. \tag{2.6}$$

2.2.1 Dynamics

Spherical accretion is the simplest pattern of all symmetric setups. We need to solve the basic model first to move then to a more realistic pattern. Construction of the minimal maximally symmetric model is the subject of the following study.

I employ the natural for the problem spherical coordinates (r, θ, ϕ) and average over angular variables (θ, ϕ). The results depend only on the radial variable r and not on time t in the assumption that angular averaging is the same as time averaging. I need now to determine the essential quantities and derive the closed system of equations on them.

Essential quantities of a non-magnetized solution in Bondi (1952) are the inflow speed $v(r)$, density $\rho(r)$, and temperature $T(r)$. Turbulent magnetized case requires several more. As I release the assumption of isotropy, there are two special directions: along the radial vector $\mathbf{e}_r$ and perpendicular to the radial vector. To describe realistic Magneto Hydrodynamic turbulence, I need at least 6 quantities: squares of radial and perpendicular magnetic fields B_r^2 and $B_\perp^2$, squares of radial and perpendicular random fluid speeds u^2 and $u_\perp^2$, characteristic length scale L, and dimensionless magnetic helicity ξ. The last

quantity will be described in detail in the corresponding subsection 2.2.4. For simplicity I consider random velocity to be isotropic and denote it as $u(r)$.

Total velocity of a fluid parcel

$$\mathbf{V}(r,\theta,\phi,t) = v(r)\mathbf{e}_r + \mathbf{u}(r,\theta,\phi,t) \tag{2.7}$$

is a sum of averaged inflow speed $v(r)$ and instantaneous random velocity $\mathbf{u}(r,\theta,\phi,t)$, where by definition angular average of turbulent velocity vanishes

$$\int \mathbf{u}(r,\theta,\phi,t)d\Omega = 0. \tag{2.8}$$

General continuity equation (2.1) can be averaged with the aid of equations (2.6) and (2.8) to

$$4\pi\rho(r)v(r)r^2 = \dot{M}, \tag{2.9}$$

where $\dot{M}$ is the mass accretion rate.

I derive the averaged force equation from general momentum equation (2.3). Tensor $\rho V_i V_k$ averages out into the diagonal form $\rho v^2\delta_{rr} + \rho u^2\delta_{ik}/3$. Because there are no sources of magnetic field (eq. [2.6]) and spherical geometry is assumed, no regular magnetic field exists. Following Scharlemann (1983), I add $B_r\nabla\mathbf{B}/(4\pi\rho)$ to the radial magnetic force $F_r = [\mathbf{B}\times[\nabla\times\mathbf{B}]]_r/(4\pi\rho)$, average over the solid angle, and then set $B_\phi = B_\perp$ and $B_\theta = B_\perp$. Cross-terms with $(B_\theta B_r)$, $(B_\phi B_r)$, and $(B_\phi B_\theta)$ cancel on average over the solid angle. Finally, I obtain

$$F_r = \frac{(r^4 B_r^2)'_r}{8\pi\rho r^4} - \frac{(r^2 B_\perp^2)'_r}{4\pi\rho r^2} \tag{2.10}$$

for the magnetic force. I denote by $()'_r$ radial derivatives. I omit bulk viscosity term that results from $\nu\triangle\mathbf{V}$. Paczynski-Wiita gravitational potential (Paczynski & Wiita, 1980)

$$\phi_{\rm g} = -\frac{r_{\rm g}c^2}{2(r-r_{\rm g})} \tag{2.11}$$

is used to imitate the effects of General Relativity, where

$$r_{\rm g} = \frac{2GM}{c^2} \tag{2.12}$$

is a Schwarzschild radius of an object with mass M. I take gas pressure to be that of an ideal gas $p = \rho RT/\mu$, where μ is a mean molecular weight. Combining all the terms, I come to the averaged force equation

$$vv'_r + \frac{r_{\rm g}c^2}{2(r-r_{\rm g})^2} + \frac{R}{\mu}\frac{(\rho T)'_r}{\rho} + \frac{(\rho u^2)'_r}{3\rho} + \frac{(r^2 B_\perp^2)'_r}{4\pi\rho r^2} - \frac{(r^4 B_r^2)'_r}{8\pi\rho r^4} = 0. \tag{2.13}$$

Averaged energy advection equation can be derived directly from general energy equation (2.4). Enthalpy term should include contribution from random fluid motions as well as from gas. Isotropic random motions of fluid exert isotropic pressure $p_{\rm rand} = \rho u^2/3$ and have the internal energy density $\varepsilon_{\rm rand} = u^2/2$. Total enthalpy w is

$$w = w_{\rm gas} + w_{\rm rand}, \quad \text{where} \quad w_{\rm gas} = \frac{RT(f_e a_e(T) + f_i a_i(T) + 1)}{\mu} \quad \text{and} \quad w_{\rm rand} = \frac{5}{6}u^2. \tag{2.14}$$

Fractions of electrons $f_e \approx 0.54$ and ions $f_i \approx 0.46$ are calculated for a gas with twice solar abundance of elements. Such high concentration of helium and metals was assumed by Baganoff et al. (2003) for spectrum fitting of Sgr A*. Correspondent mean molecular weight is $\mu \approx 0.7$g cm^{-3}. Integral heat capacity per particle $a_e(T)$ and $a_i(T)$ are different for electrons and ions. Ions are non-relativistic down to $r_{\rm g}$ (Narayan & Yi, 1995). Therefore $a_i(T) = 3/2$. General expression (Chandrasekhar, 1957) should be used for thermal relativistic electrons $a_e(T) = \Theta^{-1}(3K_3(\Theta^{-1}) + K_1(\Theta^{-1}))/(4K_2(\Theta^{-1}) - 1)$. Here $\Theta = kT/m_e c^2$ is dimensionless temperature, $K_x(Y)$ are modified Bessel functions of the second kind. Expression for non-relativistic enthalpy is

$$w_{NR} = \frac{5RT}{2\mu} + \frac{5}{6}u^2. \tag{2.15}$$

It is valid in the limit $\Theta \ll 1$. Time derivatives in energy equation (2.4) vanish under averaging. Equation takes the form $\nabla \mathbf{q} = 0$, where $\mathbf{q}$ is the energy flux. Part of flux proportional to random velocity $\mathbf{u}$ averages out, because turbulence is incompressible and u is zero on average (eq. [2.8]). Applying continuity relation (2.9), I finally obtain

$$v v_r' + \frac{r_{\rm g} c^2}{2(r - r_{\rm g})^2} + w_r' + \frac{1}{2\pi} \left(\frac{B_\perp^2}{\rho} \right)_r' = 0, \tag{2.16}$$

where again $B_\theta^2 = B_\phi^2 = B_\perp^2$. I assumed the term $\int [\mathbf{B} \times [\mathbf{u} \times \mathbf{B}]] d\Omega$ to also be zero along with all viscous energy transfer terms. I limit this study to Advection Dominated flows by deliberately cutting off diffusion and convection (see Appendix 2.10).

Subtracting force equation (2.13) from energy advection equation (2.16) I get the heat balance equation that reads in non-relativistic limit

$$\frac{R}{\mu} \left(\frac{3}{2} T_r' - \frac{\rho_r'}{\rho} T \right) + \left(\left(\frac{u^2}{2} \right)_r' - \frac{\rho_r'}{\rho} \frac{u^2}{3} \right) + \frac{\rho r^2}{4\pi} \left(\frac{B_\perp^2}{\rho^2 r^2} \right)_r' + \frac{1}{8\pi\rho r^4} (r^4 B_r^2)_r' = 0, \tag{2.17}$$

similar to entropy conservation in hydrodynamics. Work done by gas is represented by $-\rho_r'/\rho T$. The first term has exactly the form of the second, if I make the substitution of the mean square particles velocity

$$v_p^2 = \frac{3RT}{\mu}. \tag{2.18}$$

Work done by the magnetic field enters the expression as derivatives of ρ and r in the magnetic part.

2.2.2 Evolution of Turbulence

Dynamics is the only part of ideal Bondi problem (Bondi, 1952). In reality, flow always has some small scale turbulence that exerts back-reaction on the mean flow. The magnitude of back-reaction terms should be determined from additional equations that

describe the evolution of random magnetic field and fluid motions. Since no complete theory of turbulence exists, I make a lot of approximations. The model is adjusted to agree with the results of several numerical simulations. I also apply analytical tests similar to that in Ogilvie (2003) to assure the model reproduces the basic properties of observed turbulence.

I need non-ideal induction equation (2.5) and Navier-Stokes equation (2.2) to derive how turbulence evolves. My goal is to compound reasonable equations on average squares of radial magnetic field B_r^2, perpendicular magnetic field $B_\perp^2$, isotropic velocity u^2. I also need equations on characteristic length scale of turbulence L and dimensionless magnetic helicity ξ.

Radial part of induction equation (2.5) easily gives the equation on B_r^2, when the former is multiplied by $2B_r$ and averaged over the solid angle:

$$2B_r\frac{\partial B_r}{\partial t} = 2B_r[\nabla\times[v\mathbf{e}_r\times\mathbf{B}]]_r + 2B_r[\nabla\times[\mathbf{u}\times\mathbf{B}]]_r + 2\nu_M B_r(\triangle\mathbf{B})_r, \tag{2.19}$$

where indices $()_r$ without primes denote the radial parts. The left-hand side vanishes as all time derivatives. The first term on the right-hand side represents the uniform increase of magnetic field due to flux freezing. I combine it with the continuity equation (2.9) to eliminate v derivatives. The second term is the dynamo action. It cannot be easily averaged. Characteristic turbulence length scale L may be used to approximate derivatives

$$\frac{\partial B_i}{\partial x_k}\sim\frac{B_i}{L}\mathbf{e}_k \quad\text{and}\quad \frac{\partial u_i}{\partial x_k}\sim\frac{u_i}{L}\mathbf{e}_k, \quad \mathbf{e}_k- \text{ unit vector.} \tag{2.20}$$

Then we arrive at dynamo action with characteristic timescale $\tau_{\rm dyn} = c_{Bu}\tau_{\rm edd}$ about eddy turn-over time $\tau_{\rm edd} = u/L$. The averaged expression is quadratic in magnetic field. I take coefficient to be c_{Bu1} at any B_i^2 and c_{Bu2} at any B_iB_k with $i\neq k$. The final form

of the dynamo term reads $2B_r[\nabla \times [\mathbf{u} \times \mathbf{B}]]_r = (c_{Bu1}B_r^2 + c_{Bu2}B_r(B_\theta + B_\phi))u/L$, and characteristic

$$B_r = \sqrt{B_r^2} \quad \text{and} \quad B_\theta = B_\phi = B_\perp = \sqrt{B_\perp^2} \tag{2.21}$$

should be taken. The last term on the right-hand side of equation (2.19) represents magnetic field dissipation. Dissipation term $\nu_M \triangle \mathbf{B}$ of induction equation (2.5) is macroscopic in turbulence even for vanishing magnetic diffusivity ν_M (Biskamp, 2003). I approximate radial dissipation to have a timescale $\tau_{\rm dyss} = c_{BB}\tau_{Ar}$ about Alfven timescale $\tau_{Ar} = v_{Ar}/L$. The averaged expression is also quadratic in magnetic field. I take coefficient to be c_{BB1} at any B_i^2 and c_{BB2} at any B_iB_k with $i \neq k$. Finally, $\nu_M B_r(\triangle \mathbf{B})_r = v_A(c_{BB1}B_r^2 + c_{BB2}(B_\theta + B_\phi)B_r)/L$. Collecting all the terms, I obtain

$$\frac{v}{r^4}\frac{\partial(B_r^2 r^4)}{\partial r} = \frac{-(c_{Bu1}B_r^2 + 2c_{Bu2}B_rB_\perp)u + (c_{BB1}B_r^2 + 2c_{BB2}B_rB_\perp)v_{Ar}}{L} \tag{2.22}$$

for the radial magnetic field in the absence of external energy sources.

Perpendicular part of induction equation (2.5), for example θ part, gives the equation on B_θ^2 when equation (2.5) is multiplied by B_θ and averaged over the solid angle. The flux freezing condition for perpendicular field is different from that for radial field: $B_\theta vr = \text{const}$ represents perpendicular flux freezing. I repeat the calculations made for radial field B_r to find dynamo and dissipation terms. Dynamo term takes form $(c_{Bu1}B_\theta^2 + c_{Bu2}B_\theta(B_\phi + B_r))u/L$. Dissipation term is $v_{A\theta}(c_{BB1}B_\theta^2 + c_{BB2}(B_\phi + B_r)B_\theta)/L$ with perpendicular Alfven timescale for dissipation. Here I take $B_\perp^2 = B_\theta^2 = B_\theta B_\phi = B_\phi^2$. Finally, I obtain

$$v\rho^2 r^2 \frac{\partial}{\partial r}\left(\frac{B_\perp^2}{\rho^2 r^2}\right) = \tag{2.23}$$
$$\frac{-((c_{Bu1} + c_{Bu2})B_\perp^2 + c_{Bu2}B_\perp B_r)u + ((c_{BB1} + c_{BB2})B_\perp^2 + c_{BB2}B_\perp B_r)v_{A\perp}}{L},$$

where continuity equation (2.9) is used. Radial v_{Ar} and perpendicular $v_{A\perp}$ Alfven speeds and random velocity u are

$$v_{Ar} = \frac{\sqrt{B_r^2}}{\sqrt{4\pi\rho}}, \qquad v_{A\perp} = \frac{\sqrt{B_\perp^2}}{\sqrt{4\pi\rho}}, \qquad u = \sqrt{u^2}. \tag{2.24}$$

Coefficients $c_{Bu1}, c_{Bu2}, c_{BB1}, c_{BB2}$ are yet to be determined.

Evolution equation for squared random fluid velocity u^2 can be found from momentum equation (2.3), when it is multiplied by $2\mathbf{u}$ and averaged over the solid angle. Potential energy and pressure terms average out and only three terms are left

$$2\mathbf{u}\left((\mathbf{V}\ \nabla)\mathbf{V} + \frac{\nabla(\rho\mathbf{V})}{\rho}\right) = 2\frac{\mathbf{u}[\mathbf{B}\times[\nabla\times\mathbf{B}]]}{4\pi\rho} + 2\mathbf{u}\nu\triangle\mathbf{u}. \tag{2.25}$$

I apply the same averaging procedure as for magnetic field evolution equations (2.22) and (2.23). The final result is

$$v\rho^{2/3}\frac{\partial}{\partial r}\left(\frac{u^2}{\rho^{2/3}}\right) = \frac{c_{uu}u^3 - (c_{uB1}v_A^2 + (2c_{uB1} + c_{uB2})v_{A\perp}^2 + 2c_{uB2}(v_A v_{A\perp}))u}{L}, \tag{2.26}$$

with additional three coefficients c_{uu}, c_{uB1} and c_{uB2}. Some of these and other c_{xx}-like coefficients can be taken from numerical simulations of isotropic turbulence, some of them can be inferred from analytical tests. They may not simply be set to convenient values like Ogilvie (2003) did.

2.2.3 Correspondence to Numerical Simulations

Isotropic turbulence is studied quite thoroughly in numerical simulations. Some results are reproduced by a number of researchers (see Biskamp (2003) for the review). That is why we may believe in these results and base a model on them. Three simulations of different turbulence regimes can provide four conditions that let us uniquely determine

four combinations of coefficients c_{xx}. These regimes are decaying HD turbulence, decaying MHD turbulence, and dynamo growth of small seed magnetic field. I assume then that c_{xx} are constants independent of regime and extend the derived model to any anisotropic case.

Let me consider my model in isotropic incompressible case of box turbulence. In these settings $B_r^2 = B_\theta^2 = B_\phi^2$. Squared magnetic field B^2 equals $B^2 = 3B_r^2$. Transition to the co-moving frame of averaged inflow in turbulence evolution equations (2.22), (2.23), (2.26) is done by stating $d/dt = -v\partial/\partial r$. Now I should write time derivatives instead of radius derivatives and set $r = \text{const}$, since matter is not moving anywhere from the box. I obtain equations of evolution of isotropic turbulent Alfven speed v_A and isotropic turbulent velocity u:

$$\left(u^2\right)'_t = \frac{\hat{c}_{uB} v_A^2 u - \hat{c}_{uu} u^3}{L}, \qquad \left(v_A^2\right)'_t = \frac{\hat{c}_{Bu} v_A^2 u - \hat{c}_{BB} v_A^3}{L}. \tag{2.27}$$

Here $v_A = \sqrt{B^2}/\sqrt{4\pi\rho}$ and $\rho = \text{const}$. Coefficients with hats are

$$\begin{aligned} \hat{c}_{Bu} &= c_{Bu1} + 2c_{Bu2}, \qquad \hat{c}_{BB} = \frac{c_{BB1} + 2c_{BB2}}{\sqrt{3}}, \\ \hat{c}_{uu} &= c_{uu1}, \qquad \hat{c}_{uB} = c_{uB1} + c_{uB2} \end{aligned} \tag{2.28}$$

in terms of previously defined c_{xx}.

I have a freedom to set L, because it enters the equations only in combinations c_{xx}/L, but c_{xx} are not yet determined. For simplicity of further derivation I take $L(r)$ to be the effective size of energy containing eddies for isotropic incompressible turbulence:

$$u^2 = \int_{2\pi/L}^{\infty} |u_k|^2 dk \quad \text{and} \quad v_A^2 = \int_{2\pi/L}^{\infty} |v_{Ak}|^2 dk. \tag{2.29}$$

Isotropic decay of hydrodynamic turbulence is the simplest simulation. The convenient

constant of decay is Kolmogorov constant C_{HD}. It is defined as

$$C_{HD} = E_k k^{5/3} \epsilon^{-2/3} \quad \text{with} \quad \epsilon = -\frac{d}{dt}\left(\frac{u^2}{2}\right) \quad \text{and} \quad E_k = \frac{|u_k|^2}{2}, \tag{2.30}$$

where E_k is energy spectrum, ϵ is a decay rate. Kolmogorov constant was found to be $C_{HD} \approx 1.65$ in the large set of simulations (Sreenivasan, 1995). I substitute this number into equation (2.30) and evaluate the first integral in equation (2.29) to find

$$\hat{c}_{uu} = \frac{4\pi}{(3C_{HD})^{3/2}} \approx 1.14 \tag{2.31}$$

for isotropic equations (2.27).

Isotropic decay of magneto hydrodynamic turbulence gives two conditions. MHD Kolmogorov constant is defined similarly to HD case equation (2.30) as

$$C_{MHD} = E_k k^{5/3} \epsilon^{-2/3} \quad \text{with} \quad \epsilon = -\frac{d}{dt}\left(\frac{u^2 + v_A^2}{2}\right) \quad \text{and} \quad E_k = \frac{|u_k|^2 + |v_{Ak}|^2}{2}. \tag{2.32}$$

MHD turbulence is more difficult to model numerically, but the value of $C_{MHD} \approx 2.2$ is rather rigorous (Biskamp, 2003). In addition, kinetic energy was found to decay in exactly the same rate as magnetic energy. Evaluation of the sum of two integrals (2.29) with definitions (2.32) and known C_{MHD} yields

$$\hat{c}_{BB} - \hat{c}_{Bu} = \hat{c}_{uu} - \hat{c}_{uB} \approx 2\pi \left(\frac{2}{3C_{MHD}}\right)^{3/2} \approx 1.05. \tag{2.33}$$

Dynamo simulations explore the regime $v_A^2 \ll u^2$. Exponential growth of small magnetic field corresponds to some value of coefficient $\hat{c}_{Bu}$ in equations (2.27) as

$$B^2 \propto \exp\left(\hat{c}_{Bu}\frac{ut}{L}\right). \tag{2.34}$$

External driving is purely mechanical for $v_A^2 \ll u^2$, so external source of magnetic field does not alter the picture of field amplification by dynamo. Characteristic length scale

in dynamo simulations is usually the size of energy containing eddies L consistent with definition (2.29), so renormalization of length scale is not required. Older simulations (Kida et al., 1991) have found $b = 0.39$ that corresponds to $\hat{c}_{Bu} \approx 0.61$. Later results (Schekochihin et al., 2004) indicate a bit higher value $\hat{c}_{Bu} \approx 0.7$ that I will use for my model. Finally,

$$\begin{aligned} \hat{c}_{Bu} &= 0.70, \qquad \hat{c}_{BB} = 1.75, \\ \hat{c}_{uu} &= 1.14, \qquad \hat{c}_{uB} = 0.09. \end{aligned} \tag{2.35}$$

The values of four $\hat{c}_{xx}$ (eq. [2.35]) are not enough to obtain all seven coefficients c_{xx} in equations (2.22), (2.23), (2.26) with definitions (2.28). However, the application of common sense analytical conditions to non-isotropic system of equations puts some additional constrains on c_{xx} that allows me to complete the model with as little guessing as possible.

Analytic tests are described in Appendix 2.8. This completes the derivation and verification of turbulence evolution equations (2.22), (2.23), (2.26) with coefficients

$$\begin{aligned} 4c_{BB1} &= 3.03, \qquad c_{BB2} = 0.00, \qquad c_{Bu1} = 0.41, \qquad c_{Bu2} = 0.29, \\ c_{uu} &= 1.14, \qquad c_{uB1} = 0.09, \qquad c_{uB2} = 0.00 \end{aligned} \tag{2.36}$$

that I obtain summarizing equations (2.28), (2.35), (2.85), and (2.86). However, not all major effect have been included so far.

2.2.4 Magnetic Helicity

Certain correlation called "magnetic helicity" may strongly influence magnetic field dissipation. This quantity is defined as

$$H = \int_V (\mathbf{A} \cdot \mathbf{B}) dV, \tag{2.37}$$

where $\mathbf{A}$ is a vector potential with a defined gauge condition (Biskamp, 2000). Time derivative of magnetic helicity is very small compared to the time derivative of magnetic energy in high Reynolds number astrophysical plasma (Biskamp, 2003):

$$\frac{dH}{dE_M} \frac{E_M}{H} \ll 1. \tag{2.38}$$

Constancy of magnetic helicity defines the rules of selective decay. Magnetic energy E_M decays in free turbulence down to non-zero value, allowed by constant magnetic helicity $H = \text{const}$. The final force-free configuration has zero random kinetic energy E_K and has aligned current density and magnetic field $\mathbf{j} \uparrow\uparrow \mathbf{B}$ (Biskamp, 2003).

However, the derived system of turbulence evolution equations (2.75) and, therefore, equations (2.22), (2.23), (2.26) cannot handle selective decay. Decay of magnetic energy must be modified in order to have the transition to zero dissipation rate at certain v_{Ar} and $v_{A\perp}$ as a function of magnetic helicity H. First, I should employ the proper magnetic helicity constancy. Then I should quantify the relation between critical v_{Ar}, $v_{A\perp}$, and H.

Let me consider the region S that evolves together with the mean flow of fluid. This region has the constant angle boundaries $\theta = \text{const}$ and $\phi = \text{const}$. Its radial elongation L_r scales as inflow velocity: $L_r \propto v$. The region S contains constant mass $m = \text{const}$ of matter, because matter flux through its boundaries is zero by definition. If I neglect diffusion by

random velocity, frozen magnetic field lines do not move through the boundaries of the region. Because of this, magnetic helicity in S is constant $H = \text{const}$ (Biskamp, 2003).

The simplest order of magnitude relation between magnetic energy E_M and H is

$$E_M L_H = H = \text{const} \tag{2.39}$$

in the region S, where L_H is magnetic helicity characteristic length scale (Biskamp, 2003). As magnetic field decays in turbulence, L_H grows according to equation (2.39).

I can parametrize L_H to be a fraction of L :

$$L_H = \xi L. \tag{2.40}$$

Volume of the region of interest S is

$$V = \frac{m}{\rho} \tag{2.41}$$

with $m = \text{const}$. Total magnetic energy E_M is

$$E_M = \frac{V}{8\pi}(B_r^2 + 2B_\perp^2). \tag{2.42}$$

I substitute relations (2.40), (2.41), and (2.42) into equation (2.39) and use the definitions (2.24) of Alfven velocities to come to

$$L(v_{Ar}^2 + 2v_{A\perp}^2)\xi = \text{const}. \tag{2.43}$$

Now I need to include ξ into the turbulence evolution equations (2.22), (2.23), (2.26) so that they can handle selective decay. The natural limit of L_H growth is the characteristic size of energy containing eddies L. So regime $\xi \ll 1$ corresponds to non-helical turbulence and regime $\xi \sim 1$ to turbulence, where magnetic helicity significantly inhibits dissipation. Regime $\xi \gg 1$ does not occur. The basic way to modify the equations is to decrease by

a smooth multiplier $f(\xi) < 1$ magnetic field decay rate. For qualitative agreement with experiment (Biskamp, 2003) I can employ

$$f(\xi) = \exp(-\xi), \tag{2.44}$$

what means that magnetic energy dissipation timescale becomes $\exp(\xi)$ times larger. Terms with both u and one of v_{Ar} and $v_{A\perp}$ in magnetic field evolution equations (2.22), (2.23) do not need to be modified, since random velocity energy decays to zero and these terms do not matter. However, I multiply the term with both random velocity and Alfven speed in turbulent velocity evolution equation (2.26) by $\exp(-\xi)$ to make random velocity u decay to zero.

2.2.5 System of Equations with Source Terms

With only minor corrections, the final system of equations can be written down. In general, turbulence has external sources of energy that sustain finite magnetic and kinetic energies even in case of box turbulence. I can add source terms to incompressible system (2.75) and consequently to the system of compressible equations (2.22), (2.23), (2.26).

System (2.75) with coefficients (2.35) and (2.36), modifier (2.44), and source terms reads

$$\frac{d(v_{Ar}^2)}{dt} = \frac{(0.70v_{Ar}^2 + 0.58(v_{A\perp} - v_{Ar})v_{Ar})u - 3.03v_{Ar}^3\exp(-\xi)}{L} + c_0\frac{v_p^3}{L}, \tag{2.45a}$$

$$\frac{d(v_{A\perp}^2)}{dt} = \frac{(0.70v_{A\perp}^2 + 0.29(v_{Ar} - v_{A\perp})v_{A\perp})u - 3.03v_{A\perp}^3\exp(-\xi)}{L} + c_1\frac{v_p^3}{L}, \tag{2.45b}$$

$$\frac{d(u^2)}{dt} = \frac{0.09(v_{Ar}^2 + 2v_{A\perp}^2)u\exp(-\xi) - 1.14u^3}{L} + c_2\frac{v_p^3}{L}, \tag{2.45c}$$

where v_p is the mean square particles speed (eq. [2.18]) and c_0, c_1, and c_2 are dimensionless

coefficients. These coefficients determine the rates of external energy input into turbulent fields.

I denote by σ the ratio of total turbulent energy to thermal energy:

$$\sigma = \frac{E_K + E_M}{E_{\rm th}}, \quad \text{so that} \quad \sigma\frac{3RT}{2\mu} = \sigma\frac{v_p^2}{2} = \frac{u^2}{2} + \frac{v_{Ar}^2}{2} + v_{A\perp}^2. \tag{2.46}$$

Unlike conventional plasma magnetization, magnetization σ with definition (2.46) includes the energy of random fluid motions.

In the dynamic equilibrium of constant v_{Ar}, $v_{A\perp}$, u and known ξ system (2.45) gives three algebraic equations for ratios v_{Ar}/v_p, $v_{A\perp}/v_p$, and u/v_p as functions of c_0, c_1, and c_2. To estimate c_0, c_1, and c_2 I take stationary driven isotropic turbulence with kinetic energy E_K equal to magnetic energy E_M. Isotropic turbulence of interest has $v_{Ar} = v_{A\perp} = u/\sqrt{3}$. Such turbulence occurs far from the central object, where outer magnetization is a constant σ_∞. Solving system (2.45) I obtain using equation (2.46)

$$c_0 = c_1 \approx 0.124\sigma_\infty^{3/2}, \qquad c_2 = 3c_0 \approx 0.371\sigma_\infty^{3/2} \tag{2.47}$$

in case $\xi = 0$. I apply these values even to turbulence with $\xi > 0$. Total external energy input Q_+ into E_K and E_M is

$$Q_+ \approx 0.742\sigma_\infty^{3/2}\frac{v_p^3}{L}. \tag{2.48}$$

This energy adds up to thermal gas energy after being processed through turbulence. However, I do not adjust my dynamical equations (2.13) and (2.16) for Q_+. I self-consistently omit external heating and radiative or diffusive cooling. This omission is physically justified sufficiently far from the central object, where cooling Q_- balances external heating Q_+. It is also justified in the inner region, where both Q_+ and Q_- are negligible compared to the internal driving and energy advection. Internal driving

represents build-up of self-sustained turbulence in a converging flow due to conservation of magnetic flux (Coker & Melia, 2000).

Only the size L of energy containing eddies should be specified to complete the derivation of closed system of equations. In the case when energy input Q_+ does not matter, the problem has only one relevant scale that is the size of the system r. Therefore, I can set L to be the fraction of radius

$$L = \gamma r \tag{2.49}$$

with the proportionality constant γ about unity. However, energy input from external sources Q_+ is relatively large far from the central source. This causes medium with constant Q_+, constant v_p, and constant σ_∞ to have constant size of largest eddies

$$L = L_\infty = \text{const} \tag{2.50}$$

because of equation (2.48). This equality holds for radii larger than some $r_0 \approx L_\infty/\gamma$. I introduce a function with a smooth transition from relation (2.49) for $r \ll r_0$ to relation (2.50) for $r \gg r_0$:

$$L(r) = L_\infty \left(1 - \exp\left(-\frac{\gamma r}{L_\infty}\right)\right) \tag{2.51}$$

This completes derivation and verification of 8 equations (2.9), (2.13), (2.16), (2.22), (2.23), (2.26), (2.43), (2.51)with coefficients (2.35), (2.36), and (2.47) on 8 quantities $L(r)$, $\xi(r)$, $v(r)$, $u(r)$, $v_{Ar}(r)$, $v_{A\perp}(r)$, $T(r)$, $\rho(r)$ that are the characteristic turbulent length scale, normalized magnetic helicity, matter inflow velocity, turbulent velocity, radial Alfven speed, perpendicular Alfven speed, temperature, and density. I rewrite the equations once again in terms of named quantities:

$$4\pi\rho v r^2 = \dot{M}, \tag{2.52a}$$

$$vv'_r + \frac{r_{\rm g}c^2}{2(r-r_{\rm g})^2} + \frac{R}{\mu}\frac{(\rho T)'_r}{\rho} + \frac{(\rho u^2)'_r}{3\rho} + \frac{(r^2\rho v^2_{A\perp})'_r}{\rho r^2} - \frac{(r^4\rho v^2_{Ar})'_r}{2\rho r^4} = 0, \tag{2.52b}$$

$$vv'_r + \frac{r_{\rm g}c^2}{2(r-r_{\rm g})^2} + w'_r + \frac{5}{3}uu'_r + 2(v^2_{A\perp})'_r = 0 \quad \text{with} \tag{2.52c}$$

$$w = w_R = \frac{RT}{\mu}\left(0.54\frac{3K_3(\Theta^{-1}) + K_1(\Theta^{-1})}{\Theta(4K_2(\Theta^{-1}) - 1)} + 1.69\right) + \frac{5}{6}u^2 \quad \text{or} \quad w = w_{NR} = \frac{5RT}{2\mu} + \frac{5}{6}u^2,$$

$$v\frac{(\rho v^2_{Ar}r^4)'_r}{\rho r^4} = \frac{3.03v^3_{Ar}\exp(-\xi) - (0.70v^2_{Ar} + 0.58(v_{A\perp} - v_{Ar})v_{Ar})u}{L} - \frac{0.64}{L_\infty}\left(\frac{RT_\infty\sigma_\infty}{\mu}\right)^{3/2}, \tag{2.52d}$$

$$v\rho r^2\left(\frac{v^2_{A\perp}}{\rho r^2}\right)'_r = \frac{3.03v^3_{A\perp}\exp(-\xi) - (0.70v^2_{A\perp} + 0.29(v_{Ar} - v_{A\perp})v_{A\perp})u}{L} - \frac{0.64}{L_\infty}\left(\frac{RT_\infty\sigma_\infty}{\mu}\right)^{3/2}, \tag{2.52e}$$

$$v\rho^{2/3}\left(\frac{u^2}{\rho^{2/3}}\right)'_r = \frac{1.14u^3 - 0.09(v^2_{Ar} + 2v^2_{A\perp})u\exp(-\xi)}{L} - \frac{1.93}{L_\infty}\left(\frac{RT_\infty\sigma_\infty}{\mu}\right)^{3/2}, \tag{2.52f}$$

$$L(v^2_{Ar} + 2v^2_{A\perp})\xi = 3L_\infty\xi_\infty\frac{RT_\infty\sigma_\infty}{\mu}, \tag{2.52g}$$

$$L = L_\infty\left(1 - \exp\left(-\frac{\gamma r}{L_\infty}\right)\right). \tag{2.52h}$$

Here $\Theta = kT/m_ec^2$. Since my prescription for external driving of turbulence is $Q_+ = \text{const}$, I take v_p and L to be constant in the source terms. Relativistic w_R (eq. [2.14]) and non-relativistic w_{NR} (eq. [2.15]) values of enthalpy w are employed. In the next section I describe the values of boundary conditions and parameters for the equations I solve.

2.3 Boundary Conditions and Parameters

The system (2.52) consists of 5 differential and 3 algebraic equations and should be integrated inward from some outer boundary at r_x. This requires knowledge of at least

eight constants. Seven of them are the values "at infinity" L_∞, T_∞, ρ_∞, ξ_∞, u_∞, $v_{Ar\infty}$, $v_{A\perp\infty}$. The eighth is the accretion rate $\dot{M}$. It is usually determined by some extra condition and is not adjustable. I assume isotropic turbulence with $E_K = E_M$ at the outer boundary. Therefore,

$$v_{Ar\infty} = v_{A\perp\infty} = \left(\frac{RT_\infty\sigma_\infty}{\mu}\right)^{1/2} \quad \text{and} \quad u_\infty = \left(\frac{3RT_\infty\sigma_\infty}{\mu}\right)^{1/2}, \tag{2.53}$$

and I have one model parameter σ_∞ instead of 3 velocities $v_{Ar\infty}$, $v_{A\perp\infty}$, and u_∞. Another adjustable parameter of the model is γ that determines the size of energy containing eddies L near the object (eq. [2.52h]).

Parameter γ is not free in principle, but its value cannot be determined within the proposed theory. Neither there exist anisotropic MHD simulations that could provide γ. All simulations to date show γ to be within $0.2 - 2$ (Tennekes & Lumley, 1972; Landau & Lifshitz, 1987; Biskamp, 2003) in both HD and MHD case. I assume the same range of γ in my calculations.

2.3.1 Outer Medium Transition

Bondi radius

$$r_B = r_{\rm g}\frac{c^2}{c_\infty^2} \quad \text{with} \quad c_\infty = \left(\frac{5RT_\infty}{3\mu}\right)^{1/2} \tag{2.54}$$

is the natural length scale of the spherical accretion flow (Bondi, 1952). Density ρ and temperature T of plasma are constant for radii $r \gg r_B$, because gravitational energy and gas regular kinetic energy are negligible there compared to gas internal energy (Bondi, 1952). Averaged magnetic field and averaged random velocity are also constant for $r \gg r_B$, because constant external energy input balances dissipation in this region. As a consequence, $\xi = \xi_\infty$ and $L = L_\infty$ for $r \gg r_B$.

I set the outer boundary at $r_x = 3r_B$, where matter is almost uniform. Length scale L_∞ should be determined from known external energy input Q_+ and outer magnetization σ_∞. However, Q_+ is not known. I assume for simplicity $L_\infty = \gamma r_B$, so that L changes its behavior near r_B together with temperature and density.

Bondi radius is about $r_B \approx 3 \times 10^5 r_{\rm g}$ for our Galactic Center (Ghez et al., 2003). The properties of gas at $3r_B$ are somewhat constrained from observations. I take the values for uniformly emitting gas model with temperature $T_\infty \approx 1.5 \times 10^7$ K, electron and total number densities $n_{e\infty} = 26{\rm cm}^{-3}$, $n_\infty = 48{\rm cm}^{-3}$ (Baganoff et al., 2003) at $r_x = 3r_B$ that corresponds to $5''$ in the sky. The presence of dense cold component can make the average temperature much lower and the average density much higher (Cuadra et al., 2006), but I am leaving these uncertainties for future research.

Expanding and colliding hyperalfvenic stellar winds provide magnetic field into the region. Its strength near Bondi radius is not known. Only the very general estimate can be made. Matter magnetization is likely to be lower than the saturation value of $\sigma_\infty = 1$. I take the values in the range $\sigma_\infty = 0.001 - 1$ to cover all reasonable magnetization states of matter at $3r_B$. If magnetic field is rather a product of decay than dynamo amplification, then the local dimensionless helicity ξ may be close to unity. I cover the range $\xi_\infty = 0.001 - 0.5$ in simulations to determine the possible dynamical significance of non-zero magnetic helicity.

2.3.2 Transition to Rotationally Supported Flow

The system of equations (2.52) has the same property as spherically symmetric system of hydrodynamic equations (Bondi, 1952): subsonic solution exists for all accretion rates

$\dot{M}$ up to maximum $\dot{M}^*$, transonic solution is valid for the only value $\dot{M}^*$, and no solution exists for $\dot{M} > \dot{M}^*$. The solution with

$$\dot{M} = \dot{M}^*(\text{for transonic solution}) \tag{2.55}$$

is preferable, because it has the highest rate of energy transfer towards the equilibrium state of the system matter-SMBH. The same argument is valid for a general hydrodynamic nozzle (Landau & Lifshitz, 1987). It is reasonable to expect that maximum mass flux solution for system with magnetic field (2.52) also obeys the condition (2.55). However, even small amount of angular momentum can change the picture.

Every real astrophysical accretion flow has non-zero specific angular momentum at the outer boundary

$$l = \lambda r_{\rm g} c, \quad \text{or equivalently,} \quad l = v_{K\rm cir} r_{\rm cir}, \tag{2.56}$$

where $r_{\rm cir}$ is a radius where matter becomes rotationally supported and $v_{K\rm cir}$ is Keplerian velocity at $r_{\rm cir}$. General Newtonian expression for Keplerian velocity at radius r is

$$v_K = c\sqrt{\frac{r_{\rm g}}{2r}}. \tag{2.57}$$

At larger radii $r > r_{\rm cir}$ angular momentum exerts relatively small force $F_l \propto l^2/r^3$ on plasma, since F_l decreases with radius faster than gravitational force $F_{\rm g} \propto r_{\rm g} c/r^2$. Numerical simulations (Cuadra et al., 2006) suggest $r_{\rm cir} \sim 3 \times 10^3 r_{\rm g}$ for our Galactic Center.

When angular momentum (eq. [2.56]) is large, $\lambda \gg 1$, it should be able to travel outward through the outer quasi-spherical solution by means of $r\phi$ component of stress tensor $t_{\alpha\beta}$. The angular averaged form of this component is

$$t_{r\phi} = \frac{< B_r B_\perp >_\Omega}{4\pi}, \tag{2.58a}$$

where I neglect the kinetic part for the estimate. It can be transformed with the aid of Schwartz formula $< xy > \leq \sqrt{< x^2 >}\sqrt{< y^2 >}$ into inequality

$$t_{r\phi} \leq \frac{B_r B_\perp}{4\pi} \tag{2.58b}$$

with definitions (2.21) of rms B_r and $B_\perp$.

Let us take a disk (Shakura & Sunyaev, 1973) with height H and write the angular momentum transfer equation as

$$\frac{d(r^2 H t_{r\phi})}{dr} = 0. \tag{2.59a}$$

The result of integration is (Gammie & Popham, 1998)

$$\dot{M} l = 4\pi H r^2 t_{r\phi}, \tag{2.59b}$$

in case of large dimensionless angular momentum $\lambda \gg 1$ (Gammie & Popham, 1998). I take specific angular momentum l from equation (2.56) and the accretion rate to be

$$\dot{M} = 2\pi r H \rho v. \tag{2.60}$$

I substitute angular momentum l from relation (2.56), accretion rate $\dot{M}$ from equation (2.60), Alfven speeds from definitions (2.24), Keplerian velocity from equation (2.57), and inequality (2.58b) on $t_{r\phi}$ into angular momentum transfer equation (2.59b) to obtain

$$\frac{v v_K}{v_A v_{A\perp}} \sqrt{\frac{r_{\rm circ}}{r}} = 2\chi, \qquad \chi \leq 1 \tag{2.61a}$$

that should be valid at any radius r. Sometimes, this inequality is valid for $r > r_{\rm cir}$ if it is valid at $r_{\rm cir}$, so that condition (2.61a) can in some cases be simplified to

$$\frac{v v_K}{v_A v_{A\perp}} \leq 2 \quad \text{at} \quad r_{\rm cir}. \tag{2.61b}$$

Height of the disk H cancels out of final expression, thus conditions (2.61) are approximately valid even for flows with $H \approx r$. Such flows are likely to describe the

realistic transition region from outer quasi-spherical inflow to inner rotational solution. There are no extra degrees of freedom to put conditions on the surface of compact object, so I consider an object to be effectively a black hole.

Condition of angular momentum transport (2.61) may be stronger than maximum accretion rate condition (2.55). This depends on the value of specific angular momentum l and viscous α parameter (Shakura & Sunyaev, 1973). Viscous α is approximately $\alpha \sim \chi\ \sigma$ according to my definitions (2.46) and (2.61a). If $\alpha \gtrsim 0.5$, then accretion proceeds without direct dynamical effect of rotation (Narayan et al., 1997). Thus, two types of solutions are possible:

- maximum accretion rate solutions that describe radial flows with small angular momentum $l \lesssim cr_{\rm g}$ or large viscosity $\chi\ \sigma \gtrsim 0.5$ (subsection 2.4.1),
- flows with the rotational support that work for large angular momentum $l \gg cr_{\rm g}$ and small viscosity $\chi\ \sigma \lesssim 0.5$ (subsection 2.4.2).

The condition (2.61) gives a crude estimate of the inflow velocity and accretion rate $\dot{M}$, since it assumes specific angular momentum to be constant down to $r_{\rm cir}$. As matter travels to $r_{\rm cir}$, the amount of specific angular momentum left becomes smaller. Nevertheless, I calculate the solutions with effective angular momentum transport using condition (2.61) to illustrate the dependence of accretion rate on model parameters for the rotating flow.

2.4 Results

2.4.1 Maximum Rate Solution

Let me first disregard the angular momentum transport condition (2.61) and calculate the flow with small angular momentum $l \ll r_{\rm g}c$, when mean rotation is not dynamically important.

The system of equations I solve (2.52) can be rewritten as

$$\frac{(F_i)'_r}{F_i} = \frac{N_i(\mathbf{F}, r)}{D} \quad \text{for} \quad i = 1..8. \tag{2.62}$$

Here $F_i(r)$ are 8 functions I solve for, $N_i(\mathbf{F}, r)$ are function- and radius- dependent numerators, and

$$D = 1 - \frac{v^2}{V_s^2} \tag{2.63}$$

is a common denominator. Critical velocity V_s is

$$V_s^2 = c_{sg}^2 + 2v_{A\perp}^2 \quad \text{with} \quad c_{sg}^2 = c_s^2 + \frac{5u^2}{3}. \tag{2.64}$$

Effective sound speed c_{sg} is equal to that of plasma with effective particles velocity $v_{pg}^2 = v_p^2 + u^2$.

According to the maximum-rate condition (2.55) I search for a smooth solution that has a sonic point at some radius r_s. The condition at r_s is $D(r_s) = 0$. Zero denominator requires all the numerators $N_i(\mathbf{F}, r)$ to be zero at r_s. It can be shown from system (2.52) that all eight conditions $N_i(\mathbf{F}(r_s), r_s) = 0$ collapse into just one, what indicates that maximum accretion rate solution is smooth. Two equalities

$$D(r_s) = 0 \quad \text{and} \quad N_1(\mathbf{F}(r_s), r_s) = 0 \tag{2.65}$$

give the missing 8-th condition on $\dot{M}$ for system (2.52) and the sonic radius r_s. Thus, I have 7 conditions at the boundary at $3r_B$ and 1 condition somewhere in the region. I employ the shooting method to search for $\dot{M}$ and r_s that satisfy the relation (2.65).

I obtain the Bondi hydrodynamic model (Bondi, 1952), if I set all Alfven velocities and turbulent velocity to zero and use non-relativistic prescription for enthalpy w_{NR} (eq. [2.52c]). Therefore, the accretion rate $\dot{M}$ equals Bondi accretion rate of monatomic gas

$$\dot{M}_B = \frac{\pi}{4} r_{\rm g}^2 c^4 \rho_\infty \left(\frac{3\mu}{5RT_\infty}\right)^{3/2} \approx 4 \times 10^{-6} M_\odot {\rm year}^{-1} \tag{2.66}$$

in the limiting case of no turbulence. The number is calculated for the Black Hole in our Galactic Center with $r_{\rm g} = 1.1 \times 10^{12}$cm (Ghez et al., 2003), $T = 1.5 \times 10^7$K, and $n \approx 48{\rm cm}^{-3}$ (Baganoff et al., 2003). Accretion rate $\dot{M}$ appears to be lower than $\dot{M}_B$ when turbulent energy is non-zero (Fig. 2.1).

Inhibition of accretion by turbulence has the following explanation. First, energy of magnetic field increases inward, therefore it exerts back-reaction force stopping matter (Shvartsman, 1971). Second, magnetic field serves a very effective mechanism of energy conversion from gravitational to thermal via dissipation of turbulence (Igumenshchev & Narayan, 2002). Larger thermal energy corresponds to larger gas pressure that also stops matter. Within the deduced model I can estimate the actual decrease of accretion rate $\dot{M}$ from Bondi value $\dot{M}_B$.

I take my reference model to have the values $\gamma = 1$, $\sigma_\infty = 1$, $\xi_\infty = 0.025$ of, correspondingly, dimensionless scale of turbulence, outer magnetization, and outer magnetic helicity. The found accretion rates are $0.14\dot{M}_B$ for non-relativistic equation of state and $0.24\dot{M}_B$ for relativistic equation of state. I can now consider the whole ranges of all three parameters and explain the observed correlations between them and accretion

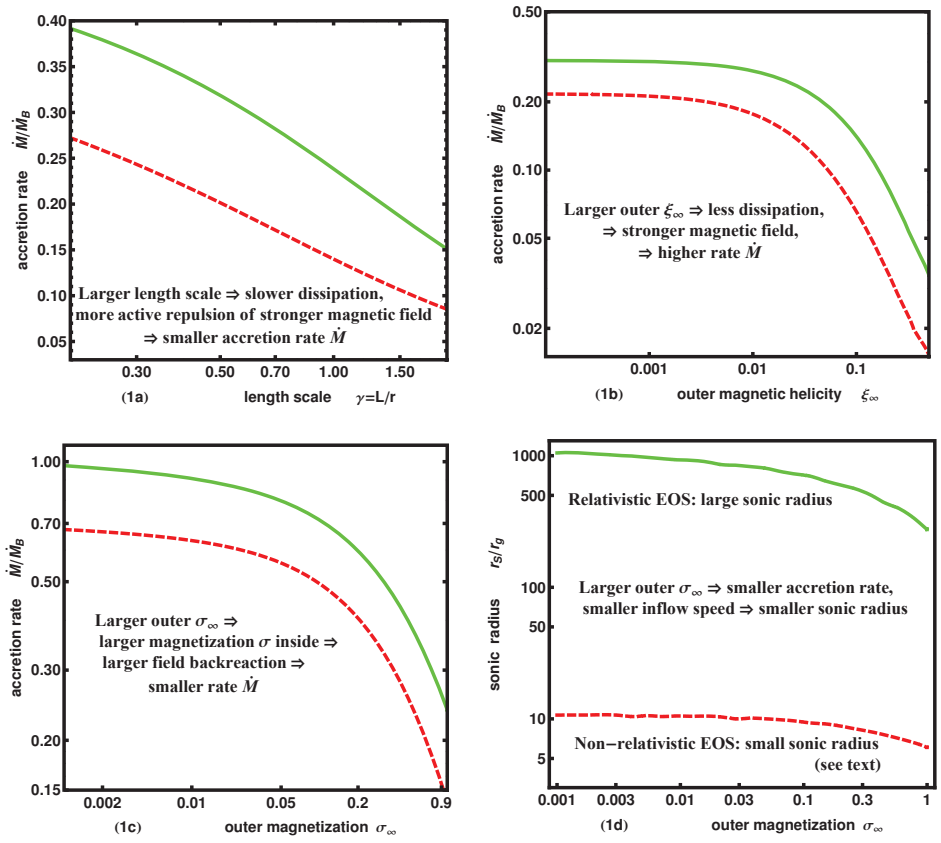

Figure 2.1.— **Maximum accretion rate solution.** Dependence of the accretion rate in units of Bondi rate on dimensionless parameters: characteristic length scale γ (Fig. 2.1a), outer magnetic helicity ξ_∞ (Fig. 2.1b), outer matter magnetization σ_∞ (Fig. 2.1c). Dependence (Fig. 2.1d) of sonic radius on outer magnetization σ_∞. I take the reference model to have the following values of parameters: $\gamma = 1$, $\sigma_\infty = 1$, $\xi_\infty = 0.025$. One parameter is varied to make one plot. Non-relativistic 1-T equation of state (dashed) versus relativistic 1-T equation of state (solid).

rate $\dot{M}$.

Larger flow magnetization σ results in lower accretion rate $\dot{M}$. Larger magnetic field and turbulent velocity field exerts larger back-reaction force on matter. Also, transformation of gravitational energy into thermal happens more readily if magnetization is larger. Larger thermal energy means larger gas pressure and larger back-reaction force on matter striving to fall onto the central object.

Several factors lead to higher magnetization. Larger outer magnetization σ_∞ makes magnetization in the entire flow σ larger. Then larger dissipation length scale γ allows for smaller dissipation of magnetic field. Larger magnetic helicity ξ also lowers magnetic energy dissipation and leads to larger magnetization σ. These correlations can be observed on Figure 2.1. Increase of the relative length scale of energy containing eddies γ from 0.2 to 2 results (Fig. 2.1a) in about 2 times drop in accretion rate $\dot{M}$. Accretion rate stays constant (Fig. 2.1b) at small values of outer magnetic helicity ξ_∞. However, $\dot{M}$ drops an order of magnitude as turbulence approaches highly helical state at outer boundary $3r_B$ with ξ_∞ close to 0.5. The dependence of $\dot{M}$ on outer magnetization σ_∞ is not quite steep: accretion rate gradually decreases about 4 times as outer magnetization increases 3 orders of magnitude from 0.001 to 1. Surprisingly, accretion rate does not rise to $\dot{M}_B$ (Fig. 2.1c) even for very small outer magnetization $\sigma_\infty \sim 0.001$ for non-relativistic equation of state. Even small outer magnetic field increases inwards and influences flow dynamics.

Accretion rate is systematically about 40% higher (Fig. 2.1) for relativistic equation of state (solid line) compared to non-relativistic equation of state (dashed line), because magnetized system has some properties of a non-magnetized one. Formula for Bondi mass accretion rate (2.66) is valid only for non-relativistic monatomic gas that has an adiabatic

index $\Gamma = 5/3$. Accretion rate is higher for lower Γ and is about 3 times larger (Shapiro & Teukolsky, 1983) in case of ultrarelativistic particles with adiabatic index $\Gamma = 4/3$. Accretion rate $\dot{M}$ is determined by relation (2.65) at a sonic radius r_s that is smaller than $10^3 r_{\rm g}$ (Fig. 2.1d). Electrons become relativistic at somewhat larger radius about $10^3 r_{\rm g}$ in the solutions of system (2.52). This leads to gas adiabatic index Γ (magnetic field is disregarded) lower than 5/3 at sonic point $r = r_s$. Thus accretion rate is considerably larger in case of relativistic equation of state.

It is also instructive to trace the dependence of sonic radius r_s on parameters. Sonic radius for hydrodynamic accretion of non-relativistic monatomic gas is equal to several Schwarzschild radii $r_s = 2 - 10 r_{\rm g}$ (Beskin & Pidoprygora, 1995). Sonic radius is a considerable fraction of r_B for a gas with adiabatic index Γ substantially smaller than 5/3 for non-magnetized accretion (Bondi, 1952). Magnetized accretion has the same properties. Non-relativistic EOS (solid line) results in very small sonic radius $r_s = 7 - 11 r_{\rm g}$ (Fig. 2.1d). Sonic radius for relativistic EOS (dashed line) is $r_s = 300 - 1200 r_{\rm g}$ about the radius where electrons become relativistic $r \sim 10^3 r_{\rm g}$. The value of sonic radius drops several times as plasma outer magnetization σ_∞ increases from 0.001 to 1. As outer magnetization σ_∞ increases, accretion rate drops (Fig. 2.1c), because density ρ and gas inflow speed v decrease. Then effective sound speed V_s equals the inflow speed v at a point closer to the black hole.

Inflow velocity v as well as other characteristic velocities of the flow are depicted on Figure 2.2 as functions of radius r for the reference model with $\sigma_\infty = 1$, $\gamma = 1$, $\xi_\infty = 0.025$. All velocities are normalized to the free-fall speed

$$v_{ff} = c\sqrt{\frac{r_{\rm g}}{r - r_{\rm g}}}. \tag{2.67}$$

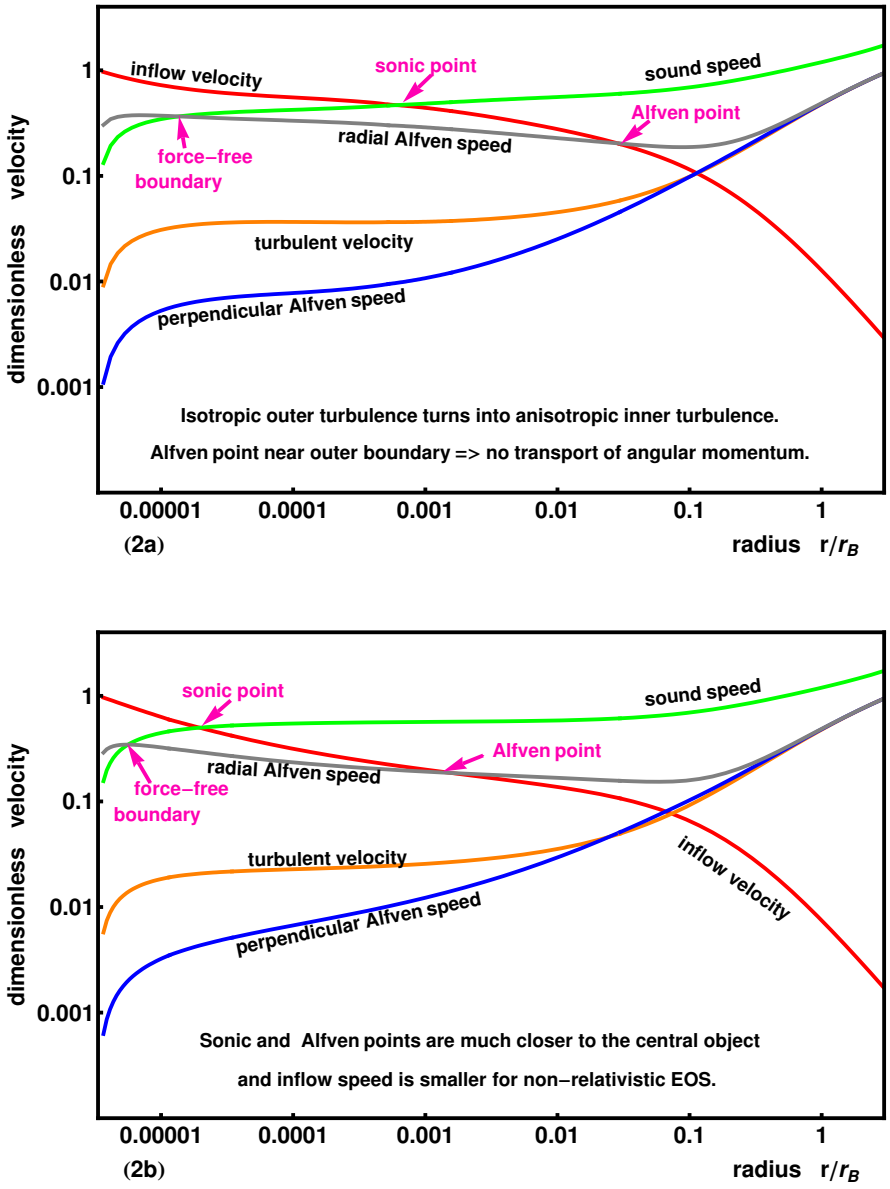

Figure 2.2.— Flow velocities, normalized to free-fall speed versus radius for **maximum-rate solution**: sound speed, inflow velocity, radial Alfven speed, 1-D perpendicular Alfven speed, turbulent velocity. Parameters $\sigma_\infty = 1$, $\gamma = 1$, $\xi_\infty = 0.025$. Relativistic 1-T equation of state is on Figure 2.2a, non-relativistic 1-T EOS is on Figure 2.2b.

I also normalize perpendicular Alfven velocity $v_{A\perp}$ and turbulent speed u to one dimension. Horizontal line on Figure 2.2 corresponds to radial dependence $r^{-1/2}$.

Inflow velocity v monotonically increases inwards, whereas sound speed c_s monotonically decreases with intersection almost at the sonic point. Radial Alfven velocity v_{Ar}, perpendicular Alfven velocity $v_{A\perp}$ and turbulent velocity u (Fig. 2.2) start out as constants from the outer boundary at $3r_B$, where turbulence is sustained by external pumping. Then these velocities increase and deviate from one another. Radial Alfven velocity v_{Ar} appears to be much larger than $v_{A\perp}$ and u in the inner accretion region. This fulfills the expectations of earlier models (Shakura & Sunyaev, 1973; Scharlemann, 1983; Beskin & Karpov, 2005). At small radius turbulence is driven by freezing-in amplification of magnetic field and random velocity. Left-hand sides of turbulence evolution equations (2.52d), (2.52e), and (2.52f) dominate over corresponding terms with external driving for radius $r \lesssim 10^4 r_{\rm g}$. Internal driving of v_{Ar} is much more effective than driving of $v_{A\perp}$ and u. Therefore radial Alfven velocity v_{Ar} is larger than other two speeds. This refutes any model with isotropic magnetic field.

Several pairs of lines intersect on velocity plot (Fig. 2.2). I consider three main intersection points for the reference model with $\sigma_\infty = 1$, $\gamma = 1$, $\xi_\infty = 0.025$, and relativistic EOS (Fig. 2.2a). Crossing of inflow velocity v and sound speed c_s occurs almost at the sonic point at r_s, determined by relation (2.65) with critical velocity V_s (eq. [2.64]). No plasma waves can escape from within the region with high inflow velocity $v > V_s$. Approximately $c_s \approx V_s$ at sonic point $r_s \approx 6 \times 10^{-4} r_B$, because of low magnetization $\sigma \approx 20\%$ in that region (Fig. 2.3a). Alfven point is determined by equality $v = v_{Ar}$ at radius r_A. Alfven waves cannot escape from within the region where inflow speed is greater than radial Alfven speed v_{Ar}. Equality holds at relatively large radius $r_A \approx 0.03 r_B$. The

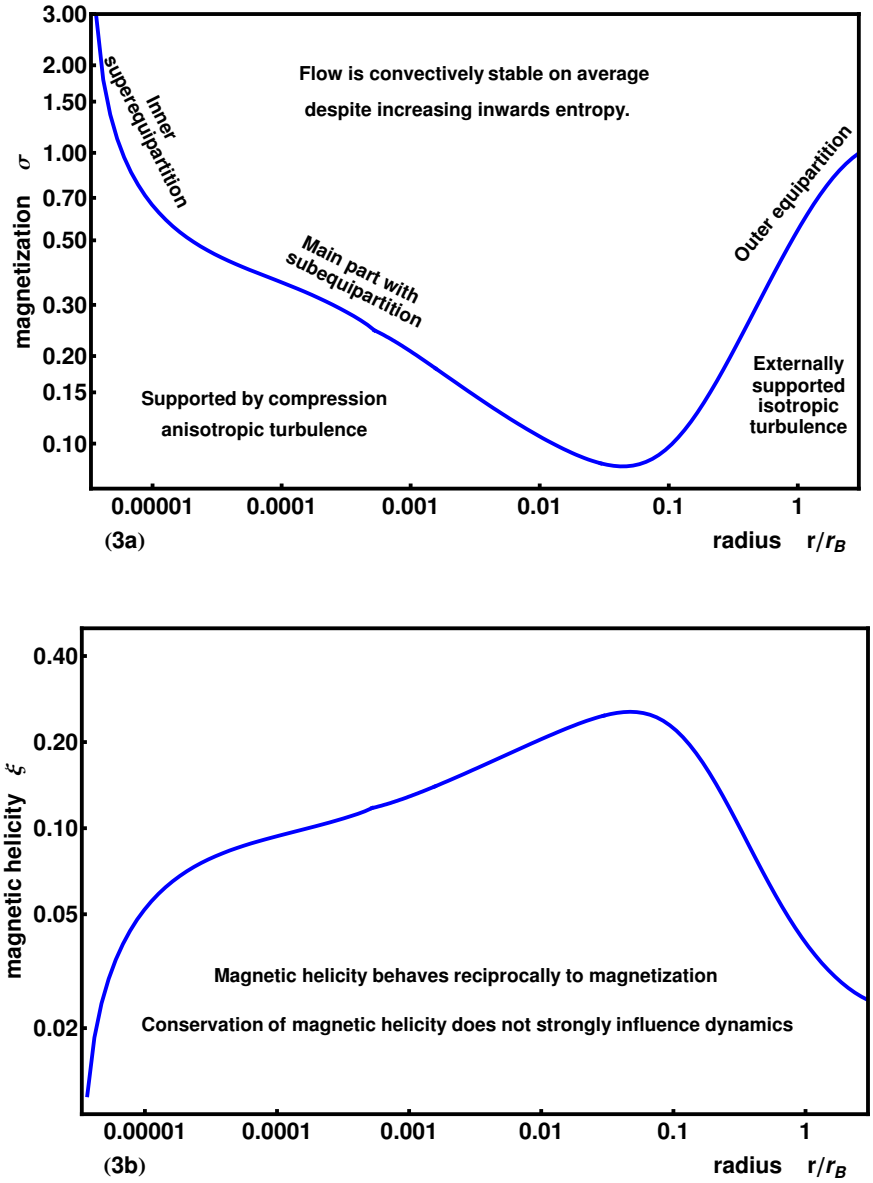

Figure 2.3.— Magnetization σ versus dimensionless distance from the compact object r/r_B is on Figure 2.3a. Dimensionless magnetic helicity ξ versus dimensionless distance from the compact object r/r_B is on Figure 2.3b. Both are for the **maximum-rate solution** with relativistic equation of state.

third combination of the same three velocities also gives a characteristic intersection point. Radial Alfven speed v_{Ar} increases faster inwards and becomes equal to sound speed c_s at about $r \approx 4r_{\rm g}$. Further relative increase of v_{Ar} leads to magnetic energy dominated flow, what can be traced on magnetization plot (Fig. 2.3a).

Figure 2.3a shows evolution of plasma magnetization σ with radius r for the reference model. Thermal energy equipartition assumption does not hold, id est turbulent energy does not equal to constant fraction of thermal energy $\sigma \neq$ const. Magnetization σ varies more than one order in magnitude from 0.07 to 3. It starts out at initial $\sigma_\infty = 1$ at $3r_B$, where turbulence is supported by external energy input $Q_+ =$ const. Then σ deviates down as r decreases. Magnetization σ drops, because length scale L decreases with radius r that causes turbulence to decay faster. At about $0.03r_B$ magnetization starts to rise as internal turbulence driving takes over. Inflow velocity v slightly deviates up from Alfven velocity v_A as r decreases. Since internal driving rate is proportional to v (left-hand sides of equations (2.52d), (2.52e), and (2.52f) dissipation rate is proportional v_{Ar}, parameter σ grows slightly with decreasing radius. The growth is about a factor of 5 for 3.5 orders of magnitude decrease in radius. Magnetization σ jumps up in the region very close to the event horizon of the black hole. However, this jump may originate from inconsistent treatment of General Relativity.

The dependence of magnetic helicity ξ on radius is shown on Figure 2.3b. Helicity ξ behaves almost reciprocally to magnetization σ from Figure 2.3a. Such a behavior can be seen from magnetic helicity equation (2.52g). Magnetization σ decreases order of magnitude during the transition from externally supported to internally supported turbulence around $r \approx 0.03r_B$. Magnetic helicity ξ also increases an order of magnitude from 0.025 to 0.2. Then ξ gradually decreases down to initial value. Thus magnetic helicity

ξ does not change dynamics if it is initially small $\xi_\infty \lesssim 0.1$. Only when ξ_∞ is large, accretion rate drops.

Deviation of inflow velocity v from the free-fall scaling $r^{-1/2}$ makes a density profile in magnetized flow different from that in standard Advection Dominated Accretion Flow (ADAF). I consider the flow where energy is only advected inward. Nevertheless, I obtain

$$\rho \propto r^{-\zeta} \quad \text{with} \quad \zeta \approx 1.25 \tag{2.68}$$

almost independently on the parameters or the equation of state, somewhat shallower than $\rho \propto r^{-1.5}$ in ADAF.

The only question left is how well this flow with maximum accretion rate can describe the real situation with large angular momentum l. Given the solution of the system (2.52) I can check whether the condition for effective angular momentum transport condition (2.61) holds. Condition (2.61) breaks when evaluated for maximum-rate solution with parameters ξ_∞, σ_∞, and γ within the chosen ranges and circularization radius $r_{\rm cir} > r_{\rm g}$. This means a flow with maximum accretion rate is unable to effectively transport the angular momentum outward. The same conclusion can be made simpler. The transport of angular momentum is a magnetic process. So, l can be transported only by Alfven waves. However, Alfven waves cannot escape from the region within $r_A \approx 0.03 r_B$ from the compact object that makes angular momentum transport impossible even from quite large radius.

2.4.2 Solution with Effective Angular Momentum Transport

Solution with large outer angular momentum $l \gg r_{\rm g} c$ and small viscosity may have properties, substantially different from those of maximum-rate solution. The actual details

of the solution and allowed accretion rate depend on how this angular momentum is transported. For the simple estimate I suppose that the accretion rate is determined by the equality in angular momentum transport condition (2.61). Maximum accretion rate $\dot{M}$ for condition (2.61) appears to be about two orders of magnitude lower than Bondi rate $\dot{M}_B$ (eq. [2.66]).

I add one parameter in modeling: unknown circularization radius $r_{\rm cir}$ for specific angular momentum l (eq. [2.56]). I take it to be $r_{\rm cir} = 10^3 r_{\rm g}$ for the reference model. Plots of the accretion rate versus model parameters are shown on Figure 2.4. Dependencies for the rotating solution (Fig. 2.4) have the opposite slopes to those for the maximum-rate solution on Figure 2.1. Accretion rate $\dot{M}$ increases with increasing outer magnetization σ_∞ (Fig. 2.4b) and increasing outer magnetic helicity ξ_∞ (Fig. 2.4c). Both effects lead to higher plasma magnetization σ. I showed in the previous subsection 2.4.1 that the magnetic field plays an inhibiting role on matter inflow, and that the larger the magnetic field is, the smaller the accretion rate $\dot{M}$ is. However, the correlation between the magnetic field and accretion rate is the opposite in case of the rotating flow. Accretion rate quantitatively agrees with relation for ADAF flows $\dot{M} \sim \alpha \dot{M}_B \sim \sigma\chi \dot{M}_B$ (Narayan et al., 1997) with $\sigma \sim 0.01$ at $r_{\rm cir}$ (Fig. 2.6a).

The allowed by condition (2.61) inflow speed v is proportional to the product of radial Alfven speed v_{Ar} and perpendicular Alfven speed $v_{A\perp}$. Larger magnetic field results in larger transport of angular momentum outward, so larger inflow velocity v and larger accretion rate are possible. Larger outer magnetization σ_∞ and larger outer magnetic helicity ξ_∞ both lead to higher magnetization σ and higher magnetic field. Inhibiting effect of magnetic field is smaller in case of lower accretion rates $\dot{M}$ and lower inflow velocities v. Lower v results in lower relative driving of turbulence that makes magnetic field weaker.

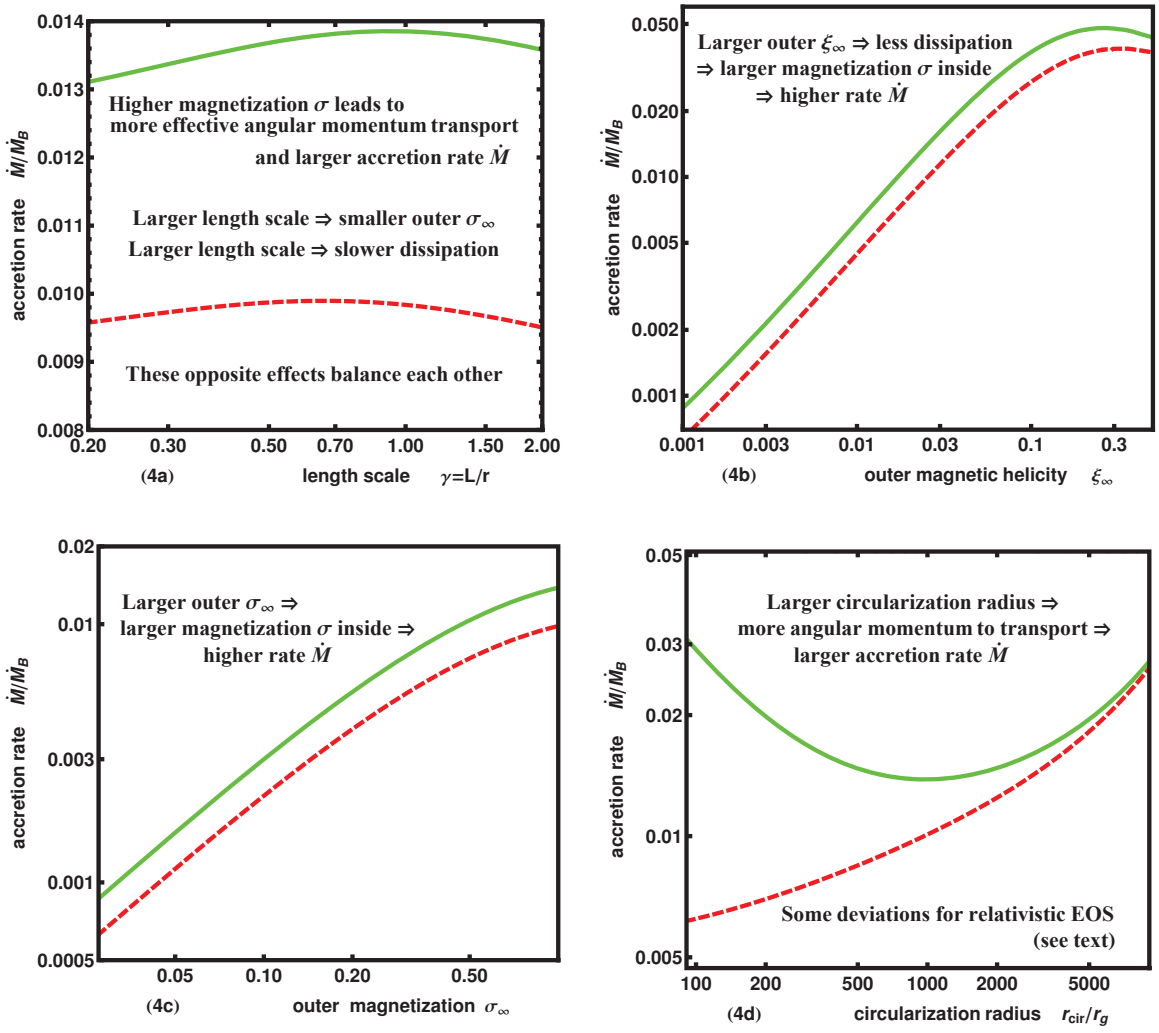

Figure 2.4.— **Solution with angular momentum transport.** Dependence of the accretion rate in units of Bondi rate on dimensionless parameters: characteristic length scale γ (Fig. 2.4a), outer magnetic helicity ξ_∞ (Fig. 2.4b), outer magnetization σ_∞ (Fig. 2.4c), and circularization radius $r_{\rm cir}$ in units of $r_{\rm g}$ (Fig. 2.4d). I take the reference model to have the following parameters: $\gamma = 1$, $\sigma_\infty = 1$, $r_{\rm cir} = 10^3 r_{\rm g}$, $\xi_\infty = 0.025$. Non-relativistic 1-T equation of state (dashed) versus relativistic 1-T equation of state (solid).

Weaker magnetic field has weaker influence on dynamics. In sum, larger magnetic field B results in larger accretion rate $\dot{M}$, when it needs to transfer angular momentum.

The dependence of $\dot{M}$ on length scale γ is obscured by the dependence of external driving on γ. Accretion rate $\dot{M}$ is smaller for smaller magnetic field, but the state of low magnetization can be achieved in two different ways. Firstly, magnetic field decays faster when L decreases. However, the plasma at circularization radius $r_{\rm cir} = 10^3 r_{\rm g}$ is still partially influenced by the outer boundary conditions. Internal driving does not depend on L, whereas external driving is stronger and magnetization σ is higher, when L is small. The described two effects balance each other and make accretion rate $\dot{M}$ almost independent of dimensionless length scale γ (Fig. 2.4a).

Accretion rate $\dot{M}$ decreases with the decrease of circularization radius $r_{\rm cir}$ (Fig. 2.4d) for non-relativistic equation of state. To explain this, I trace on Figure 2.5b all the quantities that enter angular momentum transport condition (2.61b) for the reference model. Velocities normalized by the free-fall speed (eq. [2.67]) are shown on Figure 2.5b. Inflow speed v and radial Alfven velocity v_{Ar} reach free-fall scaling at about $0.02 r_B$. Only perpendicular Alfven velocity $v_{A\perp}$ has a different dependence on distance from the central object for $r < 0.02 r_B$. Because $v_{A\perp}$ decreases with radius, the allowed v and $\dot{M}$ are smaller for smaller circularization radius.

However, the accretion rate increases for small circularization radii for 1-T equation of state (Fig. 2.4d, solid line). This is the consequence of the decreasing gas adiabatic index, when electrons reach relativistic temperatures. Solutions with lower adiabatic index are known to have larger accretion rates (Bondi, 1952) that is equivalent to the lower inflow speeds v in the solutions for the fixed matter inflow rate. Velocity v (Fig. 2.5a)

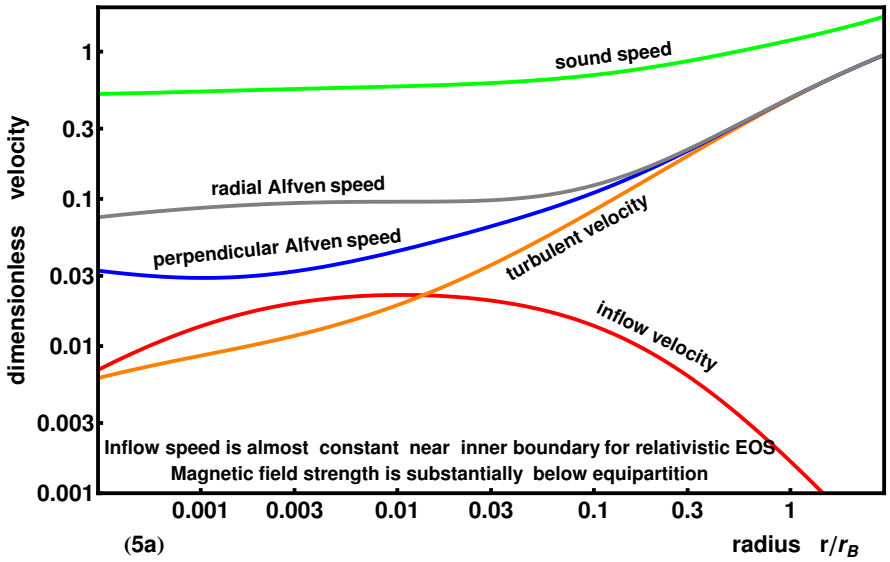

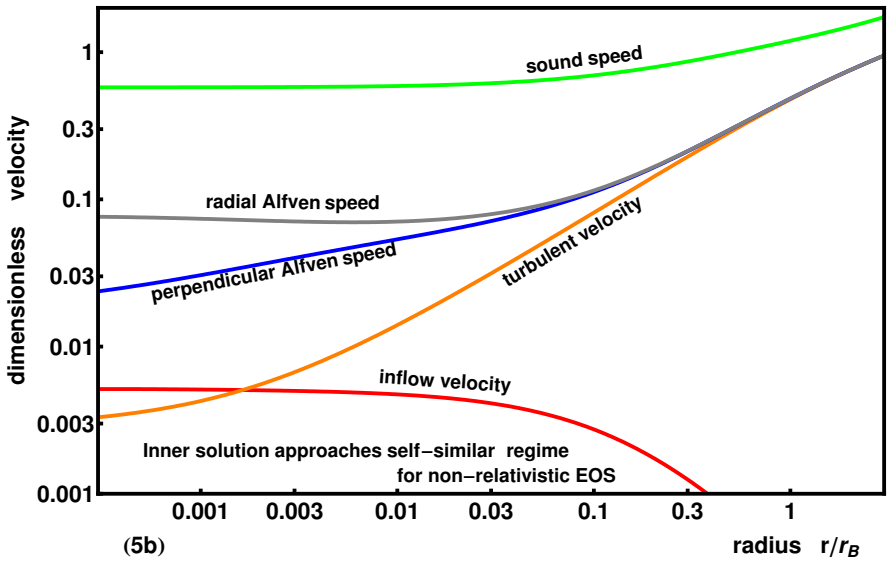

Figure 2.5.— Flow velocities, normalized to free-fall speed versus radius for **solution with angular momentum transport**: sound speed, inflow velocity, radial Alfven speed, 1-D perpendicular Alfven speed, turbulent velocity. Parameters $\sigma_\infty = 1$, $\gamma = 1$, $\xi = 0.025$, $r_{\rm cir} = 10^3 r_{\rm g}$. Relativistic 1-T EOS on Figure 2.5a, non-relativistic 1-T EOS on Figure 2.5b.

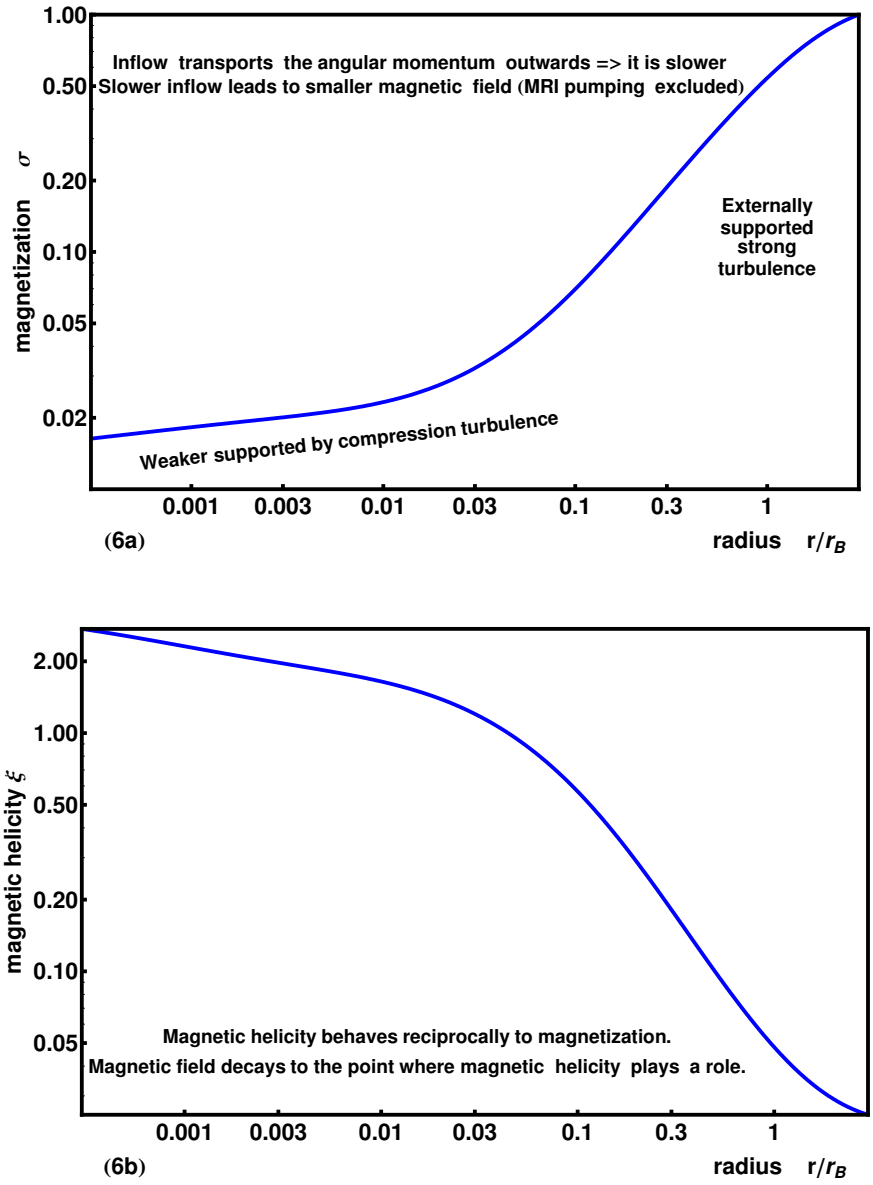

Figure 2.6.— Magnetization σ versus dimensionless distance from the compact object r/r_B is on Figure 2.6a. Dimensionless magnetic helicity ξ versus dimensionless distance from the compact object r/r_B is on Figure 2.6b. Both are for **solution with angular momentum transport**. Circularization radius is $r_{\rm cir} = 10^3 r_{\rm g}$.

starts deviating down from the self-similar $r^{-1/2}$ solution at approximately $10^3 r_{\rm g}$, making the solutions with higher $\dot{M}$ possible. In fact, condition (2.61) for the solutions with small $r_{\rm cir}$ becomes critical at some fixed point $r_d > r_{\rm cir}$ instead of reaching equality at $r_{\rm cir}$ (eq. [2.61b]). Therefore, according to condition (2.61a), maximum value of the inflow speed grows with the decrease of circularization radius as $v \propto r_{\rm cir}^{-1/2}$, explaining the rise of accretion rate for small $r_{\rm cir}$ (Fig. 2.4d, solid line) for 1-T equation of state.

Solution for non-relativistic equation of state, in turn, possess its own feature. Self-similar flow (see Appendix 2.9) settles in at $10^3 r_{\rm g}$, making accretion rate almost independent on circularization radius (Fig. 2.4d). Magnetic helicity ξ in such a flow is a number about unity what is consistent with self-similar solution obtained in Appendix 2.9. Self-similar flow can not establish for 1-T equation of state, because relativistic effects become important before it establishes and break self-similarity.

In fact, magnetization σ and magnetic helicity ξ (Fig. 2.6) are not constant at small radii for correct 1-T EOS, because these relativistic corrections work. At about $0.01 r_B$ magnetization reaches almost constant level $\sigma \approx 0.02$ (Fig. 2.6a) and then starts to slightly deviate down, because equilibrium σ for matter with lower gas adiabatic index $\Gamma < 5/3$ is lower. Magnetic helicity ξ behaves (Fig. 2.6b) the opposite way to magnetization σ : magnetic helicity reaches $\xi \approx 1.5$ at $0.01 r_B$ and starts to slightly deviate up as the radius decreases.

2.5 Discussion of the Model

I present the sophisticated analytical model to determine the properties of spherical magnetized accretion. The common assumptions of magnetic field isotropy and thermal

equipartition are released, but many assumptions are still left. As usually in fluid dynamics a lot of simplifications are made during the course of elaboration. The validity of almost everything can be questioned. The system of equations (2.52) may not describe the real flow (subsection 2.5.1) or may have some inaccuracies (subsection 2.5.2). Gas cooling may not be neglected (subsections 2.5.3). Convection and diffusion may change the flow structure (subsection 2.5.4). The equation of state was also found to influence the dynamics (subsection 2.5.5). Let me discuss all these topics and determine the practical significance of the model.

2.5.1 Real Flow

Presented model is partially applicable to the real systems. It may describe some gas flows onto Supermassive Black Holes in Low Luminosity Galactic Centers, in particular in the center of our Galaxy. These flows are geometrically thick (Narayan & Yi, 1995) and may have low angular momentum (Moscibrodzka et al., 2006). However, the real flows may have properties that my model cannot handle in its current state. First of all, the sources of matter and external driving should be explicitly accounted for. Secondly, the self-consistent angular momentum transport theory is needed.

The material is mainly supplied to the central parsec of the Milky Way by stellar winds (Quataert, 2004). The wind-producing stars have a broken power-law distribution as a function of radius (Baganoff et al., 2003). Some stars are as close to the central black hole as $0.1r_B$ (Ghez et al., 2003). The stars supply too much material to be accreted, therefore there exist an outflow (Quataert, 2004). Bondi radius coincides with the radius where inflow starts to dominate outflow in numerical simulations with the accretion rate

$\dot{M} \sim 10^{-6} M_{\odot}\text{year}^{-1}$ (Cuadra et al., 2006). Maximum accretion rate in the solution with zero angular momentum is $0.2\dot{M}_B \approx 10^{-6} M_{\odot}\text{year}^{-1}$ and $0.01\dot{M}_B$ for the rotating flow. So that the transition from the outflow to the inflow happens at $r \gtrsim 10^5 r_{\rm g}$.

I can show that outflow from $r \gtrsim 10^5 r_{\rm g}$ does not change the accretion rate from calculated. Outflows substantially alter the value and the sign of inflow velocity v in the system (2.52). However, the differences in inflow velocity do not influence any other quantity as long as three conditions are satisfied:

1. v is much smaller than gas particles velocity v_p, bulk kinetic energy of gas is negligible in the outflow region,
2. external driving of turbulence Q_+ dominates over internal driving there,
3. condition on $\dot{M}$ is set in the inflow region.

The first two conditions are satisfied down to $r \sim 10^4 r_{\rm g}$ (Fig. 2.2 and Fig. 2.5). The third condition holds for maximum rate solution, because condition on $\dot{M}$ is set at the sonic point about $10^3 r_{\rm g}$ from the central object. It also hold for the solution with angular momentum transport, because the condition on $\dot{M}$ is usually set at the inner boundary $10^3 - 10^4 r_{\rm g}$. All three above conditions hold, hence outflows of stellar winds do not substantially change the accretion rate or any quantity in the system.

2.5.2 Treatment of Magnetic Field

The long history of accretion theory has many accepted models based on ideas, extended beyond the area of applicability of these ideas. For example, general relativity was substituted with Paczynski-Wiita gravitational potential (Paczynski & Wiita, 1980; Shakura & Sunyaev, 1973). Magnetic field was long treated similar to the normal

matter (Narayan & Yi, 1995; Coker & Melia, 2000). Displacement current was neglected in magnetic field dynamics that allowed to treat magnetic field without electric field (Scharlemann, 1983). System of viscous equations describe viscosity by a single parameter (Shakura & Sunyaev, 1973; Landau & Lifshitz, 1987; Landau et al. , 1984; Biskamp, 2003). Gyrokinetics is used to solve the problems with non-Maxwellian distribution functions (Sharma et al., 2007a), power-law non-thermal electrons are usually present in plasma (Yuan et al., 2002).

Described above model is extended in several ways, mainly with regard to magnetic field. Isotropic MHD system of turbulent equations (2.27) describes the real box collisional turbulence quite well, because it corresponds to convergent set of simulations. Collisionality assumes that medium behaves like many particles with short-range interactions. However, astrophysical medium of interest is always collisionless with prevailing long-range interactions. I inconsistently use the results of numerical simulations of collisional MHD (eqs. [2.1-2.6]) with magnetic resistivity ν_M on the order of viscosity ν, because the realistic simulations of collisionless plasma turbulence are not done and are unlikely to be done in the near future (Schekochihin et al., 2004).

Observations of astrophysical turbulence may give more information than numerical simulations. A special case of collisionless plasma is plasma with random kinetic energy much smaller than random magnetic energy. This regime is a good picture of Sun corona with all plasma effects into play (Aschwanden, 2005). Dissipation of magnetic loops with low kinetic energy proceeds mainly via reconnections. The timescale of reconnective dissipation was found to be

$$\tau_{\rm rec} \approx 20 \frac{L}{v_A} \tag{2.69}$$

in solar flares (Noglik et al., 2005). The same number was also predicted by Lazarian &

Vishniac (1999). Collisional MHD turbulence has much smaller dissipation timescale

$$\tau_{\rm diss} \approx 1 \frac{L}{v_A} \tag{2.70}$$

(eqs. [2.27, 2.35]). Plasma has large kinetic energy in the outer region of accretion flow, where turbulence is externally supported. Timescale $\tau_{\rm diss}$ (eq. [2.70]) may be appropriate there. Kinetic energy E_K decreases to smaller radii and magnetization σ increases (Fig. 2.2) in case of zero angular momentum (2.4.1). Accretion flow there may resembles solar Corona (Aschwanden, 2005). Dissipation timescale may increase order of magnitude and be close to $\tau_{\rm rec}$ (eq. [2.69]). This increase would lead to much lower accretion rate, because higher magnetic field leads to lower $\dot{M}$. Matter infall may eventually proceed through channels of lower magnetic field (Igumenshchev, 2006).

Even if I assume that box isotropic turbulent system of equations (2.27) with coefficients (2.35) is applicable to isotropic turbulence, there are at least four complications in building the full anisotropic theory.

First of all, I need to introduce arbitrary coefficients c_{uB2}, c_{BB2}, c_{Bu2} to describe isotropization of anisotropic magnetic field and anisotropic energy transfer between magnetic field and fluid motions. Reasonable values of these coefficients were taken to satisfy rather loose analytical tests (Appendix 2.8). However, changes in these coefficients do not lead to dramatically different accretion rate or flow structure. Setting $c_{BB2} = c_{BB1}$ instead of $c_{BB2} = 0$ leads to only 10% of $\dot{M}$ change for the reference model. All seven introduced coefficients c_{xx} may themselves depend on anisotropy of the magnetic field. The details of anisotropic MHD are still debatable (Goldreich & Sridhar, 1995; Boldyrev, 2006). I leave the incorporation of anisotropic MHD model into accretion theory for future work.

Secondly, the presented theory is not general relativistic. Accretion rate $\dot{M}$ appears to be insensitive to the choice of gravitational potential. The condition on $\dot{M}$ is set at about $10^3 r_{\rm g}$ in case of relativistic EOS and zero angular momentum l. Sonic point is situated close to the black hole at $r_s = 5 - 10 r_{\rm g}$ for non-relativistic equation of state. But 1% increase of $\dot{M}$ leads to the sonic point at $r_s > 100 r_{\rm g}$, independent of the way to mimic general relativity. However, the region near the black hole is important, because part of synchrotron IR radiation as well as part of radio emission comes from several Schwarzschild radii (Narayan et al., 1998; Falcke & Markoff, 2000; Marrone et al., 2007). Thus, to fully constrain theory by observations general relativistic magnetohydrodynamics is a must.

In third, magnetic helicity H involves numerous complications. Magnetic helicity evolves in the region that is frozen into matter. The distance $L_{||}$ between radial boundaries of this region is proportional to inflow velocity v, thus $L_{||}$ increases with increasing v and at some point $L_{||} > r$, whereas size in the angular direction is about $L = \gamma r$. A part of the region is getting sucked into the black hole, while a part is still situated at fairly large radius r. Equation of magnetic helicity evolution (2.52g) holds only if I assume even redistribution of magnetic helicity over the mass of plasma. This holds for frozen magnetic field, but in reality diffusion and convection are present. Diffusion may change the results for H (eq. [2.52g]) as well as for the entire flow pattern. I also leave these uncertainties for future research.

In fourth, it was recently suggested by Beskin & Karpov (2005) that ions and electrons should be viewed in accretion as confined by magnetic field lines. This is the opposite of standard picture where magnetic field lines are frozen into matter (Scharlemann, 1983). The former case has higher heating rate of matter under contraction (Beskin & Karpov, 2005), because of conservation of the first adiabatic invariant $I = 3cp_t^2/(2eB) = \text{const}$

(Landau & Lifshitz, 1975). Here p_t is a particles momentum in the direction perpendicular to **B**. However, only highly magnetized flows with magnetization $\sigma > 1$ conserve I. Non-linear collective interactions of particles in low-σ plasma are likely to isotropize their distribution. When particles are heated isotropically under contraction, general Magneto-Hydrodynamics (eqs. [2.1-2.6]) works (Landau et al. , 1984) and heating rate stays unchanged. Magnetization in computed models is below unity (Fig. 2.3a and Fig. 2.6a). Thus application of first adiabatic invariant conservation to magnetized accretion flow seems irrelevant.

Finally, mean rotation of the flow also creates anisotropy. Because the inner gas rotates faster than the outer, MagnetoRotational Instability (MRI) works. It produces the additional driving of magnetic field that may be concurrent to other sources. MRI (Hawley & Balbus, 2002) has a timescale

$$\tau_{MRI} = -\left(r\frac{d(l/r^2)}{dr}\right)^{-1}. \tag{2.71}$$

When MRI timescale becomes larger then dynamic timescale $\tau_{\rm dyn} = r/v$, field amplification occurs mainly because of regular shear tangential motion, instead of regular radial motion. MRI may be crucial even in the region without rotational support. Full consideration of effects of angular momentum on the flow is the subject of the next study.

2.5.3 Radiative Cooling

The system of equations (2.52) describes the accretion flow, where all the energy is stored in the same piece of matter where it initially was. There is no energy loss by diffusive or radiative cooling. But whether such a model is realistic.

Let me estimate the radiative cooling first. Line cooling is more effective than

bremsstrahlung cooling for temperatures about $T_\infty \approx 1.5 \times 10^7 K$. Line cooling function is $\Lambda \approx 6 \times 10^{-23} n^2 (T/10^7 K)^{-0.7}$ erg cm^{-3} s^{-1} (Sutherland & Dopita, 1993). Thus characteristic cooling time $\tau_{\rm cool}$ is

$$\tau_{\rm cool} = \frac{3RT\rho}{2\Lambda\mu} \approx 1 \times 10^{12} {\rm s} \tag{2.72}$$

for our Galactic Center accretion. The dynamic timescale $\tau_{\rm dyn} = r/v$ for accretion with rate $\dot{M} = 0.1\dot{M}_B$ (eq. [2.66]) is

$$\tau_{\rm dyn} = \frac{\rho r^3}{\dot{M}} \approx 5 \times 10^{10} {\rm s} \tag{2.73}$$

with continuity equation (2.9) at radius $r = r_B$ (eq. [2.54]). Cooling time is about 20 times larger than inflow time in the region where outflows dominate. Nevertheless, anisotropy of stellar winds may lead to significant cooling of some clumps of matter (Cuadra et al., 2005). Even the disk may form (Cuadra et al., 2006). Careful calculation with line cooling is yet to be done.

2.5.4 Convection & Diffusion

The system (2.52) does not include diffusive or convective transport of quantities. Thus the system represents Advection-Dominated flow, where magnetic field and gas can exchange energy between each other. The exact model would include transport of momentum, energy, magnetic field, magnetic helicity that may or may not influence the dynamics.

First or all, any type of convective or diffusive motion would happen at a speed v_c not exceeding the maximum of turbulent speeds, radial Alfven speed $v_c < v_{Ar}$. This leads to the transition from convection dominated to advection dominated flow at several dozens

$r_{\rm g}$ in the case with rotation (Abramowicz et al., 2002). Correspondingly, inflow speed v becomes large $v_c \sim v$ (Gammie & Popham, 1998). Transport becomes ineffective at $r \lesssim r_A$, where r_A is the radius of Alfven point. According to Fig. 2.2a, Alfven point in my spherical solutions lies at $r_A \sim 0.03 r_B$. Thus diffusion and convection are strongly suppressed in the inner flow. By the same reason, magneto-thermal instability (MTI)(Parrish & Stone, 2005) is not supposed to play any role for spherical inflow, but may play a role in a case with rotation. For the non-conductive convective stability criterion see Appendix 2.10.

However, speed of electrons v_e may overcome the speed of sound c_s, so electron conduction may in principle transport energy from within r_A (Johnson & Quataert, 2007). It is yet unclear whether electron conduction is suppressed at high inflow velocity $v > v_{Ar}$, because electrons may be bound to the field lines of tangled magnetic field. The efficiency of conduction is a free parameter. If efficiency is close to maximum and conduction is not inhibited, then accretion rate may be $1-2$ orders of magnitude lower than Bondi rate $\dot{M}_B$ (Johnson & Quataert, 2007), thus accretion rate would be limited by conduction and not by backreaction of the magnetic field. Other types of energy transport (Parrish & Stone, 2005) may kick in for lower accretion rates. The correct calculation with magnetic field and better prescription for conductivity is yet to be done.

2.5.5 Equation of State

The difference in accretion rate $\dot{M}$ between one-temperature relativistic and 1-T non-relativistic EOSs is up to 40% for maximum-rate solution (subsection 2.4.1) and up to several times for solution with effective angular momentum transport (subsection 2.4.2). Solution with smaller gas adiabatic index Γ has larger accretion rate $\dot{M}$ (Shapiro &

Teukolsky, 1983). Gas adiabatic index gradually falls from $\Gamma = 5/3$ to $\Gamma = 1.43$ in case of relativistic EOS as matter approaches the black hole.

However, the electron temperature T_e is unlikely to be equal to ion temperature T_i. Electron temperature T_e is usually modelled to be lower than T_i (Narayan & Yi, 1995). This two-temperature model has lower gas pressure support and larger gas adiabatic index Γ than 1-T model with $T = T_i$. Lower gas pressure leads to higher accretion rate, larger Γ leads to lower accretion rate. The combination of these two effects is expected to change the accretion rate by about the same 40% as between relativistic and non-relativistic 1-T EOSs. The exact details depend on the two-temperature model chosen.

2.6 Observations

Proposed quasi-spherical magnetized accretion model is aimed to explain plasma flow onto SuperMassive Black Hole Sgr A* in our Galactic Center. Many observations of this source are made. These observations reasonably agree with the results of my model.

A common misconception about Chandra X-Ray observations of Sgr A* exists in literature. X-Rays mainly originate in the region that lies further than Bondi radius r_B from the central object. Thus characteristic density ρ_∞ and temperature T_∞ far from the Black Hole can be found (Baganoff et al., 2003). If one knows the mass M, this automatically gives Bondi accretion rate $\dot{M}_B$ (eq. [2.66]). However, accretion rate is not necessarily determined by this formula (2.66), unlike some papers suggest (Bower et al., 2005). In my model accretion rate $\dot{M}$ is independent on radius and is smaller than $\dot{M}_B$.

IR (Eckart et al., 2006a) and Radio (Shen, 2006) observations are difficult to interpret,

because fluxes in these wavebands depend strongly on the accretion model. Density of matter ρ is better constrained by observations than accretion rate $\dot{M}$. The general agreement (Yuan et al., 2002) is that density ρ should be lower than in Bondi solution ρ_B in the region close to the black hole. Solutions with outflows (Yuan et al., 2003) and Convectively-Dominated flows (Quataert & Gruzinov, 2000a) were invented to explain this lower density. Magnetized solution without angular momentum does well the same job. Let me consider the reference magnetized model with $\sigma_\infty = 1$, $\gamma = 1$, $\xi_\infty = 0.025$, $l = 0$, 1-T relativistic equation of state. The ratio of density in a reference magnetized model to density in a non-magnetized solution is

$$\frac{\rho_{\rm magn}}{\rho_{\rm nonmagn}} \approx 0.27 \quad \text{at} \quad 10 r_{\rm g}. \tag{2.74}$$

Density in a magnetized model is much lower than in a non-magnetized one. However, all types of models can be made to fit the data by adjusting temperature (Quataert & Gruzinov, 2000b), whether advection dominated or convection or outflow dominated.

Faraday rotation of submillimeter radiation offers a good differentiation mechanism between ADAF flows and flows with outflows or convection. Rotation measure is proportional to both magnetic field and electron density and has a relativistic temperature factor (Marrone et al., 2007). Model B predicts magnetization $\sigma = 0.7$ and number density $n = 2 \cdot 10^7 {\rm cm}^{-3}$ at $3 r_{\rm g}$ that is consistent with (Hawley & Balbus, 2002). The observed Faraday rotation measure is ${\rm RM} = -6 \cdot 10^{-5} {\rm rad\ m}^{-1}$. (Marrone et al., 2007). Fitting the relativistic rotation measure for temperature gives $T_e = 4 \cdot 10^{10}$ K in excellent agreement with (Sharma et al., 2007a). Accretion rate in the reference model is about $9 \cdot 10^{-7} M_\odot {\rm year}^{-1}$, what is 30 times lower than in (Sharma et al., 2007a). However, the electron density in my model is close to that in the rotating model (Sharma et al., 2007a), because inflow velocity in the rotating model is α times lower. For densities to agree I need

$\alpha \sim 0.03$ that is somewhat smaller than found in numerical simulations $\alpha \gtrsim 0.2$ (Hawley & Balbus, 2002). This means my solution overestimates density n by about a factor of 5, what results in larger then observed IR flux (Eckart et al., 2006a). Effects of angular momentum transport, outflows (Yuan et al., 2002) or conduction (Johnson & Quataert, 2007) must come into play to allow for successful fitting for both IR flux and Faraday rotation measure.

2.7 Conclusions

Though many ways of dealing with inefficient accretion were invented, my approach is substantially different from all previous efforts. **I elaborated the model that**

- has very few free parameters,
- self-consistently includes averaged turbulence, combining geometrical effects of freezing-in amplification with dissipation,
- ties evolution of random magnetic field and random velocity field to numerical simulations,
- connects outer externally supported turbulence to inner self-sustained turbulence,
- predicts the accretion rates $\dot{M}$ and flow patterns for the flows with negligible angular momentum,
- gives the order of magnitude estimate of $\dot{M}$ for large angular momentum flows.

The model predicts

- accretion rate $\dot{M}$ of magnetized fluid $0.2 - 0.7$ of Bondi rate $\dot{M}_B$ even for small outer magnetization σ_∞,

- subequipartition magnetic field in the outer part of the flow and superequipartition in the inner part,
- several times lower density than in Bondi model near the central object, what with addition of other effects would explain the observations of Sgr A*,
- half an order of magnitude effect of different equations of state on the accretion rate,
- unimportance of magnetic helicity conservation,
- ineffectiveness of convection. Convection and diffusion should be accounted for together.

The future version of the model will include

- more anisotropic effects, in particular, magneto-rotational instability,
- two-temperature equations of state,
- full treatment of angular momentum transport,
- diffusion of momentum, heat and magnetic field.

Acknowledgements

The author is grateful to Ramesh Narayan for fruitful discussions. The author thanks Pascal Demoulin for useful comments about magnetic helicity and Ya. N. Istomin for general comments.

2.8 Appendix: Analytical Tests

Let me consider my model in anisotropic incompressible case of box turbulence. I substitute $-v\partial/\partial r = d/dt$ in equations (2.22), (2.23), (2.26) and set $r = \text{const}$. The box

has infinite volume. I express some of unknown c_{xx} in terms of known $\hat{c}_{xx}$ from equations (2.28). The system now reads

$$\frac{d(v_{Ar}^2)}{dt} = \frac{(\hat{c}_{Bu}v_{Ar}^2 + 2c_{Bu2}(v_{A\perp} - v_{Ar})v_{Ar})u - (\sqrt{3}\hat{c}_{BB}v_{Ar} + 2c_{BB2}(v_{A\perp} - v_{Ar}))v_{Ar}^2}{L}, \tag{2.75a}$$

$$\frac{d(v_{A\perp}^2)}{dt} = \frac{(\hat{c}_{Bu}v_{A\perp}^2 + c_{Bu2}(v_{Ar} - v_{A\perp})v_{A\perp})u - (\sqrt{3}\hat{c}_{BB}v_{A\perp} + c_{BB2}(v_{Ar} - v_{A\perp}))v_{A\perp}^2}{L}, \tag{2.75b}$$

$$\frac{d(u^2)}{dt} = \frac{(\hat{c}_{uB}(v_{Ar}^2 + 2v_{A\perp}^2) - c_{uB2}(v_{Ar} - v_{A\perp})^2)u - c_{uu}u^3}{L}. \tag{2.75c}$$

I need to determine three coefficients c_{BB2}, c_{uB2}, and c_{Bu2} and prove the entire system (2.75) makes sense.

There are three kinds of analytical tests divided by the degree of their certainty. The tests from the first group have solid physical grounds. The tests from the second group represent how turbulence is believed to work, these are the general relations with clear physical insight. The third group of tests consists of the order of magnitude relations and the disputable ideas.

The tests of the first group are proven to work. Only one test of this kind can be applied to our system. This is the energy decay test. Free incompressible MHD turbulence has decreasing with time total energy, because energy decrease corresponds to the increase of entropy of the system gas/magnetic field (Landau et al. , 1984).

$$\frac{d}{dt}\left(\frac{v_{Ar}^2 + 2v_{A\perp}^2 + u^2}{2}\right) < 0 \quad \text{for at least one of} \quad v_{Ar}, v_{A\perp}, u \quad \text{non} - \text{zero}. \tag{2.76}$$

I take sum with proper coefficients of the right-hand sides of system (2.75). Then I maximize it with respect to $v_{A\perp}/v_{Ar}$ and v_A/u. I find that when

$$2c_{Bu2} + c_{uB2} \geq -2.2, \tag{2.77}$$

total energy decreases with time for any non-zero v_{Ar}, $v_{A\perp}$, and u. Let me remind the reader that all these velocity are non-negative according to definitions (2.24). Condition (2.77) is weak. Some tests from the second and the third categories constrain c_{uB2} and c_{Bu2} better, thus making equation (2.77) valid.

The typical test of the second category deals with dynamo amplification of anisotropic field. Dynamo action not only amplifies magnetic field, but also isotropizes it. I take isotropization condition to be

$$\frac{d(v_{Ar} - v_{A\perp})}{dt(v_{Ar} - v_{A\perp})} \leqslant 0. \tag{2.78}$$

Taking expressions for derivatives from system (2.75) I arrive at

$$(\hat{c}_{Bu} - 3c_{Bu2})u - \sqrt{3}c_{BB2}(v_{Ar} + v_{A\perp}) + c_{BB2}(2v_{Ar} + v_{A\perp}) \leqslant 0 \tag{2.79a}$$

This condition should hold when any speed in inequality (2.79a) is much larger then two others. Therefore, inequality (2.79a) is equivalent to

$$c_{\hat{Bu}} < 3c_{Bu2}, \qquad c_{BB2} < \frac{\sqrt{3}}{2}\hat{c}_{BB}. \tag{2.79b}$$

Another second category dynamo test states that magnetic field should always increase, if dynamo operates without dissipation or any energy transfer. This occurs when Alfven speeds are much smaller than turbulent velocity field u. Positive amplification condition then reads

$$\frac{dv_{Ar}^2}{dt\ v_{Ar}^2} > 0, \qquad \frac{dv_{A\perp}^2}{dt\ v_{A\perp}^2} > 0. \tag{2.80}$$

Taking the expressions for derivatives from system (2.75) and applying the limit $v_{Ar} \ll u$ and $v_{A\perp} \ll u$ I obtain that inequalities (2.80) are valid for any balance between v_{Ar} and $v_{A\perp}$ when

$$\hat{c}_{Bu} > 2c_{Bu2}. \tag{2.81}$$

Inequalities (2.79b) and (2.81) give tight constrains on c_{Bu2}.

The similar test exists for the random velocity. Magnetic field is supposed to increase the turbulent velocity in the limit $v_{Ar} \sim v_{A\perp} \gg u$. The correspondent condition

$$\frac{d}{dt}\left(\frac{u^2}{2}\right) > 0 \quad \text{for} \qquad v_{Ar} \sim v_{A\perp} \gg u \tag{2.82}$$

reduces for system (2.75) to the condition of constant positive acceleration that initially steady magnetic field applies to matter. Finally

$$c_{uB2} < \hat{c}_{uB}. \tag{2.83}$$

Decay of isotropic MHD turbulence offers the following test of the second kind. Numerical simulations show equality of magnetic field dissipation rate and random velocity dissipation rate (2.33) when initial magnetic energy equals initial kinetic energy. However, this equality should be stable, otherwise kinetic and magnetic energy would diverge from each other after any perturbation and equality of u and v_A would not have been observed. Stability condition is

$$\frac{d(v_{Ar}^2 + 2v_{A\perp}^2 - u^2)}{dt\ (v_{Ar}^2 + 2v_{A\perp} - u^2)} < 0 \tag{2.84}$$

for $v_{Ar} = v_{A\perp} = u$.

The are no more proven or justified assumptions I can make. I need to make use of inequalities (2.77), (2.79b), (2.81), (2.83), and (2.84) and apply unjustified tests. I take the value of c_{Bu2} to be in the middle of the allowed interval

$$c_{Bu2} = \frac{1}{2}\left(\frac{1}{2} + \frac{1}{3}\right)\hat{c}_{Bu} \approx 0.29. \tag{2.85}$$

The value of c_{uB} is small compared to the values of other coefficients. There is no physical sense in the sharp increase of u^2 build-up when magnetic field becomes anisotropic that

would be the case for $c_{uB2} \ll (-\hat{c}_{uB})$ Turbulent velocity may be expected to increase regardless of the direction of magnetic field in equation (2.75c). This idea leads to $|c_{uB2}| < \hat{c}_{uB}$. I take

$$c_{uB2} = 0 \tag{2.86}$$

for the simple estimate. Similar estimate allows me to set

$$c_{BB2} = 0. \tag{2.87}$$

In this case isotropization of magnetic field has a timescale about the dissipation timescale.

2.9 Appendix: Self-Similar Solution

Let me describe the self-similar solution, when the differential system of equations (2.52) can be reduced to the algebraic system. I set the proper scalings of quantities with radius and make weak additional assumptions. I introduce the standard dimensionless variables $T(x), \rho(x), L(x), aa(x), bb(x), pp(x), vel(x)$ to replace, respectively, $T(r), \rho(r), L(r),\ u(r), v_{Ar}(r), v_{A\perp}(r), v(r)$ as follows:

$$\begin{aligned} T(r) &= T_\infty T(x), \qquad v(r) = vel(x)\left(\frac{2RT(x)}{\mu}\right)^{1/2}, \qquad L(r) = (r/x)L(x), \\ u(r) &= aa(x)\left(\frac{2RT(x)}{\mu}\right)^{1/2}, \qquad v_{Ar}(r) = bb(x)\left(\frac{2RT(x)}{\mu}\right)^{1/2}, \\ v_{A\perp}(r) &= pp(x)\left(\frac{2RT(x)}{\mu}\right)^{1/2}. \end{aligned} \tag{2.88}$$

Radius is normalized to Bondi radius (eq. [2.54]) as $r = r_B\ x$. The natural power-law radial dependencies of these quantities (2.88)

$$3T(x) = T_{\rm SS}x^{-1}, \qquad vel(x) = v_{\rm SS}x^{-1/2}, \qquad L(x) = \gamma, \tag{2.89}$$

$$aa(x) \;=\; u_{\rm SS}x^{-1/2}, \qquad bb(x) = v_{Ar\rm SS}x^{-1/2}, \qquad pp(x) = v_{A\perp\rm SS}x^{-1/2}$$

make my system of equations (2.52) independent of x under the following restrictions:

- gravity is Newtonian,
- external turbulence driving is negligible,
- equation of state is non-relativistic.

These assumptions are valid in the intermediate region $10^3 r_{\rm g} \lesssim r \lesssim 0.1 r_B$. Gravity is Newtonian for $r \gg r_{\rm g}$. Turbulence driving is mainly internal for $r \lesssim 0.1 r_B$ (see subsections (2.4.1), (2.4.2) and Fig. 2.1b, Fig. 2.5b). Electrons become relativistic at around $10^3 r_{\rm g}$. The found range of r where all above assumptions hold is small. I can instead consider a non-relativistic equation of state with $w = w_{NR}$ (eq. [2.52c]) everywhere. This makes standard self-similar solution possible from $0.1 r_B$ down to several Schwarzschild radii $r_{\rm g}$.

Dimensionless magnetic helicity ξ appears to be constant in self-similar regime. Relations (2.52h), (2.52g), and (2.46) lead to

$$\xi = \frac{3\sigma_\infty}{4T_{SS}(v_{ArSS}^2 + 2v_{A\perp SS}^2)}\xi_\infty. \tag{2.90}$$

Continuity equation (2.52a) can be used to obtain the scaling of density $\rho \sim x^{-3/2}$. Heat balance equation (2.17) reduces to the equality of radial and total perpendicular magnetic fields

$$v_{ASS}^2 = 2v_{A\perp SS}^2. \tag{2.91}$$

Euler equation (2.52b) gives the formula for self-similar temperature

$$T_{SS} = 5/(15 + 10u_{SS}^2 + 9v_{ArSS}^2 + 6v_{A\perp SS}^2 + 6v_{SS}^2). \tag{2.92}$$

Turbulence evolution equations (2.22), (2.23), (2.26) are now treated without source terms. They give, correspondingly, three relations

$$2u_{SS}v_{ArSS}c_{Bu11} - 2v_{ArSS}^2 c_{BB11}\exp(-\xi) + 4u_{SS}c_{Bu22}v_{A\perp SS} + 3v_{ArSS}v_{SS}\gamma = 0, \quad (2.93)$$

$$2u_{SS}(v_{ArSS}c_{Bu22} + (c_{Bu11} + c_{Bu22})v_{A\perp SS}) - v_{A\perp SS}(2c_{BB11}\exp(-\xi)v_{A\perp SS} + 3v_{SS}\gamma) = 0,$$

$$-u_{SS}^2 c_{uu} + c_{uB11}\exp(-\xi)(v_{ArSS}^2 + 2v_{A\perp SS}^2) = 0,$$

where definitions of Alfven and turbulent velocities (2.24) are used.

Let me first set magnetic helicity to zero $\xi = 0$ and consider four equations (2.91) and (2.93) on four velocities v_{SS}, u_{SS}, v_{ArSS}, $v_{A\perp SS}$. The only solution of this system has all the velocities identical zeroes. No self-similar solution is possible for zero magnetic helicity ξ.

However, the non-linear algebraic system of equations on ξ and velocities (2.90), (2.91), (2.93) possesses a non-trivial self-similar solution. For the full system (2.52) I need the additional condition to determine the accretion rate and solve for radial dependencies of quantities. This condition is either condition for maximum accretion rate (2.64) or condition for effective angular momentum transport (2.61). I can transform both into self-similar form. Maximum $\dot{M}$ condition (2.64) reads

$$5 + 10u_{SS}^2 + 12v_{A\perp SS} = 6v_{SS}^2. \quad (2.94a)$$

Effective angular momentum transport condition (2.61) gives

$$\frac{\sqrt{5/3}\ v_{SS}}{4v_{ArSS}\ v_{A\perp SS}\sqrt{T_{SS}}} \leq 1 \quad (2.94b)$$

regardless of circularization radius $r_{\rm cir}$.

Let me first find the self-similar solution in case of large angular momentum. I solve equality in relation (2.94b) and 5 equations (2.90), (2.91), (2.92), (2.93) for 7 quantities ξ,

T_{SS}, u_{SS}, v_{ArSS}, $v_{A\perp SS}$, $\gamma\ v_{SS}$, and the product $\sigma_\infty\xi_\infty$. I normalize the results to free-fall velocity (eq. [2.67]) to be able to directly compare with the numbers on Figure 2.5b:

$$\begin{aligned} \frac{c_s(r)}{v_{ff}(r)} &= 0.58, \quad \frac{u(r)}{\sqrt{3}v_{ff}(r)} = 0.0094, \quad \frac{v_{Ar}(r)}{v_{ff}(r)} = 0.041, \\ \frac{v_{A\perp}(r)}{v_{ff}(r)} &= 0.029, \quad \frac{v(r)}{v_{ff}(r)} = 0.0033, \quad \sigma_\infty\xi_\infty = 0.00718 \end{aligned} \tag{2.95}$$

for $r \gg r_{\rm g}$. Figure 2.5b shows profiles of velocities for the reference model with $\sigma_\infty = 1$, $\xi_\infty = 0.025$, $\gamma = 1$. The actual velocities on the inner boundary at $r = 3 \times 10^{-4} r_B = 90 r_{\rm g}$ are

$$\begin{aligned} \frac{c_s(r)}{v_{ff}(r)} &= 0.58, \quad \frac{u(r)}{\sqrt{3}v_{ff}(r)} = 0.0033, \quad \frac{v_{Ar}(r)}{v_{ff}(r)} = 0.076, \\ \frac{v_{A\perp}(r)}{v_{ff}(r)} &= 0.024, \quad \frac{v(r)}{v_{ff}(r)} = 0.0051. \end{aligned} \tag{2.96}$$

The reference model has $\sigma_\infty\xi_\infty = 0.025$ about 3 times larger than in self-similar solution (2.95), magnetic field in the reference model is stronger. Therefore, higher values of all characteristic velocities are expected in the actual solution (2.96). I obtain inflow velocity v and radial Alfven speed v_{Ar} correspondingly 1.5 and 1.8 times higher for solution (2.96). Sonic speeds are the same in self-similar (2.95) and actual (2.96) solutions, because almost all gravitational energy goes into thermal energy in both cases. However, perpendicular Alfven velocity $v_{A\perp}$ and turbulent velocity u do not qualitatively agree with self-similar solution. They are correspondingly 1.2 and 2.8 times lower in the actual solution (2.96). The naive estimate for accretion rate is

$$4\pi\rho_\infty v(r_B) r_B^2 \approx 0.05\dot{M}_B. \tag{2.97}$$

This appears to be 8 times larger than the actual accretion rate $0.0061\dot{M}_B$. Velocity near Bondi radius (eq. [2.54]) is much smaller than self-similar value, what leads to an overestimate of $\dot{M}$. Thus, self-similar solution can give an order of magnitude estimates for

all characteristic velocities of the flow and even for accretion rate $\dot{M}$. However, self-similar solution has only 2 free parameters instead of 3, because $\sigma_\infty \xi_\infty$ is treated as one constant. Therefore, solution of the full system (2.52) is required to probe the entire parameter space and to achieve more precise results.

Self-similar solution in case of maximum rate flow with condition (2.94a) does not exist. The formal solution of equations (2.94a), (2.90), (2.91), (2.93) leads to negative product $\sigma_\infty \xi_\infty$. The absence of self-similar solution in this case is reasonable, since the actual solution does not exhibit self-similar scalings (Fig. 2.1b).

2.10 Appendix: Convection

Let me elaborate the stability criterion against convection in my model. As I noted in the main text (subsection 2.5.4), small scale perturbations of quantities are smeared out by diffusion. Thus high-frequency analysis by Scharlemann (1983) is not appropriate to determine the convective stability. Timescale of diffusion $\tau_{\rm diff}$ is

$$\tau_{\rm diff} \sim \frac{h}{u}, \tag{2.98}$$

where l is the scale of perturbation. As h decreases, diffusion time also decreases and becomes smaller than perturbation growth timescale $\tau_{\rm grow}$. If $\tau_{\rm diff} < \tau_{\rm grow}$, convection is ineffective that is likely to happen at small scales h. Thus I need to consider the motion of the large blobs of the size $h \sim L$.

I consider a blob of plasma displaced at some small Δr from its equilibrium position (Fig. 2.7). The density of the blob itself changes by $\Delta\rho_{\rm blob}$, when it is moved. The density of outer medium changes by $\Delta\rho_{\rm fluid}$ between two positions of the blob. The goal is to

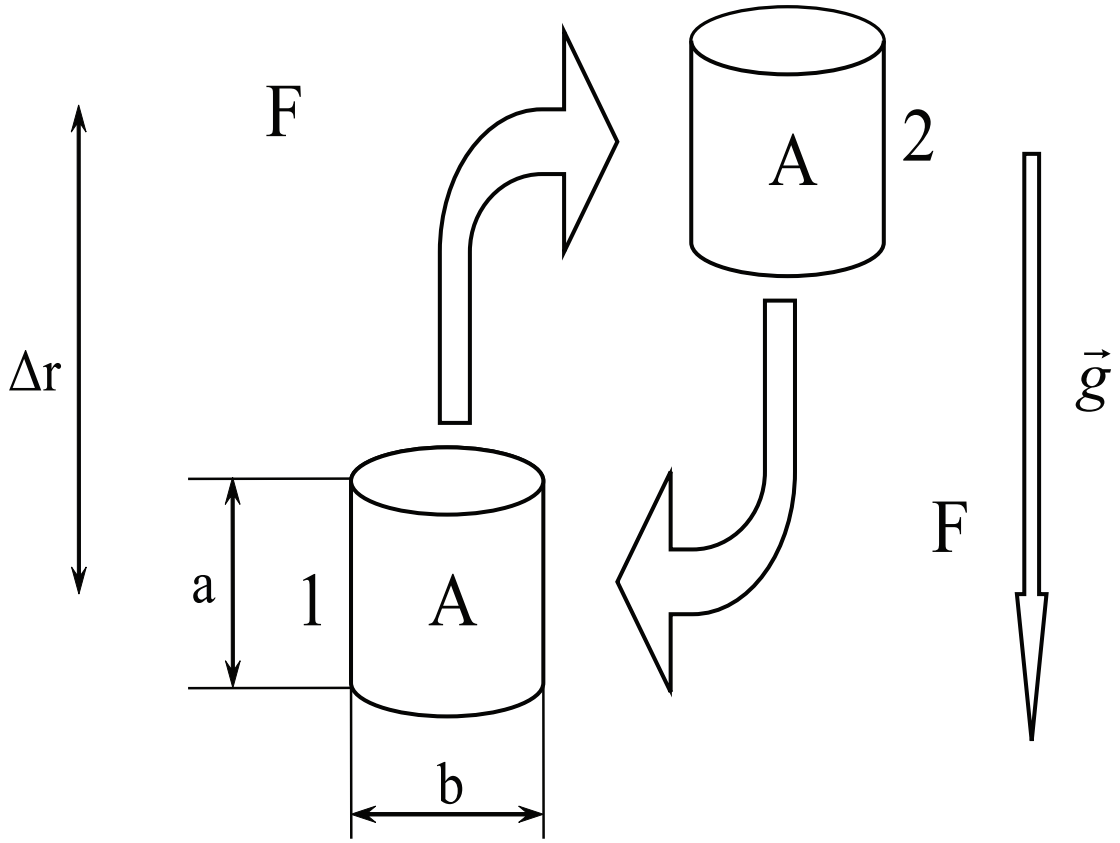

Figure 2.7.— Scheme of convection. Large magnetized blob is in perpendicular and radial pressure balance. Energy does not dissipate inside the blob.

calculate the difference in density differences $\Delta\rho_{\rm fluid} - \Delta\rho_{\rm blob}$ between the outer medium and the blob. Positive difference $\Delta\rho_{\rm fluid} - \Delta\rho_{\rm blob} > 0$ for positive $\Delta r > 0$ implies convective instability. Rising blob of gas is rarified compared to the fluid and buoyant. The results for $\Delta\rho$ may be affected by external driving that is somewhat artificial in my model. Thus I need to calculate $\Delta\rho$ in the inner accretion region where external driving is not important. Motion of the blob is adiabatic and governed by the same adiabatic dynamical equations (2.52b) and (2.52c), as the rest of the fluid. I neglect energy, associated with gas regular velocity v. Term v^2 cannot be neglected only in the region, where v approaches sound speed c_s. However, convection ceases if $v \sim c_s$ (Narayan et. al., 2002). I denote by index A physical quantities in the blob and by index F quantities in the rest of the fluid.

Euler equation (2.52b) results in the following equations on differences in the blob

$$\frac{R}{\mu}\Delta_A(\rho T) + \frac{1}{3}\Delta_A(\rho u^2) + \frac{1}{r^2}\Delta_A(r^2\rho v_{A\perp}^2) - \frac{1}{2r^4}\Delta_A(r^4\rho v_A^2) = 0 \qquad (2.99a)$$

and in the fluid

$$\frac{R}{\mu}\Delta_F(\rho T) + \frac{1}{3}\Delta_F(\rho u^2) + \frac{1}{r^2}\Delta_F(r^2\rho v_{A\perp}^2) - \frac{1}{2r^4}\Delta_F(r^4\rho v_A^2) = 0. \qquad (2.99b)$$

In both equations I take variations between quantities at $r + \Delta r$ and r. I introduce the difference operator

$$\Delta() = \Delta_F() - \Delta_A() \qquad (2.100)$$

and calculate the variations of all quantities between the fluid and the blob. Subtracting equation (2.99b) from equation (2.99a), I find the radial pressure balance in the first order in Δr

$$\frac{R}{\mu}\Delta(\rho T) + \frac{1}{3}\Delta(\rho u^2) + \Delta(\rho v_{A\perp}^2) - \frac{1}{2}\Delta(\rho v_A^2) = 0. \qquad (2.101)$$

Blob of plasma should be in equilibrium also in perpendicular direction, not only in radial direction. I use the same technique to deduce it, as I used to derive the radial force

equation (2.13) from general momentum equation (2.3). Component θ of magnetic force in equations (2.2) and (2.3) reads $F_\theta = [\mathbf{B} \times [\nabla \times \mathbf{B}]]_\theta/(4\pi\rho)$. I subtract $B_\theta(\nabla \times \mathbf{B})/(4\pi\rho)$ from it and average over ϕ direction. I obtain

$$F_\theta = \frac{(B_r^2)'_\theta}{8\pi\rho r} \tag{2.102}$$

for $B_\theta^2 = B_\phi^2$ and $B_r B_\theta = 0$ on average over ϕ. The final form of force balance in θ direction is

$$\frac{\partial}{\partial\theta}\left(\frac{R}{\mu}\rho T + \frac{1}{3}\rho u^2 + \frac{1}{2}\rho v_A^2\right) = 0. \tag{2.103}$$

Perpendicular force balance (2.103) has the same form in any direction perpendicular to the radial vector owing to the symmetry of the problem. I apply operator Δ (eq. [2.100]) to the integral form of perpendicular pressure balance and get

$$\frac{R}{\mu}\Delta(\rho T) + \frac{1}{3}\Delta(\rho u^2) + \frac{1}{2}\Delta(\rho v_A^2) = 0. \tag{2.104}$$

Heat balance equation (2.17) gives the third relation

$$\frac{R}{\mu}\left(\frac{3}{2}\Delta T - \frac{\Delta\rho}{\rho}T\right) + \left(u\Delta u - \frac{u^2}{3}\frac{\Delta\rho}{\rho}\right) + \rho\Delta\left(\frac{v_{A\perp}^2}{\rho}\right) + \frac{1}{2\rho}\Delta(\rho v_A^2) = 0. \tag{2.105}$$

Expansion or contraction of a blob is non-uniform. Perpendicular b and parallel a sizes (Fig. 2.7) deform in different ways. Continuity equation for the fluid (2.9) can be written as

$$\frac{\Delta_F\rho}{\rho} + \frac{\Delta_F v}{v} + 2\frac{\Delta r}{r} = 0 \tag{2.106a}$$

I consider the parcel with constant mass $m = \rho V$. Therefore

$$\frac{\Delta_A\rho}{\rho} + \frac{\Delta a}{a} + 2\frac{\Delta b}{b} = 0 \tag{2.106b}$$

is the continuity relation for the parcel. Finally I subtract equation (2.106a) from equation 2.106b and obtain

$$\frac{\Delta\rho}{\rho} + \frac{\Delta v}{v} + 2\frac{\Delta r}{r} - \frac{\Delta a}{a} - 2\frac{\Delta b}{b} = 0 \tag{2.107}$$

for the change of density according to definition (2.100). Inflow velocity v is clearly associated with the fluid, but I omit subscript F at v. I also omit subscript A at dimensions of the blob.

Now I need to quantify the variation of the turbulent magnetic field and the random velocity. I assume that the blob moves at a speed $V(r)$ much higher than the inflow velocity $V(r) \gg v(r)$, therefore magnetic field does not dissipate in the parcel. Differences of turbulence evolution equations (2.52d), (2.52e), and (2.52f) are

$$2u\Delta u - \frac{2}{3}u^2\frac{\Delta\rho}{\rho} = \frac{\Delta r}{vL}(c_{uu}u^3 - c_{uB11}(v_A^2 + 2v_{A\perp}^2)u\exp(-\xi)) \tag{2.108a}$$

$$\Delta(\rho v_A^2) + 4\rho v_A^2\left(\frac{\Delta r}{r} - \frac{\Delta b}{b}\right) = \frac{\rho\Delta r}{vL}(c_{BB11}v_A^3\exp(-\xi) - (c_{Bu11}v_{Ar}^2 + 2c_{Bu22}v_{Ar}v_{A\perp})u) \tag{2.108b}$$

$$\Delta(\rho v_{A\perp}^2) + 2\rho v_{A\perp}^2\left(\tfrac{\Delta r}{r} + \tfrac{\Delta v}{v} - \tfrac{\Delta a}{a} - \tfrac{\Delta b}{b}\right) = \tag{2.108c}$$

$$= \tfrac{\rho\Delta r}{vL}(c_{BB11}v_{A\perp}^3\exp(-\xi) - ((c_{Bu11} + c_{Bu22})v_{A\perp}^2 - c_{Bu22}v_{Ar}v_{A\perp})u).$$

Magnetic helicity variation does not directly influence the dynamics of the blob. Solving the system of 7 equations (2.101), (2.104), (2.105), (2.107), (2.108abc) on 7 quantities $\Delta T, \Delta\rho, \Delta v_A, \Delta v_{A\perp}, \Delta u, \Delta a, \Delta b$, I obtain

$$\frac{\Delta\rho_{\text{correct}}}{\rho\Delta r} \approx \tag{2.109}$$

$$v_{Ar}\frac{2.02\exp(-\xi)v_{Ar}v_{A\perp}(v_{Ar} + 2v_{A\perp}) - u(0.39(v_{Ar}^2v_{A\perp} + v_{A\perp}^3) + v_{Ar}(1.21v_{A\perp}^2 - 0.63u^2))}{c_s^2Lv(v_{Ar}^2 + v_{A\perp}^2)}.$$

The actual expression is much longer. I take only the largest terms in the numerator and the denominator.

Let me compare this result (eq. [2.109]) with the naive estimate, when magnetic field dissipation increases gas internal energy only (Bisnovatyi-Kogan & Ruzmaikin, 1974), and gas pressure balance is used instead of parallel and perpendicular pressure balances (2.101), (2.104). Gas pressure balance is

$$\Delta(\rho T) = 0. \tag{2.110}$$

Naive heat balance (2.16) for the unit mass is

$$\frac{R}{\rho\mu}\left(\frac{3}{2}\rho\Delta T - T\Delta\rho\right) \approx \tag{2.111}$$
$$\frac{\Delta r}{Lv}(0.41v_{Ar}^2u + 1.16v_{Ar}uv_{A\perp} + 1.4uv_{A\perp}^2 - 3.03(v_{Ar}^3 + 2v_{A\perp}^3)\exp(-\xi) - 1.14u^3)$$

Eliminating ΔT from relations (2.110) and (2.111), I find

$$\frac{1}{\rho}\frac{\Delta\rho_{\rm naive}}{\Delta r} \approx \frac{0.61(v_{Ar}^3 + 2v_{A\perp}^3)\exp(-\xi) + 0.23u^3 - 0.82v_{Ar}^2u - 0.23v_{Ar}uv_{A\perp} - 0.28uv_{A\perp}^2}{c_s^2Lv} \tag{2.112}$$

I evaluate the convective derivatives of density (2.109) and (2.112) in the inner region of the reference solution with angular momentum transport (subsection 2.4.2). Parameters of the reference model are $\xi_\infty = 0.025$, $\sigma_\infty = 1$, $\gamma = 1$, non-relativistic EOS. Correspondent velocities are shown on Figure 2.5b. I take the values (2.96) of velocities and magnetic helicity on the inner boundary of integration at $r = 3 \times 10^{-4} r_B \approx 90 r_{\rm g}$. Change of density appears to be negative $\Delta\rho < 0$ for $\Delta r > 0$ in the result of full calculation (eq. [2.109]). Naive calculation shows positive $\Delta\rho > 0$ for $\Delta r > 0$.

$$\frac{\Delta\rho_{\rm correct}}{\Delta\rho_{\rm naive}} \approx -0.2. \tag{2.113}$$

Naive calculation suggests that the flow is convectively unstable, whereas the full calculation under reasonable assumptions indicates a convectively stable flow.

The calculated result (2.113) is applicable only to the inner regions of solution with angular momentum transport (subsection 2.4.2). Excluded external driving is important in the outer regions. In turn, solution with maximum accretion rate has large inflow velocity v that approaches gas sound speed c_s, and convection is suppressed (subsection 2.5.4). As a bottom line, either flow appears to be convectively stable on average or convection is suppressed in all calculated solutions without electron conductivity.

However, numerical simulations by (Igumenshchev, 2006) of non-rotating flows find evidence of convection. This convection may be physical. My model averages heat from all dissipation events over the fluid. Local reconnection events can lead to burst-type local heating that leads to buoyancy of blobs. Also, magnetic buoyancy and diffusion play important role in transfer processes (Igumenshchev, 2006). The correct inclusion of convection, magnetic buoyancy and diffusion is the subject of future studies.

Chapter 3

Inflow-Outflow Model with Conduction and Self-Consistent Feeding for Sgr A*

Abstract

We propose a two-temperature radial inflow-outflow model near Sgr A* with self-consistent feeding and conduction. Stellar winds from individual stars are considered to find the rates of mass injection and energy injection. These source terms help to partially eliminate the boundary conditions on the inflow. Electron thermal conduction is crucial for inhibiting the accretion. Energy diffuses out from several gravitational radii, unbinding more gas at several arcseconds and limiting the accretion rate to $< 1\%$ of Bondi rate. We successfully fit the X-Ray surface brightness profile found from the

extensive Chandra observations and reveal the X-Ray point source in the center. The super-resolution technique allows us to infer the presence and estimate the unabsorbed luminosity $L \approx 4 \cdot 10^{32}$erg s^{-1} of the point source. The employed relativistic heat capacity and direct heating of electrons naturally lead to low electron temperature $T_e \approx 4 \cdot 10^{10}$ K near the black hole. Within the same model we fit 86 GHz optically thick emission and obtain the order of magnitude agreement of Faraday rotation measure, thus achieving a single accretion model suitable at all radii.

3.1 Introduction

Our Galaxy hosts a supermassive black hole (BH) with a mass $M = 4.5 \cdot 10^6 M_\odot$ (Ghez et al., 2008; Reid et al., 2008) at a distance $R = 8.4$ kpc. The BH exhibits low luminosity state probably due to inefficient feeding and cooling. Almost all available matter outflows from the region, whereas only the small fraction accretes (Quataert, 2004). This feeding region within several arcseconds contains X-Ray emitting gas, but some X-Rays are expected from a synchrotron self-Compton (SSC) or synchrotron source from accretion at several Schwarzschild radii $r_{\rm g}$. The study of X-Rays offers a unique opportunity to test the full range of accretion scales from several $''$ to $r_{\rm g} = 10^{-5}{}''$ and construct a single model.

Modeling the accretion flow with such a huge range of scales is a challenge. 3D SPH simulations are performed in the outer region between $1''$ and $10''$ (Rockefeller et al., 2004; Cuadra et al., 2008). Latest MHD simulations (Sharma et al., 2008) are limited to 3 orders of magnitude in radius and axial symmetry. Only the one-dimensional calculation (Quataert, 2004) can in principle resolve the flow everywhere. Thus, 1D modeling is the approach we adopt extending it down to the BH horizon.

We analyze the quiescent observations (Muno et al., 2008) of X-Ray emission from central several arcseconds around Sgr A* in §3.2. The total exposure is 25 times longer compared to previously analyzed data (Baganoff et al., 2003). The super-resolution processing based on spacecraft dithering helps resolving sub-pixel scales. The up-to-date data on stellar wind emitters are summarized in §3.3. We smooth matter ejection rates of individual stars over radius and sum them into a single feeding rate, also properly averaging the wind velocity. This presents a significant improvement over an ad-hoc feeding in Quataert (2004). The dynamical two-temperature equations are derived in §3.4. We consider the electron conduction the main energy transport mechanism, approximating the unsaturated heat flux by a simple formula. The Bondi flow (Bondi, 1952) without heat transport overestimates the X-Ray luminosity by a factor of 10^3. The other important effects considered are the relativistic heat capacity of electrons and superadiabatic heating equivalent to entropy production. The ways to solve the resulting system of equations and corresponding results are presented in §3.5. We employ the shooting method and find the minimum χ^2 fit for X-Ray surface brightness profile, simultaneously fitting 86 GHz flux. The best fit model requires X-Ray point source. The viability of a non-cooling radial flow is examined.

3.2 Observations

Central several arcseconds of the Galaxy were observed quite often over the past several years. The rich region contains point sources identified as X-Ray binaries (Muno et al., 2009) and extended emission features (Muno et al., 2008) together with the source coincident with Sgr A*. The latter is expected from hot accreting gas, and source confusion

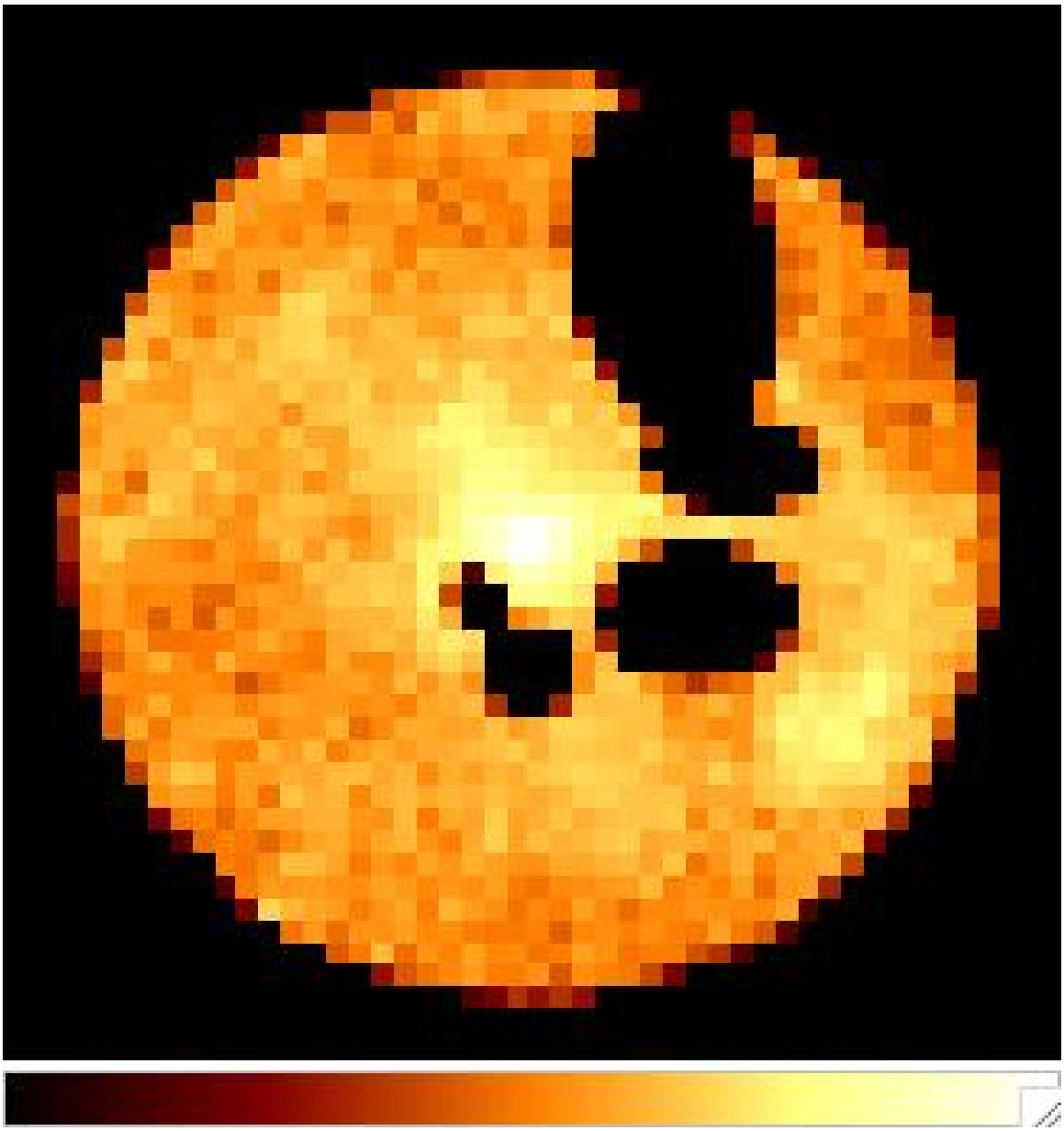

Figure 3.1.— Chandra image of central 6" around Sgr A*. Point sources and strong extended features are subtracted.

is practically impossible (Baganoff et al., 2003). Sgr A* source exhibits significant X-Ray flares associated with the SSC mechanism (Baganoff et al., 2001) or synchrotron (Dodds-Eden et al., 2009). We are interested in quiescent emission, so we exclude the flaring state. We bin the observations in 628 seconds as a compromise between the time resolution and the number of counts. About 4 photons on average are received during 628 seconds and we take only the observations with less than 15 photons, thereby accumulating 953 ks in the quiescent state. The quiescent state also produces some point source X-Rays, likely associated with SSC (Moscibrodzka et al., 2009). We model these by a PSF-broadened central point source. We eliminate the emission from the point sources and bright extended sources offset from Sgr A* (see Figure 3.1). The bright extended emission may arise from the colliding winds of two strong close emitters or from the collision of hot outflowing material with cold molecular material. We exclude both effects from modeling of an averaged flow pattern.

We construct the surface brightness profile in counts per pixel squared for the duration of observation as a function of distance from the BH. The size of Chandra pixel is $0.5''$, which may seem to pose a limit on radial binning of brightness profile. However, the position of satellite is not steady over the duration of observations, but is findable with the $0.1''$ accuracy by comparing with the known positions of bright point sources. Then we can achieve $0.1''$ super-resolution accuracy in surface brightness profile from knowing the orientation of the detector pixels at any given time. The final profile is shown on Figure 3.2 (error bars) together with the point-spread function (PSF) (dashed) found from the nearby point source J174540.9-290014 (Muno et al., 2009). The PSF is scaled to match the contribution from the point source. The counts cease to be monotonic at about $5''$ due probably to the production of X-Rays in collisions of cold and hot regions. Therefore, only

radiation within the central $5''$ is to be modeled. As we are interested in how symmetric the surface brightness profile is, we divide the emitting region into 4 sectors 90 deg each centered on Sgr A* and extract the surface brightness profile in each sector. The standard deviation of counts between sectors is below 2σ the noise within $5''$, but rises to several σ outward from $5''$. This justifies our choice of the outer radiation boundary and proves the applicability of the radial model. Let us now look in more details on manufacturing of the X-Ray emitting gas.

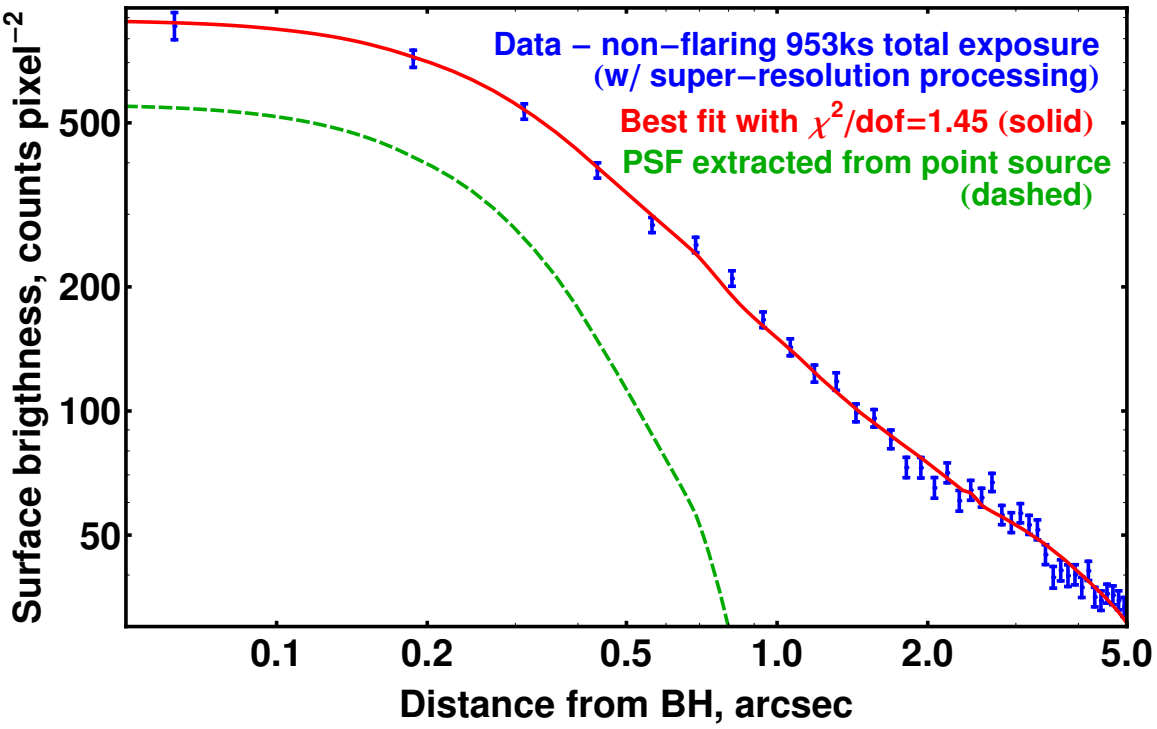

Figure 3.2.— Observed radial surface brightness profile (error bars), best fit (solid) and the point source contribution to emission (dashed). The point source contribution is the scaled PSF.

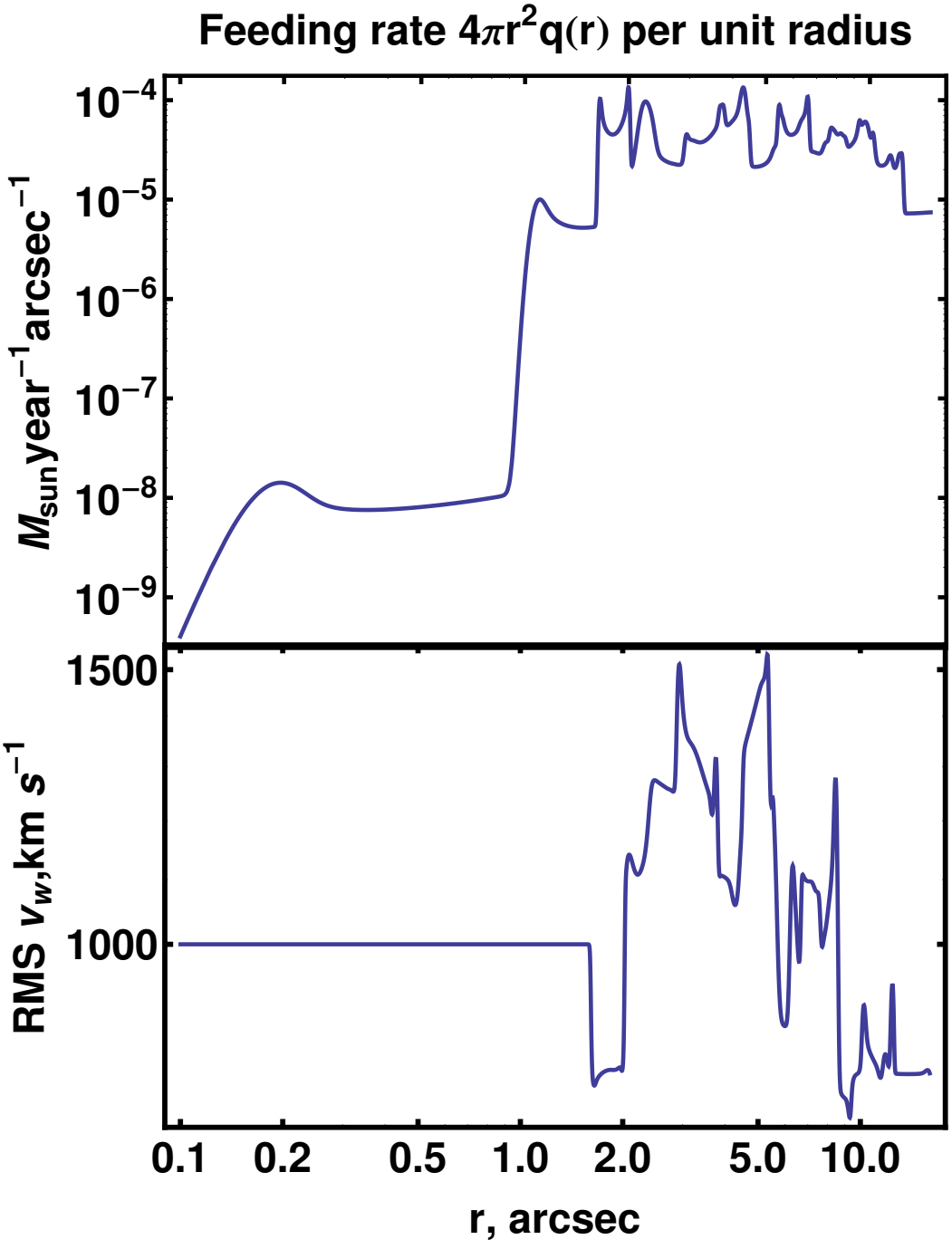

Figure 3.3.— Mass input into the feeding region around the BH on the upper panel. Square averaged wind velocity v_w on the lower panel. Feeding is averaged over stellar orbits. Each wiggle represents a turning point of a single orbit. Only S02 star feeds matter within 0.8".

3.3 Stellar Winds Feeding

The Galactic Center region has a concentration of massive Wolf-Rayet and blue giant stars, expelling strong winds from their surfaces (Martins et al., 2007). As the strongest wind emitters are usually the brightest stars, all wind emitters are easily identifiable. We take the latest data on ejection rates and velocities (Martins et al., 2007; Cuadra et al., 2008) and complement them with the orbital parameters of stars (Paumard et al., 2006; Lu et al., 2009). Following Cuadra et al. (2008), we minimize eccentricities for the stars not belonging to the stellar disks as identified by Lu et al. (2009). The wind speeds v_w and ejection rates are taken directly from Cuadra et al. (2008).

There are several ways to treat the winds. Rockefeller et al. (2004) performed a simulation with winds from steady stars, whereas Cuadra et al. (2008) considered moving stars. In both cases the time to reach the quasi-steady solution $300-1000$ yrs is comparable to or longer than the orbital period at the stagnation point 350 yrs. Thus, it is reasonable to average over stellar orbits in a search for a steady-state prescription of feeding. We reconstruct the full 3D orbits, but retain only the apocenter and pericenter distances for the stars. We smooth the total wind ejection rate for each star over the radial extent of its orbit and then smooth with the narrow Gaussian filter to eliminate the divergences at the turning points.

We add the resultant feeding profiles together to obtain the total feeding rate as a function of radius (see Figure 3.3). We square average the wind velocities weighing the contribution of each star by its mass loss rate. However, the winds also acquire the velocity of a star as viewed by a distant observer. We neglect stars' proper motions in calculations of wind energy. They are negligible at several arcseconds, but would rather contribute to

the angular velocity of matter within $1''$, where feeding is dominated by few stars. The dependence of the averaged wind speed on radius is shown on Figure 3.3. Quataert (2004) assumed the power-law mass injection rate $q(r) \propto r^{-\eta}$ for $r \in [2'', 10'']$. The power-law index $\eta = 2$ corresponds to zero slope of $\dot{M}(r) \propto r^2 q(r)$ (see Figure 3.3) and agrees better with the present calculations, whereas their choice of constant wind velocity does not agree with the present estimate.

We also incorporate S02 star (Martins et al., 2008) into the calculations. The mass loss rate $\dot{M}_{S02} = 6 \cdot 10^{-8} M_{\odot}\mathrm{year}^{-1}$ of S02 is taken to coincide with that of τ Sco. S02 has a spectral type $B0 - 2.5V$ and a mass $M \approx 16 M_{\odot}$ (Mokiem et al., 2005; Martins et al., 2008), whereas τ Sco has a very close type $B0.2V$ and a mass $M \approx 15 M_{\odot}$ (Mokiem et al., 2005). The inferred accretion rate onto the black hole (Sharma et al., 2007a,b) $3 \cdot 10^{-8} M_{\odot}\mathrm{year}^{-1}$ is actually smaller than $\dot{M}_{S02}$, thus the whole accreted material can in principle be provided by a single weak wind emitter. This result is very different from Cuadra et al. (2008), who assumed all the matter accretes from the inner boundary of the simulation, thus obtaining in a simplified treatment a much larger accretion rate. However, the direct feeding mechanism (Loeb, 2004) by S02 does not work, as its revised $\dot{M}_{S02}$ is much below the value required for feeding without the angular momentum. In turn, the direct feeding by IRS 13E3 (Moscibrodzka et al., 2006) produces too large accretion rate in the absence of conduction.

3.4 Dynamical Equations

3.4.1 Energy Transport Mechanism

Radiatively inefficient flows can be mediated significantly by the energy transfer from the inner regions to the outer (Blandford & Begelman, 1999; Johnson & Quataert, 2007; Sharma et al., 2008). Such transfer happens in two distinct ways: via convection or via diffusive energy transport. Convection is seen in numerical simulations. It happens via Alfven instability (Igumenshchev, 2006) and magneto-thermal instability (MTI) (Sharma et al., 2008) and modifies the density profile. Let us show that the electron heat conduction wins over convection in the accretion flow. First, the MTI is driven by thermal conduction, at any moment the electron conduction flux is larger then the MTI-induced heat flux. Convection implies the motion of large-scale magnetized eddies, which in turn split into smaller eddies and develop the whole turbulent cascade. In such settings the electron conduction is only inhibited a factor of ~ 5 (Narayan & Medvedev, 2001). The speed of electrons is a factor of $\sqrt{m_p/m_e}$ larger than the sound speed and the convection is subsonic; the same factor lowers the ion diffusive heat transport. The relative strength of convective heat flux is proportional to the gradient of logarithmic entropy, which is normally weaker than the proportionality to the gradient of logarithmic temperature of conductive flux. Combining both effects we conclude that, if there is convection or diffusion, then there is stronger conduction. Severe inhibition of electron conduction happens, if the turbulent cascade does not develop and mixing is absent. This is not the case when the gas accretes. The strength of turbulent magnetic field increases then in the convergent flow leading to dissipation and effective mixing (Shvartsman, 1971; Shcherbakov, 2008a). It is reasonable to think that the whole turbulent cascade develops and the electrons relatively freely find

their way around magnetic field lines to connect the different regions of the flow. When the electrons and ions get decoupled from each other, the ion entropy may get equilibrated by convection, whereas the electron temperature levels due to conduction. The investigation of this possibility is left for future research. In present chapter we take the energy transport to happen solely via electron conduction.

There are several different regimes of conduction. First, the collisionality of the flow changes from the large radii to the inner radii as the mean free path of particles l exceeds the flow size r. As the flow gets only weakly collisional at several arcseconds, the conductivity is well approximated by a collisionless formula with $\kappa \propto r$. Another assumption of the kind deals with the electron velocity. As electrons can get only mildly relativistic, we take conductivity to be proportional to square root of electron temperature $\kappa \propto \sqrt{T_e}$, instead of proportionality to relativistic electron velocity $\kappa \propto v_c$ (Johnson & Quataert, 2007). When the gradient of electron temperature gets too large, the electrons transport heat via a constant saturated flux, instead of the flux proportional to the gradient of temperature (Cowie & McKee, 1977). We check a posteriori that the flow is in an unsaturated heat flux regime. Finally, we have for the heat flux $Q = -\kappa k_B dT_e/dr$

$$\kappa = 0.1\sqrt{k_B T_e/m_e} r n, \tag{3.1}$$

where $n = n_e$ is the electron density (Cowie & McKee, 1977).

3.4.2 System of Equations

Gravitational energy of gas in the potential of an accretor is the ultimate inflow driver. It gets transformed directly in several types: kinetic energy of bulk toroidal and radial motion, energy of turbulent magnetic and velocity fields, thermal energy. Turbulent

energy can also originate from the toroidal shearing flow in a disk. Turbulence dissipates into thermal motions of ions and electrons on the dynamical timescale, whereas ions and electrons exchange energy by slow Coulomb collisions. The faster collective modes of ion-electron energy exchange may exist, though they may not lead to equilibration of temperatures (Shkarofsky et al., 1966). We do not separate the turbulent term or write an equation on it for the purpose of current work, as its direct dynamical influence is smaller than the influence of additional thermal energy produced via dissipation of turbulence and entropy production (Shcherbakov, 2008a). Following Johnson & Quataert (2007), we introduce the fractions f_p and f_e of changes of gravitational energy, which go directly into thermal energy of ions and electrons, but relate them via a direct heating mechanism (Sharma et al., 2007a). For the purpose of numerical stability we enhance Coulomb collisions by a factor of 1000, which effectively makes ion and electron temperatures equal at large distances from the BH, but does not influence T_e near the BH. Let us convert the qualitative ideas into equations.

The composition of plasma determines the exact balance of the black hole gravitational pull and supporting gas pressure. Let us define the source function q, so that the ejected mass of stellar winds per second is $\dot{M}_w = \int 4\pi\ r^2\ q\ dr$. We denote the electron density by $n = n_e$ and write the continuity equation as

$$\frac{\partial n}{\partial t} + \frac{1}{r^2}\frac{\partial (n v_r r^2)}{\partial r} = \frac{q(r)}{\mu_{av}}, \tag{3.2}$$

where

$$\mu_{av} \approx 1.14 \tag{3.3}$$

is the average atomic mass per one electron for assumed solar abundance of fully ionized elements (Najarro et al., 2004). The ratio of number densities of atomic nuclei to electrons

is

$$d = n_{\rm non-el}/n \approx 0.93. \tag{3.4}$$

We write separate energy equations for electrons (e) and all ions (p) in terms of

$$c_{se} = \sqrt{\frac{k_B T_e}{m_p}} \quad \text{and} \quad c_{sp} = \sqrt{\frac{k_B T_p}{m_p}}, \tag{3.5}$$

assuming all ions have the same temperature. We set the speed of light equal unity $c = 1$ and normalize to it all velocities. The ideal gas law gives normalized gas pressure

$$p_{\rm gas} = p_p + p_e = n(c_{se}^2 + d \cdot c_{sp}^2) \tag{3.6}$$

to be substituted into the Euler equation

$$\frac{Dv_r}{Dt} + \frac{1}{n\mu_{av}}\frac{\partial p_{\rm gas}}{\partial r} + \frac{r_{\rm g}}{2(r - r_{\rm g})^2} + \frac{q(r)}{n\mu_{av}} v_r = 0, \tag{3.7}$$

where $D/Dt = \partial/\partial t + v_r \partial/\partial r$. The last term corresponds to zero bulk radial velocity of emitted stellar winds.

The electron internal energy density can be approximated as

$$u_e = m_e \left(\frac{3K_3(\theta_e^{-1}) + K_1(\theta_e^{-1})}{4K_2(\theta_e^{-1})} - 1 \right) \approx \tag{3.8}$$
$$\approx \frac{3}{2}\frac{0.7 + 2c_{se}^2 m_p/m_e}{0.7 + c_{se}^2 m_p/m_e} m_p c_{se}^2.$$

This takes into account the differential heat capacity of particles (Shkarofsky et al., 1966). The ion internal energy per particle is $u_p = 3/2 m_p c_{sp}^2$.

The energy exchange rate by Coulomb collisions is (Shkarofsky et al., 1966)

$$F_{pe} = 4.3 \cdot 10^{-19} \frac{n^2}{c_{se}^3}(c_{sp}^2 - c_{se}^2). \tag{3.9}$$

The non-relativistic formula is used everywhere, as F_{pe} rate is only significant in the region of non-relativistic electrons. The energy equation for electrons is then

$$n\frac{D}{Dt}\left(\frac{3}{2}\frac{0.7+2c_{se}^2 m_p/m_e}{0.7+c_{se}^2 m_p/m_e}c_{se}^2\right)-c_{se}^2\frac{Dn}{Dt}=CF_{pe}+ \\ -f_e n\frac{r_{\rm g}v_r}{2r^2}+\frac{q(1+d)}{2\mu_{av}}\left(\frac{v_r^2}{2}+\frac{v_w^2}{2}-\frac{5}{2}c_{se}^2\right) \\ +\frac{1}{r^2}\partial_r(r^2\kappa\partial_r c_{se}^2), \tag{3.10}$$

where $C\sim 1000$ is the enhancement of collisions and conductivity is given by equation (3.1). The left-hand side of the equation (3.10) represents the compressive heating in the adiabatic flow. The Paczynski-Wiita gravitational potential (Paczynski & Wiita, 1980) is implemented for gravitational force, but not in the entropy production term. This reflects the fact that the dissipation of turbulence ceases near the BH as having slower timescale compared to the inflow time. The energy equation for ions reads

$$n\frac{D}{Dt}\left(\frac{3}{2}c_{sp}^2\right)-c_{sp}^2\frac{Dn}{Dt}=-CF_{pe}+ \\ -f_p n\frac{r_{\rm g}v_r}{2r^2}+\frac{q(1+d)}{2\mu_{av}}\left(\frac{v_r^2}{2}+\frac{v_w^2}{2}-\frac{5}{2}c_{sp}^2\right). \tag{3.11}$$

The energy injection rate into ions is chosen to be the same per electron as the energy injection rate into electrons to facilitate the equality of ion and electron temperatures. Let us write a condition on f_p and f_e to decrease the number of free parameters. We assume the ratio of heating fractions to be given by the direct heating mechanism (Sharma et al., 2007a) as

$$\frac{f_e}{f_p}=\frac{1}{3}\sqrt{\frac{T_e}{T_p}}, \tag{3.12}$$

despite this calculation is non-relativistic and a large fraction of energy dissipates at the small scales instead of direct large-scale heating.

3.5 Solutions and Discussions

We solve the derived system of equations from the outer boundary of the feeding region at $14'' = 1.3 \cdot 10^6 r_{\rm g}$ to the inner boundary at about $1.3 r_{\rm g}$, thus covering 6 orders of magnitude in radius. Such a huge dynamic range requires the special solution technique, the solution of a time-dependent system of equations (Quataert, 2004) not being an option. We employ the shooting method and find the smooth transonic solution through the inner sonic point at $\sim 3 r_{\rm g}$. In the presence of conduction the point, where sound speed equals inflow velocity is not special anymore, and instead the point, where isothermal speed equals the inflow velocity, plays the role of transonic surface (Johnson & Quataert, 2007). The system of equations is reduced to one temperature in the outflow by setting $T_e = T_p$ and adding the equations (3.10) and (3.11). The inner boundary is set at a point $r_{\rm in}$, where $dT_e/dr = 0$ in a non-conductive solution. Then for any non-zero conductivity the zero heat flux condition $dT_e/dr = 0$ is enforced at $r_{\rm in}$. The outer boundary condition at $r_{\rm out}$ is uncertain. It is natural to think the outflow would be transonic (Lamers & Cassinelli, 1999), however, significant outer pressure may hold the gas in the subsonic regime near $r_{\rm out}$. The position of zero velocity stagnation point $r_{\rm st}$ determines the accretion rate $\dot{M}$. Instead of setting the pressure at the outer boundary we regulate that pressure by setting temperature $T_{\rm st}$ at the stagnation point. Thus, we have 4 independent variables in the fit: accretion rate $\dot{M}$, temperature at stagnation point $T_{\rm st}$, the ion heating rate f_p and the normalization N of the point source contribution. They are all found iteratively to minimize χ^2. We also iteratively find the positions of sonic point and stagnation point. The positions of inner boundary and outer boundary are unchanged while solving the 4-point boundary value problem.

The observed surface brightness radial profile is the data we fit. We generate a surface brightness profile corresponding to the dynamical model by performing the optically thin ray tracing of X-Rays at a set of photon energies and projected distances from the BH. We employ the up-to-date bremsstrahlung emissivities (Gould (1980) and errata) and account for the emission by heavy elements, excluding iron. Solar metallicity interstellar absorption (Morrison & McCammon, 1983) is assumed with hydrogen column $N_{\rm H} = 10^{23}{\rm cm}^{-2}$. The fluxes are convolved with the response of Chandra to find counts, then blurred with the energy-independent PSF (see Figure 3.2) and integrated over the radial extent of each bin.

The model with $\dot{M} = 6 \cdot 10^{-8} M_{\odot}{\rm year}^{-1}$, $f_p = 0.46$, $T_{\rm st} = 3.2 \cdot 10^7$ K and 550counts pixel^{-2} produced at $r = 0$ by a point source gives an excellent fit with the minimum reduced $\chi^2 = 1.45$ and weighed $\chi^2_{\rm wei} = 0.68$ with $1/r$ weights. The stagnation point is at $r_{\rm st} = 1.01''$. The correspondent unabsorbed point source luminosity $L = 4 \cdot 10^{32}{\rm erg\ s}^{-1}$ is estimated for monoenergetic photons at 4 keV and agrees with the estimates of SSC luminosity in Moscibrodzka et al. (2009). Energy 4 keV is chosen as the energy Chandra is most sensitive to for assumed $N_{\rm H}$. The minimum reduced $\chi^2 = 15$ is achieved for the model without the point source. The models with the outer sonic point instead of finite bounding pressure underpredict the X-ray surface brightness at several arcseconds, assuming fixed $N_{\rm H} = 10^{23}{\rm cm}^{-2}$. The reliable fitting for $N_{\rm H}$ is possible only with the use of spectral data and is left for future research. The assumption $T_p = T_e$ represents the additional point of concern. Temperature equilibrium might not hold at the stagnation point at $1''$ (Quataert, 2004), however the thermalization rate exceeds the outflow rate at $5''$ in our subsonic dense outflow, thus $T_p = T_e$ holds there. The reliable modeling of non-equilibrium flows requires the modeling of the whole spatial structure of the stellar winds and is left for the future research as well.

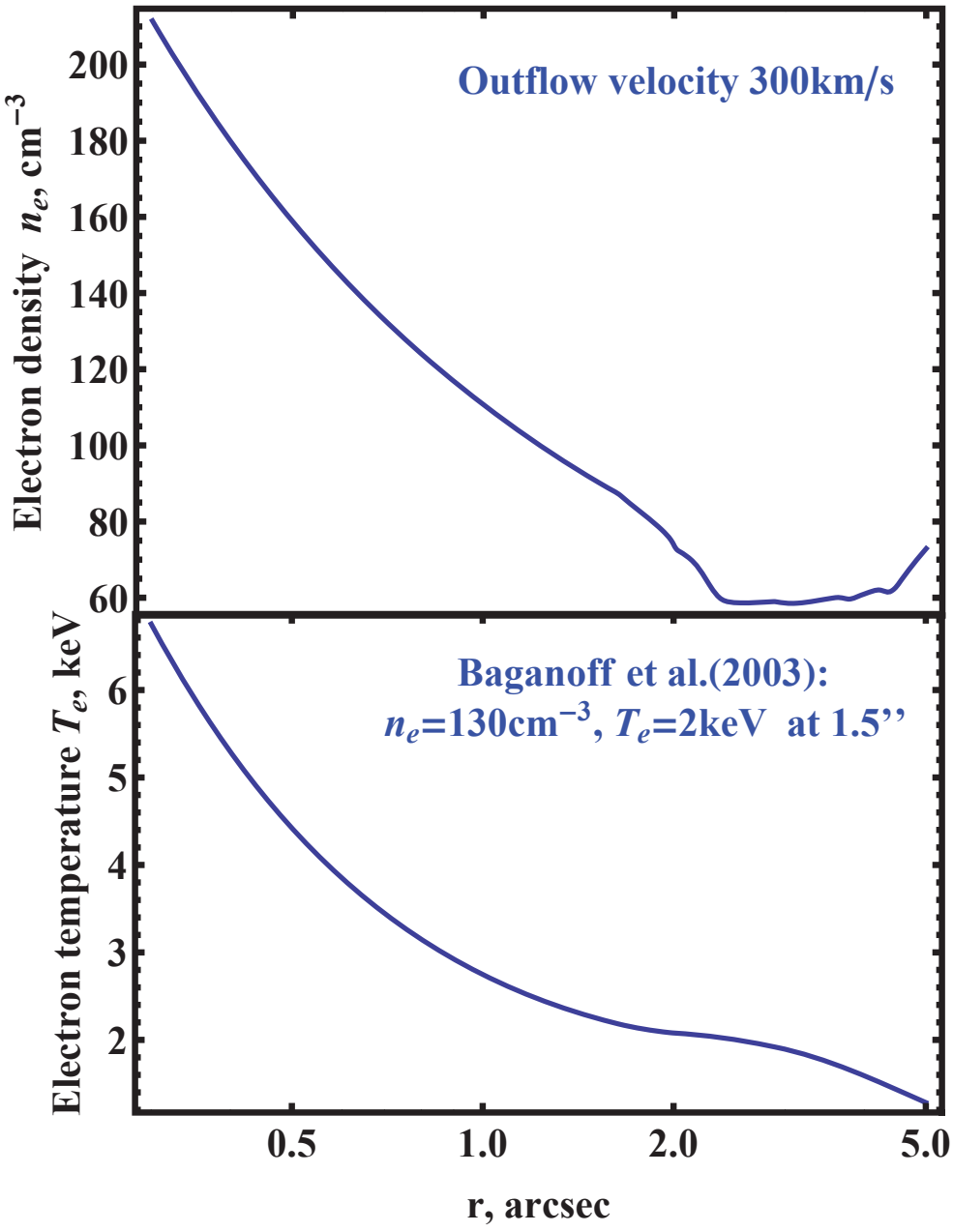

Figure 3.4.— Radial profiles of electron density $n = n_e$ in cm $^{-3}$ (upper panel) and electron temperature T_e in keV (lower panel) in the feeding region.

The profiles of electron density n_e and temperature T_e within several arcseconds from the BH are shown on Figure 3.4 and compare well with the simple earlier estimates (Baganoff et al., 2003; Quataert, 2004). The difference is that our best fit is a subsonic flow supported by the outer medium with the density bounce at $5''$. Though the achieved outflow velocity $v_{\rm out} = 300{\rm km\ s}^{-1}$ is almost independent of radius for $r > 2''$. The line cooling (Sutherland & Dopita, 1993) reduces the heat contents only by several percent for gas reaching $5''$, bremsstrahlung cooling being less important.

The profiles of dimensionless electron temperature $k_B T_e/(m_e c^2)$ and ratio T_p/T_e within several Schwarzschild radii from the BH are shown on Figure 3.5. The electron temperature $T_e = 4 \cdot 10^{10}$ K and density $n_e = 2 \cdot 10^6 {\rm cm}^{-3}$ are found close to the BH. This dynamical model gives an excellent fit to the optically thick luminosity $L = 1.73$ Jy at 86 GHz (Krichbaum et al., 2006) for assumed equipartition of thermal energy with the magnetic field. The model overpredicts by a factor of 20 the observed Faraday rotation measure $RM \sim 50{\rm cm}^{-2}$ at 230 GHz (Marrone et al., 2007), but this may well be a geometric factor. The accretion rate, temperature and density near the BH are in good agreement with more complicated models specifically focusing on sub-mm emission (Sharma et al., 2008; Moscibrodzka et al., 2009). We notice that the ratio of ion and electron temperatures T_p/T_e is significantly larger than predicted by Moscibrodzka et al. (2009), but probably because of the significantly lower T_p in their numerical simulations of the limited domain.

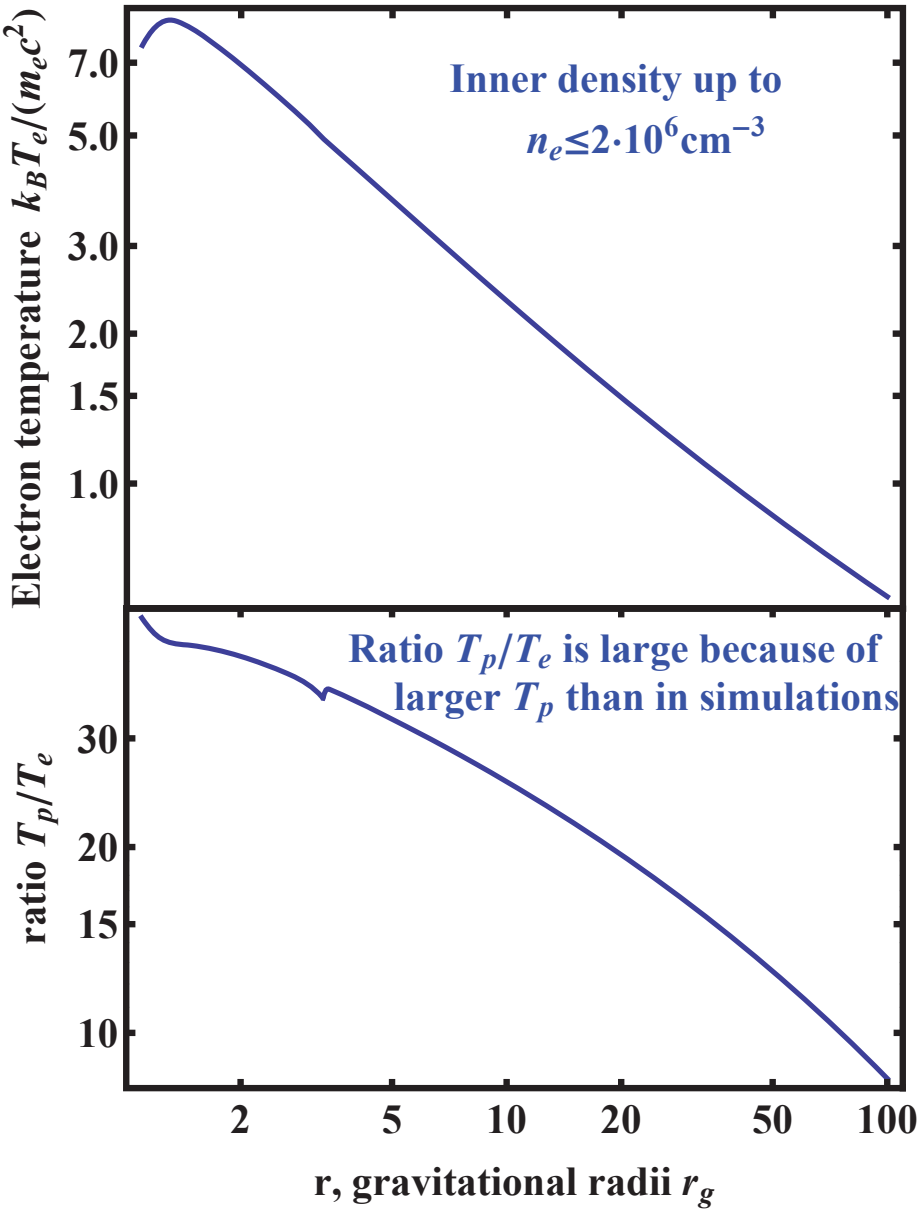

Figure 3.5.— Radial profiles of dimensionless electron temperature normalized to electron mass $k_B T_e/(m_e c^2)$ (upper panel) and ratio of ion to electron temperatures T_p/T_e (lower panel) close to the BH. The inner sonic point is at $3r_{\rm g}$.

Acknowledgements

The authors are grateful to Ramesh Narayan for fruitful discussions, referee Eliot Quataert, Fu-Guo Xie for encouraging us with the shooting method, Feng Yuan, Jorge Cuadra, Avi Loeb for useful comments. The work is supported by NASA grants NNX08AX04H, NNX08AH32G, Chandra Award GO9-0101X, SAO Award 2834-MIT-SAO-4018 and NSF grant AST-0805832.

Chapter 4

Propagation Effects in Magnetized Transrelativistic Plasmas

Abstract

The transfer of polarized radiation in magnetized and non-magnetized relativistic plasmas is an area of research with numerous flaws and gaps. The present chapter is aimed at filling some gaps and eliminating the flaws. Starting from a Trubnikov's linear response tensor for a vacuum wave with $\mathbf{k} = \omega/c$ in thermal plasma, the analytic expression for the dielectric tensor is found in the limit of high frequencies. The Faraday rotation and Faraday conversion measures are computed in their first orders in the ratio of the cyclotron frequency Ω_0 to the observed frequency ω. The computed temperature dependencies of propagation effects bridge the known non-relativistic and ultra-relativistic limiting formulas. The fitting expressions are found for high temperatures, where the higher orders in Ω_0/ω cannot be neglected. The plasma eigenmodes are found to become linearly

polarized at much larger temperatures than thought before. The results are applied to the diagnostics of the hot ISM, hot accretion flows, and jets.

4.1 Introduction

We learn much of our information about astrophysical objects by observing the light they emit. Observations of the polarization properties of light can tell us the geometry of the emitter, strength of the magnetic field, density of plasma, and temperature. The proper and correct theory of optical activity is essential for making accurate predictions. While the low-temperature propagation characteristics of plasma are well-established (Lifshits & Pitaevskii, 1981), the theory of relativistic effects has not been fully studied. In this chapter I discuss the propagation effects through a homogeneous magnetized relativistic plasma. A non-magnetized case emerges as a limit of the magnetized case. The discussion is divided into three separate topics.

Two linear plasma propagation effects are Faraday rotation and Faraday conversion (Azzam & Bashara, 1987). Traditionally, these effects are considered in their lowest orders in the ratio β of the cyclotron frequency Ω_0 to the circular frequency of light ω, id est in a high-frequency approximation. The distribution of particles is taken to be thermal

$$dN = \frac{n \exp(-\gamma/T)}{4\pi m^2 T^2 K_2(T^{-1})} d^3p \tag{4.1}$$

with the dimensionless temperature T in the units of particle rest mass temperature mc^2/k_B. The Faraday rotation measure RM and conversion measure are known in a non-relativistic $T \ll 1$ and an ultra-relativistic $T \gg 1$ limits (Melrose, 1997c). I derive a surprisingly simple analytic expression for arbitrary temperature T.

The smallness of $\beta = \Omega_0/\omega$, $\beta \ll 1$ in the real systems led some authors (Melrose, 1997a) to conclude that the high-frequency approximation will always work. However, there is a clear indication that it breaks down at high temperatures $T \gg 1$. It was claimed that the eigenmodes of plasma are linearly polarized for high temperatures $T \gg 1$ (Melrose, 1997c), because the second order term $\sim \beta^2$ becomes larger than the first order term $\sim \beta$ due to the T dependence. The arbitrarily large T-factor may stand in front of higher order expansion terms in β of the relevant expressions. I find the generalized rotation measure as a function of β and T without expanding in β and compare the results with the known high-frequency expressions. The high-T behavior of the plasma response is indeed significantly different.

Plasma physics involves complicated calculations. This led to a number of errors in the literature (Melrose, 1997c), some of which have still not been fixed. In the article I check all the limiting cases numerically and analytically and expound all the steps of derivations. Thus I correct the relevant errors and misinterpretations made by previous authors, hopefully not making new mistakes. The analytical and numerical results are obtained in Mathematica 6 system. It has an enormous potential in these problems (Marichev, 2008).

The chapter is organized as follows. The formalism of plasma response and calculations are described in §4.2. Several applications to observations can be found in §4.3. I conclude in §4.4 with a short summary and future prospects.

4.2 Calculations

4.2.1 Geometry of the Problem

I assume the traditional geometry depicted on Figure 4.1:

- Euclidean basis ($\tilde{\mathbf{e}}^1$, $\tilde{\mathbf{e}}^2$, $\tilde{\mathbf{e}}^3$),
- magnetic field along the third axis $\tilde{\mathbf{B}} = (0, 0, B)^T$,
- a wave vector of the wave $\tilde{\mathbf{k}} = k(\sin\theta, 0, \cos\theta)^T$ with an angle θ between $\tilde{\mathbf{k}}$ and $\tilde{\mathbf{B}}$.

The basis is rotated from ($\tilde{\mathbf{e}}^1$, $\tilde{\mathbf{e}}^2$, $\tilde{\mathbf{e}}^3$) to ($\mathbf{e}^1$, $\mathbf{e}^2$, $\mathbf{e}^3$), so that the wave propagates along $\mathbf{k} = (0, 0, k)^T$ in the new basis. The transformation has the form

$$\mathbf{e}^1 = \tilde{\mathbf{e}}^1 \cos\theta - \tilde{\mathbf{e}}^3 \sin\theta, \quad \mathbf{e}^2 = \tilde{\mathbf{e}}^2, \quad \mathbf{e}^3 = \tilde{\mathbf{e}}^1 \sin\theta + \tilde{\mathbf{e}}^3 \cos\theta, \tag{4.2}$$

which can be conveniently written as

$$\mathbf{e}^\mu = \tilde{\mathbf{e}}^\nu S^{\nu\mu}, \quad S^{\nu\mu} = \begin{pmatrix} \cos\theta & 0 & \sin\theta \\ 0 & 1 & 0 \\ -\sin\theta & 0 & \cos\theta \end{pmatrix}. \tag{4.3}$$

Vectors and tensors then rotate according to

$$A^\mu = (S^T)^{\mu\nu} \tilde{A}^\nu, \quad \alpha^{\mu\nu} = (S^T)^{\mu\sigma} \tilde{\alpha}^{\sigma\delta} S^{\delta\nu}. \tag{4.4}$$

4.2.2 Linear Plasma Response

The propagation of weak electromagnetic (EM) waves in a homogeneous magnetized plasma can be fully described by the response tensor $\alpha^{\mu\nu}$. It expresses the linear proportionality between the induced current density and the vector potential $j^\mu(\omega) =$

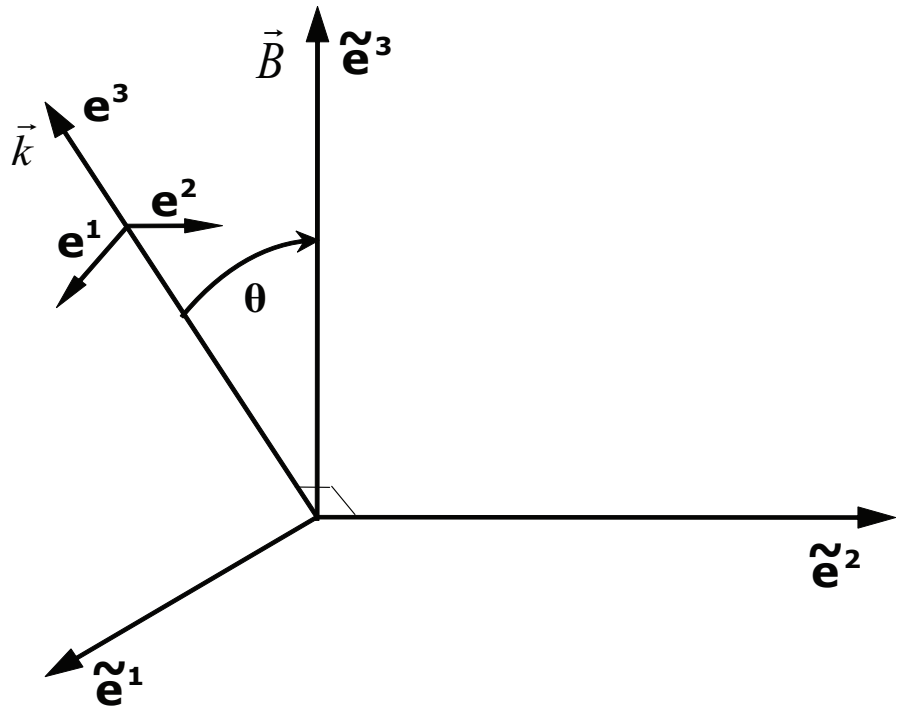

Figure 4.1.— Geometry of the problem.

$\alpha^\mu{}_\nu A^\nu(\omega)$. The spatial projection of such defined 4-D tensor $\alpha^\mu{}_\nu$ is equal to the 3-D tensor α_{ij} defined by $\mathbf{j} = \alpha_{ij}\mathbf{A}$.

I consider Trubnikov's form of the response tensor (Trubnikov, 1958; Melrose, 1997a). I work in a low-density regime, where the plasma response is calculated for a vacuum wave with $|\mathbf{k}| = \omega/c$. I take the tensor $\tilde{\alpha}^{\mu\nu}$ from the first-hand derivations (Trubnikov, 1958; Melrose, 1997a), make the transformation (4.4), and take the 1-st and 2-nd components in both indices. Thus the projection onto the $(\mathbf{e}^1, \mathbf{e}^2)$ plane in CGS units is

$$\alpha^\mu{}_\nu(k) = \frac{iq^2 n\omega\rho^2}{cmK_2(\rho)} \int_0^\infty d\xi \left[t^\mu{}_\nu \frac{K_2(r)}{r^2} - R^\mu \overline{R}_\nu \frac{K_3(r)}{r^3} \right], \tag{4.5}$$

$$t^\mu{}_\nu = \begin{pmatrix} \cos^2\theta\cos\Omega_0\xi + \sin^2\theta & \eta\cos\theta\sin\Omega_0\xi \\ -\eta\cos\theta\sin\Omega_0\xi & \cos\Omega_0\xi \end{pmatrix}, \tag{4.6}$$

$$R^{\mu} = \frac{\omega \sin\theta}{\Omega_0} \left(\cos\theta(\sin\Omega_0\xi - \Omega_0\xi), -\eta(1-\cos\Omega_0\xi)\right), \tag{4.7a}$$

$$\overline{R}_{\nu} = \frac{\omega \sin\theta}{\Omega_0} \left(\cos\theta(\sin\Omega_0\xi - \Omega_0\xi), \eta(1-\cos\Omega_0\xi)\right), \tag{4.7b}$$

and

$$r = \left[\rho^2 - 2i\omega\xi\rho + \frac{\omega^2\sin^2\theta}{\Omega_0^2}\left(2 - \Omega_0^2\xi^2 - 2\cos\Omega_0\xi\right)\right]^{1/2}, \tag{4.8}$$

where η is the sign of the charge, $K_n(r)$ is the n-th Bessel function of the second kind[1]. The quantity ρ is the dimensionless inverse temperature,

$$\rho = T^{-1} = \frac{mc^2}{k_B T_p}, \tag{4.9}$$

where T_p the actual temperature of particles. The response of plasma is usually characterized by the dielectric tensor. Its projection onto the $(\mathbf{e}^1, \mathbf{e}^2)$ plane is

$$\varepsilon^{\mu}{}_{\nu} = \delta^{\mu}{}_{\nu} + \frac{4\pi c}{\omega^2}\alpha^{\mu}{}_{\nu}. \tag{4.10}$$

The wave equation for transverse waves in terms of $\varepsilon^{\mu}{}_{\nu}$ is

$$(n_{\rm r}^2\delta^{\mu}{}_{\nu} - \varepsilon^{\mu}{}_{\nu}) \begin{pmatrix} E_1 \\ \\ E_2 \end{pmatrix} = 0, \tag{4.11}$$

where E_1 and E_2 are the components of the electric field along $\mathbf{e}^1$ and $\mathbf{e}^2$ and $n_{\rm r}^2 = k^2c^2/\omega^2$ (Swanson, 2003).

[1]Note that the analogous expression in Melrose (1997c) has an extra factor $\Omega_0\xi$ in the component t^{11} and the opposite sign of $R^{\mu}\overline{R}^{\nu}$ term by an error. The author has corrected his formulas in Melrose (2010).

4.2.3 High Frequency Limit

Let me first calculate the limiting expression for $\alpha^{\mu}{}_{\nu}$ in the high-frequency limit $\Omega_0 \ll \omega$. I denote

$$\alpha = \omega\xi, \qquad \beta = \frac{\Omega_0}{\omega}, \tag{4.12}$$

substitute the definitions (4.12) into the expression (4.5), and expand the response tensor $\alpha^{\mu}{}_{\nu}$ in β. I retain only up to the 2-nd order of the expansion, which gives the conventional generalized Faraday rotation (Melrose, 1997c). The first terms of the series of r, $t^{\mu}{}_{\nu}$, and $R^{\mu}\overline{R}_{\nu}$ read

$$r^2 = r_0^2 + \delta r^2, \quad r_0^2 = \rho^2 - 2i\alpha\rho, \quad \delta r^2 = -\frac{\sin^2\theta}{12}\beta^2\alpha^4, \tag{4.13}$$

$$t^{\mu}{}_{\nu} = \begin{pmatrix} 1 - \cos^2\theta \cdot \alpha^2\beta^2/2 & \alpha\beta\eta\cos\theta \\ -\alpha\beta\eta\cos\theta & 1 - \alpha^2\beta^2/2 \end{pmatrix}, \tag{4.14}$$

$$R^{\mu}\overline{R}_{\nu} = -\frac{\alpha^4\beta^2}{4}\sin^2\theta \begin{pmatrix} 0 & 0 \\ 0 & 1 \end{pmatrix}. \tag{4.15}$$

Melrose (1997c) used the approximation $r_0^2 = -2i\alpha\rho$ instead of the expansion (4.13) and obtained the approximate high-T expressions as his final answers.

However, one can take the emergent integrals, if one considers the exact expansions (4.13,4.14,4.15). Three terms appear in the expanded expression for $\alpha^{\mu}{}_{\nu}$:

$$\int_0^{\infty} d\alpha \left[t^{\mu}{}_{\nu} \frac{K_2(r_0)}{r_0^2} \right], \tag{4.16a}$$

$$\int_0^{\infty} d\alpha \left[t^{\mu}{}_{\nu} \frac{K_3(r_0)\delta r^2}{r_0^3} \right], \tag{4.16b}$$

$$\int_0^{\infty} d\alpha \left[R^{\mu}\overline{R}_{\nu} \frac{K_3(r_0)}{r_0^3} \right]. \tag{4.16c}$$

The 2-nd term (4.16b) originates from the expansion of $K_2(r)/r^2$ in r^2 to the first order

$$\frac{K_2(r)}{r^2} - \frac{K_2(r_0)}{r_0^2} = -\frac{\delta r^2}{2}\frac{K_3(r_0)}{r_0^3}. \tag{4.17}$$

Integrals (4.16a,4.16b,4.16c) can be evaluated knowing that

$$\int_0^\infty d\alpha \left[\alpha^n \frac{K_2(\sqrt{\rho^2 - 2i\rho\alpha})}{\rho^2 - 2i\rho\alpha}\right] = n! i^{n+1}\frac{K_{n-1}(\rho)}{\rho^2}, \tag{4.18a}$$

$$\int_0^\infty d\alpha \left[\alpha^n \frac{K_3(\sqrt{\rho^2 - 2i\rho\alpha})}{(\rho^2 - 2i\rho\alpha)^{3/2}}\right] = n! i^{n+1}\frac{K_{n-2}(\rho)}{\rho^3}. \tag{4.18b}$$

4.2.4 Components in High-Frequency Limit

I substitute the high-frequency expansions (4.13,4.14,4.15) into the expression (4.10) for the projection of the dielectric tensor $\varepsilon^\mu{}_\nu$ with the projection of the response tensor $\alpha^\mu{}_\nu$ (4.5) and take the integrals (4.16a,4.16b,4.16c) analytically. The components of the dielectric tensor (4.10) in the lowest orders in Ω_0/ω are then

$$\varepsilon^1{}_1 = 1 - \frac{\omega_p^2}{\omega^2}\left(\frac{K_1(\rho)}{K_2(\rho)}\left(1 + \frac{\Omega_0^2}{\omega^2}\cos^2\theta\right) + \frac{\Omega_0^2\sin^2\theta}{\omega^2\rho}\right), \tag{4.19a}$$

$$\varepsilon^2{}_2 = 1 - \frac{\omega_p^2}{\omega^2}\left(\frac{K_1(\rho)}{K_2(\rho)}\left(1 + \frac{\Omega_0^2}{\omega^2}\right) + \frac{7\Omega_0^2\sin^2\theta}{\omega^2\rho}\right), \tag{4.19b}$$

$$\varepsilon^1{}_2 = -\varepsilon^2{}_1 = -i\eta\frac{\omega_p^2\Omega_0}{\omega^3}\frac{K_0(\rho)}{K_2(\rho)}\cos\theta, \tag{4.20}$$

where the plasma frequency ω_p in CGS units is

$$\omega_p^2 = \frac{4\pi n q^2}{m}. \tag{4.21}$$

The results reproduce the non-relativistic limits for $\rho \to +\infty$:

$$\varepsilon^1{}_1 = 1 - \frac{\omega_p^2}{\omega^2}\left(1 + \frac{\Omega_0^2}{\omega^2}\cos^2\theta\right), \tag{4.22a}$$

$$\varepsilon^2{}_2 = 1 - \frac{\omega_p^2}{\omega^2}\left(1 + \frac{\Omega_0^2}{\omega^2}\right), \tag{4.22b}$$

$$\varepsilon^1{}_2 = -\varepsilon^2{}_1 = -i\eta\frac{\omega_p^2\Omega_0}{\omega^3}\cos\theta, \tag{4.22c}$$

where all Bessel functions of ρ approach unity[2] (Lifshits & Pitaevskii, 1981; Trubnikov, 1996; Swanson, 2003; Bellan, 2006). The corresponding relativistic limits $\rho \to 0$ of the same components are

$$\varepsilon^1{}_1 = 1 - \frac{\omega_p^2}{\omega^2}\left(\frac{1}{2T}\left(1 + \frac{\Omega_0^2}{\omega^2}\cos^2\theta\right) + T\frac{\Omega_0^2\sin^2\theta}{\omega^2}\right), \tag{4.23a}$$

$$\varepsilon^2{}_2 = 1 - \frac{\omega_p^2}{\omega^2}\left(\frac{1}{2T}\left(1 + \frac{\Omega_0^2}{\omega^2}\right) + T\frac{7\Omega_0^2\sin^2\theta}{\omega^2}\right), \tag{4.23b}$$

$$\varepsilon^1{}_2 = -\varepsilon^2{}_1 = -i\eta\frac{\omega_p^2\Omega_0}{\omega^3}\frac{\ln(T)}{2T^2}\cos\theta, \tag{4.23c}$$

consistent with Melrose (1997c); Quataert & Gruzinov (2000b)[3]. The ultra-relativistic non-magnetized dispersion relation then reads

$$\omega^2 = \frac{\omega_p^2}{2T} + c^2k^2 = \frac{2\pi nq^2}{mT} + c^2k^2 \tag{4.24}$$

according to the relation (4.11). The expression (4.24) is consistent with Lifshits & Pitaevskii (1981), chapter 32.

The plasma propagation effects can usually be described in terms of only the difference of the diagonal components and the non-diagonal component of $\varepsilon^\mu{}_\nu$. I define $\mathbf{X}$ to be a vector of T, θ, Ω_0/ω. I introduce the multipliers $f(\mathbf{X})$ and $g(\mathbf{X})$ to correct

[2]The non-diagonal term has a wrong sign in Melrose (1997c).

[3]The diagonal plasma response is 2 times larger in Melrose (1997c) by an error.

the expressions, when the high-frequency limit breaks. I write the difference between the diagonal components with a multiplier $f(\mathbf{X})$ as

$$\varepsilon^1{}_1 - \varepsilon^2{}_2 = f(\mathbf{X})\frac{\omega_p^2\Omega_0^2}{\omega^4}\left(\frac{K_1(T^{-1})}{K_2(T^{-1})} + 6T\right)\sin^2\theta \tag{4.25}$$

and the non-diagonal component with a multiplier $g(\mathbf{X})$ as

$$\varepsilon^1{}_2 = -i\eta g(\mathbf{X})\frac{\omega_p^2\Omega_0}{\omega^3}\frac{K_0(T^{-1})}{K_2(T^{-1})}\cos\theta. \tag{4.26}$$

Both multipliers equal unity in the high-frequency limit $f(\mathbf{X}) = g(\mathbf{X}) = 1$. Now we can turn to a more general case.

4.2.5 Fitting Formulas for Higher Temperatures

The ultra-relativistic expressions (4.23a,4.23b,4.23c) allow me to trace the T-factors in front of the first 3 expansion coefficients of the dielectric tensor in β. The coefficient at β^2 is $\sim T^3/\ln(T)$ times larger than at β. Thus at temperature $T \gtrsim 10$ the 2-nd order becomes larger than the 1-st order for the ratio $\Omega_0/\omega \sim 10^{-3}$. This indicates that the expansion in β may become invalid at these plasma parameters[4]. The multipliers $f(\mathbf{X})$ and $g(\mathbf{X})$ are likely to be far from 1. I consider only the real parts of these multipliers, since the imaginary parts correspond to absorption. The contour plots of the numerically calculated $f(\mathbf{X})$ and $g(\mathbf{X})$ for somewhat arbitrary $\theta = \pi/4$ are shown on Figure 4.2 and Figure 4.3, respectively.

Let me define X to be the following combination of the parameters

$$X = T\sqrt{\sqrt{2}\sin\theta\left(10^3\frac{\Omega_0}{\omega}\right)}. \tag{4.27}$$

[4]One cannot claim that the diagonal magnetized terms become larger then the non-diagonal (Melrose, 1997c).

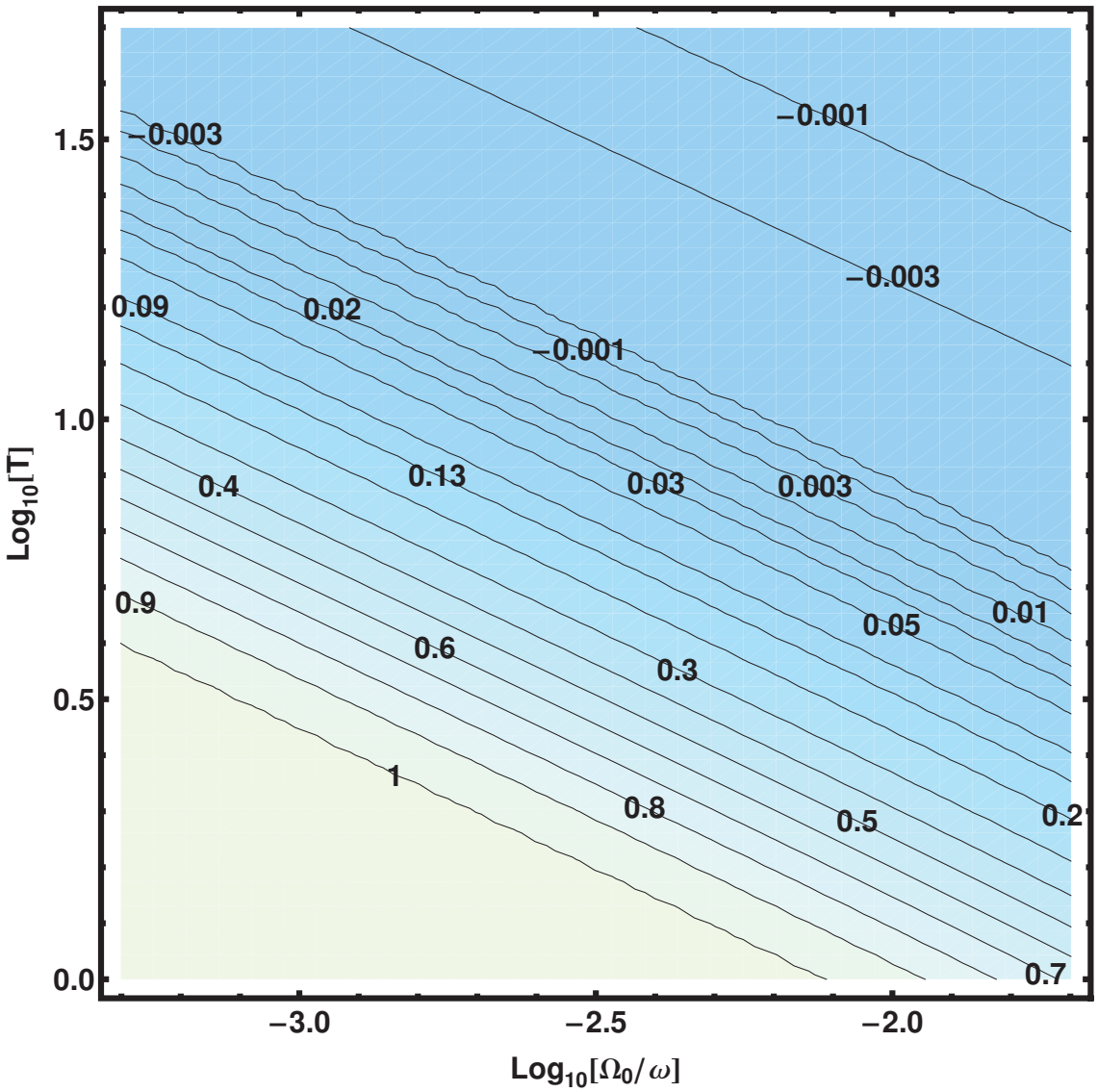

Figure 4.2.— Multiplier $f(\mathbf{X})$ for the difference of the diagonal components $\varepsilon^1{}_1 - \varepsilon^2{}_2$ for $\theta = \pi/4$.

For the fiducial $\Omega_0/\omega = 10^{-3}$, $\theta = \pi/4$ the parameter X is just temperature $X = T$.

I first identify the boundaries, where the high-frequency limit is valid. Then I find

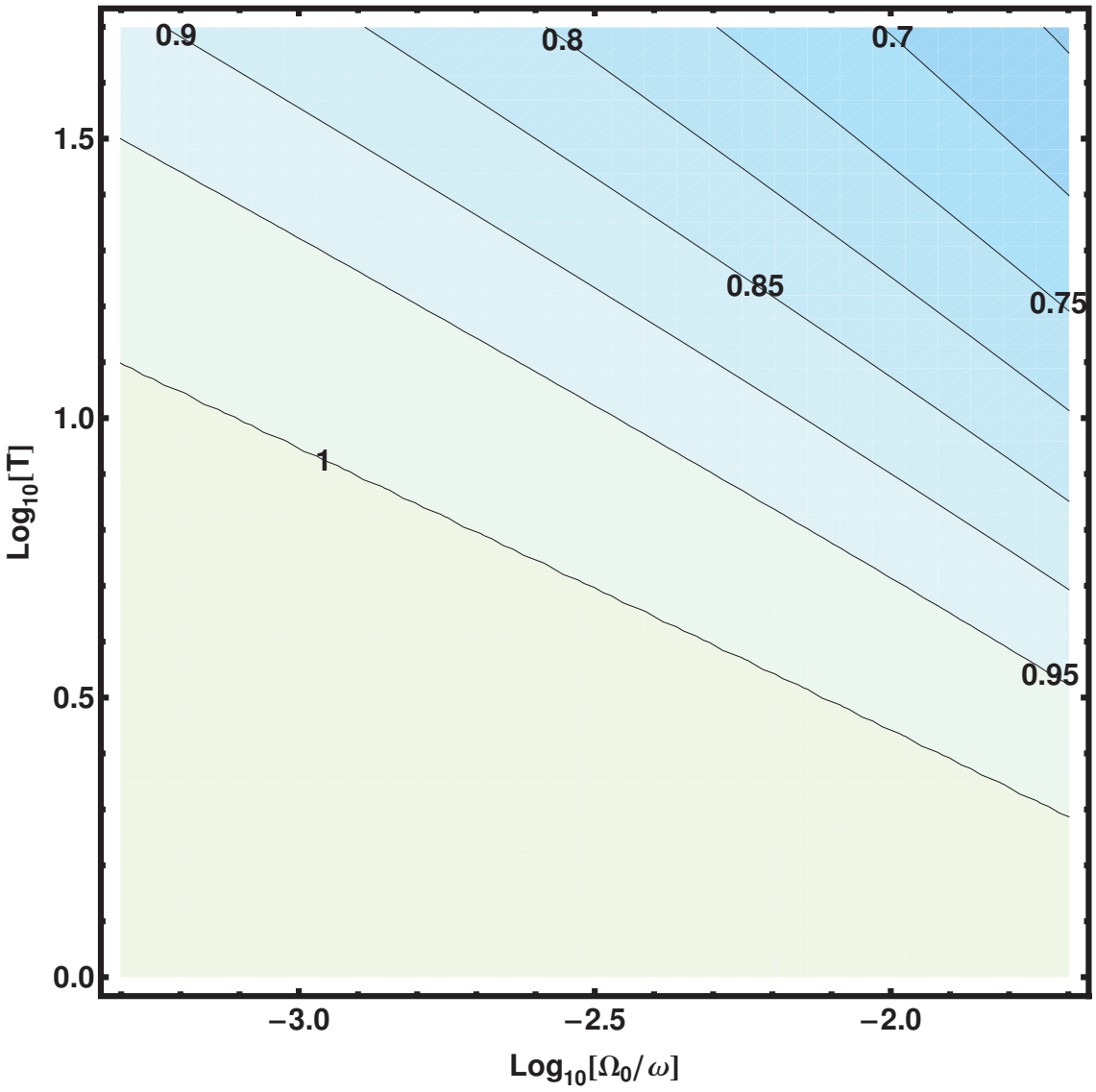

Figure 4.3.— Multiplier $g(\mathbf{X})$ for the non-diagonal component $\varepsilon^1{}_2$ for $\theta = \pi/4$.

a fit for the multipliers at higher X. The expression (4.25) for the difference $\varepsilon^1{}_1 - \varepsilon^2{}_2$ is accurate within 10% for $X < 0.1$ if we set $f(X) = 1$. The expression (4.26) for $\varepsilon^1{}_2$ is accurate within 10% for $X < 30$ if we set $g(X) = 1$. The accuracy depends on the

parameter X rather than on the individual parameters T, Ω_0/ω, θ. The expression

$$f(X) = 2.011 \exp\left(-\frac{X^{1.035}}{4.7}\right) - \\ - \cos\left(\frac{X}{2}\right) \exp\left(-\frac{X^{1.2}}{2.73}\right) - 0.011 \exp\left(-\frac{X}{47.2}\right) \tag{4.28}$$

extends the applicability domain of the formula (4.25) up to $X \sim 200$. Figure 4.4 shows the fit for $f(X)$ in comparison with the numerical results. The expression

$$g(X) = 1 - 0.11 \ln(1 + 0.035X) \tag{4.29}$$

extends up to $X \sim 200$ the domain of the formula (4.26). Figure 4.5 shows the fit for $g(X)$ in comparison with the numerical results.

4.2.6 Exact Plasma Response

The expression for the response tensor (4.5) is written for a vacuum wave with $|\mathbf{k}|c = \omega$. In the real plasma, the wave is modified by the plasma response. A more general self-consistent response tensor should be used (Trubnikov, 1958; Melrose, 1997c). One needs to solve a dispersion relation similar to the relation (4.11) to obtain the eigenmodes. Thus the eigenmodes and the response tensor should be computed self-consistently. One should not forget about the antihermitian and longitudinal components of the dielectric tensor $\varepsilon^{\mu}{}_{\nu}$ that modify the dispersion relation.

4.2.7 Eigenmodes

The above calculation is applicable also to a non-magnetized plasma. Dispersion relation of EM waves in a non-magnetized plasma reads

$$\omega^2 = k^2c^2 + \omega_p^2 \frac{K_1(T^{-1})}{K_2(T^{-1})} \tag{4.30}$$

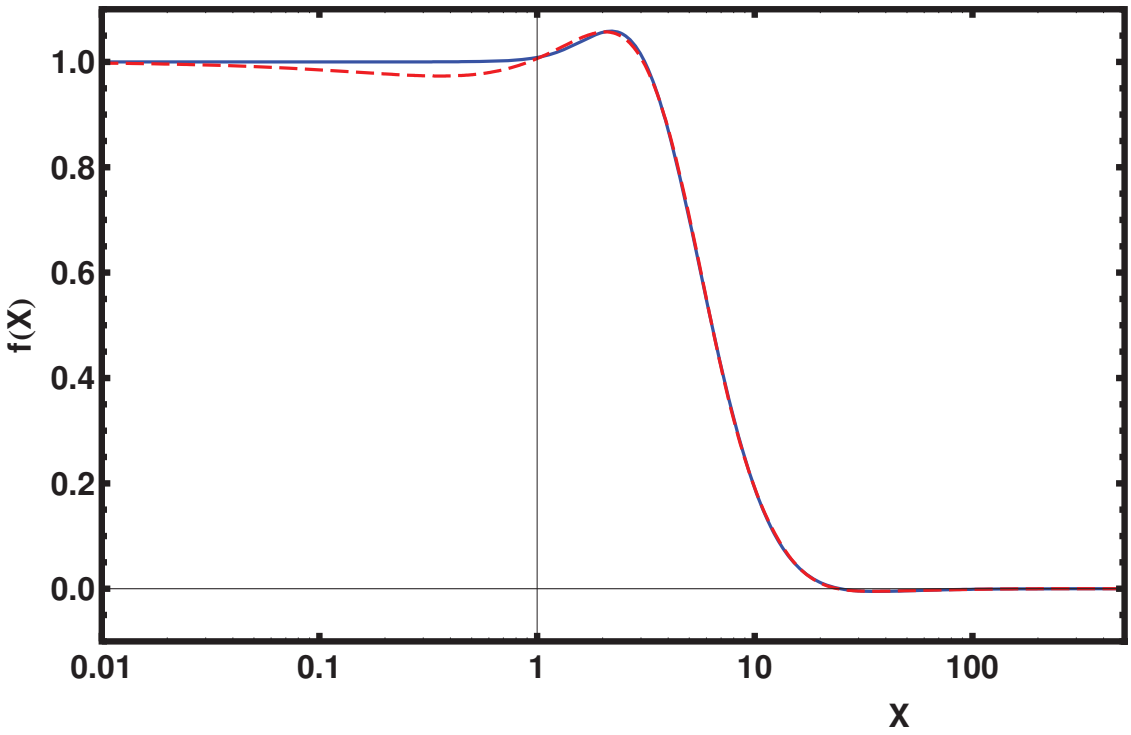

Figure 4.4.— Multiplier $f(X)$ for the difference of the diagonal components $\varepsilon^1{}_1 - \varepsilon^2{}_2$. Dashed line — fitting formula (4.28).

in a high-frequency approximation $\omega \gg \omega_p$. The opposite limit of $kc \ll \omega$ was considered by Bergman & Eliasson (2001).

Now we turn to the magnetized case. Melrose (1997c) only considered the first terms of in the expansion of $\alpha^\mu{}_\nu$ in β to get the eigenmodes. I do the next step: consider the full expression in β in the low-density regime $kc = \omega$, but consider only the hermitian part of $\alpha^\mu{}_\nu$ in computations. The ellipticity $\Upsilon = (\varepsilon^1{}_1 - \varepsilon^2{}_2) : |\varepsilon^1{}_2|$ determines the type of eigenmodes. If $|\Upsilon| \gg 1$, then the eigenmodes are linearly polarized unless θ is close to 0. If $|\Upsilon| \ll 1$, then the eigenmodes are circularly polarized for θ far from $\pi/2$. Let me

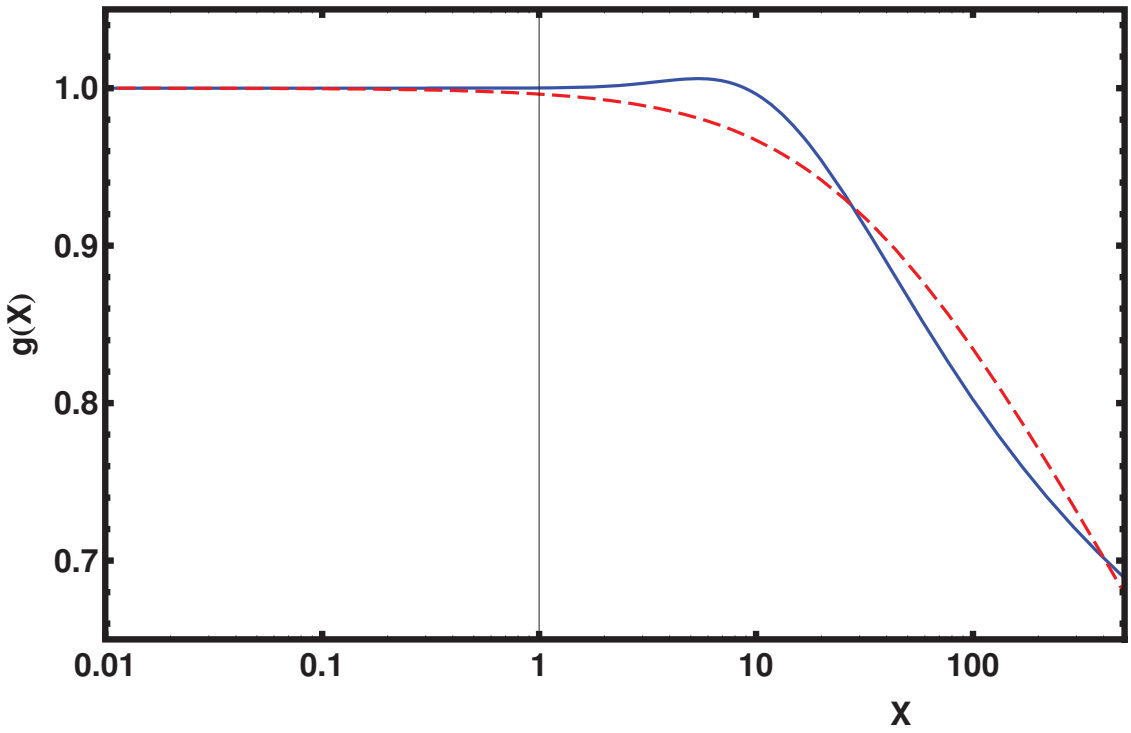

Figure 4.5.— Multiplier $g(X)$ for the non-diagonal component $\varepsilon^1{}_2$. Dashed line — fitting formula (4.29).

consider the fiducial model with $\Omega_0/\omega = 10^{-3}$ and $\theta = \pi/4$. Figure 4.6 shows the ratio Υ calculated in a high-frequency approximation (see § 4.2.3) (dashed line) and in a general low-density approximation (see § 4.2.5) (solid line). The high-frequency approximation produces the linear eigenmodes already at $T \gtrsim 10$ consistently with Melrose (1997c). However, the general low-density limit produces the eigenmodes with $\Upsilon \sim 1$ up to very high temperatures $T \sim 50$. Unexpectedly, the sign of the diagonal difference $(\varepsilon^1{}_1 - \varepsilon^2{}_2)$ changes at about $T \approx 25$.

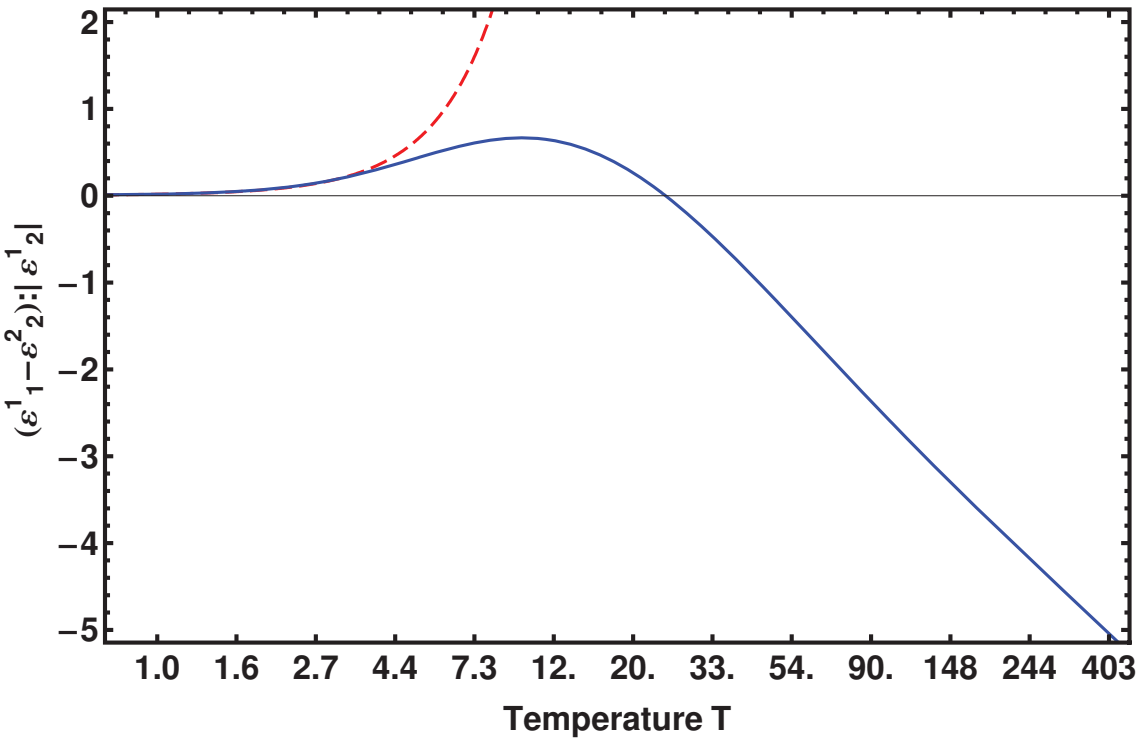

Figure 4.6.— Ellipticity $\Upsilon = (\varepsilon^1{}_1 - \varepsilon^2{}_2) : |\varepsilon^1{}_2|$ of eigenmodes. The absolute value of the ratio Υ much above unity — linear eigenmodes, much below unity — circular eigenmodes. Solid line — this chapter, dashed line — previous calculations.

4.3 Applications

The calculated transrelativistic propagation effects have far-reaching consequences in many topics of astronomy. Let me concentrate on four applications: propagation delay, Faraday rotation measure of light from the Galactic Center (GC), circularly polarized light from the GC, diagnostics of jets.

4.3.1 Dispersion Measure

Propagation delay is an important effect in pulsar dispersion (Phillips & Wolszczan, 1992). The relativistic part of this delay can be obtained from the dispersion relation (4.30). I retain only the first-order correction in T, since $T \ll 1$ in the interstellar medium (Cox & Reynolds, 1987). Since $K_1(T^{-1})/K_2(T^{-1}) \approx 1 - 3T/2$ at low T, the non-relativistic Dispersion Measure (DM) should be modified as

$$DM_{\rm rel} = DM_{\rm nonrel}\left(1 - \frac{3}{2}T\right). \tag{4.31}$$

This shows that the gas density is slightly underestimated, if the non-relativistic formulas are used[5]. However, the relativistic correction to the DM is small and can be neglected in most practical cases when $T \ll 1$. The effects in magnetized plasma are also relevant for pulsars.

4.3.2 Magnetized Radiative Transfer

General Formulae

Relativistic plasmas exhibit a generalized Faraday rotation for a general orientation of the magnetic field (Azzam & Bashara, 1987). One can decompose it into two effects: Faraday rotation and Faraday conversion. The former operates alone at $\theta = 0, \pi$, the latter operates alone at $\theta = \pi/2$, and both should be considered together for the intermediate angles. The transfer equations (Mueller calculus) for the Stokes parameters I, Q, U, V were devised to treat together the propagation effects, emission, and absorption (Azzam & Bashara, 1987; Melrose & McPhedran, 1991). Good approximations for emission and

[5]The formula in Phillips & Wolszczan (1992) has no references/checks and is not correct.

absorption have been long known (Trubnikov, 1958; Rybicki & Lightman, 1979; Melrose & McPhedran, 1991; Wolfe & Melia, 2006). Now one can combine them with the proper approximations of the propagation effects given by

$$\frac{d}{ds}\begin{pmatrix} I \\ Q \\ U \\ V \end{pmatrix} = \begin{pmatrix} 0 & 0 & 0 & 0 \\ 0 & 0 & -\rho_V & \rho_U \\ 0 & \rho_V & 0 & -\rho_Q \\ 0 & -\rho_U & \rho_Q & 0 \end{pmatrix} \begin{pmatrix} I \\ Q \\ U \\ V \end{pmatrix}, \tag{4.32}$$

$$\rho_V = -\frac{\omega}{c} i\varepsilon^1{}_2, \quad \rho_Q = -\frac{\omega}{2c}(\varepsilon^1{}_1 - \varepsilon^2{}_2), \quad \rho_U = 0, \tag{4.33}$$

and do the radiative transfer calculations. Here $\varepsilon^\mu{}_\nu$ stands for the Hermitean part given by the relations (4.28,4.29) with the real multipliers $f(X)$ and $g(X)$. One of the most interesting objects for such calculations is our Galactic Center Sgr A*.

The transfer equations were recently solved for a simple time-independent dynamical model of the GC accretion (Huang et al., 2008). The authors treat the ordinary and extraordinary modes as linearly polarized. They assume these eigenmodes constitute a basis, where either U or Q components of emissivity and propagation coefficients vanish. Actually, U components vanish ($\rho_U = 0$) already in the basis $(\mathbf{e}^1, \mathbf{e}^2)$, since the projection of the magnetic field onto $(\mathbf{e}^1, \mathbf{e}^2)$ is parallel to $\mathbf{e}^1$ (see Melrose & McPhedran (1991) p.184). As I have shown in the § 4.2.7, plasma modes are far from being linearly polarized at temperatures $T \lesssim 10$ estimated for the GC (Sharma et al., 2007a). Thus, the propagation coefficients should be taken from equations (4.25) and (4.26). The Faraday conversion coefficient ρ_Q cannot be defined via emissivities and Faraday rotation coefficient ρ_V as in Huang et al. (2008). The Faraday rotation measure was calculated from a simulated accretion profile in Sharma et al. (2007b). However, the chapter considered only the Faraday rotation and did not carry out the self-consistent treatment of propagation. It

is impossible to disentangle the effects of Faraday rotation and Faraday conversion in a relativistic plasma.

Faraday Rotation

The crucial part of any radiative transfer is the proper transfer coefficients. It allows one to estimate the electron density near the accreting object (Quataert & Gruzinov, 2000b; Shcherbakov, 2008a). Several formulas were suggested for the temperature dependence of the component $\varepsilon^1{}_2$ responsible for Faraday rotation. These formulas were yet given for the high-frequency approximation (see § 4.2.3). Let me compare them with the exact temperature dependence (4.20) $J = K_0(T^{-1})/K_2(T^{-1})$ and its limits. The limits are $J \to 1$ as $T \to 0$ and $J \to \ln(T)/(2T^2)$ as $T \to +\infty$. The results of this comparison are shown on Figure 4.7.

Ballantyne et al. (2007)[6] divided the thermal distribution into ultra-relativistic and non-relativistic parts as marked by the electron energy $\gamma_{\rm crit} = 10$. They sum the contributions of both species with calculated densities. To make a plot, I take their effective temperature Θ of plasma above $\gamma_{\rm crit}$ to be just temperature $\Theta = T$ and not the average kinetic energy as Ballantyne et al. (2007) suggest. This brings Θ to lower values and decreases the rotation measure. Even with this decrease the rotation measure is severely overestimated at $T \sim 1$. The convergence to the relativistic limit is not achieved even at $T \sim 30$. The paper Huang et al. (2008) found the simpler fitting formula that reproduces the limits. Their expression is quite accurate.[7]

[6]The paper Ballantyne et al. (2007) has likely confused the 3-D projection of the 4-D response tensor in $j^\mu = \alpha^{\mu\nu}A_\nu$ (Melrose, 1997c) with the 3-D response tensor $\mathbf{j} = \alpha_{ij}\mathbf{A}$ that has the opposite sign.

[7]"Temperature" γ_c in Huang et al. (2008) should be redefined as $\gamma_c = 1 + T$, otherwise the lower limit is not reproduced.

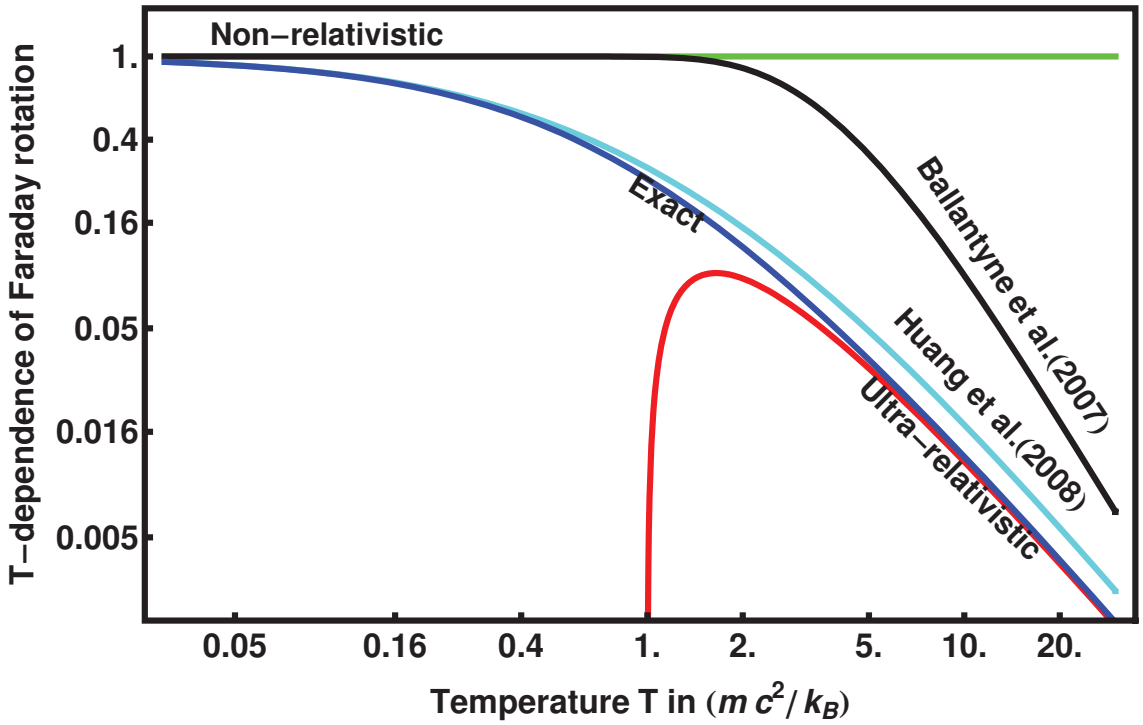

Figure 4.7.— Temperature dependence of the Faraday rotation measure.

Faraday Conversion

The increase in the circular polarization of Sgr A* at frequency 1THz is predicted by Huang et al. (2008). The phase of Faraday conversion approaches unity and the destructive interference does not occur at this frequency. The result seems to be qualitatively correct regardless of the expression for the conversion measure, but the proper expressions (4.25) and (4.26) should be used for quantitative predictions.

Jets

The better treatment of propagation effects may also play a role in observations of jets. As we saw in § 4.2.5, the propagation effects in thermal plasma cannot be described in the lowest orders in Ω_0/ω, if the temperature T is sufficiently high. Power-law distribution of electrons can have a quite high effective temperature. Thus the high-frequency limit (Sazonov, 1969; Jones & O'Dell, 1977; Melrose, 1997b) may not approximate well the hermitian part of the response tensor. Careful analysis of jet observations (Beckert & Falcke, 2002; Wardle et al., 1998) may be needed. It should be based at least on the expressions for $\varepsilon^{\mu}{}_{\nu}$ in a general low-density regime.

4.4 Discussion & Conclusion

This chapter presents several new calculations and amends the previous calculations of propagation effects in uniform magnetized plasma with thermal particle distribution equation (4.1). The expression (4.5) for the correct response tensor is given in a high-frequency approximation. The exact temperature dependence (4.19) and (4.20) is found in first orders in Ω_0/ω in addition to the known highly-relativistic and non-relativistic results. The higher order terms may be important for relativistic plasmas in jets and hot accretion flows. The fitting expressions (4.28) and (4.29) are found for the dielectric tensor components (4.25) and (4.26) at relatively high temperatures.

The results of numerical computations are given only when the corresponding analytical formulas are found. One can always compute the needed coefficients numerically for every particular frequency ω, plasma frequency ω_p, cyclotron frequency Ω_0, and

distribution of electrons. However, the analytic formulas offer a simpler and faster way of dealing with the radiative transfer for a non-specialist. The eigenmodes were not considered in much detail, since radiative transfer problems do not require a knowledge of eigenmodes. However the knowledge of eigenmodes is needed to compute the self-consistent response tensor (see § 4.2.6).

The response tensor in the form (4.5) can be expanded in Ω_0/ω and ω_p/ω. This expansion is of mathematical interest and will be presented in a subsequent paper as well as the expressions for a power-law electron distribution. Propagation through non-magnetized plasmas will also be considered separately.

Acknowledgements

The author is grateful to Ramesh Narayan for fruitful discussions and Diego Munoz for pointing out relevant references. I thank the anonymous referee for helpful suggestions that improved the chapter.

Chapter 5

General Relativistic Polarized Radiative Transfer: Building a Dynamics-Observations Interface

Abstract

The rising amount of polarized observations of relativistic sources requires the correct theory for proper model fitting. The equations for general relativistic (GR) polarized radiative transfer are derived starting from the Boltzmann equation and basic ideas of general relativity. The derivation is aimed at providing a practical guide to reproducing the synchrotron part of radio & sub-mm emission from low luminosity active galactic nuclei (LLAGNs), in particular Sgr A*, and jets. The recipe for fast exact calculation of cyclo-synchrotron emissivities, absorptivities, Faraday rotation and conversion coefficients

is given for isotropic particle distributions. The multitude of physical effects influencing simulated spectrum is discussed. The application of the prescribed technique is necessary to determine the black hole (BH) spin in LLAGNs, constraining it with all observations of total flux, linear and circular polarization fractions, and electric vector position angle as functions of the observed frequency.

5.1 Introduction

The good model of radiative transfer is the key in bridging the plasma dynamics and the observations of compact accreting sources. The dynamics of plasma evolved from hydrodynamics (Ruffert, 1994) to magneto hydrodynamics (MHD) (Hawley & Balbus, 2002) and particle-in-cell (PIC) simulations (Sironi & Spitkovsky, 2009). The modelling of compact object's gravity has turned from quasi-Newtonian potential (Hawley & Krolik, 2001; Igumenshchev & Narayan, 2002) to the full general relativistic (GR) MHD (De Villiers et al., 2003; Shafee et al., 2008). Only GRMHD simulations allow to fully account for the spin of the compact object. The radiative transfer approximations were improving as well. The simple quasi-Newtonian ray propagation (Chan et al., 2009) gave way to null-geodesics tracing in Kerr metric (Schnittman et al., 2006; Noble et al., 2007; Moscibrodzka et al., 2009). The huge amount of polarization observations demanded the polarized radiative transfer.

The main principles of GR polarized radiative transfer were formulated in Broderick (2004). However, that formulation was not ready for applications as it lacked, for example, the Faraday conversion and the suppression of Faraday rotation in hot plasmas. The first application to the real object was done in Huang et al. (2009a). Their calculations included

Faraday conversion, but made several approximations, some of which can be substantially improved upon. For example, their simple relation on V and Q emissivities and Faraday rotation and conversion constitutes an approximation that almost never holds. Their emissivities are calculated in synchrotron regime, which breaks for temperatures about the electron mass. Their frame of plasma does not fully account for the fluid motion. We are improving on their work in the present chapter, in particular treating exactly the plasma response and extending it to non-thermal particle distributions.

Another important issue is the complexity of GR polarized radiative transfer. The errors and implicit strong approximations may slip into the equations of almost every author. This is more likely the case, when certain derivation is done half-way by one author and then continued by another author, e.g. the derivation of the Faraday conversion coefficient in the mixture of thermal and non-thermal plasmas in Melrose (1997c) and Ballantyne et al. (2007) neglected the importance of the finite ratio of cyclotron to observed frequencies. Another good example is the definition of the sign of circular polarization V. It varies from article to article and the consistent definition in a single derivation is essential.

Therefore, there appeared a need for the present chapter. In a single derivation from the basic principles we provide the necessary applied expressions for GR polarized radiative transfer. We start in §5.2 by consistently defining the polarization tensor, Stokes parameters, and plasma response tensor and incorporating the response tensor into the Newtonian radiative transfer. In §5.3 we recast the derivation of the response tensor from Boltzmann equation for general isotropic particle distribution and do the special case of thermal distribution. We provide the applied expressions for response tensor in the plane perpendicular to the ray and give the consistent sign notation for both positive and negative charges in §5.3.3. The resultant formulas for absorptivities/emissivities, Faraday

rotation and conversion coefficients are exact and easy to evaluate. By means of locally-flat co-moving reference frame we extend the radiative transfer to full GR in §5.4. We highlight the various physical effects important for real astrophysical objects in §5.5. Finally, in §5.6 we briefly summarize the methods and the ways to generalize them even further.

5.2 Newtonian Polarized Radiative Transfer

The proper treatment of polarization of radiation is necessary to take the full advantage of polarized observations. Let us start formulating the dynamics of polarization by defining the basis. Let $\tilde{\mathbf{e}}^3$ be the direction of uniform magnetic field $\mathbf{B}_0$. Then define the orthonormal triad $\mathbf{k}$, $\mathbf{e}^1$, and $\mathbf{e}^2$ in the standard way (Rybicki & Lightman, 1979; Sazonov, 1969; Pacholczyk, 1970): wave propagates along $\mathbf{k}$ vector,

$$\begin{aligned} \mathbf{e}^1 &= C(\mathbf{B}_0 \times \mathbf{k}), \\ \mathbf{e}^2 &= \mathbf{k} \times \mathbf{e}^1, \end{aligned} \tag{5.1}$$

where the scalar C can have either sign. We choose the axes as on Fig. 5.1: $\mathbf{e}^1$ is perpendicular to $(\mathbf{B}_0, \mathbf{k})$ plane and $\mathbf{B}_0$ lies in $(\mathbf{k}, \mathbf{e}^2)$ plane. The rotation around $\mathbf{e}^1$ transforms basis ($\tilde{\mathbf{e}}^1$, $\tilde{\mathbf{e}}^2$, $\tilde{\mathbf{e}}^3$) to the basis ($\mathbf{e}^1$, $\mathbf{e}^2$, $\mathbf{e}^3$) as

$$\begin{aligned} \mathbf{e}^1 = \tilde{\mathbf{e}}^1, \quad \mathbf{e}^2 = \tilde{\mathbf{e}}^2 \cos\theta - \tilde{\mathbf{e}}^3 \sin\theta, \\ \mathbf{e}^3 = \mathbf{k} = \tilde{\mathbf{e}}^2 \sin\theta + \tilde{\mathbf{e}}^3 \cos\theta, \end{aligned} \tag{5.2}$$

which can be conveniently written as

$$\mathbf{e}^k = \tilde{\mathbf{e}}^i M_{ik}, \quad M_{ik} = \begin{pmatrix} 1 & 0 & 0 \\ 0 & \cos\theta & \sin\theta \\ 0 & -\sin\theta & \cos\theta \end{pmatrix}. \tag{5.3}$$

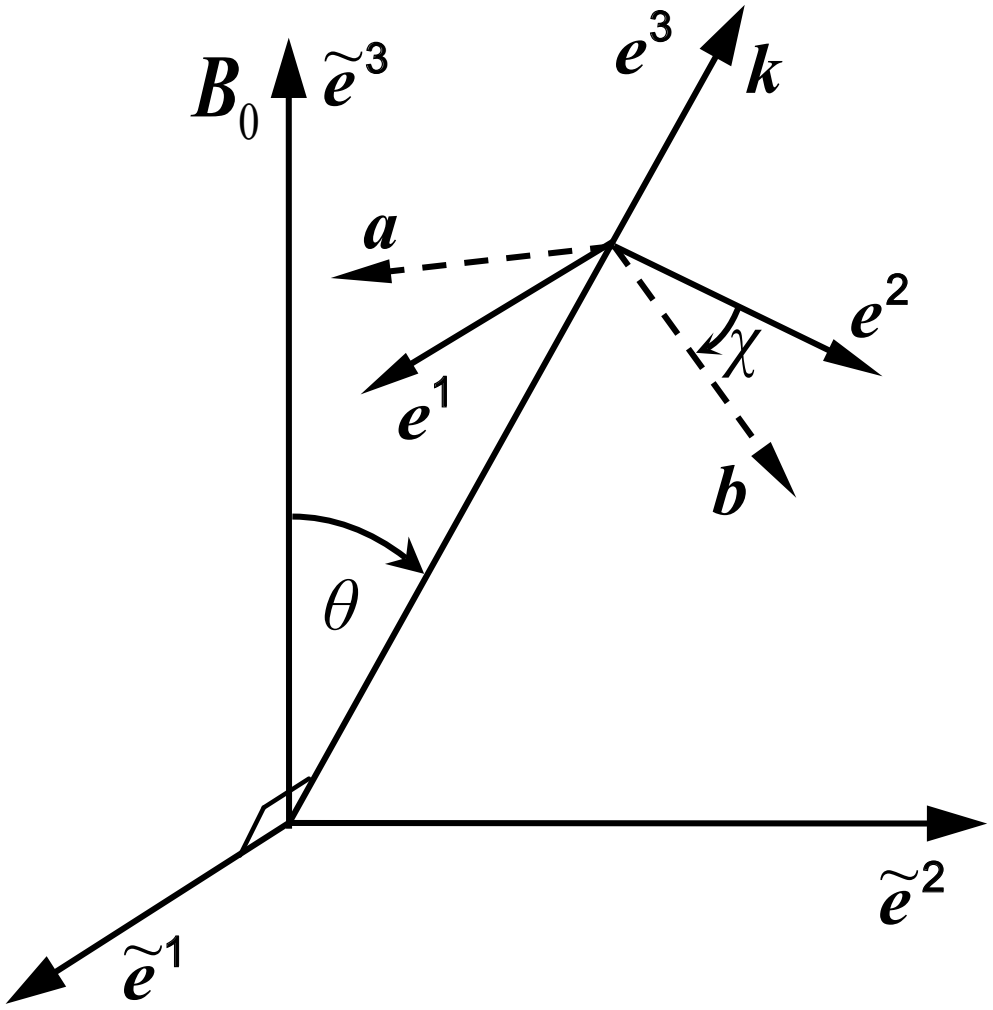

Figure 5.1.— Geometry of the problem. Vector $\mathbf{B}_0$ represents uniform magnetic field. The transverse plane wave travels along $\mathbf{k}$ and has electric field $\mathbf{E}$ oscillating in $(\mathbf{e}^1\mathbf{e}^2)$ plane. Vectors $\mathbf{a}$ and $\mathbf{b}$ represent parallel transported basis orthogonalized with $\mathbf{k}$.

Vectors and tensors then rotate according to

$$A_k = (M^T)_{ki}\tilde{A}_i, \quad \alpha_{ki} = (M^T)_{km}\tilde{\alpha}_{mn}M_{ni}, \tag{5.4}$$

where $()^T$ is a transposed matrix and the quantities with tildes are taken in a frame with the basis ($\tilde{\mathbf{e}}^1$, $\tilde{\mathbf{e}}^2$, $\tilde{\mathbf{e}}^3$). The angle θ can be found from

$$\cos\theta = \frac{\mathbf{k}\cdot\mathbf{B}_0}{kB_0}. \tag{5.5}$$

For the electric field components E_1 along $\mathbf{e}^1$ and E_2 along $\mathbf{e}^2$ the Stokes parameters are defined as

$$\begin{aligned} I &= \langle E_1 E_1^* \rangle + \langle E_2 E_2^* \rangle\,, \\ Q &= \langle E_1 E_1^* \rangle - \langle E_2 E_2^* \rangle\,, \\ U &= \langle E_1 E_2^* \rangle + \langle E_2 E_1^* \rangle\,, \\ V &= \imath(\langle E_1 E_2^* \rangle - \langle E_2 E_1^* \rangle), \end{aligned} \tag{5.6}$$

where the last formula chooses the IAU/IEEE definition (Hamaker & Bregman, 1996) of V, actively used by observers. That is for positive V the rotation of electric field is counter-clockwise as seen by the observer. Nevertheless, all astrophysics textbooks agree on the opposite definition of V (Sazonov & Tsytovich, 1968; Legg & Westfold, 1968; Rybicki & Lightman, 1979; Rochford, 2001; Wilson et al., 2009). Let us visualize the electric field rotation. Take the electric field

$$E_1 = E_{1\omega}\exp(\imath(kz - \omega t + \delta)), \quad E_2 = E_{2\omega}\exp(\imath(kz - \omega t)) \tag{5.7}$$

with positive amplitudes (Fourier coefficients) $E_{1\omega}, E_{2\omega} > 0$ and substitute it to the definition (5.6). Then

$$\begin{aligned} I &= E_{1\omega}^2 + E_{2\omega}^2, \qquad Q = E_{1\omega}^2 - E_{2\omega}^2 \\ U &= 2E_{1\omega}E_{2\omega}\cos\delta, \quad V = -2E_{1\omega}E_{2\omega}\sin\delta \end{aligned} \tag{5.8}$$

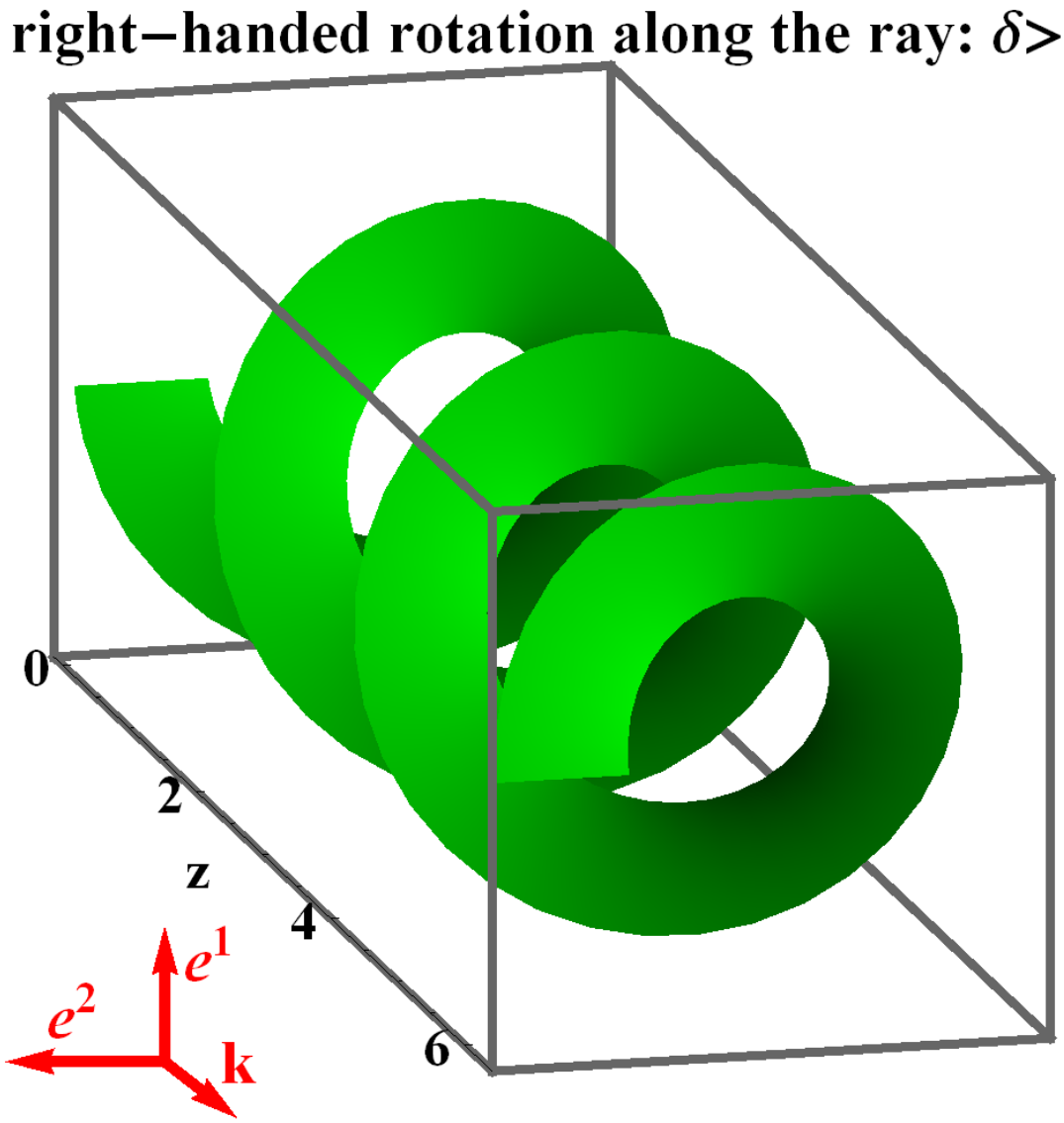

Figure 5.2.— Right-handed rotation of electric field along the ray at fixed time t corresponding to negative circular polarized wave $V < 0$. Electric field is $E_1 = E_{1\omega} \exp(\imath(kz + \delta))$, $E_2 = E_{2\omega} \exp(\imath kz)$, $\delta = \pi/2$, where $E_{1\omega}$ is along $\mathbf{e}^1$, $E_{2\omega}$ along $\mathbf{e}^2$, and the wave propagates along $\mathbf{k}$. Vectors $\mathbf{e}^1$, $\mathbf{e}^2$, $\mathbf{k}$ constitute the right-handed triad.

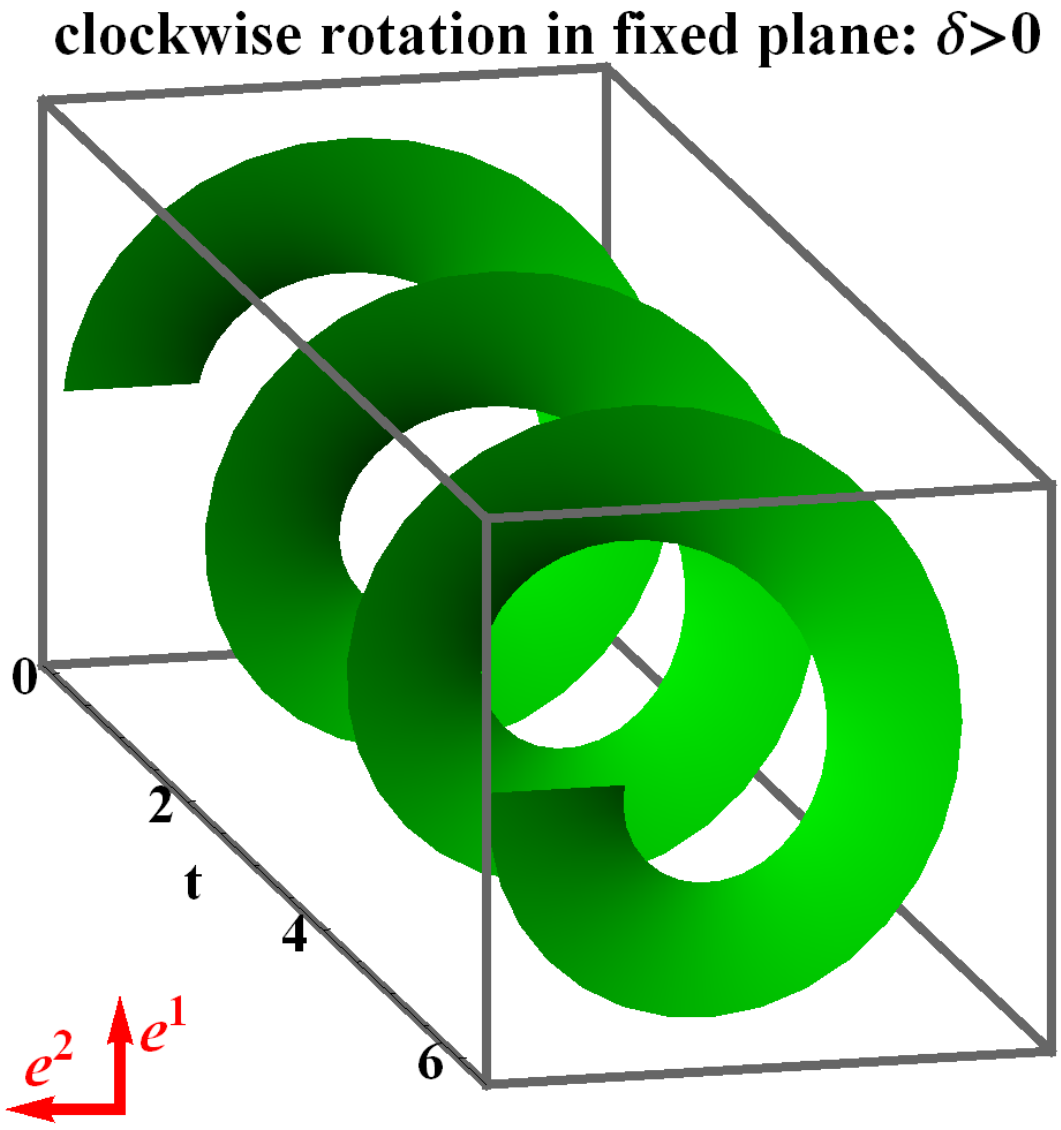

Figure 5.3.— Left-handed rotation of electric field at fixed coordinate z with time corresponding to negative circular polarized wave $V < 0$. Electric field is $E_1 = E_{1\omega} \exp(\imath(-\omega t + \delta))$, $E_2 = E_{2\omega} \exp(-\imath\omega t)$, $\delta = \pi/2$, where $E_{1\omega}$ is along $\mathbf{e}^1$, $E_{2\omega}$ along $\mathbf{e}^2$.

and $V < 0$ for $\delta \in (0, \pi)$. Let us fix time $t = 0$, $\delta = \pi/2$ and draw the electric field vector in space along the ray (see Fig. 5.2). We see that the electric field corresponds to a right-handed screw. However, if we fix a plane in space by setting $z = 0$ and draw the evolution of the electric field vector, then the rotation direction is the opposite: electric field vector rotates counter-clockwise, if viewed along the ray (see Fig. 5.3). These opposite directions of rotation is a common point of confusion (Rochford, 2001). Correspondingly, the observer sees the clockwise-rotating electric field for $\delta = \pi/2$, as she is situated at a fixed z, and counter-clockwise rotating electric field for $\delta = -\pi/2$ and positive $V > 0$. The definition (5.6) of V has a marginal advantage: the electrons generate positive V for propagation along the magnetic field. Let us take an electron on a circular orbit in $(\tilde{\mathbf{e}}^1\tilde{\mathbf{e}}^2)$ plane. It moves from the direction of $\tilde{\mathbf{e}}^1$ to the direction of $\tilde{\mathbf{e}}^2$, id est clockwise as viewed along the magnetic field. Then the wake of the electric field follows the charge and rotates clockwise. The resultant wave propagates along $\mathbf{B}_0$ and constitutes a left-handed screw, which gives the positive $V > 0$.

The polarization tensor is obtained automatically from equation (5.6) as

$$I_{ij} = \left\langle E_i E_j^* \right\rangle = \frac{1}{2} \begin{pmatrix} I+Q & U-\imath V \\ U+\imath V & I-Q \end{pmatrix}. \tag{5.9}$$

The polarization vector is

$$\mathbf{S} = (I, Q, U, V)^T. \tag{5.10}$$

Note that Melrose & McPhedran (1991) uses the same definitions, however, their $\mathbf{k}$, $\mathbf{e}^1$, $\mathbf{e}^2$ constitute a left triad instead of a right triad.

The plasma response is characterized by the 4×4 response tensor $\alpha^\mu{}_\nu$

$$j^\mu_\omega = \alpha^\mu{}_\nu A^\nu_\omega \tag{5.11}$$

as the proportionality between the four-vectors of vector potential amplitude and the current density amplitude. There is freedom in choosing the gauge condition for A^μ. Let us choose the Lorenz gauge

$$A^\mu u_\mu = 0 \tag{5.12}$$

at each point along the ray and enforce it by adding to A^μ a vector, proportional to k^μ, what does not change the polarization tensor (5.9) (Misner et al., 1973). The gauge condition makes $A^0 = \phi = 0$ and establishes the proportionality of wave electric field $\mathbf{E}$ and $\mathbf{A}$ in the locally flat co-moving frame (Anile & Breuer, 1974; Landau & Lifshitz, 1975). Thus, in that frame the spatial components of $\alpha^\mu{}_\nu$ coincide exactly with the spatial 3×3 response tensor α_{ik} in $(j_\omega)_i = \alpha_{ik}(A_\omega)_k$. We will derive the tensor α_{ik} below. It is usually incorporated within the dielectric tensor

$$\varepsilon_{ik} = \delta_{ik} + \frac{4\pi c}{\omega^2}\alpha_{ik}. \tag{5.13}$$

The wave equation for transverse waves in terms of ε_{ik} is

$$(n_{\rm r}^2\delta_{ik} - \varepsilon_{ik}) \begin{pmatrix} E_1 \\ \\ E_2 \end{pmatrix} = 0, \tag{5.14}$$

where the indices $i, k = 1, 2$, so that only the transverse 2×2 part of ε_{ik} in ($\mathbf{e}^1$, $\mathbf{e}^2$, $\mathbf{k}$) basis is taken, and $n_{\rm r}^2 = k^2c^2/\omega^2$ (Swanson, 2003; Shcherbakov, 2008b). The correspondent transport equation is (Melrose & McPhedran, 1991)

$$\frac{dE_i}{ds} = \frac{\imath\omega}{2n_{\rm r}c}\Delta\varepsilon_{ik}E_k, \tag{5.15}$$

where $\Delta\varepsilon_{ik} = \varepsilon_{ik} - \delta_{ik}$. We take the equation (5.15), its conjugate, multiply correspondingly by E_k^* and E_k, add and obtain

$$\frac{d\left\langle E_iE_k^*\right\rangle}{ds} = \frac{\imath}{\nu}(\alpha_{il}\left\langle E_lE_k^*\right\rangle - \alpha_{kl}^*\left\langle E_iE_l^*\right\rangle) \tag{5.16}$$

for $n_{\rm r} = 1$ with the observed frequency $\nu = \omega/(2\pi)$ neglecting emission. Again, $i, k, l = 1, 2$. Note that $\alpha_{12} = -\alpha_{21}$ according to Onsager principle (Lifshits & Pitaevskii, 1981) (p. 273). By solving the definitions of the Stokes parameters (eq. (5.6)) for $\langle E_i E_k^* \rangle$ and substituting the result into the equation (5.16) we get the transport equation for the Stokes parameters

$$\frac{d\mathbf{S}}{ds} = \begin{pmatrix} \varepsilon_I \\ \varepsilon_Q \\ 0 \\ \varepsilon_V \end{pmatrix} - \begin{pmatrix} \alpha_I & \alpha_Q & 0 & \alpha_V \\ \alpha_Q & \alpha_I & \rho_V & 0 \\ 0 & -\rho_V & \alpha_I & \rho_Q \\ \alpha_V & 0 & -\rho_Q & \alpha_I \end{pmatrix} \mathbf{S} \tag{5.17}$$

with the polarization $\mathbf{S}$ vector (5.10) by adding the emission, where

$$\begin{aligned} \alpha_I &= {\rm Im}(\alpha_{22} + \alpha_{11})/\nu, \\ \alpha_Q &= {\rm Im}(\alpha_{11} - \alpha_{22})/\nu, \\ \alpha_V &= 2{\rm Re}(\alpha_{12})/\nu, \\ \rho_V &= 2{\rm Im}(\alpha_{12})/\nu, \\ \rho_Q &= {\rm Re}(\alpha_{22} - \alpha_{11})/\nu. \end{aligned} \tag{5.18}$$

5.3 Derivation of Response Tensor

The response tensor is derived for thermal plasma in Trubnikov (1958); Melrose (1997c); Swanson (2003). However, there is a need to recast the derivation, since we want to consider both signs of charge, extend the results to non-thermal isotropic particle distributions, and seek for extensions to non-isotropic distributions. The importance of notation consistency cannot be overemphasized, also the orientation of our coordinate axes is different from some of the above sources. On the way we discover the practical

significance of the response tensor: it offers expressions for fast evaluation of plasma absorptivities and rotativities.

5.3.1 General Isotropic Particle Distribution

Throughout this subsection and next subsection we employ vectors and tensors in ($\tilde{\mathbf{e}}^1$, $\tilde{\mathbf{e}}^2$, $\tilde{\mathbf{e}}^3$) basis, but skip tildes to avoid clutter. Only tildes over the response tensors are drawn. For simplicity of notation we define the dimensionless momentum

$$p = \sqrt{\gamma^2 - 1}, \tag{5.19}$$

where $\gamma = En/(mc^2) \geq 1$ is the γ-factor for particles of energy En and mass m. Then the Boltzmann equation on the distribution function $f(\mathbf{x}, \mathbf{p})$ is

$$\frac{\partial f}{\partial t} + \mathbf{v} \cdot \nabla f + \eta e \left(\mathbf{E} + \frac{\mathbf{v}}{c} \times (\mathbf{B}_0 + \mathbf{B}) \right) \cdot \frac{\nabla_{\mathbf{p}} f}{mc} = 0. \tag{5.20}$$

Here the velocity vector is

$$\mathbf{v} = \mathbf{p}c/\gamma, \tag{5.21}$$

$\mathbf{B}_0$ is the background magnetic field, $\mathbf{E}$ and $\mathbf{B}$ are the wave electric and magnetic fields, η is the sign of the charge and $e > 0$. Let us assume a general isotropic particle distribution $f_0(p)$ instead of thermal. The wave with the phase $\exp(\imath(\mathbf{k} \cdot \mathbf{r} - \omega t))$ causes perturbation in a form

$$f_1 = \exp(\imath(\mathbf{k} \cdot \mathbf{r} - \omega t)) f_0 \Phi(\mathbf{p}), \tag{5.22}$$

which implements the general function $\Phi(\mathbf{p})$ of momentum $\mathbf{p}$. Note that the perturbation (5.22) is small and further analysis is valid only when $|\mathbf{B}| \ll |\mathbf{B}_0|$, which corresponds to low radiation pressure medium. Following Trubnikov (1958); Swanson (2003) we introduce

the cylindrical coordinates with axis along $\mathbf{B}_0$, so that

$$p_x = p_\perp \cos\phi, \quad p_y = p_\perp \sin\phi \tag{5.23}$$

with angle ϕ in (xy) plane. Then

$$\mathbf{k}\cdot\mathbf{p} = k_z p_z + k_\perp p_\perp \sin\phi. \tag{5.24}$$

The Boltzmann equation (5.20) results in

$$\begin{aligned} -\imath\omega f_1 &+ \frac{\imath(k_z p_z + k_\perp p_\perp \sin\phi)c}{\gamma} f_1 \\ &+ \eta e\mathbf{E}\cdot\frac{\nabla_{\mathbf{p}} f_0}{mc} + \frac{\eta e}{\gamma}(\mathbf{p}\times\mathbf{B}_0)\cdot\frac{\nabla_{\mathbf{p}} f_1}{mc} = 0 \end{aligned} \tag{5.25}$$

after dropping the second-order terms upon substitution of f_1 from equation (5.22). For general isotropic $f_0(p)$ the relation $(\mathbf{p}\times(\mathbf{B}_0+\mathbf{B}))\cdot\nabla_{\mathbf{p}} f_0 = 0$ holds, and it does not hold for non-isotropic distributions. Only the cylindrical ϕ component is non-zero in a triple product $(\mathbf{p}\times\mathbf{B}_0)\cdot\nabla_{\mathbf{p}} f_1$. After some transformations we obtain an equation on $\Phi(\mathbf{p})$

$$\begin{aligned} -\imath\omega\Phi &+ \frac{\imath(k_z p_z + k_\perp p_\perp \sin\phi)c}{\gamma}\Phi \\ &+ \frac{d\ln f_0}{d\gamma}\frac{\eta e}{\gamma mc}(\mathbf{p}\cdot\mathbf{E}_\omega) - \frac{\eta\omega_B}{\gamma}\frac{\partial\Phi}{\partial\phi} = 0 \end{aligned} \tag{5.26}$$

for general isotropic particle distribution, where $\mathbf{E}_\omega$ is an amplitude such that $\mathbf{E} = \mathbf{E}_\omega \exp(\imath(\mathbf{k}\cdot\mathbf{r} - \omega\mathbf{t}))$. Here the cyclotron frequency is

$$\omega_B = \frac{eB_0}{mc}, \quad \nu_B = \frac{\omega_B}{2\pi}. \tag{5.27}$$

We define the ratio β

$$\beta = \frac{\nu_B}{\nu}. \tag{5.28}$$

Alternatively, the equation (5.26) reads

$$\imath(a - b\sin\phi)\Phi + \partial\Phi/\partial\phi = F \tag{5.29}$$

with

$$a = \frac{\gamma - n_z p_z}{\eta\beta}, \quad b = \frac{n_\perp p_\perp}{\eta\beta}, \quad F = \frac{d\ln f_0}{d\gamma}\frac{\mathbf{p}\cdot\mathbf{E}_\omega}{B_0}. \tag{5.30}$$

Here $n_z = \cos\theta$ and $n_\perp = \sin\theta$ assuming $|\mathbf{k}|c = \omega$. The solution is

$$\Phi(\phi) = \exp(-\imath(a\phi + b\cos\phi))\int_{\phi_0}^{\phi}\exp(\imath(a\psi + b\cos\psi))F(\psi)d\psi, \tag{5.31}$$

where the lower boundary ϕ_0 is chosen at $t = -\infty$. The negative charge moves in the positive ϕ direction and the positive charge in the negative ϕ direction, therefore $\phi_0 = -\eta\infty$. The solution of a homogeneous equation vanishes over the finite time. Knowing the particle distribution and the definition of a current density $\mathbf{j} = \eta e\int f_1\mathbf{v}d^3p$ we calculate the current density amplitude

$$\mathbf{j}_\omega = \eta e\int f_0\Phi(\mathbf{p})\frac{\mathbf{p}c}{\gamma}d^3p. \tag{5.32}$$

Then we relate it to the electric field $\mathbf{E}_\omega$ and the vector potential $\mathbf{A}_\omega$ wave amplitudes as

$$(j_\omega)_i = \sigma_{ik}(E_\omega)_k = \alpha_{ik}(A_\omega)_k, \tag{5.33}$$

where $\alpha_{ik} = \imath\omega\sigma_{ik}/c$. Let us calculate α_{ik}. Substituting the solution (5.31) into the definition of the current density equation (5.32) and changing the integration variable as $\psi = \phi - \xi$ we get

$$\begin{aligned}(j_\omega)_i &= \imath\frac{\eta e\omega}{c}\int d^3p\int_0^{-\eta\infty}\exp(-\imath a\xi + \imath b(\cos(\phi-\xi) - \cos\phi)) \\ &\times\quad p_i\quad (p_k(A_\omega)_k)_{\phi\to\phi-\xi}\,\frac{c}{\gamma B_0}\frac{df_0}{d\gamma}d\xi.\end{aligned} \tag{5.34}$$

One can (Trubnikov, 1958; Lifshits & Pitaevskii, 1981; Swanson, 2003) introduce the differentiation with respect to vectors $\mathbf{s}$ and $\mathbf{s}'$ to eliminate the momenta $\mathbf{p}$ in the integral expressions, then due to uniform convergence of the integrals in $d\xi$ and dp move the

derivatives outside the integrals. We also do the transformation $\xi \to -\eta\beta\xi$ to finally get in ($\tilde{\mathbf{e}}^1$, $\tilde{\mathbf{e}}^2$, $\tilde{\mathbf{e}}^3$) basis

$$\begin{aligned}\tilde{\alpha}_{\imath k} &= -\frac{\imath e^2}{mc}\int d^3p \int_0^\infty \frac{\partial^2 \exp(\imath\xi\gamma - \imath\mathbf{h}\cdot\mathbf{p})}{\partial s_i \partial s'_k}\frac{df_0}{\gamma d\gamma}d\xi \\ &= -\frac{4\pi\imath e^2}{mc}\frac{\partial^2}{\partial s_i \partial s'_k}\int_1^\infty d\gamma \frac{df_0}{d\gamma}\int_0^\infty \exp(\imath\xi\gamma)\frac{\sin(hp)}{h}d\xi\end{aligned} \tag{5.35}$$

with

$$\begin{aligned}h_x &= \frac{n_\perp}{\beta\eta}(1-\cos(\beta\xi)) + \imath(s_x + \cos(\beta\xi)s'_x + \eta\sin(\beta\xi)s'_y), \\ h_y &= \frac{\sin(\beta\xi)n_\perp}{\beta} + \imath(s_y - \eta\sin(\beta\xi)s'_x + \cos(\beta\xi)s'_y), \\ h_z &= \xi n_z + \imath(s_z + s'_z), \\ h &= \sqrt{h_x^2 + h_y^2 + h_z^2}.\end{aligned} \tag{5.36}$$

5.3.2 Thermal Particle Distribution

Let us now consider the special case of an isotropic thermal distribution of particles

$$f_0 = \frac{n_e}{4\pi}\frac{\exp(-\gamma/\theta_e)}{\theta_e K_2(\theta_e^{-1})} \tag{5.37}$$

normalized as

$$\int_0^{+\infty} f_0 4\pi p^2 dp = n_e. \tag{5.38}$$

Here and below $K_n(x)$ is a Bessel function of the second type of order n with argument x. The normalized particle temperature is

$$\theta_e = \frac{k_B T}{mc^2}. \tag{5.39}$$

Then the response tensor (5.35) is

$$\tilde{\alpha}_{\imath k} = \frac{\imath e^2 n_e}{mc}\int\int_0^\infty \frac{\partial^2}{\partial s_i \partial s'_k}\frac{\exp(-A'\gamma - \imath\mathbf{h}\cdot\mathbf{p})}{4\pi\gamma\theta_e^2 K_2(\theta_e^{-1})}d\xi d^3p \tag{5.40}$$

with $A' = 1/\theta_e - \imath\xi$ and the rest of quantities defined by equation (5.36). The integral over d^3p can be taken analytically (Trubnikov, 1958) to give

$$\tilde{\alpha}_{ik} = \frac{\imath e^2 n_e}{mc\theta_e^2 K_2(\theta_e^{-1})} \frac{\partial^2}{\partial s_i \partial s'_k} \int_0^\infty \frac{K_1(\sqrt{A'^2 + h^2})}{\sqrt{A'^2 + h^2}} d\xi. \tag{5.41}$$

Performing the differentiation in Mathematica 7 to avoid errors, one gets 3×3 response tensor

$$\tilde{\alpha}_{ik} = \frac{\imath e^2 n_e}{mc\theta_e^2 K_2(\theta_e^{-1})} \int_0^\infty d\xi \left(\tilde{T}^1_{ik} \frac{K_2(\mathcal{R})}{\mathcal{R}^2} - \tilde{T}^2_{ik} \frac{K_3(\mathcal{R})}{\beta^2 \mathcal{R}^3} \right) \tag{5.42}$$

with

$$\mathcal{R} = \sqrt{\frac{1}{\theta_e^2} - \frac{2\imath\xi}{\theta_e} - \xi^2 \sin^2\theta + \frac{2\sin^2\theta}{\beta^2}(1 - \cos\beta\xi)}. \tag{5.43}$$

Here

$$\tilde{T}^1_{ik} = \begin{pmatrix} \cos\beta\xi & \eta\sin\beta\xi & 0 \\ -\eta\sin\beta\xi & \cos\beta\xi & 0 \\ 0 & 0 & 1 \end{pmatrix}, \tag{5.44}$$

$$\tilde{T}^2_{ik} = \tag{5.45}$$

$$\begin{pmatrix} -(1-\cos\beta\xi)^2\sin^2\theta & \eta(1-\cos\beta\xi)\sin\beta\xi\sin^2\theta & \eta\beta\xi(1-\cos\beta\xi)\cos\theta\sin\theta \\ -\eta(1-\cos\beta\xi)\sin\beta\xi\sin^2\theta & \sin^2\beta\xi\sin^2\theta & \beta\xi\sin\beta\xi\sin\theta\cos\theta \\ -\eta\beta\xi(1-\cos\beta\xi)\cos\theta\sin\theta & \beta\xi\sin\beta\xi\sin\theta\cos\theta & \beta^2\xi^2\cos^2\theta \end{pmatrix}.$$

The expressions (5.42-5.45) are hiding inside two almost transverse and one almost longitudinal damped eigenwaves.

5.3.3 Rotation of Thermal Response Tensor

Let us apply the transformation (5.4) to tensors $\tilde{T}^1_{ik}$ and $\tilde{T}^2_{ik}$ and take the transverse 2×2 part to obtain correspondingly

$$T^1_{ij}=\begin{pmatrix} \cos\beta\xi & \eta\sin\beta\xi\cos\theta \\ -\eta\sin\beta\xi\cos\theta & \cos\beta\xi\cos^2\theta+\sin^2\theta \end{pmatrix} \tag{5.46}$$

and $T^2_{ij}=R_i\overline{R}_j$ with

$$R_i=\sin\theta(\eta(1-\cos\beta\xi),\cos\theta(\sin\beta\xi-\beta\xi)), \tag{5.47}$$
$$\overline{R}_j=\sin\theta(-\eta(1-\cos\beta\xi),\cos\theta(\sin\beta\xi-\beta\xi))$$

for

$$\alpha_{ij}=\frac{\imath e^2 n_e}{mc\theta_e^2 K_2(\theta_e^{-1})}\int_0^\infty d\xi\left(T^1_{ij}\frac{K_2(\mathcal{R})}{\mathcal{R}^2}-T^2_{ij}\frac{K_3(\mathcal{R})}{\beta^2\mathcal{R}^3}\right). \tag{5.48}$$

The integration over ξ converges very slowly, if performed along the real axis. The way to accelerate the convergence is to perform the integration in a complex plane at a positive angle to the real axis. The wave frequency ν in the above calculations has a small positive imaginary part $\mathrm{Im}(\nu)>0$ to account for the energy pumped into particles from passing waves. Then $\mathrm{Im}(\beta)<0$ and the expression (5.43) has zeros only in the lower plane $\mathrm{Im}(\xi)<0$ of ξ. Thus, deforming the integration contour to the upper plane of ξ does not change the response tensor (5.48). Note that all absorptivities α_I, α_Q, and α_V and rotativities ρ_Q and ρ_V are positive for electrons for $\theta\in(0,\pi/2)$ under the definitions (5.18), what gives an easy way to check the implementation of radiative transfer algorithm. The evaluation of these coefficients will be reported in the subsequent paper Huang & Shcherbakov(2011, in prep.). We will also evaluate the validity of a transverse approximation for waves.

Following Huang et al. (2009a) we define the parallel transported vectors **a** and **b** in addition to the right triad $\mathbf{e}^1$, $\mathbf{e}^2$, **k**, so that in the co-moving locally-flat reference frame

$$(\mathbf{a}, \mathbf{b}) = (\mathbf{e}^1, \mathbf{e}^2) \begin{pmatrix} \cos\chi & \sin\chi \\ -\sin\chi & \cos\chi \end{pmatrix}. \tag{5.49}$$

Then the transformation with -2χ angle

$$R(\chi) = \begin{pmatrix} 1 & 0 & 0 & 0 \\ 0 & \cos(2\chi) & -\sin(2\chi) & 0 \\ 0 & \sin(2\chi) & \cos(2\chi) & 0 \\ 0 & 0 & 0 & 1 \end{pmatrix} \tag{5.50}$$

serves to get the vector of emissivities ε and the matrix of rotativities/absorptivities K in (**a**, **b**, **k**) basis as

$$\begin{aligned} \varepsilon &= R(\chi) \begin{pmatrix} \varepsilon_I \\ \varepsilon_Q \\ 0 \\ \varepsilon_V \end{pmatrix}, \\ K &= R(\chi) \begin{pmatrix} \alpha_I & \alpha_Q & 0 & \alpha_V \\ \alpha_Q & \alpha_I & \rho_V & 0 \\ 0 & -\rho_V & \alpha_I & \rho_Q \\ \alpha_V & 0 & -\rho_Q & \alpha_I \end{pmatrix} R(-\chi). \end{aligned} \tag{5.51}$$

Define the perpendicular magnetic field

$$\mathbf{B}_{0\perp} = \mathbf{B}_0 - \mathbf{k}(\mathbf{k}\cdot\mathbf{B}_0)/k^2. \tag{5.52}$$

The trigonometric factors are related to the magnetic field as

$$\sin\chi = (\mathbf{a}\cdot\mathbf{B}_{0\perp})/B_{0\perp}, \quad \cos\chi = -(\mathbf{b}\cdot\mathbf{B}_{0\perp})/B_{0\perp}. \tag{5.53}$$

The radiative transfer equation is then

$$d\mathbf{S}/ds = \varepsilon - K\mathbf{S} \tag{5.54}$$

for the polarization vector $\mathbf{S}$ defined in ($\mathbf{a}$, $\mathbf{b}$, $\mathbf{k}$) basis.

5.4 Extension to General Relativity

Let us consider two reference frames: locally-flat co-moving reference frame with 4-velocity $\hat{u}^\alpha = (1, 0, 0, 0)$ and flat metric and the lab frame with Kerr metric and the fluid moving at u^α. We denote by hats $\hat{()}$ the quantities in the co-moving frame. Consider the radiative transfer equation (5.54) in the co-moving frame. The set of Stokes parameters $\mathbf{S}$ can be generalized to the corresponding set of photon occupation numbers

$$\mathbf{N} = \mathbf{S}/\nu^3, \tag{5.55}$$

which are invariant under the orthogonal coordinate transformations (Misner et al., 1973; Anile & Breuer, 1974; Ellis, 2009). Photons propagate along null-geodesics with the affine parameter λ, so that the wave four-vector is

$$k^\alpha = k_0 \frac{dx^\alpha}{d\lambda}, \tag{5.56}$$

and

$$\frac{d\mathbf{N}}{d\lambda} = 0. \tag{5.57}$$

Here k_0 is a constant photon energy, which relates to the observed frequency as

$$\nu_\infty = \frac{k_0 c}{2\pi}. \tag{5.58}$$

Under such normalization of λ approximately $ds \approx d\lambda$ far from the BH. One calculates the null geodesic starting from the observer's plane. The perpendicular unit vector a^α has a

special orientation on that plane, and is transported along the geodesic according to

$$a^\alpha(\lambda=0)=a_0^\alpha, \quad a_0^\alpha a_{\alpha 0}=1, \quad k^\sigma\nabla_\sigma a^\alpha=0, \tag{5.59}$$

where ∇_σ is the covariant derivative. The unit vector b^α is transported the same way.

Just as in a flat space case the charged particles lead to the increase of occupation numbers $\mathbf{N}$ due to emission, to decrease of $\mathbf{N}$ due to absorption, and to exchange of $\mathbf{N}$ components due to Faraday rotation and Faraday conversion. These are all the processes occuring in linear regime. The invariant number of photons emitted per unit solid angle per unit frequency per unit volume per unit time is proportional to the invariant $\varepsilon(\nu)/\nu^2=\hat{\varepsilon}(\hat{\nu})/\hat{\nu}^2$ (Mihalas & Mihalas, 1984) as

$$\frac{d\mathbf{N}}{d\lambda}\propto\frac{\varepsilon(\nu)}{\nu^2}, \tag{5.60}$$

where

$$\nu=-k^\mu u_\mu \tag{5.61}$$

is the photon frequency in the lab frame for $(-,+,+,+)$ signature of metric. By $\hat{\nu}$ the photon frequency in the co-moving frame is denoted. The invariant change of photon states due to absorption and propagation effects is proportional to the co-moving frame matrix K (see eq.(5.54)) taken within unit frequency unit solid angle unit volume unit time. Thus the proportionality to the invariant $\nu K(\nu)=\hat{\nu}\hat{K}(\hat{\nu})$ is established (Mihalas & Mihalas, 1984) as

$$\frac{d\mathbf{N}}{d\lambda}\propto-\nu K(\nu)\mathbf{N}, \tag{5.62}$$

where the whole form of the absorption/state change matrix is preserved. The full GR radiative transfer equation

$$\nu_\infty\frac{d\mathbf{N}}{d\lambda}=\frac{\hat{\varepsilon}(\hat{\nu})}{\hat{\nu}^2}-\hat{\nu}\hat{K}(\hat{\nu})\mathbf{N} \tag{5.63}$$

is obtained. The equation (5.63) is similar to the GR polarized transfer equation in Huang et al. (2009a). However, their usage of primed and unprimed quantities is potentially confusing. It is their primed quantity $\mathbf{S}'$, which should be generalized to GR as $\mathbf{N}_S = \mathbf{S}'/\nu^3$.

5.4.1 Transformation to Locally-flat Co-moving Frame

The angle χ in the expression (5.53), θ in the response tensor, and similar quantities need to either be evaluated in the locally-flat reference frame, where fluid is at rest, or properly calculated in GR. We choose the first path as a transparent one with the following recipe. First, one traces the null geodesic from the observer's plane to the BH horizon or the sphere far from the BH and finds the vectors k^α and a^α (see eqs.(5.56,5.59)). At each point on the ray one knows the vectors k^α, a^α, fluid four-velocity u^α, and the four-vector of magnetic field B_0^α defined in McKinney & Gammie (2004) in the lab frame. The next step is to transform all vectors to the co-moving frame. Let us construct an orthonormal basis in Kerr metric in lab frame

$$\begin{aligned} e^\alpha_{(t)} &= (u^t, u^r, u^\theta, u^\phi), \\ e^\alpha_{(r)} &\propto (u^t u_r, -(u^t u_t + u^\phi u_\phi), 0, u^\phi u_r), \\ e^\alpha_{(\theta)} &\propto (u^t u_\theta, u^r u_\theta, u^\theta u_\theta + 1, u^\phi u_\theta), \\ e^\alpha_{(\phi)} &\propto (-u_\phi/u_t, 0, 0, 1), \end{aligned} \tag{5.64}$$

where lower-index velocity is $u_\alpha = g_{\alpha\beta}u^\beta$ and $g_{\alpha\beta}$ is the lower index Kerr metric

$$g_{\alpha\beta} = \begin{pmatrix} -1 + \frac{2r}{\rho} & 0 & 0 & -\frac{2ar\sin^2\theta_a}{\rho} \\ 0 & \rho/\Delta & 0 & 0 \\ 0 & 0 & \rho & 0 \\ -\frac{2ar\sin^2\theta_a}{\rho} & 0 & 0 & \frac{\Sigma\sin^2\theta_a}{\rho} \end{pmatrix} \tag{5.65}$$

in (t, r, θ_a, ϕ) spherical polar coordinates with polar angle θ_a, radius r, spin a, $\rho = r^2 + a^2 \cos^2 \theta_a$, $\Delta = r^2 - 2r + a^2$, $\Sigma = (r^2 + a^2)^2 - a^2 \Delta \sin^2 \theta_a$. Then make a transformation to

$$\begin{aligned} \hat{e}^{\alpha}_{(t)} &= (1, 0, 0, 0), \\ \hat{e}^{\alpha}_{(r)} &= (0, 1, 0, 0), \\ \hat{e}^{\alpha}_{(\theta)} &= (0, 0, 1, 0), \\ \hat{e}^{\alpha}_{(\phi)} &= (0, 0, 0, 1) \end{aligned} \tag{5.66}$$

via

$$S_{(t,r,\theta,\phi)\beta} = (-e^{\alpha}_{(t)}, e^{\alpha}_{(r)}, e^{\alpha}_{(\theta)}, e^{\alpha}_{(\phi)}) g_{\alpha\beta}. \tag{5.67}$$

The transformation of a four-vector A^{β} to the co-moving frame is then

$$\hat{A}_{(t,r,\theta,\phi)} = S_{(t,r,\theta,\phi)\beta} A^{\beta}. \tag{5.68}$$

The metric in the new frame

$$S_{(i)\alpha} g^{\alpha\beta} (S_{(k)\beta})^T = \eta_{ik} \tag{5.69}$$

coincides with Minkowski metric $\eta_{ik} = \mathrm{diag}(-1, 1, 1, 1)$. The velocity four-vector u^{β} transforms to $\hat{u}_{(i)} = (1, 0, 0, 0)^T$. Thus, the basis change (5.68) with matrix (5.67) and vectors (5.64) constitutes the transformation to the locally-flat co-moving reference frame. This procedure is the alternative of the numerical Gramm-Schmidt orthonormalization applied in Moscibrodzka et al. (2009). The basis vectors (5.64) are presented in Krolik et al. (2005); Beckwith et al. (2008a), our expressions being a simplified version of vectors in Beckwith et al. (2008a). Note, that despite the vectors (5.64) do not explicitly depend on the metric elements, the expressions rely on the properties of Kerr metric and are not valid for general $g^{\alpha\beta}$.

Upon transforming u^α, k^α, a^α, B_0^α to the co-moving frame we easily find the wave frequency $\nu = -\hat{k}_{(0)}$, then $\hat{\mathbf{k}} = \hat{k}_{(1,2,3)}$. The perpendicular vector $\hat{\mathbf{a}}$ needs to be offset by $\hat{\mathbf{k}}$ as

$$\hat{\mathbf{a}} = \hat{a}_{(1,2,3)} - \hat{\mathbf{k}}\frac{\hat{a}_{(0)}}{\hat{k}_{(0)}} \tag{5.70}$$

and then normalized to construct a spatial unit vector. The offset is due to the enforcement of Lorenz gauge (5.12). It conveniently makes $\mathbf{a}\cdot\mathbf{k} = \hat{\mathbf{a}}\cdot\hat{\mathbf{k}} = 0$. The vector $\mathbf{b}$ is found by a simple vector product

$$\hat{\mathbf{b}} = \hat{\mathbf{a}} \times \hat{\mathbf{k}} \tag{5.71}$$

and then normalized. The spatial part ($\hat{\mathbf{e}}_{(r)}$, $\hat{\mathbf{e}}_{(\theta)}$, $\hat{\mathbf{e}}_{(\phi)}$) of basis (5.66) relates to basis ($\mathbf{e}^1$, $\mathbf{e}^2$, $\mathbf{e}^3$) via the orthonormal transformation preserving angles. The magnetic field B_0^α gets transformed to a three-vector $\hat{\mathbf{B}}_0$ and all the angles are found in correspondence to Fig. 5.1 with the help of equations (5.52,5.53) applied to hatted vectors. For example, $\cos\theta = (\hat{\mathbf{k}}\cdot\hat{\mathbf{B}}_0)/(\hat{k}\hat{B}_0)$. Then the whole matrix $\hat{K}$ is found.

5.5 Application to Compact Objects

The described GR polarized radiative transfer finds its application in accretion onto low luminosity active galactic nuclei (LLAGNs), in particular Sgr A*. The application of GR is necessary to infer the BH spin, which provides important information on the past evolution of the BH and the host galaxy itself. For example, the accretion efficiency in the AGN phase depends strongly on the value of BH spin (Shapiro, 2005). The value of spin and spin orientation constraints the accretion and merger history (Rees & Volonteri, 2007).

The detailed application to Sgr A* is reported in Shcherbakov et al. (2010). Let us describe on the example of that paper, how one connects to observations. First, one

constructs a set of dynamical models, preferably based on 3D GRMHD simulations. Then the GR polarized radiative transfer is performed for those models as described in the present work. The simulated spectral energy distributions (SEDs), linear (LP) and circular (CP) polarization fractions as functions of frequency ν_∞ are fitted to the observed quantities, representative for the quasi-quiescent state of accretion. The χ^2 analysis is performed based on the inferred error or variability of the observed quantities. Then the best fits in the parameter space can be found. The probability density can be integrated over the full parameter space to obtain the most likely values and the confidence intervals of BH spin, inclination angle, position angle, and model parameters.

Let us now describe the effects, which lead to certain observed cyclo-synchrotron spectra, LP and CP fractions, and the electric vector position angle (EVPA) as functions of frequency. The effects are plenty, what proves it hard to disentangle and provide simple explanations of observations. It is in general challenging to achieve the realistic level of details in collisionless plasma modelling. The next step in Shcherbakov et al. (2010) might not be the most self-consistent. First, the radiation from LLAGNs appears to be variable in time. The simultaneous short observations can provide only the single snapshot of a system, not necessarily representative of a long term behavior. Thus, it is necessary to obtain the statistically significant sample of variability of both observed and simulated spectra to reliably estimate the average or typical flow parameters and BH spin. As recent research suggests (Dodds-Eden et al., 2010), the modelling of a single flare can successfully be done even without invoking GR.

As in the case of Sgr A*, the cyclo-synchrotron specific flux F_ν vs ν can have a peak. The peak frequency ν^* and flux F_ν^* do not necessarily correspond to the thermal cut-off of emission. Even a small percentage of the non-thermal electrons can radiate significantly

more than the bulk of thermal electrons. For the efficient particle acceleration most of emission may come from the energetic electrons with cooling time $t_{\rm cool}$ about the time of inflow $t_{\rm in}$ from several BH gravitational radii $r_{\rm g} = GM/c^2$. The gravitational redshift and Doppler shift due to relativistic motion can strongly modify the peak ν^* and F_ν^*.

The LP fraction can provide constraints on flow density near the emitting region owing to beam depolarization effect. The LP fraction is the highest at high frequencies, where only a small region of the flow shines and beam depolarization is weak. As all regions of the flow radiate at lower frequencies, differential Faraday rotation and emission EVPA vary, the resultant LP fraction is subject to cancelations and quickly ceases with ν. However, cancelations at high ν may readily happen between two regions with similar fluxes and perpendicular EVPAs, those regions would have perpendicular magnetic fields.

The same change of EVPA with frequency can mimic the Faraday rotation. The finite rotation measure (RM)

$$RM = \frac{EVPA_1 - EVPA_2}{\lambda_1^2 - \lambda_2^2} \tag{5.72}$$

does not necessarily happen due to Faraday rotation $\sim \int n\mathbf{B}\cdot\mathbf{dl}$. Here $\lambda = c/\nu$ is the wavelength. In fact, the meaningful application of formula (5.72) is limited to a toy case of cold plasma far from the emitting region with the homogeneous magnetic field. In reality, besides the change of emission EVPA with ν, the Faraday rotation coefficient $\rho_V(\nu)$ (see eq.5.18) is a function of frequency (Shcherbakov, 2008b). The differential rotation measure

$$dRM = dEVPA/d(\lambda^2) \tag{5.73}$$

is the measured quantity (Marrone et al., 2007). It should be used in constraining the models. Also, significant Faraday rotation can happen in the emitting region, what introduces the effect of differential optical depth. Thus, one can only fit the observed

EVPA(ν) and use it along with other observables to constrain the system free parameters. As $\rho_V(\nu)$ is a steeply declining function of temperature θ_e (Shcherbakov, 2008b), the relativistic charges contribute little to this quantity.

Substantial levels of circular polarization were recently found in Sgr A* (Munoz et al. 2011, in prep.). There are several effects producing finite CP. First recognized was the emissivity ε_V in V mode. According to Melrose (1971) it only is a factor of γ weaker than the total emissivity ε_I. It produces the largest V along the magnetic field. The Faraday conversion, transformation between the linear polarization and the circular, operates perpendicular to the magnetic field. The Faraday conversion coefficient ρ_Q has a peculiar dependence on temperature of thermal plasma or particles' γ-factor (Shcherbakov, 2008b): $\rho_Q = 0$ for cold plasma, ρ_Q is exponentially inhibited for very hot plasma and reaches the maximum for transrelativistic plasma with $\theta_e \sim \gamma \sim$ several $\cdot\, mc^2/k_B$. The exponential inhibition is an effect of finite ratio ν/ν_B with peak ρ_Q only around $\theta_e \sim 10$ for $\nu/\nu_B \sim 10^3$. Thus, for hot bulk part of particle distribution with $\gamma \sim$ several $\cdot\, mc^2/k_B$ the non-thermal electrons do not contribute significantly to Faraday conversion. Note that this result supersedes Ballantyne et al. (2007), who following Melrose (1997c) neglected the importance of finite ratio ν/ν_B. Similarly to linear polarization, the beam depolarization can lower the net value of circular polarization at low frequencies due to differential Faraday conversion.

In sum, there are often several explanations for the same observable quantity. One should not settle for a simplified model trying to reproduce the observations. Instead, the rigorous ray tracing and aposteriori explanations of a fit to the observables would be the preferred reliable way.

The proposed method has its limitation. The equation (5.63) is valid for optically thick medium, but it fails to describe the behavior of a set of photons for Compton-thick medium. The encounters of photons with energetic electrons lead to significant changes in photon trajectory, whereas the previous discussion considered independent photons propagating along geodesics. Luckily, the synchrotron absorption cross-section in sub-mm is much larger than the Compton scattering cross-section, thus the optically thick medium near Sgr A* is Compton-thin and no modifications are needed for Sgr A*. However, a careful consideration of Compton scattering (Rybicki & Lightman, 1979) is needed to describe the sub-mm spectrum of Compton-thick sources.

5.6 Discussion & Conclusions

In our endeavor to provide the complete and self-consistent description of GR polarized radiative transfer we conduct the full derivation starting from definitions and basic equations. The goal is to make the easy, transparent, and error-free derivations, thus Mathematica 7 was used underway, the expressions were cross-checked. The absorptivities for thermal plasma were checked numerically against known synchrotron emissivities and cyclo-synchrotron approximations in Sazonov (1969); Leung et al. (2009). We stepped away from the standard textbooks and assumed "the opposite" observers' definition of circular polarization V, carrying the definition through all other calculations. We chose the coordinate system with coplanar $\mathbf{k}$, $\tilde{\mathbf{e}}^2$, $\mathbf{B}_0$ and derived the plasma response tensor $\tilde{\alpha}_{ik}$ in ($\tilde{\mathbf{e}}^1$, $\tilde{\mathbf{e}}^2$, $\tilde{\mathbf{e}}^3$) basis, also projecting it onto the transverse coordinates $\mathbf{e}^1$, $\mathbf{e}^2$. Repeating for completeness Huang et al. (2009a), we tie the polarized radiative transfer equation in the latter coordinates (5.17) with the transfer in $\mathbf{a}$, $\mathbf{b}$ coordinates with the help of

matrix (5.50). The generalization of radiative transfer to GR is performed in the easiest way owing to the invariance of occupation numbers in different photon states and the invariance of the transformation between the states. Lorenz gauge (5.12) helps to establish the correspondence between 4×4 and spatial 3×3 quantities and to correctly find the transverse vectors $\mathbf{a}$, $\mathbf{b}$ in the co-moving locally-flat reference frame. The transformation from the lab frame with Kerr metric to that frame is explicitly given. The intricacies of application of GR polarized radiative transfer to LLAGNs are discussed. As the transfer incorporates many physical effects, a priori guessing of the most important effects is discouraged in favor of full calculation. The provided interface of dynamical models and observations is waiting for its applications.

The treatment of particles distributions is still limited. In the current state the calculations are optimized for isotropic in pitch-angle distributions and become especially simple for thermal particle distribution. The integration over the pitch-angle in formula (5.35) is in general impossible to perform for non-isotropic distributions. In this case, the integral over ξ should be done first analytically. This calculation is left for future work.

Acknowledgments

The authors are grateful to Charles Gammie, James Moran, Diego Munoz, and Ramesh Narayan for fruitful discussions, Akshay Kulkarni and Robert Penna for help with the transformation to the locally-flat co-moving frame, and to anonymous referee for helpful comments. Charles Gammie kindly provided us a draft of their paper (Gammie et al. 2010, in prep.) on covariant formalism of polarized ray tracing. The work is partially supported by NASA grant NNX08AX04H to RVS and China Postdoctoral Science

Foundation grant 20090450822 to LH.

Chapter 6

Constraining the Accretion Flow in Sgr A* by General Relativistic Dynamical and Polarized Radiative Modeling

Abstract

The constraints on the Sgr A* black hole (BH) and accretion flow parameters are found by fitting polarized sub-mm observations. First, we compile a mean Sgr A* spectrum by averaging observations over many epochs from reports in 29 papers, which results in a robust spectrum determination with small standard errors. We find the mean flux F_ν, linear polarization (LP) fractions, circular polarization (CP) fractions, and electric vector position

angles (EVPA). We run three-dimensional general relativistic magnetohydrodynamical (3D GRMHD) simulations for dimensionless spins $a_* = 0, 0.5, 0.7, 0.9, 0.98$ over a $20000M$ time interval, construct averaged dynamical models, perform radiative transfer, and explore the parameter space of spin a_*, inclination angle θ, position angle (PA), accretion rate $\dot{M}$, and electron temperature T_e at radius $6M$. A new general relativistic polarized radiative transfer code is implemented to simulate polarized fluxes from the averaged models. Averaged dynamical models are compiled by averaging simulations over time. In the main "RMS-field" model, the magnetic field is directed along the time-averaged field and has a strength of the root-mean-square field. A model with linear time-averaged magnetic field is also tested. We perform χ^2 per degrees of freedom (dof) statistical analysis to quantify the goodness of models in fitting mean fluxes, LP and CP fractions between 88 GHz to 857 GHz. The RMS-field model favors spin $a_* = 0.9$ with minimum $\chi^2/\mathrm{dof} \approx 4.0$. Correspondent 90% confidence intervals for spin $a_* = 0.9$ simulation are $\theta = 53^\circ \pm 3^\circ$, $\mathrm{PA} = 121^\circ \pm 20^\circ$, $\dot{M} = (1.09 \pm 0.13) \times 10^{-8} M_\odot \mathrm{year}^{-1}$, $T_e = (4.62 \pm 0.56) \cdot 10^{10}$ K at $6M$. The linear averaged magnetic field model with same spin gives similar expectation values. By combining the results from spin $a_* = 0.9$ models we obtain the conservative estimates: $\theta = 50^\circ - 59^\circ$, $\mathrm{PA} = 101^\circ - 143^\circ$, $\dot{M} = (0.9 - 1.7) \times 10^{-8} M_\odot \mathrm{year}^{-1}$, $T_e = (2.7 - 5.2) \cdot 10^{10}$ K at $6M$. Fitting only the flux spectrum without LP and CP fractions results in the best $\chi^2_F/\mathrm{dof} < 1$ for $a_* = 0.7, 0.9, 0.98$ and much wider confidence intervals, thus polarization is an essential component for constraining the spin, disk orientation, and flow properties. We identify physical phenomena leading to matched LP fraction, CP fraction, EVPA by sequentially switching off radiative transfer effects. In particular, the observed amount of CP is produced by Faraday conversion. The emission region size at 230 GHz of the best-fitting RMS-field model with spin $a_* = 0.9$ is consistent with the size 37μas observed

by VLBI methods. We estimate the power-law index $\beta = 0.8 - 0.9$ of density profile $n \sim r^{-\beta}$ between Bondi radius and the inner flow. This index lies in between $\beta = 1.5$ for advection-dominated flow and $\beta = 0.5$ for convection-dominated flow. The PA of spin projection coincides with that of a tentative X-ray jet.

6.1 Introduction

Our Galactic Center black hole is one of many inactive galactic cores, the only distinctive feature being its proximity to us. The mass of the black hole (BH) is known to be $M \approx 4.5 \cdot 10^6 M_\odot$ (Ghez et al., 2003) and the spin is uncertain. It resides at a distance of about $d \approx 8.4$ kpc. Because of such proximity, many observations of the source were made in all wavelengths, which are not completely obscured by absorption: γ-rays, X-rays, IR, (sub-)mm, and radio. The origins of X-rays are bremsstrahlung from hot gas near the radius of BH gravitational influence (Narayan et al., 1995, 1998; Shcherbakov & Baganoff, 2010) and Compton-scattered emission close to the horizon (Moscibrodzka et al., 2009). X-rays at large radius are spatially resolved, which gives an opportunity to test dynamical models far from the black hole (Shcherbakov & Baganoff, 2010). The sub-mm emission is cyclo-synchrotron originating close to the black hole. Cyclo-synchrotron emission is polarized, both linear and circular polarizations were observed from Sgr A* at several sub-mm wavelengths. The accretion flow was recently resolved at 230 GHz (Doeleman et al., 2008). General relativistic (GR) effects were deemed necessary to explain the small size with full width at half maximum (FWHM) of 37μas. The radio emission is also produced by cyclo-synchrotron, but at larger distance from the BH. Thus, to study the effects of GR, one should model sub-mm polarized observations while also considering the amount

of Compton-scattered X-rays. Modeling the sub-mm in the range 88 GHz to 857 GHz is the goal of the present chapter.

First, we need to understand which observations to fit. Sgr A* is a variable source with a variability amplitude routinely reaching 30% in sub-mm. A popular approach is to fit simultaneous observations (e.g. Yuan et al. 2004; Broderick et al. 2009a), in particular the set from Falcke et al. (1998). However, one cannot easily combine two sets of observations in such an approach: the addition of a new frequency would require redoing observations of every other frequency at that instant of time. Simultaneous observations of linear polarization (LP) and circular polarization (CP) at several frequencies were not yet performed. Thus, it is quite reasonable to consider non-simultaneous statistics of all observations at all frequencies instead and find the mean values and standard errors of quantities at each frequency. We check that samples of observed fluxes and LP fractions are consistent with a Gaussian distribution at $\nu \geq 88$ GHz.

A good GR dynamical model of accretion is required to reproduce the observations. There are now numerous accretion flow models applicable to the Galactic Center: advection-dominated accretion flow (ADAF) (Narayan & Yi, 1995), adiabatic inflow-outflow solution (ADIOS) (Blandford & Begelman, 1999), jet-ADAF (Yuan et al., 2002), jet (Maitra et al., 2009), and the models directly based on numerical simulations. These quasi-analytical models in general have a large number of free parameters and also incorporate many assumptions that are not generally justifiable (Huang et al., 2008, 2009a), which leads to unreliable constraints on the properties of the black hole accretion flow. The numerical simulations require fewer inputs and settle into a quasi-steady accretion, which justifies their use. GRMHD simulations, like those performed in McKinney & Blandford (2009); Fragile et al. (2009); Noble & Krolik (2009); Moscibrodzka et al. (2009); Penna

et al. (2010), are necessary for modeling matter infall onto a rotating BH. The behavior of accretion is also different between two-dimensional and three-dimensional models (Igumenshchev, 2008) due to Cowling's anti-dynamo theorem, so we model the flow in three dimensions. Numerical simulations are limited to a region relatively close to the BH (Dexter et al., 2009; Moscibrodzka et al., 2009), whereas some emission and some Faraday rotation might happen far from the BH. Thus, we analytically extend the modeled region out to $20000M$, do radiative transfer, and find the best fit to the data. The extension to large radius allows us to define the electron temperature more consistently (Sharma et al., 2007a). We find a posteriori (see Appendix 6.9) that the simulated polarized spectra are insensitive to variations of analytic extensions of density and temperature, but may depend on the extension of the magnetic field.

A good dynamical model does not eliminate the uncertainty of comparing to data. Indeed, correct radiative transfer and statistical analysis are necessary for such a comparison. The simplest Newtonian radiation consideration (Yuan et al., 2004) does not provide a means to treat radiation close to the BH. A quasi-Newtonian approach offers some improvement (Goldston et al., 2005; Chan et al., 2009). General relativistic treatments of unpolarized light (Fuerst & Wu, 2004; Dexter et al., 2009; Dolence et al., 2009) capture most GR effects, but only polarized general relativistic radiative transfer (Broderick et al., 2009a; Gammie & Leung, 2010; Shcherbakov & Huang, 2011) is exact and captures all GR phenomena. The present chapter adopts this approach. We are able to compare the results of modeling to extensive polarization data, constraining much better the flow parameters and spin. In fact, fitting only the total flux spectrum might not constrain the spin. Spin values from $a_* = 0$ (Broderick et al., 2009a) to $a_* = 0.9$ (Moscibrodzka et al., 2009) are found in the literature. Other radiation ingredients may

include Comptonization (Moscibrodzka et al., 2009) and radiation from non-thermal electrons (Mahadevan, 1998; Özel et al., 2000; Yuan et al., 2004). We do not consider non-thermal electrons, but find that strong radio emission at $\nu < 50$ GHz is produced in polar flow regions even by thermal electrons. Emissivities are calculated in synchrotron approximation (Legg & Westfold, 1968; Sazonov, 1969; Pacholczyk, 1970; Melrose, 1971) with an exact thermal electron distribution. Emissivities in the synchrotron approximation are very close to the exact cyclo-synchrotron emissivities (Leung et al., 2009; Shcherbakov & Huang, 2011), so we use the former. However, the exact Faraday rotation and conversion expressions are employed (Shcherbakov, 2008b), as no similar approximations exist for them.

The comparison of simulations to observations were done in the past "by eye" in studies of Sgr A* until quite recently, when Broderick et al. (2009a) followed by Dexter et al. (2009) introduced statistical analyses. We extend their approach by incorporating the statistics of LP and CP fractions and comparing simulated spectra to observed ones at many frequencies simultaneously. After checking for normality of observations, computing their means and standard errors, we employ χ^2 statistics. We search the space of all parameters: spin a_*, inclination θ, ratio of proton to electron temperatures T_p/T_e at distance $6M$ from the center, and accretion rate $\dot{M}$ to find the minimum χ^2 models. We find models with χ^2 relatively close to unity. Then we integrate the χ^2 probability density function (PDF) over the entire parameter space and compute the expectation values of model parameters together with the uncertainties and 90% confidence intervals. Full statistical analysis is performed in the present work.

The chapter is constructed as follows. We summarize the observational manifestations of the accretion flow in the sub-mm in § 6.2. The 3D GRMHD simulations are described in

§ 6.3 together with the physically-motivated extension to large radii, the electron heating prescription, and the flow averaging prescription. We run simulations for dimensionless spins $a_* = a/M = 0, 0.5, 0.7, 0.9, 0.98$. As the required CPU time to compute the average of simulated spectra via many snapshots to mimic observations is prohibitively large, we perform radiative transfer over averaged models. The GR polarized radiative transfer technique is elaborated upon in § 6.5. The statistical analysis is presented in § 6.6. The set of observations considered consists of the spectral energy distribution (SED) within the 88 GHz to 857 GHz frequency range, linear polarization (LP) fractions at 88 GHz, 230 GHz, and 349 GHz, and circular polarization (CP) fractions at 230 GHz and 349 GHz. In § 6.7 we discuss numerous results: the best fits to observations, the behaviors of χ^2 near the best fits, the importance of various physical effects in producing the observed CP, LP, and electric vector position angle (EVPA), expectation values of quantities and confidence intervals, and image size estimates. We show the actual images of total and polarized intensities and generate movies. Discussion in § 6.8 compares the results to previous estimates, emphasizes the significance of polarization, notes the sources of errors, and outlines prospects for future work. We note that fitting only the total flux provides very loose constrains on the flow. In Appendix 6.9 we perform a number of convergence tests for radial extension of the dynamical model and GR polarized radiative transfer code. Throughout the chapter we measure distance and time in the units of BH mass M by setting the speed of light and gravitational constant to unity.

6.2 Observations

Sgr A* is known to be a highly variable source, yet quiescent models of Sgr A* emission are popular and useful. Unlike the drastic variations of X-ray and NIR fluxes (Baganoff et al., 2001; Genzel et al., 2003), sub-mm fluxes do not vary by more than a factor of $2-3$ (Zhao et al., 2003). Thus, it is reasonable to approximate the distribution of observed fluxes at each frequency and polarization type by a Gaussian, find the mean and the standard error and use the framework of standard χ^2 analysis. Previously, the flux spectra were modeled by Yuan et al. (2004); Broderick et al. (2009a). However, both papers summarize a limited set of observations and do not perform any averaging. Sub-mm flux data reported in Yuan et al. (2004) consists of a short set of observations by Falcke et al. (1998) and one set of SMA observations by Zhao et al. (2003). Broderick et al. (2009a) adds to these the rest of SMA total flux data (Marrone et al., 2006a,b, 2007, 2008). Thus, only 6 out of at least 29 papers on sub-mm observations of Sgr A* were employed. Our work computes a properly averaged spectrum based on all papers to date reporting sub-mm observations of Sgr A*.

Table 6.1:: Summary of Sgr A* radio/sub-mm observations

ν [GHz]	Telescopes	F_ν [Jy]	LP [%]	CP [%]	EVPA [°]
8.45	VLA	**0.683±0.032** (Serabyn et al., 1997; Falcke et al., 1998; Bower et al., 1999a; An et al., 2005)	···	**−0.26 ± 0.06**[b] (Bower et al., 1999a)	···
14.90	VLBA, VLA	**0.871 ± 0.012**[a](Serabyn et al., 1997; Falcke et al., 1998; Bower et al., 2002; Herrnstein et al., 2004; An et al., 2005; Yusef-Zadeh et al., 2009)	···	**−0.62 ± 0.26**[b](Bower et al., 2002)	···
22.50	VLBA, VLA	**0.979 ± 0.016**[a](Serabyn et al., 1997; Falcke et al., 1998; Bower et al., 1999b; Herrnstein et al., 2004; An et al., 2005; Lu et al., 2008; Yusef-Zadeh et al., 2007, 2009)	**0.20 ± 0.01**[b] (Bower et al., 1999b; Yusef-Zadeh et al., 2007)	···	···
43	GMVA, VLBA, VLA	**1.135 ± 0.026**[a](Falcke et al., 1998; Lo et al., 1998; Bower et al., 1999b; Herrnstein et al., 2004; An et al., 2005; Shen et al., 2005; Krichbaum et al., 2006; Lu et al., 2008; Yusef-Zadeh et al., 2007, 2009)	$\mathbf{0.50^{+0.27}_{-0.17}}$[b] (Bower et al., 1999b; Yusef-Zadeh et al., 2007)	···	···
88	BIMA, MPIfR, VLBA, VLA, Nobeyama, NMA, CARMA	**1.841 ± 0.080** (Falcke et al., 1998; Krichbaum et al., 1998; Bower et al., 1999b; Doeleman et al., 2001; Miyazaki et al., 2004; Shen et al., 2005; Krichbaum et al., 2006; Macquart et al., 2006; Lu et al., 2008; Yusef-Zadeh et al., 2009)	$\mathbf{1.03^{+0.21}_{-0.18}}$[c] (Bower et al., 1999b; Macquart et al., 2006)	···	**-4**[d] (Bower et al., 1999b; Shen et al., 2005; Macquart et al., 2006)
102	OVRO, CSO-JCMT, Nobeyama, NMA, IRAM	**1.91 ± 0.15** (Serabyn et al., 1997; Falcke et al., 1998; Miyazaki et al., 2004; Mauerhan et al., 2005; Yusef-Zadeh et al., 2009)	···	···	···
145	Nobeyama, NMA, IRAM, JCMT	**2.28 ± 0.26** (Falcke et al., 1998; Aitken et al., 2000; Miyazaki et al., 2004; Yusef-Zadeh et al., 2009)	···	···	···
230	IRAM, JCMT, BIMA, SMA, OVRO	**2.64 ± 0.14** (Serabyn et al., 1997; Falcke et al., 1998; Aitken et al., 2000; Bower et al., 2003, 2005; Zhao et al., 2003; Krichbaum et al., 2006; Marrone et al., 2006a, 2007, 2008; Doeleman et al., 2008; Yusef-Zadeh et al., 2009)	$\mathbf{7.02^{+0.63}_{-0.58}}$[c] (Bower et al., 2003, 2005; Marrone et al., 2007, 2008)	**−1.2 ± 0.3**[b] (Munoz et al. (2009), Munoz et al. 2011, in prep.)	**111.5 ± 5.3** (Bower et al., 2003, 2005; Marrone et al., 2007, 2008)
349	SMA, CSO, JCMT	**3.18 ± 0.12** (Aitken et al., 2000; An et al., 2005; Marrone et al., 2006b, 2007, 2008; Yusef-Zadeh et al., 2009)	$\mathbf{6.14^{+0.75}_{-0.67}}$[c] (Marrone et al., 2006b, 2007)	**−1.5 ± 0.3** [b](Munoz et al. 2011, in prep.)	**146.9 ± 2.2** (Marrone et al., 2006b, 2007)

Continued on Next Page...

Table 6.1 – Continued

ν **[GHz]**	**Telescopes**	F_ν **[Jy]**	**LP** [%]	**CP** [%]	**EVPA** [°]
674	CSO, SMA	**3.29 ± 0.35** (Marrone et al., 2006a, 2008; Yusef-Zadeh et al., 2009)	···	···	···
857	CSO	**2.87 ± 0.24** (Serabyn et al., 1997; Marrone et al., 2008; Yusef-Zadeh et al., 2009)	···	···	···

[a]Flux observations at $14.9, 22.50, 43$ GHz are inconsistent with a Gaussian distribution (Hernstein et al., 2004), while other fluxes, CP fractions and logarithms of LP fractions are consistent with Gaussian distributions.
[b]The uncertainty of the mean in these quantities is given by instrumental errors.
[c]Standard errors are computed for logarithms of LP fractions.
[d]The mean EVPA at 88 GHz is uncertain due to the ±180° degeneracy; e.g. the reported EVPA = 80° could as well be interpreted as −100°.

The reported observations vary greatly in the covered period from several hours (An et al., 2005) to several years (Zhao et al., 2003; Krichbaum et al., 2006). We know that variations of a factor of 2 may happen within several hours (Yusef-Zadeh et al., 2009), whereas more than a factor of several are never observed in the sub-mm. Thus, fluxes observed more than a day apart are weakly correlated. A question of autocorrelation timescales will be addressed in more detail in future work. We, therefore, consider the following averaging technique to robustly sample the distributions of fluxes. First, we define groups of close frequencies, where frequencies are different by no more than several percent from the mean. There are 11 groups (see Table 6.1). We have excluded papers reporting frequencies far from the mean of each group. In particular, 94 GHz and 95 GHz observations in Li et al. (2008); Falcke et al. (1998) and the 112 GHz observations in Bower et al. (2001) are excluded. A mean frequency is ascribed to represent each group. Then we take all the reported observations of each polarization type (total flux, LP and CP fraction, EVPA) for each group and draw the largest sample of fluxes/polarization fractions observed more than one day apart. When several fluxes are reported over a period of several hours (Yusef-Zadeh et al., 2009), we normally only draw one data point

from the very beginning of such an observation. There are some unreliable observations over the set of papers. Often unreliable data is produced by observing in sub-mm with large beam size. Light from Sgr A* is blended with dust and other sources. For example, SMT data (Yusef-Zadeh et al., 2009), early CSO measurements (Serabyn et al., 1997), and early JCMT measurements (Aitken et al., 2000) may have such issues. We exclude these data from the sample. The interferometric observations, especially with VLBI, help to reduce an error of otherwise unreliable observations, e.g. with BIMA array (Bower et al., 2001). However, some inconsistencies still exist for simultaneous observations at the same frequency with different instruments (Yusef-Zadeh et al., 2009).

After a robust sample of fluxes, polarization fractions, and EVPA angles is found for each frequency group, we compute the mean, the standard error and check (by Kolmogorov-Smirnov test) that the data are consistent with the resultant Gaussian distribution. For LP fractions we consider the statistics of log(LP). The summary of results is presented in Table 6.1. CP fractions of -1.2% at 230 GHz and -1.5% at 349 GHz are based on preliminary work by SMA collaboration with the reported error $\pm 0.3\%$ of instrumental nature. The p-values of the Kolmogorov-Smirnov consistency test are above 0.05 for log(LP) and EVPA in each frequency group, which shows the consistency of sample fluxes/LP fractions with Gaussians and validates the χ^2 analysis. Also, $p > 0.05$ holds for fluxes at all frequencies except $\nu = 14.90$ GHz, $\nu = 22.50$ GHz, $\nu = 43$ GHz. Exceptionally large samples of > 100 fluxes are reported in Herrnstein et al. (2004) for those frequencies. The flux distribution at $\nu \leq 43$ GHz is found to be bimodal and inconsistent with a Gaussian. However, $p = 0.7$ for the Kolmogorov-Smirnov test at $\nu = 230$ GHz despite a large sample of 50 fluxes. Thus, we prove that the current state of observations supports Gaussian distributions of F_ν, log(LP), CP, and EVPA for frequencies $\nu \geq 88$ GHz and

allows for χ^2 statistical analysis based on computed means and standard errors. Note also, that standard errors in our flux samples are smaller than the error bars of old observations (Falcke et al., 1998; Yuan et al., 2004; Broderick et al., 2009a), but the errors are still larger compared to contemporary single-observation instrumental errors (Marrone et al., 2007). Thus, we do not incorporate instrumental error in our estimates of an error of a flux sample mean. The same is true for log(LP) and EVPA. We do not incorporate the source size measurements (Doeleman et al., 2008) in calculating the χ^2, but check that the best fit model is consistent with those observations. Figure 6.1 shows a compilation of the mean quantities with their Gaussian standard errors. The data are represented by both error bars and the interpolated shaded area in between. A red dashed curve on F_ν plot represents the analytic approximation $F_\nu = 0.248\nu^{0.45}\exp(-(\nu/1100)^2)$, where flux is in Jy and frequency is in GHz.

6.3 Dynamical Model: 3D GRMHD Simulations

Our radiative transfer calculations take the results of simulations of accretion flows onto black holes as input. These simulations are similar to those in Penna et al. (2010). We review the methodology.

6.3.1 Governing Equations

We simulate radiatively inefficient accretion flows (RIAFs) onto rotating black holes using a three-dimensional fully general relativistic code (see §6.3.3). The black hole is described by the Kerr metric. We work with Heaviside-Lorentz units, so that the unit of distance is $r_{\rm g} = M$ and the unit of time equals $r_{\rm g}/c = M$. Our five simulations correspond

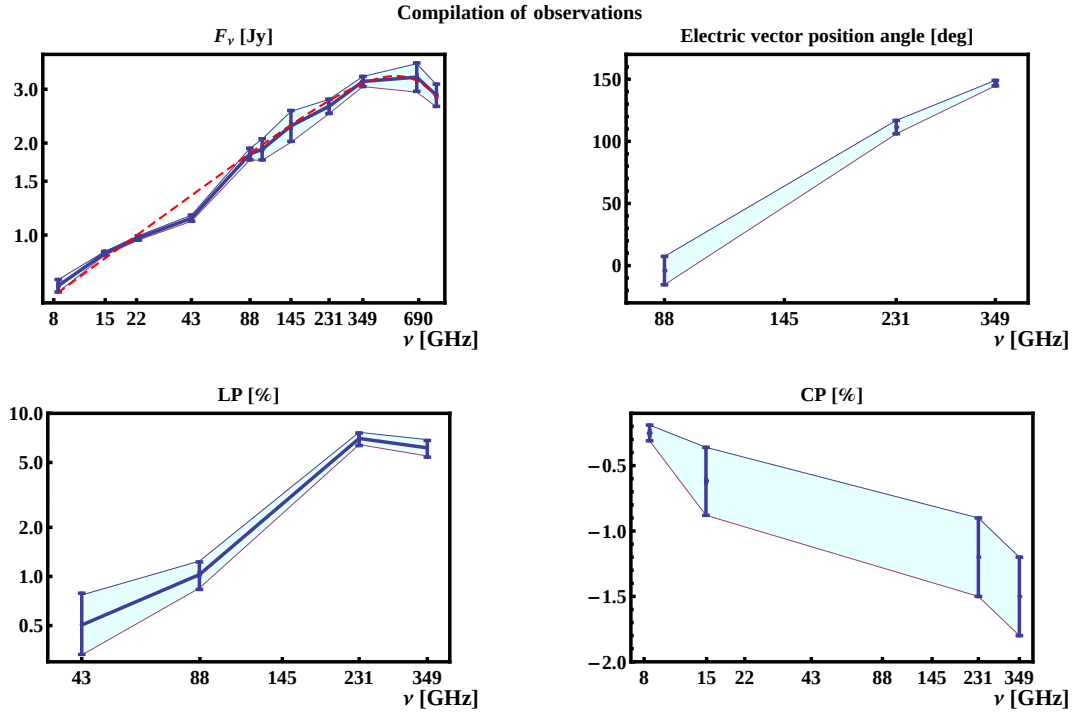

Figure 6.1.— Mean observed SEDs of specific flux F_ν, linear polarization (LP) fraction, electric vector position angle (EVPA), and circular polarization (CP) fraction. The error bars show the 1σ standard error of the mean. The dashed line on the F_ν plot represents the analytic approximation $F_\nu(\mathrm{Jy}) = 0.248\nu^{0.45}\exp(-(\nu/1100)^2)$ for frequency ν in GHz (not the simulated SED). As noted in Table 6.1, the error is instrumental for CP, whereas it is computed from a sample of observed quantities for flux, LP and EVPA.

to different choices of the dimensionless black hole spin parameter: $a_* = 0, 0.5, 0.7, 0.9$, and 0.98. The self-gravity of the RIAF is ignored.

The RIAF is a magnetized fluid, so we solve the GRMHD equations of motion (Gammie et al., 2003). Mass conservation gives:

$$\nabla_\mu(\rho u^\mu) = 0, \tag{6.1}$$

where ρ is the fluid frame rest-mass density, u^μ is the contravariant 4-velocity, and ∇_μ is the covariant derivative. Energy-momentum conservation gives

$$\nabla_\mu T^\mu_\nu = 0, \tag{6.2}$$

where the stress energy tensor T^μ_ν includes both matter and electromagnetic terms,

$$T^\mu_\nu = (\rho + u_g + p_g + b^2)u^\mu u_\nu + (p_g + b^2/2)\delta^\mu_\nu - b^\mu b_\nu, \tag{6.3}$$

where u_g is the internal energy density and $p_g = (\Gamma - 1)u_g$ is the ideal gas pressure with $\Gamma = 4/3$ [1]. The contravariant fluid-frame magnetic 4-field is given by b^μ and is related to the lab-frame 3-field via $b^\mu = B^\nu h^\mu_\nu / u^t$ where $h^\mu_\nu = u^\mu u_\nu + \delta^\mu_\nu$ is a projection tensor, and δ^μ_ν is the Kronecker delta function (Gammie et al., 2003). We often employ $\mathbf{b}$ below, which is the orthonormal magnetic field vector in a comoving locally flat reference frame (Penna et al., 2010). The magnetic energy density (u_b) and magnetic pressure (p_b) are then given by $u_b = p_b = b^\mu b_\mu/2 = b^2/2 = \mathbf{b}^2/2$. Note that the angular velocity of the gas is $\Omega = u^\phi/u^t$.

Magnetic flux conservation is given by the induction equation

$$\partial_t(\sqrt{-g}B^i) = -\partial_j[\sqrt{-g}(B^i v^j - B^j v^i)], \tag{6.4}$$

[1] Models with $\Gamma = 5/3$ show some minor differences compared to models with $\Gamma = 4/3$ (McKinney & Gammie, 2004; Mignone & McKinney, 2007).

where $v^i = u^i/u^t$, and $g = \mathrm{Det}(g_{\mu\nu})$ is the determinant of the metric. No explicit resistivity or viscosity is included.

In Penna et al. (2010), we studied both RIAFs and geometrically thin, radiatively efficient disks. For the later case, a cooling term was added to the energy-momentum equation (6.2) to describe radiative losses and keep the disk thin. The current set of models are all RIAFs, so no cooling term is needed, energy generated by viscous dissipation is advected along with the flow or transported out due to convection or in a wind.

6.3.2 Physical Models

The initial mass distribution is an isentropic equilibrium torus (Chakrabarti, 1985a,b; De Villiers et al., 2003) with pressure $p = K_0\rho^{4/3}$ for $K_0 = 0.009$. The torus inner edge is at $r_{\rm in} = 20M$ and maximum density and pressure are at $R_{\rm max} = 65M$. We initialize the solution so that $\rho = 1$ at the pressure maximum. As in Chakrabarti (1985a), the angular velocity distribution of the initial torus is a power law , where for the Chakrabarti (1985a) q-parameter we choose $q = 1.65$ (At large radii $\Omega \sim (r/M)^{-q}$.). The thickness of the torus at the pressure maximum is then $|h/r| = 0.3$, where

$$|h/r| \equiv \frac{\int\int\int |\theta - \pi/2|\, \rho(r,\theta,\phi) dA_{\theta\phi} dt}{\int\int\int \rho(r,\theta,\phi) dA_{\theta\phi} dt}, \tag{6.5}$$

where $dA_{\theta\phi} \equiv \sqrt{-g} d\theta d\phi$ is an area element in the $\theta - \phi$ plane, and the integral over dt is a time average over the period when the disk is in a steady state (see §6.3.6). A tenuous atmosphere fills the space outside the torus. It has the same polytropic equation of state as the torus, $p = K_0\rho^\Gamma$, with $\Gamma = 4/3$, and an initial rest-mass density of $\rho = 10^{-6}(r/M)^{-3/2}$, corresponding to a Bondi-like atmosphere. The torus is threaded with three loops of weak, poloidal magnetic field: the initial gas-to-magnetic pressure ratio is

$\beta = p_{\rm g,max}/p_{\rm b,max} = 100$, where $p_{\rm max}$ and $p_{b,max}$ are the maximum values of the gas and magnetic pressure in the torus. This approach to normalizing the initial field is used in many other studies (Gammie et al., 2003; McKinney & Gammie, 2004; McKinney, 2006a; McKinney & Narayan, 2007b; Komissarov & McKinney, 2007; Penna et al., 2010).

Recent GRMHD simulations of thick disks indicate that the results for the disk (but not the wind-jet, which for us is less important) are roughly independent of the initial field geometry (McKinney & Narayan, 2007a,b; Beckwith et al., 2008b). The vector potential we use is the same as in Penna et al. (2010). It is

$$A_{\phi,\rm N} \propto Q^2 \sin\left(\frac{\log(r/S)}{\lambda_{\rm field}/(2\pi r)}\right)[1 + 0.02(\rm ranc - 0.5)]\,, \tag{6.6}$$

with all other A_μ initially zero. We use $Q = (u_g/u_{g,\rm max} - 0.2)(r/M)^{3/4}$, and set $Q = 0$ if either $r < S$ or $Q < 0$. Here $u_{g,\rm max}$ is the maximum value of the internal energy density in the torus. We choose $S = 22M$ and $\lambda_{\rm field}/(2\pi r) = 0.28$, which gives initial poloidal loops that are roughly isotropic such that they have roughly 1:1 aspect ratio in the poloidal plane. The form of the potential in equation 6.6 ensures that each additional field loop bundle has opposite polarity. Perturbations are introduced to excite the magneto-rotational instability (MRI). The second term on the right-hand-side (RHS) of equation 6.6 is a random perturbation: ranc is a random number generator for the domain 0 to 1. Random perturbations were introduced in the initial internal energy density in the same way, with an amplitude of 10%. In Penna et al. (2010), it was found that similar simulations with perturbations of 2% and 10% became turbulent at about the same time, the magnetic field energy at that time was negligibly different, and there was no evidence for significant differences in any quantities during inflow equilibrium.

6.3.3 Numerical Methods

We perform simulations using a fully 3D version of HARM that uses a conservative shock-capturing Godunov scheme (Gammie et al., 2003; Shafee et al., 2008; McKinney, 2006b; Noble et al., 2006; Mignone & McKinney, 2007; Tchekhovskoy et al., 2007; McKinney & Blandford, 2009). We use horizon-penetrating Kerr-Schild coordinates for the Kerr metric (Gammie et al., 2003; McKinney & Gammie, 2004), which avoids any issues with the coordinate singularity in Boyer-Lindquist coordinates. The code uses uniform internal coordinates $(t, x^{(1)}, x^{(2)}, x^{(3)})$ mapped to the physical coordinates (t, r, θ, ϕ). The radial grid mapping is

$$r(x^{(1)}) = R_0 + \exp(x^{(1)}), \tag{6.7}$$

which spans from $R_{\rm in} = 0.9r_H$ to $R_{\rm out} = 200M$, where r_H is the radius of the outer event horizon. This just ensures the grid never extends inside the inner horizon, in which case the equations of motion would no longer be hyperbolic. The parameter $R_0 = 0.3M$ controls the resolution near the horizon. For the outer radial boundary of the box, absorbing (outflow, no inflow allowed) boundary conditions are used.

The θ-grid mapping is

$$\theta(x^{(2)}) = \left[Y(2x^{(2)} - 1) + (1 - Y)(2x^{(2)} - 1)^7 + 1\right](\pi/2), \tag{6.8}$$

where $x^{(2)}$ ranges from 0 to 1 (i.e. no cut-out at the poles) and $Y = 0.65$ is chosen to concentrate grid zones toward the equator. Reflecting boundary conditions are used at the polar axes. The ϕ-grid mapping is given by $\phi(x^{(3)}) = 2\pi x^{(3)}$, such that $x^{(3)}$ varies from 0 to 1/2 for a box with $\Delta\phi = \pi$. Periodic boundary conditions are used in the ϕ-direction. Penna et al. (2010) considered various $\Delta\phi$ for thin disks and found little difference in the results. In all of their tests, $\Delta\phi > 7|h/r|$ and we remain above this limit as well. In what

follows, spatial integrals are renormalized to refer to the full 2π range in ϕ, even if our computational box size is limited in the ϕ-direction. For the purpose of radiative transfer we combine two identical regions of size $\Delta\phi = \pi$ preserving the orientation to obtain the span of full 2π.

6.3.4 Resolution and Spatial Convergence

The resolution of the simulations is $N_r \times N_\theta \times N_\phi = 256 \times 64 \times 32$. This is the fiducial resolution of Penna et al. (2010). Shafee et al. (2008) found this resolution to be sufficient to obtain convergence compared to a similar $512 \times 128 \times 32$ model. In the vertical direction, we have about 7 grid cells per density scale height. Turbulence is powered by the MRI, which is seeded by the vertical component of the magnetic field (Balbus & Hawley, 1998). The characteristic length scale of the MRI is the wavelength of the fastest growing mode:

$$\lambda_{\rm MRI} = 2\pi \frac{v_A}{\Omega_0}, \tag{6.9}$$

where v_A is the Alfvén speed. Assuming hydrostatic equilibrium, we can rewrite this formula near the midplane of the disk in terms of the dimensionless disk thickness h/r and the plasma β:

$$\lambda_m = 2\pi(h/r)\frac{1}{\sqrt{\beta}} r. \tag{6.10}$$

Clearly the MRI is most difficult to resolve when β is large. We have local values of $\beta \sim 20 - 100$ initially and then β decreases until it is order $\beta \sim 10$ in the disk beyond the black hole and order $\beta \sim 1$ near the black hole due to the instability exponentially amplifying the initial field. We find that $\lambda_m > h$ always, and the MRI is well-resolved in the midplane of disk both initially and in the saturated state because h/r is resolved by the chosen θ grid. Penna et al. (2010) studied convergence in N_r, N_θ, and N_ϕ and found

that models with $N_r = 256$ or $N_r = 512$, $N_\theta = 64$ or $N_\theta = 128$, and $N_\phi = 64$ or $N_\phi = 32$ behaved similarly for disks with similar resolution across the disk. Our resolution of the MRI and prior convergence testing by Penna et al. (2010) for similarly-resolved disks justify our choice of grid resolution. It is currently not computationally feasible to perform a similar spin parameter study at much higher resolutions, and future studies will continue to explore whether such simulations are fully converged.

A key feature of our code is the use of a 3rd order accurate (4th order error) PPM scheme for the interpolation of primitive quantities (i.e. rest-mass density, 4-velocity relative to a zero angular momentum observer (ZAMO), and lab-frame 3-magnetic field) (McKinney, 2006a). Simulations of fully three-dimensional models of accreting black holes producing jets using our 3D GRMHD code show that this PPM scheme leads to an improvement in effective resolution by at least factors of roughly two per dimension as compared to the original HARM MC limiter scheme for models with resolution $256 \times 128 \times 32$ (McKinney & Blandford, 2009). The PPM method is particularly well-suited for resolving turbulent flows since they rarely have strong discontinuities and have most of the turbulent power in long wavelength modes. Even moving discontinuities are much more accurately resolved by PPM than minmod or MC. For example, even without a steepener, a simple moving contact or moving magnetic rotational discontinuity is sharply resolved within about 4 cells using the PPM scheme as compared to being diffusively resolved within about 8-15 cells by the MC limiter scheme.

6.3.5 Ceiling Constraints

During the simulation, the rest-mass density and internal energy densities can become quite low beyond the corona, but the code only remains accurate and stable for a finite value of b^2/ρ, b^2/u_g, and u_g/ρ for any given resolution. We enforce $b^2/\rho \lesssim 10$, $b^2/u_g \lesssim 100$, and $u_g/\rho \lesssim 10$ by injecting a sufficient amount of mass or internal energy into a fixed zero angular momentum observer (ZAMO) frame with 4-velocity $u_\mu = \{-\alpha, 0, 0, 0\}$, where $\alpha = 1/\sqrt{-g^{tt}}$ is the lapse.

We have checked the ceilings are rarely activated in the regions of interest of the flow. Figure 6.2 shows the constrained ratios, b^2/ρ, b^2/u_g, and u_g/ρ, as a function of θ at six radii ($r = 4, 6, 8, 10, 12$, and $14M$) for the $a_* = 0$ model. The data has been time-averaged over the steady state period from $t = 14000M$ to $20000M$. The ceiling constraints are shown as dashed red lines. and we see that the solution stays well away from the ceilings. This shows that the ceilings are sufficiently high.

6.3.6 Temporal Convergence

We run the simulations from $t = 0M$ to $t = 20000M$. The accretion rate, the height- and $\phi-$averaged plasma β, and other disk parameters, fluctuate turbulently about their mean values. The simulation reaches a quasi-steady state, when the mean parameter value are time-independent. Figure 6.3 shows the accretion rate and height- and $\phi-$averaged β at the event horizon as a function of time for all five models. We take the period from $t = 14000M$ to $t = 20000M$ to define steady state.

As shown in Penna et al. (2010), for disk models like the one considered, the disk outside the innermost stable circular orbit (ISCO) behaves like the α-disk model with

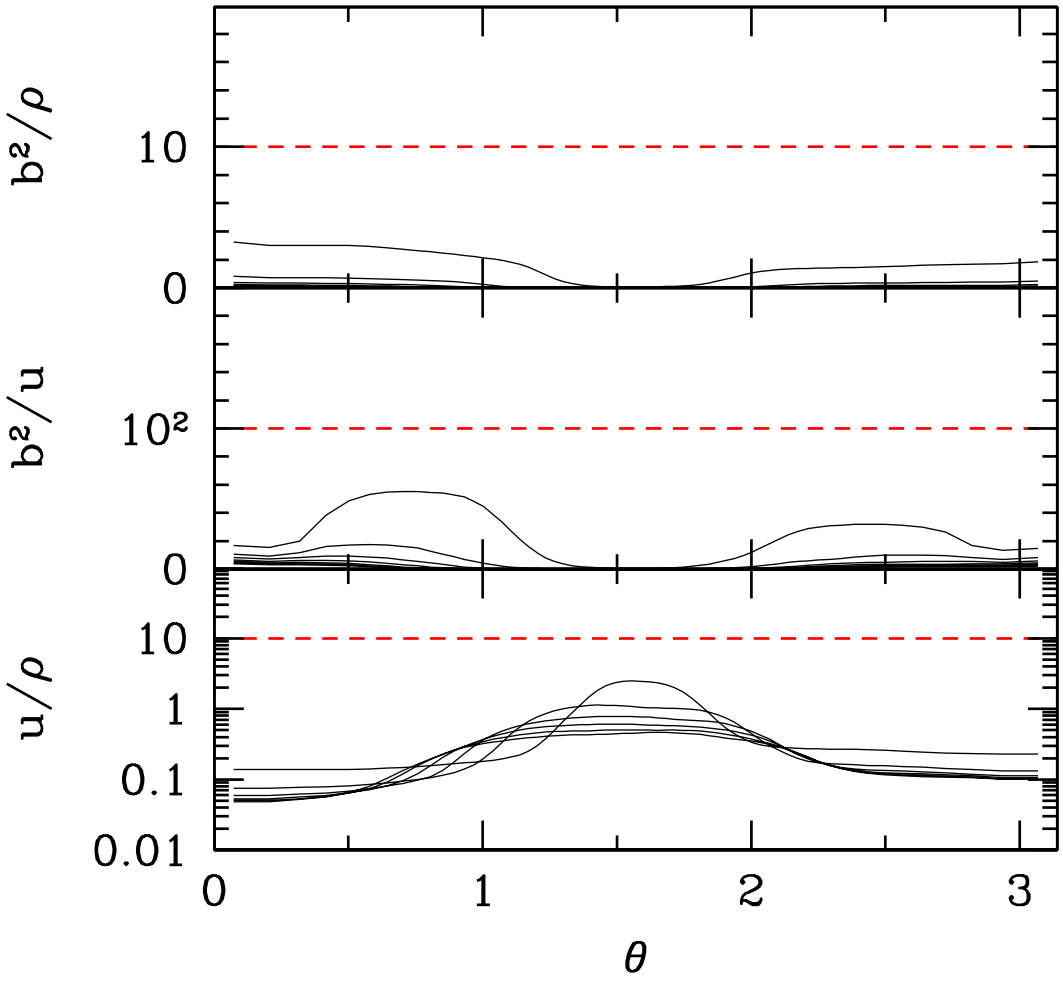

Figure 6.2.— Ratios of b^2/ρ, b^2/u_g, and u_g/ρ versus θ. Black curves correspond to different radii in the flow; from top to bottom, $r = 4, 6, 8, 10, 12$, and $14M$. The data is time-averaged over the steady state period of the flow, from $t = 14000M$ to $20000M$. Numerical ceilings constrain the solution to lie below the dashed red lines, but we see that the solution does not approach these limits.

$\alpha \sim 0.1$ across disk thicknesses of $h/r \sim 0.05 - 0.4$. This allows one to accurately infer the timescale for reaching "inflow equilibrium," corresponding to a quasi-steady flow across all quantities, at a given radius. For $h/r \sim 0.3$ by $t \sim 15000M$-$20000M$ (the simulation runs till $20000M$, but the initial $5000M$ are transients not necessarily associated with achieving inflow equilibrium for a simple viscous disk), we use the results in Appendix B of Penna et al. (2010) and find that inflow equilibrium is achieved within a radius of $r \sim 25M$-$30M$ for models with $a_* \sim 1$ and $r \sim 35M$ for models with $a_* \sim 0$. Even for a doubling of the viscous timescale, inflow equilibrium is achieved by $r \sim 20M$-$25M$ depending upon the black hole spin. This motivates using an analytical extension of the simulation solution for radii beyond $r \sim 25M$ as described later in § 6.4.2.

6.3.7 Evolved Disk Structure

Figure 6.4 shows matter stream lines as vectors and number density n_e as greyscale map. The large scale vortices existing on a single time shot (panel (a)) almost disappear, when averaged over $6000M$ (panel (b)) in between $14000M$ and $20000M$. The density is the highest in the equatorial plane on average, but deviations are present on the instantaneous map. The ISCO does not have any special significance: density and internal energy density increase through ISCO towards the black hole horizon.

Figure 6.5 shows magnetic field lines as vectors and comoving electromagnetic energy density $\propto b^2$ as a greyscale map. The structure of magnetic field at early times remembers the initial multi-loop field geometry (Penna et al., 2010), but switches at late times to a helical magnetic field structure resembling a split-monopole in meridional projection. Such switching of magnetic field structure suggests that final helix with projected split

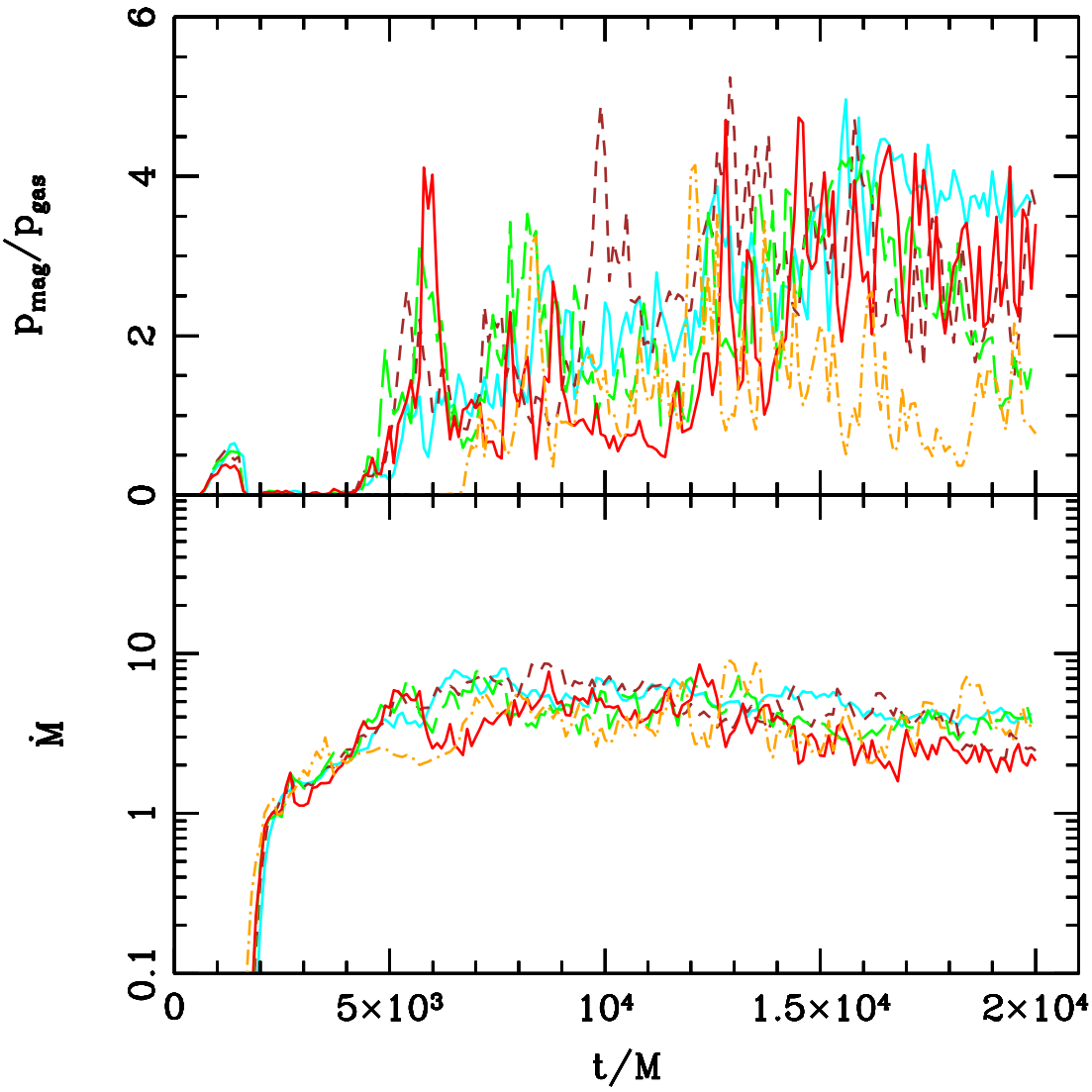

Figure 6.3.— Accretion rate and height- and $\phi-$averaged β versus time at the event horizon for all five models: $a_* = 0$ (dotted black), $a_* = 0.5$ (solid red), $a_* = 0.7$ (long-dashed green), $a_* = 0.9$ (short-dashed brown), and $a_* = 0.98$ (dot-dashed orange).

monopole is a universal configuration for any vertical flux being dragged into the black hole. The magnetic field structure of a single snapshot (panel (a)) looks quite similar to the structure of the linear average between $14000M$ and $20000M$ (panel (b)). The polar region of the flow has the strongest magnetic field.

6.4 Averaged Dynamical Model

We now discuss the link between the numerical simulations and the averaged dynamical model. We need to decide on the averaging, especially of the magnetic field, extend the simulations to large radii, and define the electron temperature.

6.4.1 Averaging

We need the time-averaged dynamical model for the purpose of analyzing the whole model parameter space of spin a_*, inclination angle θ, accretion rate $\dot{M}$, and ratio of proton to electron temperatures T_p/T_e computed at $6M$. As we will show later, it is not computationally viable to surf this parameter space, so instead average fluxes are computed over the series of simulation snapshots. The average model incorporates temporal averages at each point in the space of number density n, velocity u^α, and internal energy density u_g. There is no unique approach to averaging the magnetic field $\mathbf{b}$, the results may depend on the approach employed. We choose one reasonable prescription and test the resultant steady-state dynamical model.

For averaging $\mathbf{b}$ is computed at each point and at each time in the instantaneous comoving locally flat reference frame. The magnetic field randomly changes orientation in the midplane with time due to turbulence. So, the linear time average would underestimate

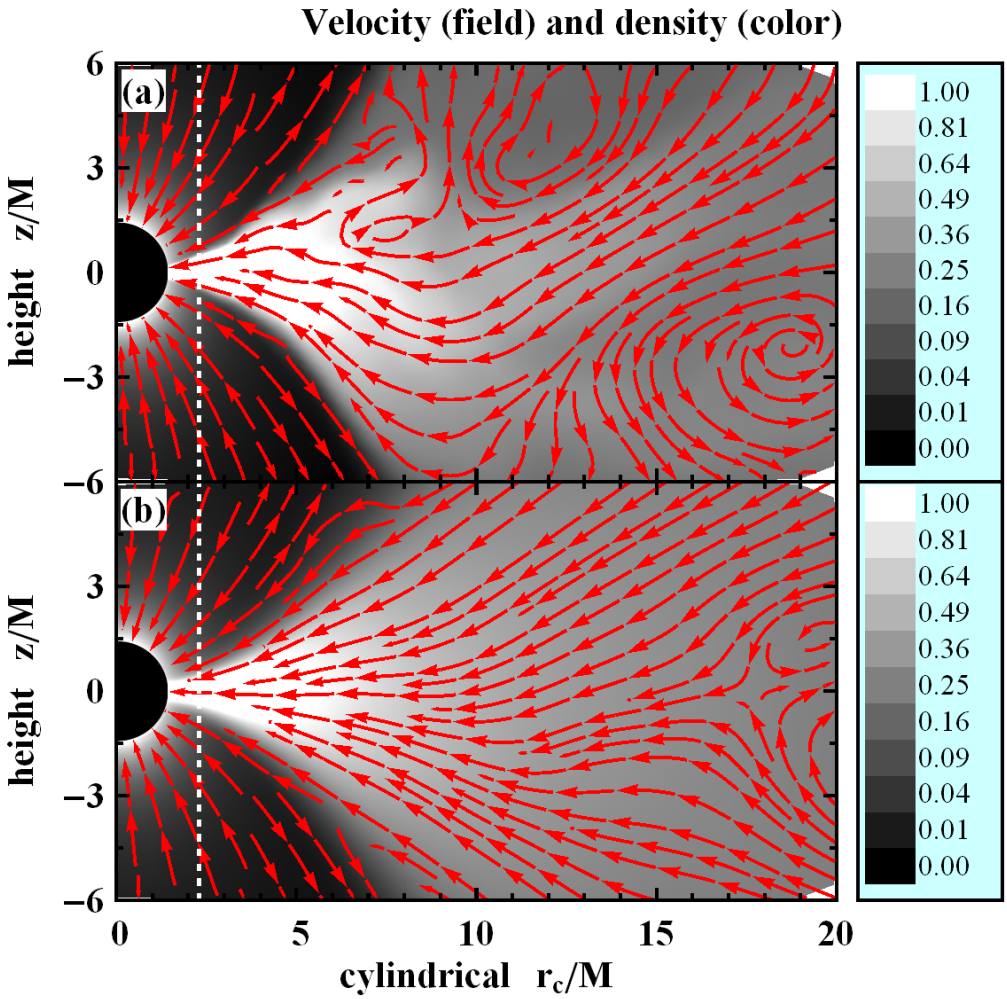

Figure 6.4.— Stream lines of velocity (red vectors) and number density n_e (greyscale map) for spin $a_* = 0.9$ at $\phi = 0$ in the meridional plane: single timeshot at $t = 14000M$ on the upper (a) panel and time average between $t = 14000M$ and $t = 20000M$ on the lower (b) panel. The correspondent calibration bars of n_e are shown on the right. Number density is normalized by its maximum value.

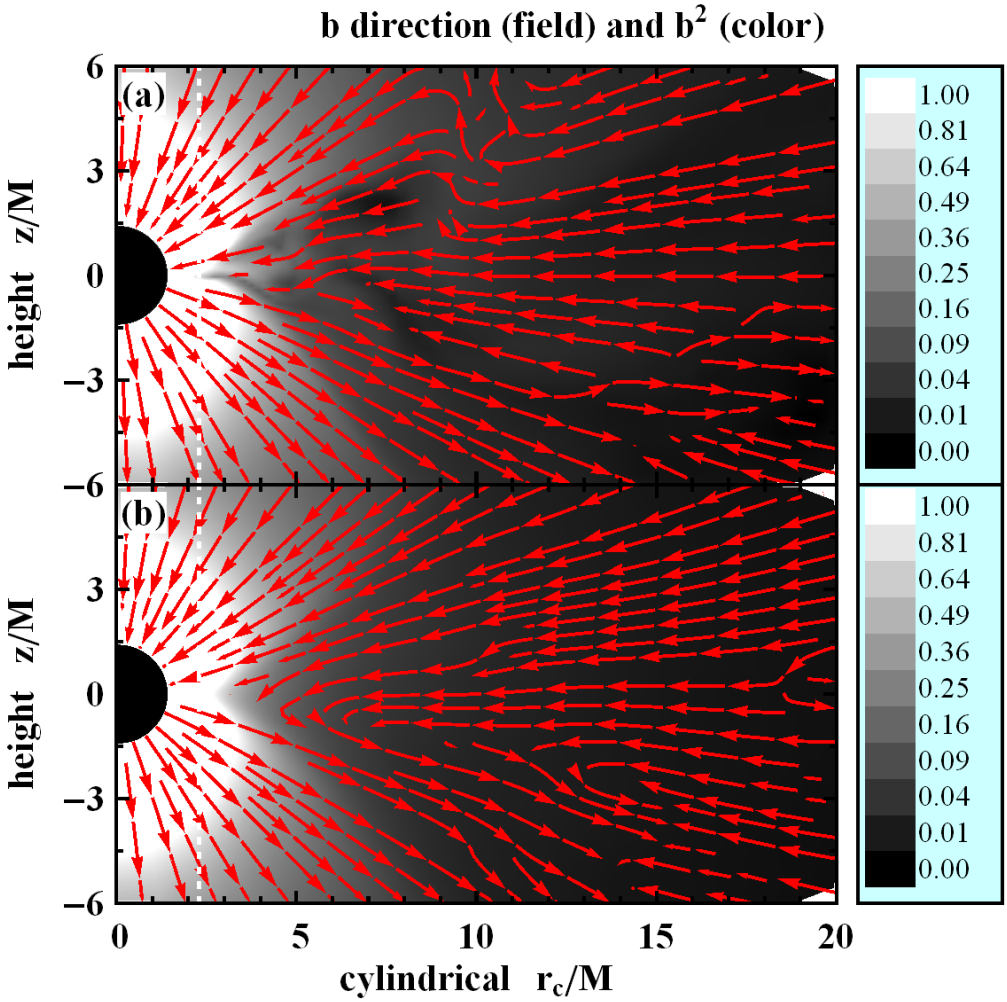

Figure 6.5.— Magnetic field lines (red vectors) and comoving electromagnetic energy density $\propto b^2$ (greyscale map) for spin $a_* = 0.9$ at $\phi = 0$ in the meridional plane (r_c as cylindrical radius): single timeshot at $t = 14000M$ on the upper (a) panel and time average between $t = 14000M$ and $t = 20000M$ on the lower (b) panel. The correspondent calibration bars of comoving b^2 are shown on the right. Magnetic field energy density is normalized by its maximum value.

the magnetic field and would not be independent of averaging period. It is more viable to modify the linear averaged $\mathbf{b}$ at each point by the value of $f = \sqrt{<\mathbf{b}^2>_t / <\mathbf{b}>_t^2}$ computed at that point. Then the dynamical model has an increased field $\mathbf{b}_{RMS} = f <\mathbf{b}>_t$ with a strength typical for a single snapshot, but likely more uniform in direction than $\mathbf{b}$ in a single snapshot. We call the latter the RMS-field model. We run radiative transfer on the top of each set of dynamical models the RMS-field averaging. To estimate the effect of using the RMS-field model, we compute radiative transfer also for the models with linear-averaged $\mathbf{b}$-field. Averaging is done over 200 snapshots during the steady state period between $t = 14000M$ and $t = 20000M$. A detailed comparison of how different averaging methods affect the polarized radiative transfer will be presented in a follow-up paper.

6.4.2 Extension to Large Radii

The flow is evolved in a quasi-steady state for $6000M$ from $14000M$ until $20000M$, which corresponds to 8 orbits at $r = 25M$. The flow is not sufficiently settled at larger radii, however, some Faraday rotation might happen and some emission might occur outside $25M$. Thus, we extend the dynamical model to larger radii $r > 25M$ in a reasonable way and check in Appendix 6.9 how much the various extensions change the results of radiative transfer. The boundary of radiative transfer is situated at $r = 20000M$. The profiles of number density n_e, internal energy density u_g, magnetic field $\mathbf{b}$ and velocity $\mathbf{v}$ are extended as power-laws until radius $r = 20000M$. The relevant power-law β is obtained for number density by matching the known value $n_e = 130\mathrm{cm}^{-3}$ at about $1.5'' \approx 3 \cdot 10^5 M$ (Baganoff et al., 2003) and the average $n_{e,\mathrm{cut}}$ value at $r = 25M$ in the equatorial plane for each model. The value of β may be different for different models. The radial flow velocity

v_r is then obtained from the continuity relation in the equatorial plane $n_e v_r r^2 = \text{const}$. The power-law of internal energy density u_g is obtained in a similar way by matching the values $T_e = T_p = 1.5 \cdot 10^7$ K and $n_e = 130\text{cm}^{-3}$ at $3 \cdot 10^5 M$ (Baganoff et al., 2003; Shcherbakov & Baganoff, 2010). The extensions of other flow velocities and magnetic field are fixed in turn. The meridional physical velocity is extended as $v_{\hat{\theta}} \propto (r/M)^{-3/2}$, toroidal as $v_{\hat{\phi}} \propto (r/M)^{-1/2}$, where the relationship $v_{\hat{i}} \approx u^i \sqrt{g_{ii}}$ is used to connect the 4-velocity components with physical velocity components. All components of comoving magnetic field are extended as $b_r, b_\theta, b_\phi \propto (r/M)^{-3/2}$. This power-law slope is similar to the one observed in the simulations between $15M$ and $25M$. However, this choice will likely underestimate the magnetic field at large radii, since the slope is shallower for equipartition assumption $b \propto \sqrt{nT_p} \propto (r/M)^{-1}$ for $n \propto (r/M)^{-1}$. Exploration of various extensions of the magnetic field will be the topic of future studies.

After defining the extension power-laws for quantities in the equatorial plane, we extend the quantities radially at arbitrary θ and ϕ in a continuous way. For example, for density at arbitrary θ and ϕ and $r > 25M$ we have

$$n_e(r, \theta, \phi) = n_e(25M, \theta, \phi) \left(\frac{r}{25M} \right)^{-\beta}, \tag{6.11}$$

where $n_e(25M, \theta, \phi)$ is taken from the simulation. We similarly extend other quantities. As we will show in Appendix 6.9, reasonable variations in power-law indices bear minimum influence on radiation intensities, linear and circular polarization fluxes.

6.4.3 Electron Temperature

Neither the proton T_p nor electron T_e temperatures are given directly by the simulation. However, it is crucial to know the electron temperature T_e to determine

the emission. Our solution is to split the total internal energy density u_g, given by the simulation and power-law extension, between the proton energy and the electron energy. The energy balance states

$$\frac{u_g}{\rho} \equiv \frac{u_{p,g} + u_{e,g}}{\rho} = c_p k_B T_p + c_e k_B T_e, \tag{6.12}$$

where $c_p = 3/2$ and $c_e \geq 3/2$ are the respective heat capacities, ρ is the rest-mass density, and k_B is Boltzmann's constant. The difference of temperatures $T_p - T_e$ is influenced by three effects: equilibration by Coulomb collisions at large radii, the difference in heating rates f_p and f_e of protons and electrons operating at intermediate radii, and the difference in heat capacities operating close to the BH. The effect of radiative cooling is excluded from the list, since, according to Sharma et al. (2007a), the radiative efficiency of the flow is negligible for realistic $\dot{M} \lesssim 10^{-7} M_\odot \mathrm{year}^{-1}$. The aforementioned important effects can be incorporated into an equation as

$$\begin{aligned} v_r \frac{d(T_p - T_e)}{dr} &= -\nu_c (T_p - T_e) + \\ &+ \left(\frac{1}{c_p} \frac{f_p}{f_p + f_e} - \frac{1}{c'_e} \frac{f_e}{f_p + f_e} \right) v_r \frac{d(u_g/\rho)}{k_B dr}, \end{aligned} \tag{6.13}$$

where

$$\nu_c = 8.9 \cdot 10^{-11} \left(\frac{T_e}{3 \cdot 10^{10}} \right)^{-3/2} \frac{n_e}{10^7} \tag{6.14}$$

is the non-relativistic temperature equilibration rate by collisions (Shkarofsky et al., 1966), all quantities being measured in CGS units. We consider protons to always have non-relativistic heat capacity and collisions to always obey the non-relativistic formula. The magnitudes of errors introduced by these simplification are negligible. The exact expressions for total electron heat capacity and differential heat capacity are approximated as

$$c_e = \frac{u_{e,g}/\rho}{k_B T_e} \approx \frac{3}{2} \frac{0.7 + 2\theta_e}{0.7 + \theta_e}, \tag{6.15}$$

$$c_e' = \frac{d(u_{e,g}/\rho)}{k_B dT_e} \approx 3 - \frac{0.735}{(0.7+\theta_e)^2} \tag{6.16}$$

correspondingly with the error $< 1.3\%$, where

$$\theta_e = \frac{k_B T_e}{m_e c^2} \tag{6.17}$$

is the dimensionless electron temperature. It was recently shown (Sharma et al., 2007a) that the ratio of heating rates in the non-relativistic regime in a disk can be approximated as

$$\frac{f_e}{f_p} = C\sqrt{\frac{T_e}{T_p}} \tag{6.18}$$

with a constant C. This formula is adopted in the relativistic regime as well, since no better prescription is available. Sharma et al. (2007a) found the value $C = 0.33$ in simulations, whereas we find $C = 0.40 - 0.45$ for the best-fitting models (see § 6.7). The proton and electron temperatures are determined at each point in the following way. We first take an averaged model (see Subsection 6.4.2) of a simulation with spin a_* extended to $r = 20000M$. Then we compute azimuthal averages of radial velocity v_r, number density n_e, and u_g/ρ at the equatorial plane, extend them as power laws to $r_{\rm out} = 3 \cdot 10^5 M$, and solve the equations (6.12,6.13) from $r_{\rm out}$ down to the inner grid cell point. Temperatures are set to $T_e = T_p = 1.5 \cdot 10^7$ K at $r_{\rm out}$ (Baganoff et al., 2003; Shcherbakov & Baganoff, 2010). On the next step we make a correspondence of the values of u_g/ρ to the calculated T_e and T_p and define functional dependence $T_e = T_e(u_g/\rho)$ and $T_p = T_p(u_g/\rho)$. At each point of the simulation (including off the equator), we draw temperatures from this correspondence. Typical profiles of proton and electron temperatures are shown on Figure 6.6. Temperatures stay equal until $\sim 10^4 M$ due to collisions despite different heating prescriptions. Within $3 \cdot 10^3 M$ the timescale of collisional equilibration becomes relatively long and electrons become relativistic, thus T_e drops down below T_p. We take

the inner part within $r < 20000M$ of the electron and proton temperature profiles to conduct the radiative transfer.

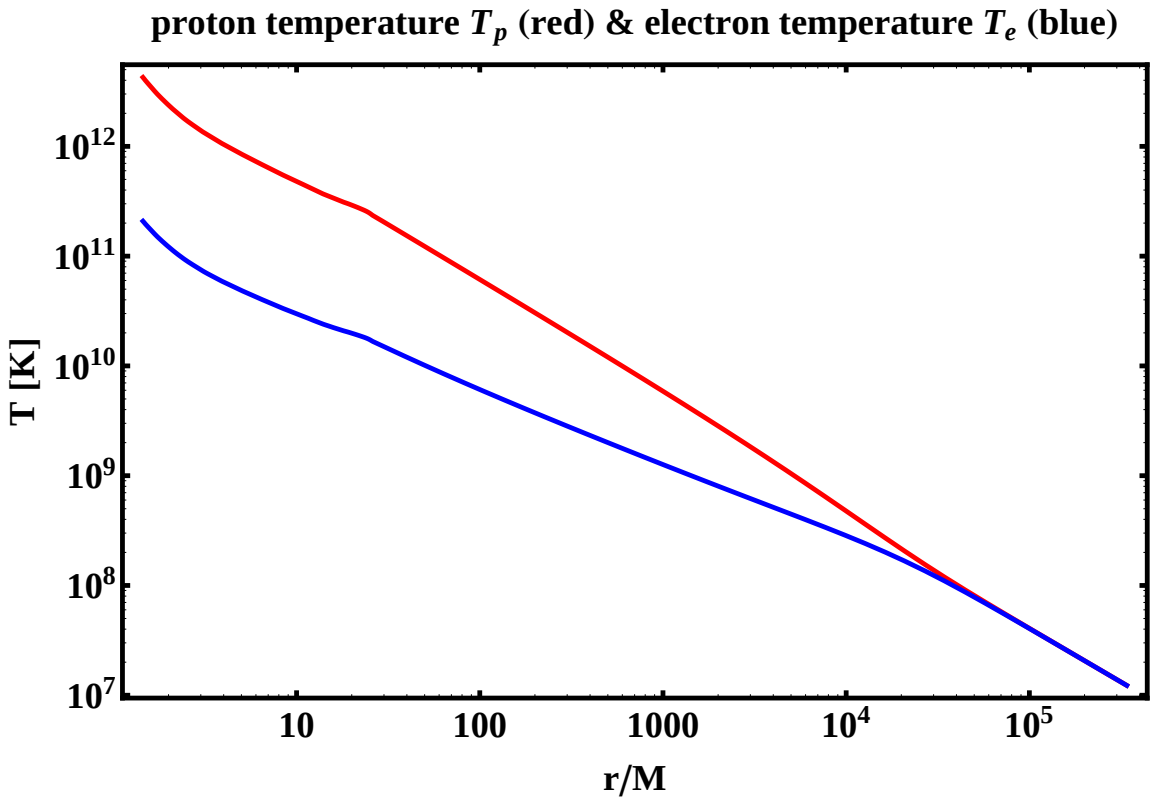

Figure 6.6.— Temperatures of protons T_p (upper red line) and electrons T_e (lower blue line) as functions of radius for heating parameter $C = 0.414$ and accretion rate $\dot{M} = 1.04 \times 10^{-8} M_{\odot}\text{year}^{-1}$, which leads to $T_p/T_e = 17.6$ and $T_e = 4.2 \cdot 10^{10}$ K at $r = 6M$. The dynamic RMS-field model with this heating prescription, this accretion rate, and spin $a_* = 0.9$ provides the fit with the lowest χ^2 to polarization observations (see § 6.7).

For a given accretion rate there exists a unique dependence of the ratio of temperatures T_p/T_e at $6M$ on the heating constant C. Thus, we interchangeably refer to the ratio of temperatures T_p/T_e at $6M$ or the correspondent heating constant C. We commonly use

the ratio of temperatures as a more straightforward quantity.

6.5 General Relativistic Polarized Radiative Transfer

General relativistic polarized radiative transfer is an essential tool for converting the dynamical model of an accretion flow into a set of observable quantities (Broderick et al., 2009a; Gammie & Leung, 2010; Shcherbakov & Huang, 2011). We closely follow Shcherbakov & Huang (2011) for the transfer technique. Similarly to Huang et al. (2009a), we define the polarized basis in the picture plane, where one vector points North, another vector points East, and the wavevector points towards the observer. We parallel transport this basis in the direction of the black hole and do the radiative transfer along the ray in the opposite direction. At each point along the ray we go to the locally-flat comoving frame, calculate the angles between the magnetic field and basis vectors, and compute the Faraday conversion, Faraday rotation, emissivities, and absorptivities. This approach appears no harder computationally compared to the covariant calculation of angles without the locally flat comoving frame (Broderick et al., 2009a; Huang et al., 2009a).

Only our calculations of plasma response is different from Shcherbakov & Huang (2011). That paper offered a way to find exact emissivities, absorptivities, Faraday rotation, and conversion coefficients for thermal and other isotropic particle distributions. Here, for simplicity, we employ fitting formulas for Faraday rotation and Faraday conversion and synchrotron approximation for emissivities in thermal plasma. We define

$$X = \frac{2}{3}\frac{\nu}{\nu_B \gamma^2 \sin\theta_B}, \tag{6.19}$$

where θ_B is **k**-**b** angle, γ is electron gamma factor, and $\nu_B = eb/(2\pi m_e c)$ is the cyclotron frequency. Then following Legg & Westfold (1968); Melrose (1971), we write down

emissivities in I, Q, and V modes as

$$\begin{aligned}
\varepsilon_I &= \frac{\sqrt{3}}{2}\frac{e^2}{c}\nu_B \sin\theta_B \int_1^{+\infty} d\gamma N(\gamma) X \int_X^{+\infty} dz K_{5/3}(z), \\
\varepsilon_Q &= \frac{\sqrt{3}}{2}\frac{e^2}{c}\nu_B \sin\theta_B \int_1^{+\infty} d\gamma N(\gamma) X K_{2/3}(X), \\
\varepsilon_V &= \frac{2}{\sqrt{3}}\frac{e^2}{c}\nu_B \cos\theta_B \int_1^{+\infty} d\gamma \frac{N(\gamma)}{\gamma} \times \\
&\times \left[X K_{1/3}(X) + \int_X^{+\infty} dz K_{1/3}(z) \right].
\end{aligned} \tag{6.20}$$

Here $K_z(x)$ is the Bessel function of the 2nd kind of order z. We employed IEEE/IAU definitions of Stokes Q, U, and V (Hamaker & Bregman, 1996), also chosen in Shcherbakov & Huang (2011): counter-clockwise rotation of electric field as seen by the observer corresponds to positive $V > 0$. Under this definition the sign of V emissivity (6.20) is opposite that in standard theoretical textbooks (Rybicki & Lightman, 1979). A variation of emissivity formulas (6.19,6.20) exists: Sazonov (1969); Pacholczyk (1970) effectively define $X = 2\nu/(3\nu_B(\gamma-1)^2 \sin\theta_B)$, integrating over particle energy instead of γ. This approximation appears to give significantly larger errors at low particle energies.

Next, one needs to specify, which particle distribution $N(\gamma)$ to use. Various $N(\gamma)$ correspond to several synchrotron approximations for thermal plasmas. The ultrarelativistic approximation (Pacholczyk, 1970; Huang et al., 2009a) with $N(\gamma) = \exp(-(\gamma-1)/\theta_e)(\gamma-1)^2/2/\theta_e^3$ gives the simplest distribution. However, the exact thermal distribution of particles

$$N(\gamma) = \gamma\sqrt{\gamma^2-1}\frac{\exp(-\gamma/\theta_e)}{\theta_e K_2(\theta_e^{-1})} \tag{6.21}$$

allows for more precise computation of radiation. Synchrotron emissivities based on the equations (6.19,6.20) with the exact thermal distribution (6.21) agree with the exact cyclo-synchrotron emissivities ε_I, ε_Q, and ε_V (Leung et al., 2009; Shcherbakov & Huang,

2011) to within 2% for typical dynamical models and frequencies > 100 GHz. Emissivities integrated over the ultrarelativistic thermal distribution normally have $\sim 10\%$ error.

Thermal absorptivities are found from emissivities (6.20) via Kirchhoff's law

$$\alpha_{I,Q,V} = \varepsilon_{I,Q,V}/B_\nu, \tag{6.22}$$

where $B_\nu = 2k_B T_e \nu^2/c^2$ is the source function for low photon energies $h\nu \ll k_B T_e$. Faraday rotation ρ_V and Faraday conversion ρ_Q coefficients are taken from Shcherbakov (2008b):

$$\begin{aligned} \rho_V &= g(Z)\frac{2n_e e^2 \nu_B}{m_e c \nu^2}\frac{K_0(\theta_e^{-1})}{K_2(\theta_e^{-1})}\cos\theta, \\ \rho_Q &= f(Z)\frac{n_e e^2 \nu_B^2}{m_e c \nu^3}\left[\frac{K_1(\theta_e^{-1})}{K_2(\theta_e^{-1})} + 6\theta_e\right]\sin^2\theta. \end{aligned} \tag{6.23}$$

Here

$$Z = \theta_e \sqrt{\sqrt{2}\sin\theta\left(10^3\frac{\nu_B}{\nu}\right)} \tag{6.24}$$

and

$$\begin{aligned} g(Z) &= 1 - 0.11\ln(1 + 0.035Z), \\ f(Z) &= 2.011\exp\left(-\frac{Z^{1.035}}{4.7}\right) - \\ &- \cos\left(\frac{Z}{2}\right)\exp\left(-\frac{Z^{1.2}}{2.73}\right) - 0.011\exp\left(-\frac{Z}{47.2}\right) \end{aligned} \tag{6.25}$$

are the fitting formulas for deviations of ρ_V and ρ_Q from analytic results for finite ratios ν_B/ν. The deviation of $f(Z)$ from 1 is significant for the set of observed frequencies ν, temperatures θ_e, and magnetic fields found in the typical models of Sgr A*. These formulas constitute a good fit to the exact result for the typical parameters of the dynamical model (Shcherbakov, 2008b).

With all the sophisticated physics incorporated into the radiative transfer, the speed of the numerical code becomes an essential constraint. Polarized radiative transfer can

take much longer to perform compared to non-polarized radiative transfer when using an explicit integration scheme to evolve the Stokes occupation numbers N_Q, N_U, and N_V. Large Faraday rotation measure and Faraday conversion measure lead to oscillations between occupation numbers. One of the solutions is to use an implicit integration scheme, while another solution is to perform a substitution of variables. In the simple case of Faraday rotation leading to interchange of N_Q and N_U, the obvious choice of variables is the amplitude of oscillations and the phase. Thus the cylindrical polarized coordinates arise

$$\begin{aligned} N_Q &= N_{QU}\cos\phi, \\ N_U &= N_{QU}\sin\phi. \end{aligned} \tag{6.26}$$

Then the amplitude N_{QU} slowly changes along the ray and the angle ϕ changes linearly, which gives an improvement in speed. In the presence of substantial Faraday conversion, the polarization vector precesses along some axis in Poincaré sphere, adding an interchange of circularly and linearly polarized light. Polar polarized coordinates would be more suitable in this case:

$$\begin{aligned} N_Q &= N_{\rm pol}\cos\phi\sin\psi, \\ N_U &= N_{\rm pol}\sin\phi\sin\psi, \\ N_V &= N_{\rm pol}\cos\psi, \end{aligned} \tag{6.27}$$

where $N_{\rm pol}$ is the total polarized intensity, the change of ϕ angle is mainly due to Faraday rotation and ψ angle changes owing to Faraday conversion. The application of this technique speeds up the code exponentially at low frequencies $\nu < 100$ GHz.

Besides improving the speed, we perform a number of convergence tests to make sure the final intensities are precisely computed. Radiative transfer involves shooting a uniform

grid of $N \times N$ geodesics from the picture plane. Even though $N = 150$ (Dexter et al., 2009) maybe a better number to use for a single snapshot, $N = 111$ works well for the averaged smooth flow giving an accuracy of $\Delta(\chi^2/\mathrm{dof}) \leq 0.02$ near best-fitting models. The metrics of relative integration error χ^2_H/dof is defined in Appendix 6.9, where the convergence tests are described. The size of the integration domain is taken to be a square in the picture plane with a side

$$a[M] = 16 + 2\left(\frac{600}{\nu[\mathrm{GHz}]}\right)^{1.5} \tag{6.28}$$

in the units of $r_\mathrm{g} \equiv M$, where frequency ν is in GHz. The size based on formula (6.28) is larger than the photon orbit visible diameter $d_\mathrm{ph} \approx 10.4M$ at the same time following the intrinsic size dependence on frequency (Shen et al., 2005; Doeleman et al., 2008) at low frequencies. Justification of this size by convergence tests is given in Appendix 6.9. A surprisingly important radiative transfer parameter is the distance from the BH, where intensity integration starts. The dependence of synchrotron emissivity on temperature and magnetic field strength is so strong that it negates the effect of gravitational redshift close to the BH. The accuracy of $\Delta(\chi^2/\mathrm{dof}) \leq 0.02$ is achieved in sub-mm for computation out from $r_{min} = 1.01r_H$, where $r_H = M(1 + \sqrt{1 - a_*^2})$ is the horizon radius. Higher r_{min} leads to larger error $\Delta(\chi^2/\mathrm{dof}) \sim 0.03$ (see Appendix 6.9).

6.6 Statistical Analysis

Statistical analysis is a necessary tool to compare the model predictions to observations and to discriminate between models. However, it has only recently been applied to the accretion flow in the Galactic Center (Dexter et al., 2009; Broderick et al., 2009a; Shcherbakov & Baganoff, 2010). When the number of model parameters is large (Huang et

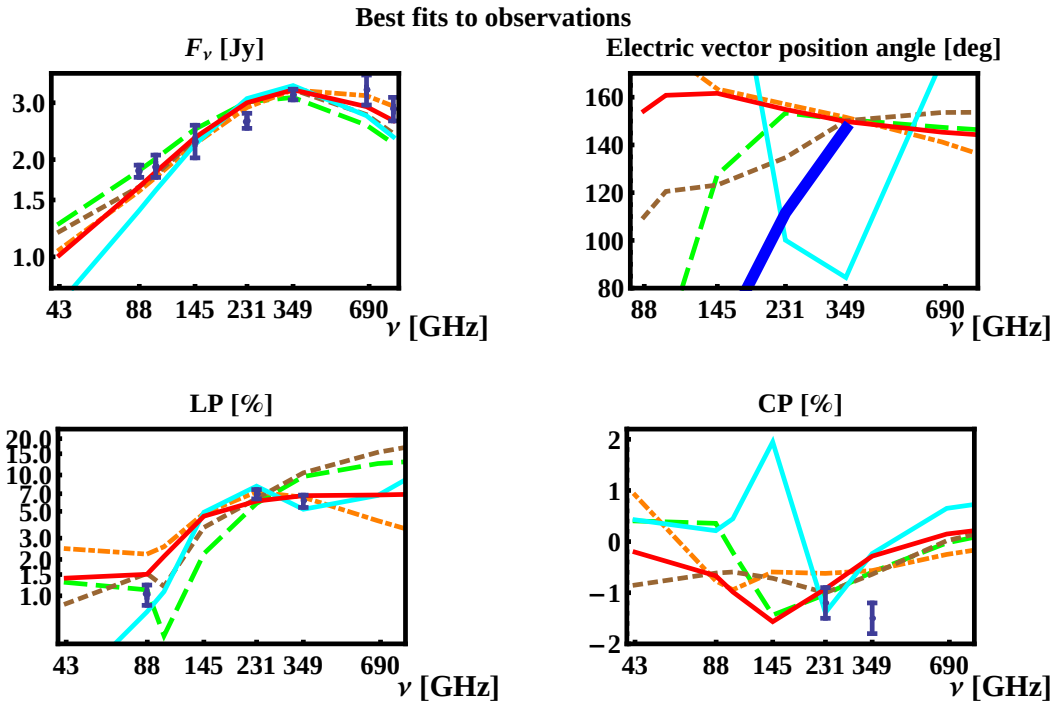

Figure 6.7.— Best fits to the observed fluxes, LP and CP fractions by best RMS-field models for each spin. The inclination angle θ, accretion rate $\dot{M}$, ratio of temperatures T_p/T_e were adjusted for each spin to minimize χ^2. Fits to total flux F are in the upper left panel, LP fraction in the lower left, and CP fraction in the lower right. Best RMS-field model with spin $a_* = 0.9$ (solid dark red) has $\chi^2/\mathrm{dof} = 4.05$, spin $a_* = 0.7$ (long-dashed green) — $\chi^2/\mathrm{dof} = 5.37$, spin $a_* = 0.5$ (short-dashed brown) — $\chi^2/\mathrm{dof} = 5.77$, spin $a_* = 0$ (solid light cyan) — $\chi^2/\mathrm{dof} = 9.03$, spin $a_* = 0.98$ (dot-dashed orange) — $\chi^2/\mathrm{dof} = 4.85$. The upper right panel shows the dependence of EVPA angle on frequency for the best models. Note, that EVPA angles are not included into our χ^2 fitting procedure. The thick blue curve represents observations. Simulated EVPA curves are arbitrarily shifted to approximate EVPA at 349 GHz. The addition of an external (to the emitting region) Faraday rotation screen helps to fit EVPA(349 GHz) − EVPA(230 GHz).

al., 2009a) or the number of considered observations is small (Moscibrodzka et al., 2009), it is possible to find an exact fit to the data or say that for some model parameters the fit does not exist. Instead, we consider a broad range of observations and explore models with only 4 parameters: spin a_*, inclination angle θ, accretion rate $\dot{M}$, ratio of proton to electron temperature T_p/T_e at $6M$.

We have proven in § 6.2 that samples of total fluxes, $\log \mathrm{LP}$ and EVPA at each frequency are consistent with a Gaussian distribution. Thus, we can directly apply χ^2 statistics. We are comparing means of observed variable fluxes to fluxes computed for the averaged simulation models. We leave the comparison of the observed samples to the samples generated over many snapshots to future work. We define χ^2_F for flux fitting as

$$\chi^2_F = \sum_{i=1}^{7} \frac{(F_{i,\mathrm{sim}} - F_{i,\mathrm{obs}})^2}{\sigma(F)^2}, \tag{6.29}$$

for the set of 7 frequencies $\nu = 88, 102, 145, 230, 349, 680$, and 857 GHz, where σ_F are the errors of the means. We add LP fraction at $88, 230$, and 349 GHz and CP fraction at 230 and 349 GHz into the full χ^2 :

$$\begin{aligned} \chi^2 = \chi^2_F \quad &+ \quad \sum_{i=1}^{3} \frac{(\log(\mathrm{LP}_{i,\mathrm{sim}}) - \log(\mathrm{LP}_{i,\mathrm{obs}}))^2}{\sigma(\log(\mathrm{LP}))^2} \\ &+ \quad \sum_{i=1}^{2} \frac{(\mathrm{CP}_{i,\mathrm{sim}} - \mathrm{CP}_{i,\mathrm{obs}})^2}{\sigma(\mathrm{CP})^2}. \end{aligned} \tag{6.30}$$

Then we take the number of degrees of freedom to be $\mathrm{dof}_F = 7 - 3 = 4$ for flux fitting and $\mathrm{dof} = 12 - 3 = 9$ for fitting all polarized data. We compute the probability density $\rho(\chi^2) = \rho(\chi^2 | a_*, \theta, \dot{M}, C)$ of the data, given a model, from the correspondent χ^2 distributions.This is a function of spin, inclination angle, accretion rate, and heating constant. Now the search for minimum χ^2 is fully defined. The probability density of model given data $\rho(a_*, \theta, \dot{M}, C | \chi^2)$ is needed for confidence intervals calculation. It is

found by Bayes' theorem with the use of priors (Broderick et al., 2009a)

$$\rho(a_*, \theta, \dot{M}, C|\chi^2) = \frac{\rho(\chi^2)\pi(\theta)\pi(a_*)\pi(\dot{M})\pi(C)}{\int \rho(\chi^2)\pi(\theta)\pi(a_*)\pi(\dot{M})\pi(C)d\theta da_* d\dot{M} dC}, \tag{6.31}$$

where we assumed a separable prior $\pi(\theta, a_*, \dot{M}, C) = \pi(\theta)\pi(a_*)\pi(\dot{M})\pi(C)$. We expect no preferred spin orientation, which requires a uniform distribution over the solid angle and the prior $\pi(\theta) = \sin\theta$. Following Broderick et al. (2009a) we take a uniform prior on spin $\pi(a_*) = 1$. The accretion rate $\dot{M}$ is largely uncertain. For our analysis we take the logarithmic prior $\pi(\dot{M}) = \dot{M}^{-1}$, which is the best non-informative prior for large range of possible values (Jaynes & Bretthorst, 2003). The value of the heating constant $C = 0.33$ cited by Sharma et al. (2007a) was based on only a small part of total energy dissipation and may be unreliable. A similar prior $\pi(C) = C^{-1}$ can be taken for the heating constant. The expectation value of any quantity Q at certain spin a_* is calculated as the integral

$$\langle Q_{a_*} \rangle = \int\int\int Q\rho(a_*, \theta, \dot{M}, C|\chi^2) \sin\theta d\theta \frac{dC}{C} \frac{d\dot{M}}{\dot{M}}, \tag{6.32}$$

and the confidence intervals are found analogously.

We explore the values of C from 0.20 to 0.75, which leads to T_p/T_e at $6M$ between 6 and 60. All models fitting F_ν SED with $C = 0.20$ underpredict the linear polarization and all models with $C = 0.75$ overpredict the linear polarization, thus we cover all good models by using a wide range of C. A full analysis in the space of accretion rate $\dot{M}$ is not possible due to limited computational resources. Instead, for each spin a_*, heating constant C, and inclination θ we find the best χ^2_F for the values of flux F_ν (see eq.6.29) and explore the region close to the best fit. As the dependence of flux on accretion rate is uniform, this guarantees that we explore all regions with good full χ^2 defined by equation (6.30). Even if there is some good fit to LP and CP curves, but the flux values are either overpredicted or underpredicted, then the total χ^2/dof would be substantially larger than unity.

6.7 Results

In previous sections we described observations, numerical simulations of the dynamical structure, averaged model, polarized radiative transfer, and statistical methods to compare the simulated spectra with the observations. Now we are ready to present the results of such a comparison, done for the first time for GR polarized radiative transfer over the model derived from 3D GRMHD simulations. We are able to achieve $\chi^2/\mathrm{dof} \sim 4$ fits to observations and constrain some model parameters.

Figure 6.7 shows best fits to observations by RMS-field (RMS magnetic field strength, mean direction) models with five different spins. Inclination angle θ, accretion rate $\dot{M}$, heating constant C were adjusted to reach the lowest χ^2. The best RMS-field model with spin $a_* = 0.9$ (solid dark red) has $\chi^2/\mathrm{dof} = 4.05$, spin $a_* = 0.7$ (long-dashed green) — $\chi^2/\mathrm{dof} = 5.37$, spin $a_* = 0.5$ (short-dashed brown) — $\chi^2/\mathrm{dof} = 5.77$, spin $a_* = 0$ (solid light cyan) — $\chi^2/\mathrm{dof} = 9.03$, spin $a_* = 0.98$ (dot-dashed orange) — $\chi^2/\mathrm{dof} = 4.85$. Let us discuss how well the models with different spins perform. Fits to fluxes F_ν on upper left are not substantially different, though models with higher spins perform better at both low and high frequencies. Larger deviations can be seen on LP (lower left) and CP (lower right) plots. Models with high spins require lower accretion rate/density to fit the flux spectrum. Then they are not subject to Faraday depolarization, which leads to decrease of LP at low ν, and the models end up having larger linear polarization fractions at 88 GHz. Not all models reproduce the observed decrease of mean LP fraction between 231 GHz and 349 GHz groups. The discrepancies in fitting CP fraction are also large: no low$-\chi^2$ model can reproduce CP $= -1.5\%$ at 349 GHz: best RMS-field models have $|\mathrm{CP}| < 1\%$ at this frequency. However, only low spin solutions reproduce

the correct sign and the order of magnitude of difference between EVPA(349 GHz) and EVPA(230 GHz), whereas the models with higher spin have shallower difference of the opposite sign EVPA(349 GHz) − EVPA(230 GHz) < 0.

The best RMS-field model with spin $a_* = 0.9$ has inclination angle $\theta = 52°$, position angle PA $= 121° \pm 20°$, accretion rate $\dot{M} = 1.04 \times 10^{-8} M_\odot \mathrm{year}^{-1}$, ratio of temperatures $T_p/T_e = 17.6$ at $6M$, which gives $T_e = 4.2 \cdot 10^{10}$ K at that distance from the center in equatorial plane. In turn, spin $a_* = 0.9$ model with linear-averaged $\mathbf{b}$ reaches minimum $\chi^2/\mathrm{dof} = 5.56$ at $\theta = 55°$, $\dot{M} = 1.5 \times 10^{-8} M_\odot \mathrm{year}^{-1}$, $T_e = 3.0 \cdot 10^{10}$ K at $6M$. Thus, the best linear-averaged model with same spin $a_* = 0.9$ has 1.5 times larger accretion rate compared to RMS-field model, but also has 1.4 times lower electron temperature. The best RMS-field model is more edge-on.

Let us now separate the physical effects responsible for the observed polarized quantities. Several comparably strong radiative transfer effects may account for observed polarized fluxes. Let us consider the production of circular polarization in the flow. Figure 6.8 shows the consequences of switching various physical effects off for the best-fitting RMS-field model with spin $a_* = 0.9$. The solid curve is the result with all physics on. The long-dashed line below is produced, when circular emissivity is set to $\varepsilon_V = 0$. The short-dashed line corresponds to zero Faraday conversion ($\rho_Q = 0$). The changes for the emissivity switched off are small, whereas setting Faraday conversion to zero leads to several times smaller CP of different sign, thus most of CP in this model is produced by Faraday conversion. It would be incorrect, however, to think that the simple linear to circular conversion explains the observed CP. The dot-dashed line in Figure 6.8 shows the CP fraction, when Faraday rotation is switched off ($\rho_V = 0$). The effect of Faraday rotation is insignificant at $\nu < 150$ GHz, but the rotation of the plane of

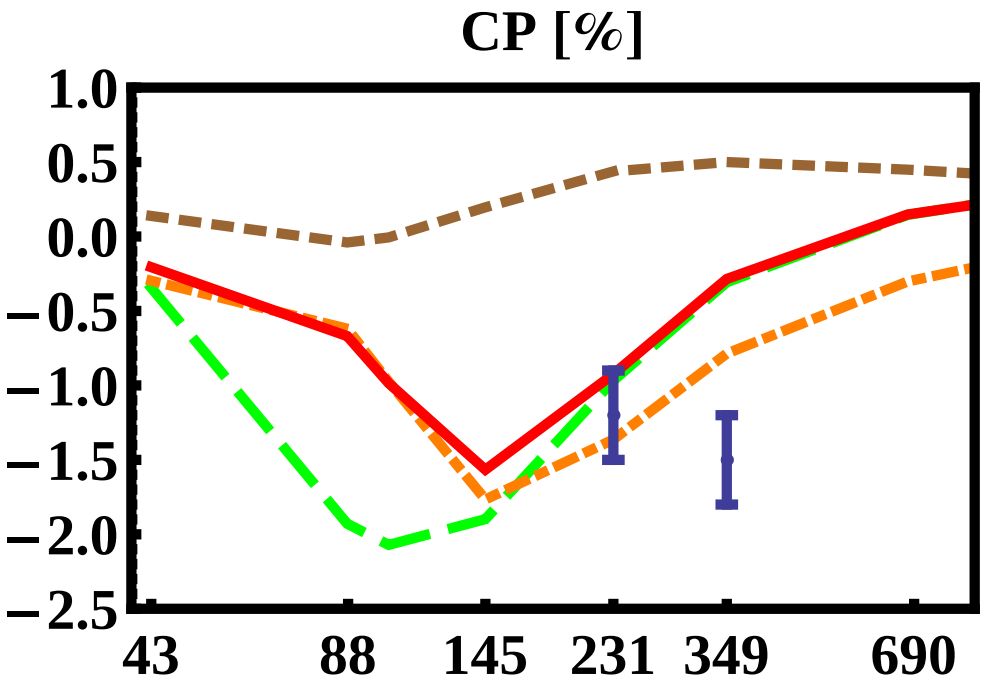

Figure 6.8.— Contributions of different effects to CP fraction dependence on frequency for best-fitting $a_* = 0.9$ model. Shown are observations (blue error bars), the best fit model (solid red line), the same dynamical model computed with zero V emissivity $\varepsilon_V = 0$ in radiative transfer so that CP is produced by Faraday conversion (long-dashed green), the same model with zero Faraday conversion $\rho_Q = 0$ (short-dashed brown), and the same model without Faraday rotation $\rho_V = 0$ (dot-dashed orange). Emissivity in circular V mode contributes little to the observed CP. Surprisingly, CP does not change sign as a function of frequency. The combined action of Faraday rotation and Faraday conversion takes places around $\nu = 145$ GHz, the sign of V changes without Faraday rotation at that frequency.

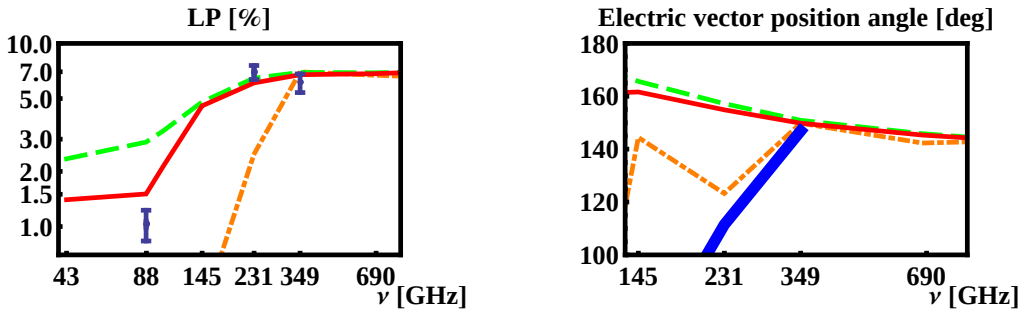

Figure 6.9.— Contributions of different effects to LP fraction (on the left) and EVPA angle (on the right) dependencies on frequency for the best-fitting RMS-field $a_* = 0.9$ model. Shown are observations (blue error bars and thick blue line), the best fit model (solid red line), the same dynamical model computed without Faraday rotation $\rho_V = 0$ in radiative transfer (long-dashed green), and the same dynamical model with 10 times stronger Faraday rotation $\rho'_V = 10\rho_V$. Beam depolarization is weak without Faraday rotation and LP stays high at low frequencies. The change of the EVPA due to Faraday rotation is comparable to the difference of intrinsic emission on EVPA, but has the opposite sign. The best-fitting model with spin $a_* = 0.9$ has about 10 times lower than observed Faraday rotation.

linear polarization simultaneous with conversion between linear and circular polarizations produces a unique effect at higher ν. This is the so-called "rotation-induced conversion" (Homan et al., 2009). The expected sign oscillations of V with frequency do not happen, whether or not Faraday rotation is involved. The best spin $a_* = 0.9$ model exhibits qualitatively similar variations in CP.

On Figure 6.9 we illustrate the influence of Faraday rotation on LP fraction (left panel) and EVPA angle (right panel). The solid curves have all physics on for the best RMS-field model with spin $a_* = 0.9$. The dashed lines are computed for switched off Faraday rotation ($\rho_V = 0$). The Faraday rotation is negligible at high frequencies and curves coincide at $\nu > 400$ GHz. As the rotation of polarization plane is much stronger at low ν, a significant phase shift accumulates between different rays at the low end of the spectrum and cancellations of LP become strong at $\nu < 150$ GHz. Thus we illustrate the effect of Faraday depolarization (Bower et al., 1999a). In the absence of Faraday rotation the dependence of EVPA on frequency is not a constant line: the variations of intrinsic emitted EVPA are significant. Thus, the change of EVPA with ν should not always be ascribed to the effect of Faraday rotation. The positive observed slope of EVPA with ν, acquired due to negative Faraday rotation ρ_V, is comparable to the slope of intrinsic emitted EVPA. The dot-dashed lines correspond to the model, where Faraday rotation is artificially increased 10 times. The model is able to fit EVPA curve, but suffers substantial beam depolarization and underpredicts LP at low frequencies.

Besides computing the best fit models, we examine regions of parameter space near those best fits in search for anomalies. For example, if there is a coincidental cancellation in one of the models, then the close-by models have much higher χ^2/dof and such a best fit may be unreliable as it is accidental. On the Figure 6.10 we plot contours of χ^2/dof

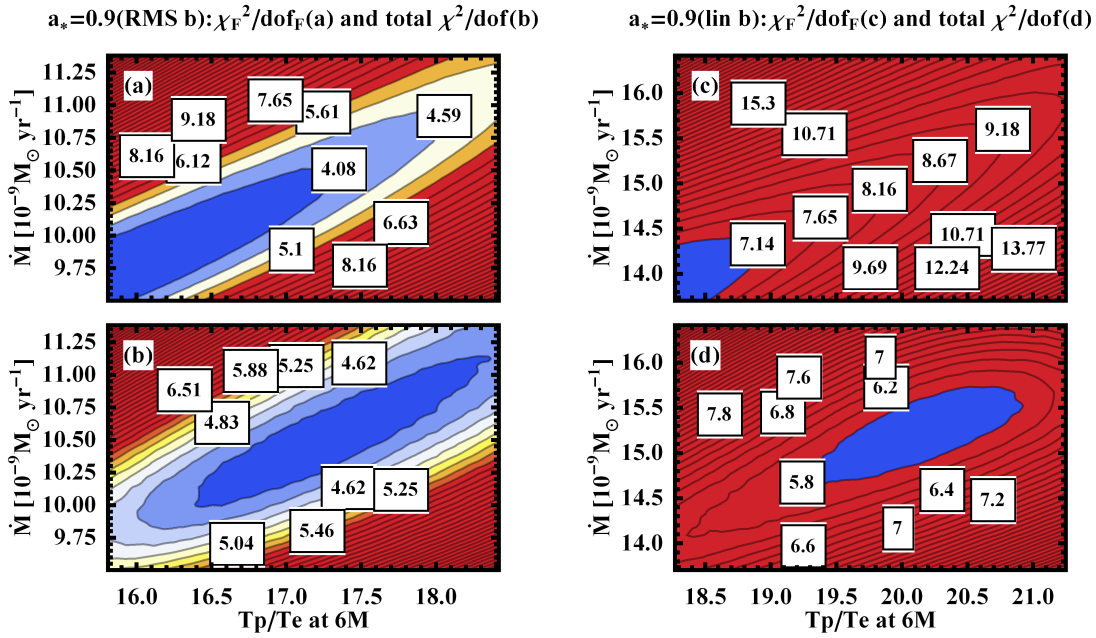

Figure 6.10.— Behavior of χ^2 near the best-fitting models with spin $a_* = 0.9$: RMS-field model with RMS-strength magnetic field **b** (left column) and model with linear averaged **b** (right column) with changing accretion rate $\dot{M}$ and ratio of temperatures T_p/T_e at $6M$. Contours of χ^2_F/dof_F for flux fitting are in the upper row, contours for full χ^2/dof are in the lower row.

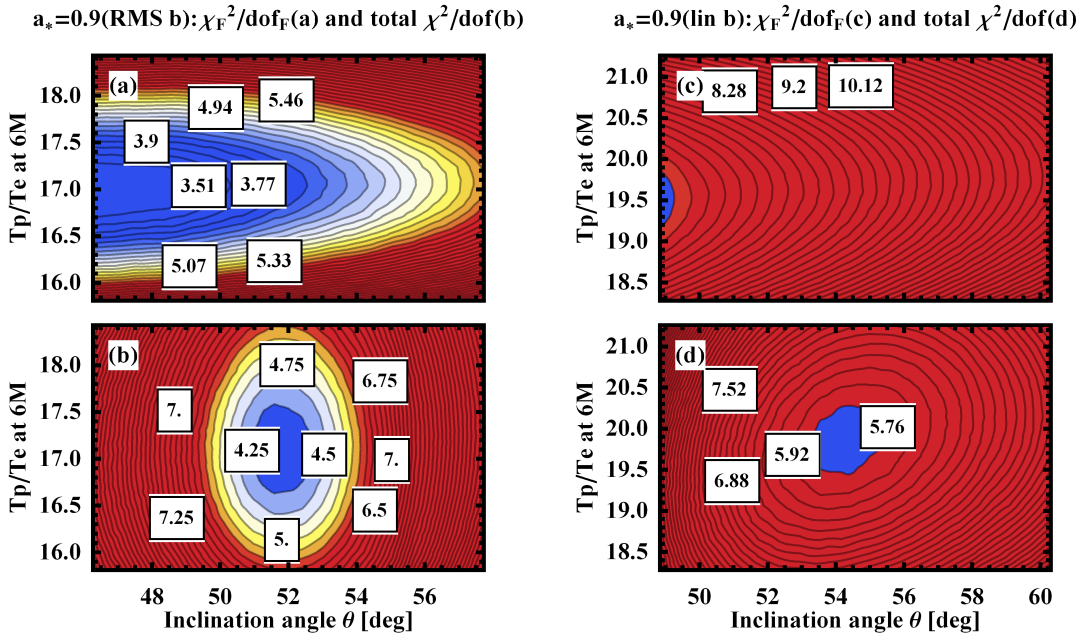

Figure 6.11.— Behavior of χ^2 near the best-fitting models with spin $a_* = 0.9$: RMS-field model with RMS magnetic field **b** (left column) and a model with linear averaged **b** (right column) with changing ratio of temperatures T_p/T_e at $6M$ and inclination angle of BH spin θ. Contours of χ^2_F/dof_F for flux fitting are in the upper row, contours for full χ^2/dof are in the lower row.

near best-fitting RMS-field model with spin $a_* = 0.9$ (left column) and linear-averaged spin $a_* = 0.9$ model (right column) in the space of ratio of temperatures T_p/T_e at $6M$ and accretion rate $\dot{M}$. The contours of χ^2/dof are color-coded from highest (red) to lowest (blue) values. The upper row shows χ^2_F/dof_F for flux F_ν fitting, whereas the lower row shows the full χ^2/dof. Plots of χ^2_F/dof_F (panels (a) and (c)) reveal significant degeneracy between the electron temperature and accretion rate: lower T_e and higher $\dot{M}$ or higher T_e and lower $\dot{M}$ both fit the flux quite well. The degeneracy breaks for the full χ^2/dof, when fitting LP and CP, which fixes the matter density. The well-fitting phase volume in the parameters of T_p/T_e and $\dot{M}$ appears to be similar for both models (panels (b) and (d)). No clear anomalies can be seen, thus none of the fits seems to be accidental. In Figure 6.11 we plot the contours of χ^2/dof and χ^2_F/dof_F for the same models in the space of the ratio of temperatures T_p/T_e at $6M$ and spin inclination angle θ. First, note that good fits for χ^2_F/dof_F (panels (a) and (c)) have almost constant electron temperature T_e correspondent to a range of inclination angles θ. A much smaller range in θ is allowed according to full χ^2/dof (panels (b) and (d)) with similar behavior for RMS-field spin and linear-averaged spin solutions with $a_* = 0.9$.

We illustrated in Figure 6.7 how the best-fitting models with different spins perform. Now we visualize in Figure 6.12 the differences between χ^2/dof and χ^2_F/dof_F for the best-fitting models. Solid curves on both panels represent RMS-field models, whereas dashed curves represent models with linear-averaged magnetic field. Blue curves on both panels show the total reduced χ^2/dof, whereas red curves on the left panel correspond to χ^2_F/dof_F for flux spectrum fitting. Panel (a) shows the best χ^2_F/dof_F and χ^2/dof as functions of spin a_*. We see that the best χ^2_F/dof_F for flux fitting is below unity for high spins $a_* = 0.7, 0.9, 0.98$, whereas good fits cannot be achieved for low spins $a_* = 0, 0.5$.

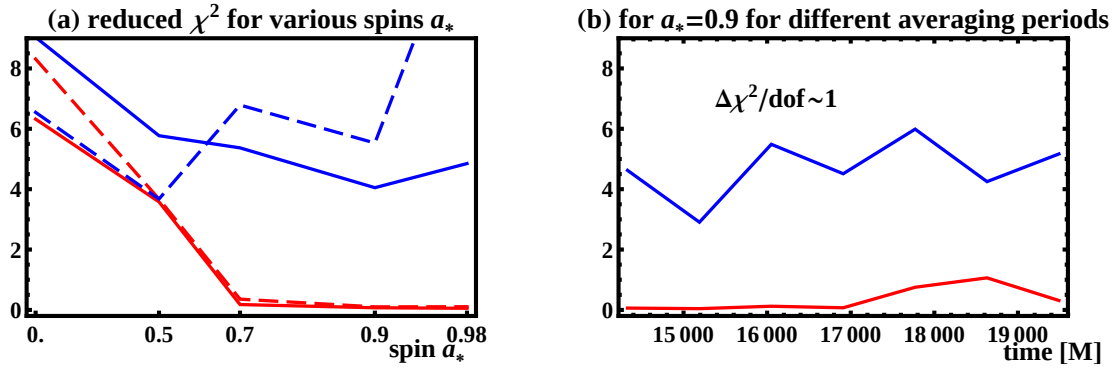

Figure 6.12.— The lowest reduced χ^2 for fits with each spin a_*. Blue upper curves correspond to total χ^2/dof for fitting total flux at 7 frequencies, LP fraction at 3 frequencies and CP at 2 frequencies. Red lower curves correspond to χ^2_F/dof_F for fitting of total flux at 7 frequencies. Solid curves correspond to RMS-field **b** models, whereas dashed lines show linear-averaged **b** models. Reduced χ^2 for spins $a_* = 0, 0.5, 0.7, 0.9, 0.98$ are shown on figure (a) for the models averaged over the period $14000 - 20000M$. Spin $a_* = 0.9$ gives the lowest reduced χ^2. Reduced χ^2 for spin $a_* = 0.9$ are shown on panel (b) for RMS-field models averaged over smaller intervals within the $14000 - 20000M$ time-range. No significant secular drift is present for converged simulations, though the variations of χ^2/dof are quite large reaching ± 1.

High spins are favored. The same is true when we fit polarized observations.

The RMS-field model with spin $a_* = 0.9$ exhibits the lowest reduced χ^2. However, the value is not close to unity, which indicates significant room is available to improve the model. The linear-averaged model with spin $a_* = 0.5$ seems to have the lowest reduced χ^2 over linear-averaged models. However, as discussed previously, we consider models with the RMS-field version of **b** to be more physical compared to models with linear-averaged **b**, thus we stick to RMS-field models in our analysis. We illustrate the stability of the best fit on panel (b) of Figure 6.12. There we show the best χ^2/dof for RMS-field models with spin $a_* = 0.9$ for several averaging periods. The periods have the duration $860M$ within the range $14000 - 20000M$: $13900 - 14760M$ interval, $14760 - 15620M$ interval etc. The values of χ^2/dof are depicted on panel (b) at the interval middles: $14330M$, $15190M$ etc. The values of χ^2/dof fluctuate between intervals by up to $\Delta\chi^2/\mathrm{dof} \sim 1$, which is comparable to the difference $\Delta\chi^2/\mathrm{dof} = 1.5$ between spin $a_* = 0.5$ and spin $a_* = 0.9$ models. Thus, we can only conclude that the RMS-field model with spin $a_* = 0.9$ is marginally better than the models with spins $a_* = 0.5, 0.7, 0.98$. Changes of best χ^2/dof with time show no secular trend, thus indirectly proving convergence of the simulations (see Section 6.3.6 for the discussion of convergence).

There is another way to test the dynamical models against observations. The intrinsic image size was recently measured (Doeleman et al., 2008) with the VLBI technique. Total flux $F = 2.4$ Jy at 230 GHz and correlated flux $F_{\rm corr} \approx 0.35$ Jy at 3.5 Gλ SMT-JCMT baseline were simultaneously measured. We plot this correlated flux with 3σ error bar in Figure 6.13 and compare it to simulated correlated fluxes, normalizing the total flux to 2.4 Jy. To simulate the correlated flux we follow Fish et al. (2009) and employ a Gaussian interstellar scattering ellipse with half-widths at half-maximum 7.0×3.8Gλ with position

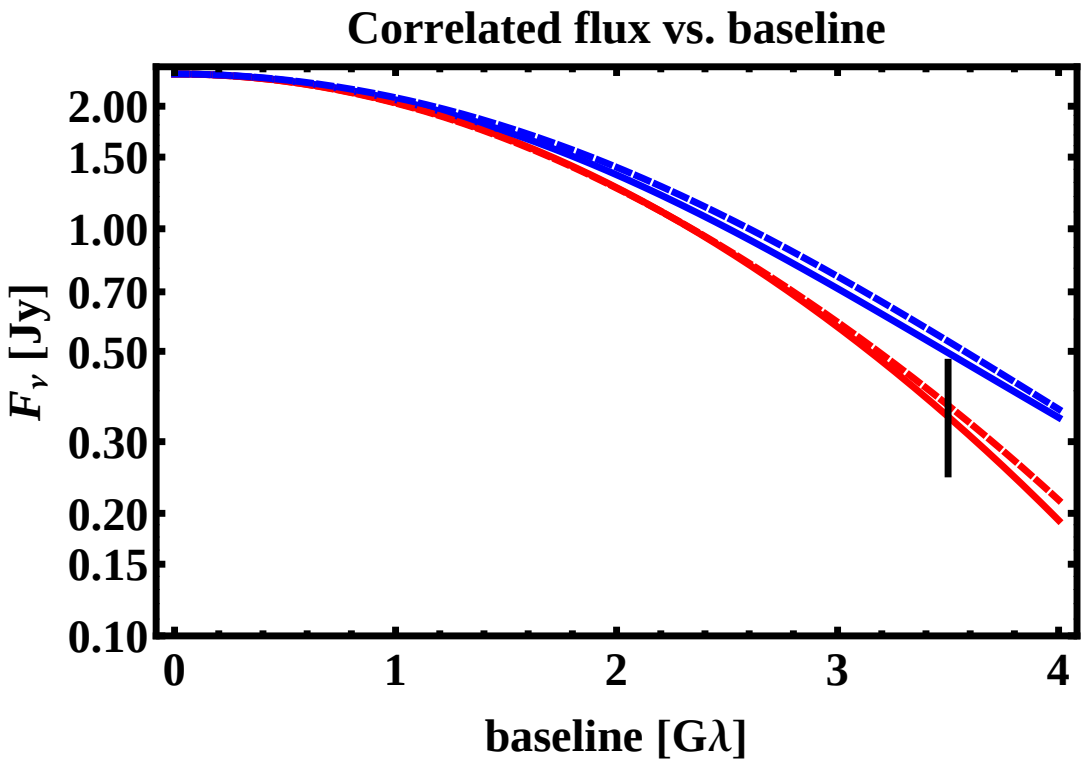

Figure 6.13.— Correlated fluxes as functions of baseline normalized to the 2.4 Jy total flux for best-fitting spin $a_* = 0.9$ model with linear averaged **b** (dashed lines) and the spin $a_* = 0.9$ RMS-field model with RMS **b** (solid lines). For each model the upper line shows the smallest size (largest correlated flux) over all position angles of BH spin axis, the lower dashed line shows the largest size (smallest correlated flux) over all position angles. An observation from Doeleman et al. (2008) with 3σ error bars at baseline 3.5 Gλ is drawn for comparison. Models fit quite well the observed emission region size.

angle 170° east of north. We vary the position angle of BH spin and plot correlated flux curves with the largest (solid line) and the smallest (dashed line) correlated flux at 3.5Gλ. The correlated fluxes for spin $a_* = 0.9$ best-fitting models are shown: blue (dark) lines correspond to maximum correlated fluxes and red (light) lines correspond to minimum correlated fluxes. Solid lines correspond to the RMS-field model and dashed lines to the model with linear-averaged **b**. Both types of models are consistent with observations, but slightly overproduce the correlated flux, which indicates the size of the shadow is slightly underpredicted. We discuss the possible ways to reconcile observations and simulations in the next section.

Having analyzed the best fits and compared the reduced χ^2, we can make a conservative estimate of the model parameters. Let us start with the inclination angle of BH spin θ ($\theta = 90°$ for the edge-on disk). On Figure 6.14 we plot probability density $\rho(\theta, a_* = 0.9|\chi^2)$ for inclination angle for two models with spin $a_* = 0.9$. This quantity represents probability density of the model given the data (6.31) integrated over heating constant and accretion rate

$$\rho(\theta, a_* = 0.9|\chi^2) \propto \int\int \rho(a_* = 0.9, \theta, \dot{M}, C|\chi^2) dC d\dot{M}. \tag{6.33}$$

Both curves are normalized to give $\int \rho(\theta, a_* = 0.9|\chi^2) d\theta = 1$. The solid line corresponds to a RMS-field model, whereas the dashed line to a linear-averaged model. The probable range of θ is quite small in each model, which gives tight constraints on θ in that particular model. The confidence interval θ(RMS **b**) for a RMS-field spin $a_* = 0.9$ model overlaps with the interval for a linear-averaged model θ(lin **b**). Thus, a narrow conservative estimate $\theta_{\rm est}$ can be provided:

$$\theta(\text{RMS } \mathbf{b}) = 53° \pm 3°, \tag{6.34}$$

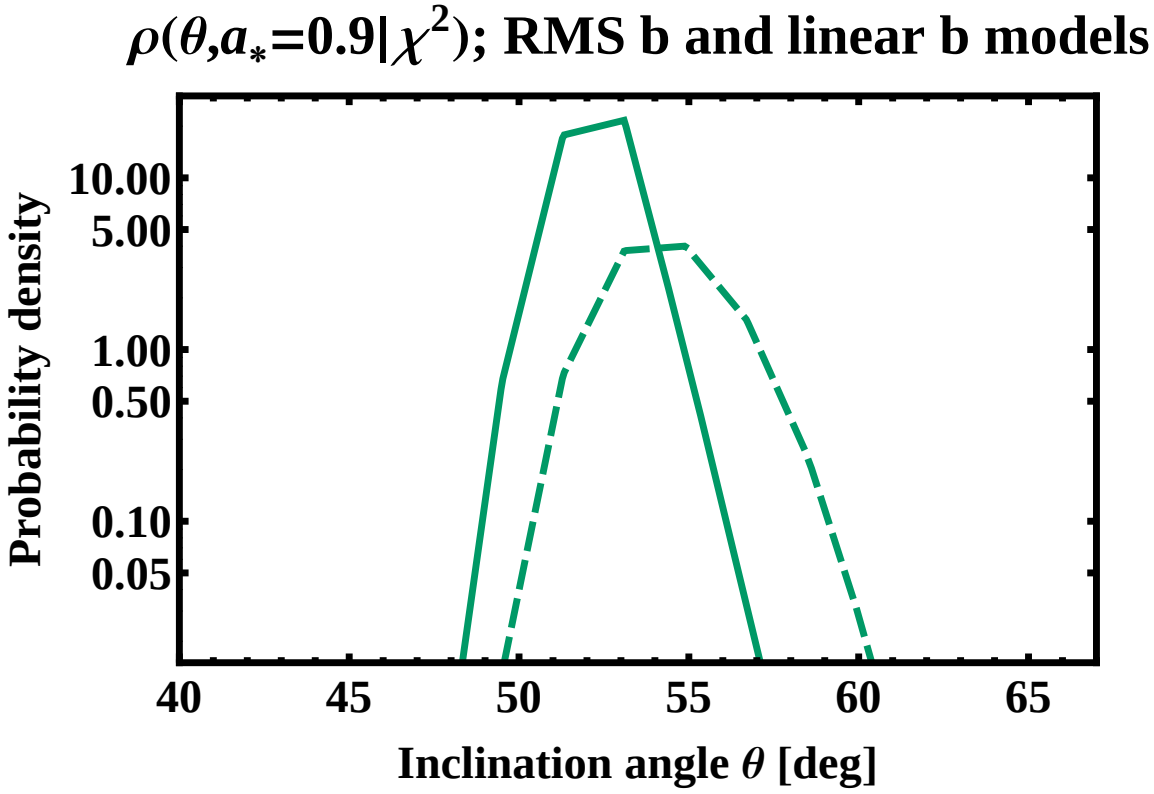

Figure 6.14.— Marginalized over heating parameter C and accretion rate $\dot{M}$, the probability densities $\rho(\theta, a_* = 0.9|\chi^2)$ over inclination angle θ for spin $a_* = 0.9$. Shown are peaks for the RMS-field model (solid line) and linear-averaged model (dashed line). The peaks do overlap, which allows for a robust estimate of the inclination angle. The values $\theta = 50^\circ - 59^\circ$ are allowed.

$$\theta(\text{lin } \mathbf{b}) = 55^\circ \pm 4^\circ,$$

$$\theta_{\rm est} = 50^\circ - 59^\circ.$$

The best θ for RMS-field models with spins $a_* = 0.5, 0.7, 0.98$ are, correspondingly, $\theta = 66^\circ, 62^\circ, 54^\circ$. Thus, our conservative estimate is quite robust.

Likewise, we can calculate the expectation value and 90% confidence intervals for electron temperature T_e at $6M$ for spin $a_* = 0.9$ models:

$$T_e(\text{RMS } \mathbf{b}) = (4.62 \pm 0.56) \cdot 10^{10} \text{ K}, \tag{6.35}$$

$$T_e(\text{lin } \mathbf{b}) = (2.86 \pm 0.16) \cdot 10^{10} \text{ K},$$

$$T_{e,\rm est} = (2.7 - 5.2) \cdot 10^{10} \text{ K}.$$

The accretion rate $\dot{M}$ has large variations between models:

$$\dot{M}(\text{RMS } \mathbf{b}) = (1.09 \pm 0.13) \times 10^{-8} M_\odot \text{year}^{-1}, \tag{6.36}$$

$$\dot{M}(\text{lin } \mathbf{b}) = (1.50 \pm 0.15) \times 10^{-8} M_\odot \text{year}^{-1},$$

$$\dot{M}_{\rm est} = (0.9 - 1.7) \times 10^{-8} M_\odot \text{year}^{-1}.$$

The RMS-field model with spin $a_* = 0.5$ gives very different accretion rate $\dot{M}(0.5)_{\rm est} \approx 4 \times 10^{-8} M_\odot \text{year}^{-1}$.

There is one more quantity we can estimate: the position angle (PA) of BH spin. Similarly to Huang et al. (2009a), we rely on observed intrinsic EVPA$\approx 111.5^\circ$ at 230 GHz and EVPA$\approx 146.9^\circ$ at 349 GHz (see § 6.2). For the model to fit the difference in EVPA, we add a Faraday rotation screen far from the BH with constant rotation measure (RM). Then we compute the required RM and the intrinsic PA to fit the simulated EVPAs at 230 and 349 GHz. The best-fitting RMS-field model with $a_* = 0.9$ gives PA = 121°

east of north, whereas the best-fitting linear-averaged model with spin $a_* = 0.9$ requires PA$= 123^\circ$. The correspondent 90% confidence intervals are

$$\begin{aligned} \mathrm{PA(RMS\ \mathbf{b})} &= 121^\circ \pm 20^\circ, \\ \mathrm{PA(lin\ \mathbf{b})} &= 123^\circ \pm 20^\circ, \\ \mathrm{PA(est)} &= 101^\circ - 143^\circ, \end{aligned} \tag{6.37}$$

where the error is dominated by the observational error of EVPA determination (see Table 6.1). The estimated position still has large uncertainty, what precludes us from tightening the size estimates (see Figure 6.13) from the models. It is reasonable to employ the minimum and maximum correlated fluxes found over all orientations.

With the estimated orientation of the BH spin, we can plot an image of radiation intensity from near the event horizon. Figure 6.15 shows images of total intensity I_ν for the spin $a_* = 0.9$ best-fitting RMS-field solution on the upper left panel, the spin $a_* = 0.9$ best-fitting linear-averaged solution on the lower left panel; LP intensity and CP intensity plots for best spin $a_* = 0.9$ RMS-field model are shown on the upper right and lower right, correspondingly. Blue (predominant) color on CP plot depicts the regions with negative CP intensity and red (subdominant) color depicts the regions with positive CP intensity. The total V flux from this solution is negative ($V < 0$). The streamlines on LP plot are aligned with EVPA direction at each point. The spin axis is rotated by PA $= 121^\circ$ east of north for spin $a_* = 0.9$ RMS-field solution and by PA $= 123^\circ$ for the linear-averaged solution. The spin axis is inclined at θ to the line of sight, so that the either right (west) or left (east) portions of the flow are closer to the observer. The color schemes on all the plots are nonlinear with correspondent calibration bars plotted on the sides. The numbers at the top of calibration bars denote normalizations.

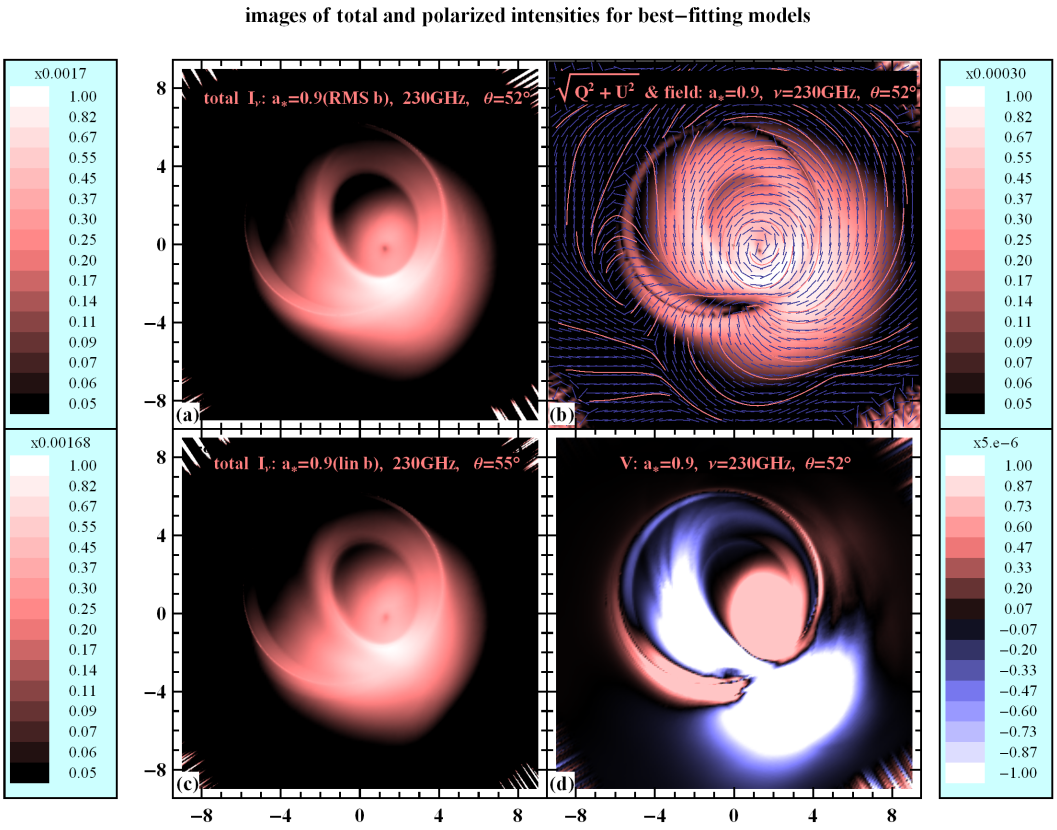

Figure 6.15.— Images of polarized intensities for the best-fitting models: total intensity for spin $a_* = 0.9$ linear-averaged model (lower left); intensities for $a_* = 0.9$ RMS-field model: total intensity (upper left), linear polarized intensity and streamlines along EVPA (upper right), and circular polarized intensity (lower right). Distances are in the units of BH mass M. Images are rotated in the picture plane to fit the best spin PA: PA = 121° for the RMS-field model and PA = 123° for the linear-averaged model. Individual calibration bars are on the sides of correspondent plots. The ill-defined polar region does not contribute significantly to the emission.

6.8 Discussion and Conclusions

Let us compare our results with estimates of Sgr A* accretion flow and BH parameters made by other groups. Two separate searches for spin based on GR numerical simulations have been reported so far: Moscibrodzka et al. (2009) and Dexter et al. (2010). The first paper browses the set of spins from $a_* = 0.5$ to 0.98 for 2D GRMHD simulations, fits X-Ray flux, 230 GHz flux, and slope at this frequency, and finds at least one model for each spin consistent with observations (see Table 3 therein). Their best-bet model has $a_* = 0.9$. Dexter et al. (2010) focuses on a set of 3D GRMHD, fits 230 GHz flux and size estimates and provides the table of spin probabilities with $a_* = 0.9$ again having the highest $P(a)$. If we were only to consider spectrum fitting, then our results would perfectly conform to the picture with high spin $a_* \sim 0.9$ being most likely. When we fit spectrum, LP and CP fractions, spin $a_* = 0.9$ solutions also give lower reduced χ^2. We are unable to provide narrow constraints on a_*, and neither do other groups. Other spin estimates have been based on analytic models. Broderick et al. (2009a, 2010) favor $a_* = 0$ solutions, Huang et al. (2009b) favor $a_* < 0.9$ although they do not explore their full model parameter space. Another poorly constrained quantity is the accretion rate. Our conservative estimate $\dot{M}_{\rm est} = (0.9 - 1.7) \cdot 10^{-8} M_\odot {\rm year}^{-1}$ is broad. Good models in Moscibrodzka et al. (2009) have similar $\dot{M}$ of $\dot{M} = 0.9 \cdot 10^{-8} M_\odot {\rm year}^{-1}$, but $\dot{M} = 12 \cdot 10^{-8} M_\odot {\rm year}^{-1}$ is also found among good fits. Dexter et al. (2010) found relatively tight boundaries for 90% confidence interval of $\dot{M}$ by looking at spin $a_* = 0.9$ solutions by incorporating flow size in χ^2 analysis. Our estimate is consistent with, but slightly narrower than the full range $\dot{M} = 5^{+15}_{-2} \times 10^{-9} M_\odot {\rm year}^{-1}$ (90%) in Dexter et al. (2010). Note, that Dexter et al. (2009) got much lower accretion rate $\dot{M}(0.9) = (1.0 - 2.3) \times 10^{-9} M_\odot {\rm year}^{-1}$ as they assumed the equality of proton and electron temperatures $T_e = T_p$.

In addition to spin and accretion rate we can constrain inclination angle θ and electron temperature T_e at $6M$. Our conservative estimate is $\theta_{\rm est} = 50^\circ - 59^\circ$, which is the narrowest of all estimates in the literature. This θ is fully consistent with the estimates $\theta = 50^\circ$ in Broderick et al. (2009a); Dexter et al. (2010). Huang et al. (2009a) and Huang et al. (2009b) favor slightly lower $\theta = 40^\circ, 45^\circ$, but have large error bars. Inclusion of polarized observations also puts stricter limits on T_e. Moscibrodzka et al. (2009) and Dexter et al. (2010) set constant T_p/T_e, whereas Huang et al. (2009a) and us calculate the profile of T_e. In all models, T_e is a shallow function of radius, which made Dexter et al. (2010) estimate the "common" $T_e = (5.4 \pm 3.0) \times 10^{10}$ K, which is the quantity calculated supposedly still at certain distance from the BH center. Setting this distance to $6M$ we arrive at the consistent, but narrower conservative estimate $T_{e,\rm est} = (2.7 - 5.2) \times 10^{10}$ K. There are two kinds of constraints on BH spin position angle: 230 GHz correlated flux fitting and EVPA fitting. The first path was adopted in Broderick et al. (2009a) and Dexter et al. (2010) with the results PA $= (-20^\circ) - (-70^\circ) = (110^\circ) - (180^\circ)$. These PAs agree quite well with polarization data. Meyer et al. (2007) predicts the range PA $= 60^\circ - 108^\circ$, whereas Huang gets either PA $\approx 115^\circ$ (Huang et al., 2009b) or PA $\approx 140^\circ$ (Huang et al., 2009a) depending on the model without calculating the range. Our estimate of PA $= 101^\circ - 143^\circ$ is quite narrow, and agrees well with Meyer et al. (2007) and other groups. Significantly larger error bars, and the fact that very few size observations are available, make PA estimates from size less reliable than those from EVPA. In addition, the size of the flow may depend substantially on luminosity state (Broderick et al., 2009a) or the presence of non-thermal structures, spiral waves, and other features.

In some astrophysical sources PA is directly known from spatially resolved jets, and Sgr A* may be one such source. A tentative jet feature was revealed in X-rays by Muno et

al. (2008), Fig. 8 with $\mathrm{PA_{jet}} = 120°$. The mean of our conservative PA interval practically coincides with $\mathrm{PA_{jet}}$, which provides support for a jet hypothesis for this feature.

Besides the estimates of accretion rate and flow properties based on the inner flow, there exist estimates based on the outer flow. Shcherbakov & Baganoff (2010) constructed an inflow-outflow model with conduction and stellar winds, which provided an excellent agreement to X-ray surface brightness profile observed by *Chandra*. Their model had an accretion rate $\dot{M} = 6 \cdot 10^{-8} M_{\odot}\mathrm{year}^{-1}$ and electron temperature $T_e = 3.6 \times 10^{10}$ K at $6M$ (Note that gravitational radius is defined as $r_{\mathrm{g}} = 2M$ in Shcherbakov & Baganoff (2010)). from the center showing a great agreement with present results. Thus, the radial extensions of density to large radius is justified. We constrain density in the outer flow by X-ray observations (Shcherbakov & Baganoff, 2010) and in the inner flow by sub-mm observations. The resultant density profile

$$\rho \propto r^{-\beta}, \quad \beta = 0.80 - 0.90 \tag{6.38}$$

is a quite robust estimate. Density power-law index β lies between $\beta = 1.5$ for ADAF flow (Narayan & Yi, 1995) and $\beta = 0.5$ for the convection-dominated accretion flow (Narayan et al., 2000; Quataert & Gruzinov, 2000a). However, the modification of the power-law index from the steep ADAF profile is likely due to conduction for Sgr A*, not convection.

In the present chapter we combined several sophisticated techniques to arrive at our conclusions. Let us now examine the viability of the approaches employed. The dynamical model, despite being based on 3D GRMHD simulations, incorporates averaging and strong approximations. Despite simulating many Keplerian orbits in the region within $25M$, the slopes of density n_e and temperatures T_p and T_e, fixed at the outer flow, break at a radius of roughly $25M$. This suggests one needs to simulate an even larger domain in

radius and potentially add other physical effects such as conduction (Johnson & Quataert, 2007; Sharma et al., 2008; Shcherbakov & Baganoff, 2010). Simulations with larger dynamic range will also help to constrain the Faraday rotation, which happens for the present models partially outside of the simulated domain. The proper simulation of the polar region of the flow may be important as well. At present we artificially limit the magnetization and temperature there. If we do not, then the numerical artifacts associated with excessive numerical dissipation and heating appear, similar to those in Moscibrodzka et al. (2009). The unanimous decision in favor of $a_* = 0.9$ spin for similar types of fitting over the simulation-based models gives a hope that the simulations of different groups are sufficiently similar and any simulation and averaging of the sort is representative.

If the non-thermal electrons provide most of energy for sub-mm peak, then this may potentially invalidate the spin estimates (Shcherbakov & Huang, 2011).

Radiative transfer, in turn, has its own assumptions. Our emissivities in the special synchrotron approximation are good enough, providing e.g. 2% agreement with exact emissivities (Leung et al., 2009; Shcherbakov & Huang, 2011) for $b = 20$ G, $\theta_B = 1$ rad, $T_e = 6.9 \cdot 10^9$ K, and observed frequency $\nu = 100$ GHz. Agreement is better for larger T_e. The non-polarized radiative transfer of total intensity (Moscibrodzka et al., 2009; Dexter et al., 2010) has an intrinsic error in comparison with polarized radiative transfer with the same total emissivity ε_I, however the error is only $1 - 5\%$. We use the averaged dynamical model to calculate radiation and do not perform the statistical analysis of radiation from many simulation shots. This is a strong approximation, which cannot be easily justified and requires future improvement. Polarized radiative transfer appears to be much slower than unpolarized, and the present computation took $17k$ CPU-hours on a supercomputer to explore the full parameter space. Reliable statistics of radiation over many snapshots

may require up to $1M$ CPU-hours, and is not viable at present.

There are still unaccounted sources of error. The mass of the BH in the Galactic Center is known to within 10% (Ghez et al., 2003) and the distance is known to 5%. We do not perform a detailed analysis here, but it seems that these uncertainties would not lead to significant changes in our predictions. A simple shift to slightly lower spin should be able to mimic the effect of smaller BH or a BH at larger distance from us.

Apart from questions of modeling, the improvement of observational data can lead to further insights on the flow structure and more reliable estimates of BH spin. The detailed comparison of flux, LP, and CP curves in Figure 6.7 show that the models with spin $a_* = 0.5$ and spin $a_* = 0.9$ have discrepancies in these regions not constrained by observations. In particular, the CP fractions at 145 GHz are different. EVPA data needs improvement as well. Despite some statistics available at 230 GHz and 349 GHz, the variability of EVPA is about 20°, which translates to $\pm 20°$ (3σ) uncertainly of the mean PA, whereas the modeling uncertainty is only several degrees. More observations of EVPA at these frequencies will help to find the Faraday rotation measure more precisely and constraint the PA of BH spin. An alternative is to observe at higher frequencies $\nu \geq 690$ GHz, where both the Faraday rotation effect and fluctuations of the intrinsic emission EVPA are small. Another important quantity is LP at 88 GHz, whose observations are only reported in 2 papers. Variations in simulated LP(88GHz) are quite large between the best models (see Figure 6.7). Refinement of the observed mean log(LP(88GHz)) could potentially help discriminate better between the $a_* = 0.5$ and $a_* = 0.9$ spin solutions. A measurement of the emitting region size or the correlated flux is also promising. Despite the correlated flux at 230 GHz being measured at the SMT-JCMT $3.5G\lambda$ baseline, the statistics of this measurement are needed to capture variations of $F_{\rm corr}$

over at least a year to be comparable with the statistics of total flux. The correlated flux observations are currently being accumulated (Fish et al., 2011). The correlated flux at this baseline is exponentially sensitive to the physical flow size, which can make slightly brighter states have significantly lower $F_{\rm corr}$. As a caveat, the conclusion on image sizes may depend on the behavior of matter in the ill-defined polar regions. Our models do not exhibit significant emission from high latitudes at 230 GHz (see Figure 6.15) or anywhere above 88 GHz.

The present work offers an improvement over the previous estimates of the Sgr A* spin, inclination, and accretion flow properties, though there is still significant room for improvement. Future work would incorporate more statistics from recent polarized observations in the sub-mm. Future 3D GRMHD simulations would have higher dynamic range converging at $r > 50M$ and likely have a more pronounced outflow. Adding Comptonization to radiative transfer would allow one to test the quiescent X-ray luminosity $L \approx 4 \cdot 10^{32}$erg s^{-1} within $2 - 10$ keV (Shcherbakov & Baganoff, 2010). So far we have focused on the mean state and discarded the information of simultaneity. These data will be used in future analysis of observations to tighten the error bars. The time variability properties can be found from the simulations and compared to the observed ones. In particular, "jet lags" (Yusef-Zadeh et al., 2008; Maitra et al., 2009) and quasi-periodic oscillations (QPOs) (Genzel et al., 2003; Eckart et al., 2006b; Miyoshi, 2010) should be investigated using the simulations.

Acknowledgements

The authors are grateful to Lei Huang for checking various emissivity prescriptions, to Ramesh Narayan for extensive discussions and comments, to Avi Loeb, Avery Broderick, James Moran, Alexander Tchekhovskoy, Cole Miller, Steven Cranmer for insightful comments. The numerical simulations and the radiative transfer calculations in this chapter were partially run on the Odyssey cluster supported by the FAS Sciences Division Research Computing Group and were partially supported by NSF through TeraGrid resources provided by NCSA (Abe), LONI (QueenBee), and NICS (Kraken) under grant numbers TG-AST080025N and TG-AST080026N. The chapter is partially supported by NASA grants NNX08AX04H (RVS&Ramesh Narayan), NNX08AH32G (Ramesh Narayan), NSF Graduate Research Fellowship (RFP), and NASA Chandra Fellowship PF7-80048 (JCM).

6.9 Appendix: Radiative Transfer Convergence

We have written a novel code for general relativistic polarized radiative transfer. As with any new code, we need to conduct a set of convergence tests to ensure it is working accurately. First, we need to devise metrics for assessing accuracy. In the present chapter we model fluxes at 7 frequencies between 88 GHz and 857 GHz, LP fractions at 3 frequencies and CP fractions at 2 frequencies and define χ^2 as to characterize goodness of fit. We employ a similar quantity χ^2_H/dof to characterize the accuracy of transfer. We define

$$\chi^2_H/\mathrm{dof} = \frac{1}{9}\sum_{i=1}^{12}\frac{(Q_{i,1}-Q_{i,2})^2}{\sigma(Q)^2}, \tag{6.39}$$

where $Q_{i,1}$ are simulated fluxes for one set of auxiliary radiative transfer parameters and $Q_{i,2}$ are for another set. The errors $\sigma(Q)$ are the observed errors of the mean, and index i runs through all fluxes, $\log \mathrm{LP}$, and CP fractions. When one of the models fits the data exactly, then χ^2_H/dof coincides with χ^2/dof. Auxiliary radiative transfer parameters designated by $P_{...}$ include:

1. dimensionless scale $P_{\rm fact}$ of the size of integration region in the picture plane,
2. distance from the center $P_{\rm ss}$ measured in horizon radii r_H, where radiative transfer starts,
3. number of points $P_{\rm snxy} = N$ along each dimension in picture plane,
4. extension power-law slope of density profile $P_{\rm rhopo}$,
5. extension slope of internal energy density profile $P_{\rm Upo}$,
6. extension slope of magnetic field profile $P_{\rm Bpo}$.

Since fluctuations and differences in χ^2/dof between different models reach 1, then values $\chi^2_H/\mathrm{dof} \lesssim 0.1$ are acceptable, but we in general strive for $\chi^2_H/\mathrm{dof} < 0.02$. We set constant $P_{\rm fact}$, $P_{\rm ss}$, $P_{\rm snxy}$ for all radiative transfer computations, but we cannot check the code accuracy for all models. We check the convergence a posteriori for the best RMS-field models at each spin value. We find reasonable values of parameters $P_{...}$ by trial-and-error method for some well-fitting model and then fix them. The resultant set of auxiliary parameters is $P_{\rm fact} = 1$, $P_{\rm ss} = 1.01 r_H$, and $P_{\rm snxy} = 111$. Whereas the values of $P_{\rm rhopo}$ and $P_{\rm Upo}$ are fixed by extensions to large radii and density in the inner flow. The tests and the values of χ^2_H are in Table 6.2. The first column describes the test: which quantity we change and how. For example, $P_{\rm fact} : 1 \to 0.8$ means that we tested the convergence of integration region relative size, the value of $P_{\rm fact}$ changed from 1 to 0.8. We change only one parameter at a time. Since the power-law slopes $P_{\rm rhopo}$ and $P_{\rm Upo}$ can vary from model

to model, we change them such that rhopo is increased by 0.2 and Upo is decreased by 0.1. This represents variation of density by a factor of 7 and variation of temperature by a factor of 2.5 at the distance $r_{\rm out} = 3 \cdot 10^5 M$, where extension starts from, yet leading to minor changes in $\chi^2_H/{\rm dof} < 0.1$ (see Table 6.2). Density and temperature at $r_{\rm out} = 3 \cdot 10^5 M$ are known better than to within a factor of several (Baganoff et al., 2003; Shcherbakov & Baganoff, 2010). Thus, the concerns are invalidated that unjustified power-law extensions of density and temperature to large radii may change substantially the polarized spectrum. We also estimate the influence of magnetic field extension power-law by steepening it from $(r/M)^{-1.5}$ to $(r/M)^{-1.75}$. The resultant $\chi^2_H/{\rm dof} \lesssim 0.2$ are small for such a change, but may be much larger for shallower slopes. The extensions as shallow as $|\mathbf{b}| \propto (r/M)^{-1}$ may provide better fits to Faraday rotation measure and should be carefully explored. Various extensions of the fluid velocity lead to practically the same polarized intensities.

Table 6.2: Values of χ^2_H/dof for radiative transfer tests over best models.

Test	spin $a_* = 0$	spin $a_* = 0.5$	spin $a_* = 0.7$	spin $a_* = 0.9$	spin $a_* = 0.98$	spin $a_* = 0.9$ (lin **b**)
$P_{\rm N} : 75 \to 111$	0.012	0.0034	0.0097	0.014	0.0046	0.0070
$P_{\rm N} : 111 \to 161$	0.0018	0.0043	0.0017	0.00087	0.0013	0.0012
$P_{\rm ss} : 1.003r_H \to 1.01r_H$	0.00072	0.0017	0.0018	0.00065	0.00041	0.0010
$P_{\rm ss} : 1.01r_H \to 1.03r_H$	0.018	0.020	0.018	0.017	0.0073	0.020
$P_{\rm fact} : 0.8 \to 1.0$	0.027	0.60	0.073	0.050	0.042	0.11
$P_{\rm fact} : 1.0 \to 1.2$	0.013	0.185	0.081	0.039	0.017	0.087
$P_{\rm rhopo} : Q \to Q+ = 0.2$	0.027	0.064	0.044	0.097	0.018	0.079
$P_{\rm Upo} : Q \to Q- = 0.1$	0.096	0.074	0.021	0.017	0.0063	0.0099
$P_{\rm Bpo} : -1.5 \to -1.75$	0.19	0.12	0.0026	0.012	0.0049	0.028

Chapter 7

Discussion and Future Directions

In this thesis I described a variety of modeling topics related to accretion onto low-luminosity AGNs and jets. The model with conduction was shown to be reasonable for connecting the outer feeding region of the flow to the inner plunging region. The inner accretion flow was described in terms of a model based on 3D GRMHD numerical simulations. Since the lightcurves of Sgr A* vary a lot in sub-mm, I fitted the mean flux spectrum and mean dependencies of CP fraction, EVPA, and log of LP fraction on frequency. These mean quantities were compiled based on a nearly complete history of 15 years of Sgr A* observations reported in 29 papers.

Significant efforts were dedicated to making theories self-consistent and rigorous. I employed statistical χ^2 tests to gauge the quality of fits. For the sub-mm spectrum of Sgr A* I even ran the Kolmogorov-Smirnov test to show that the statistical properties of the observations are consistent with a Gaussian probability distribution, thus a χ^2 test is justified. The plasma physics part of my thesis is quite rigorous. Assuming only a thermal particle distribution I computed precisely Faraday rotation and Faraday conversion

coefficients for plasma at all temperatures. Chapter 5 on GR polarized radiative transfer does not have approximations either.

However, the semi-analytical dynamical modeling reported in this work is substantially oversimplified. The work on radial accretion with MHD turbulence in Chapter 2 postulates an ad-hoc set of averaged equations, speculating on the dissipation rate of turbulence and on the interplay between different components of anisotropic magnetic field. This model does not explain any observations, neither is it believable, since the model is spherically symmetric. Conduction-mediated accretion in Chapter 3 is a relatively new concept, whereas the inclusion of feeding by stellar winds is an established process (Lamers & Cassinelli, 1999). An excellent fit with $\chi^2/dof = 1.4$ was found for the surface brightness profile. Also the model fits the orders of magnitude of sub-mm luminosity and Faraday rotation measure. A qualitatively new model was thus found to give quantitatively correct results. Yet, this model of accretion with conduction incorporates many unknowns. First, the model is again spherically symmetric, so it ignores both rotation the possibility of producing strong winds above the equatorial plane. Second, the value of conductivity κ is not known, but an order of magnitude estimate is used. It is not known at present, if conductivity is actually proportional to electron velocity and radius $\kappa \sim v_e r$ or what the precise proportionality coefficient is, if proportionality holds. The presence of magnetic field makes the estimate even more uncertain.

The most complicated model is presented in Chapter 6. It is based on averaged 3D GRMHD simulations and contains a number of approximations. Some of them can be easily lifted, but some must be allowed to make this pioneering work at all possible. There are two easy-to-lift approximations, already lifted by other groups: evolution of intensities along rays should be computed along with the dynamical evolution; means of fluxes

from radiative transfer over many snapshots should be compared to observations, not a single set of fluxes computed over the averaged model. The approximations on dynamics are more severe. The simulations presented in Chapter 6 are not necessarily converged as described by Hawley et al. (2011). Various quantities must converge, e.g. accretion rate with time, accretion rate as a function of radius, accretion rate and magnetic field strength with resolution or with changing initial conditions. Initially, only the accretion rate convergence was considered (Penna et al., 2010), but later convergence of magnetic flux and turbulence dissipation rate were also included as a requirement. No present-day accretion disk simulation can achieve convergence with turbulence dissipation, much more work in this direction is needed. The distribution of electrons and their temperature, were they thermal, is also largely uncertain.

The desire to employ precise physics is rarely rewarded in the field of Astronomy, which is driven more by puzzles and qualitatively new explanations for observed phenomena. Creating quantitatively correct theories is a minor driver of the field. On this basis I would gauge the potential future directions of my research. Radiative transfer looks promising in this respect. Polarized radiative transfer presented here was applied so far only to LLAGNs, whereas jets is an exciting other area of its application. The polarized signature of jets was only researched qualitatively (Homan et al., 2009), and the agreement of a model with data was not achieved.

Modeling of accretion with conduction holds even more promise for qualitative improvements. Emergence of outflows driven by conductive heat flux from the accretion flow was not conclusively demonstrated. Thus, a two-dimensional analytic model or numerical simulations of 2D inflow-outflow pattern may appear to be a cornerstone of accretion in a typical dormant AGN. Such a model will also be tested with X-ray

observations of Sgr A*. As 1D model was computed, which fits 1D surface brightness profile, there is another dimension of data to validate a 2D model — frequency. A *Chandra* HETG proposal to obtain the precise spectrum of Sgr A* has been submitted, and substantial spectral data are already available from previous observations. Yet, the prescription for conductivity κ should be wisely chosen for simulations with electron conduction. It might not be viable in the near future to precisely determine collisionless conductivity of magnetized plasma. But this precise treatment may not be needed as variations of conductivity prescription might not lead to even quantitative improvement of the fit.

Numerical simulations will progress in the future as more powerful computers appear according to Moore's law. Rigorous convergence tests are already developed for MHD and will be developed for simulations of collisionless plasmas. Simulations with higher resolution may lead to better agreement to observations. A not-so-great quality of fit $\chi^2/dof \approx 4$ should be improved upon. Yet, if proper averaging of the simulated lightcurves results in a better quality of fit with $\chi^2/dof \approx 1$, then the utility is small in improving the resolution of dynamical simulations. However, lots of various observational data have been accumulated for Sgr A*. It might not be possible for a long time to fit all these data within a single model. Such additional data are the dependence of EVPA angle on frequency and the inferred Faraday rotation measure, X-ray contribution from the central source produced by SSC mechanism, variability properties and correlations of polarized fluxes. Ever improving physical models will continue being involved to explain this body of observations. When more sophisticated theories are tested on Sgr A*, they will be applied to other low-luminosity AGNs and jets, where less observational data are available. It will be possible in the future to reliably extract the spins and illuminate the flow properties of

M87*, M81*, M31*, BH in 3C 279 and other supermassive black holes.

Bibliography

Abramowicz, M. A., Igumenshchev, I. V., Quataert, E., Narayan, R. 2002, ApJ, 565, 1101

Aitken, D. K., Greaves, J., Chrysostomou, A., Jenness, T., Holland, W., Hough, J. H., Pierce-Price, D., Richer, J. 2000, ApJ, 534, 173

Allen, S. W., Dunn, R. J. H., Fabian, A. C., Taylor, G. B., Reynolds, C. S. 2006, MNRAS, 372, 21

An, T., Goss, W. M., Zhao, J.-H., Hong, X. Y., Roy, S., Rao, A. P., Shen, Z.-Q. 2005, ApJ, 634, 49

Anile, A. M., Breuer, R. A. 1974, ApJ, 189, 39

Aschwanden, M. J. 2005, "Physics of the Solar Corona: An Introduction with Problems and Solutions" (Chichester, UK: Springer)

Azzam, R. M. A., Bashara, N. M. 1987, "Ellipsometry and polarized light" (Amsterdam: North Holland)

Baganoff, F. K., et al. 2001, Nature, 413, 45

Baganoff, F. K., et al. 2003, ApJ, 591, 891

Balbus, S. A., Hawley, J. F. 1991, ApJ, 376, 214

Balbus, S. A., Hawley, J. F. 1998, Reviews of Modern Physics, 70, 1

Balick, B., Brown, R. L. 1974, ApJ, 194, 265

Ballantyne, D. R., Ozel, F., Psaltis, D. 2007, ApJ, 663, L17

Barnes, J. E. 1998, in "Galaxies: Interactions and Induced Star Formation", ed. D. Friedli, L. Martinet, & D. Pfenniger (Berlin: Springer), 275

Barnes, J. E., Hernquist, L. 1992, Annual Rev. of Astronomy and Astrophysics, 30, 705

Beckwith, K., Hawley, J. F., Krolik, J. H. 2008, MNRAS, 390, 21

Beckwith, K., Hawley, J. F., Krolik, J. H. 2008, ApJ, 678, 1180

Beckert, T., Falcke, H. 2002, A&A, 388, 1106

Begelman, M. C., Volonteri, M., Rees, M. J. 2006, MNRAS, 370, 289

Begelman, M. C., Chiueh, T. 1988, ApJ, 332, 872

Begelman, M. C., Rees, M. J. 1978, MNRAS, 185, 847

Begelman, M., Rees, M. 2010, "Gravity's fatal attraction: black holes in the universe" (Cambridge, UK: Cambridge University Press)

Bellan, P. M. 2006, "Fundamentals of plasma physics" (Cambridge: Cambridge University Press)

Berger, J. O. 1985, "Statistical Decision Theory and Bayesian Analysis" (New York: Springer-Verlag)

Bergman, J., Eliasson, B. 2001, PhPl, 8, 1482

Beskin, G. M., Karpov, S. V. 2005, A&A 440, 223

Beskin, V. S., Pidoprygora, Yu. N. 1995, JETP, 80, 575

Biskamp, D. 2000, "Magnetic reconnection in plasmas" (Cambridge, UK: Cambridge University Press)

Biskamp, D. 2003, "Magnetohydrodynamic turbulence" (Cambridge, UK: Cambridge University Press)

Bisnovatyi-Kogan, G. S., Ruzmaikin, A. A. 1974, Ap&SS, 28, 45

Blandford, R. D., Konigl, A. 1979, ApJ, 232, 34

Blandford, R. D., Begelman, M. C. 1999, MNRAS, 303, L1

Boldyrev, S. 2006, Phys. Rev. Lett., 96, 5002

Bond, J. R., Arnett, W. D., Carr, B. J. 1984, ApJ, 280, 825

Bondi, H. 1952, MNRAS, 112, 195

Bower, G. C., Falcke, H., Backer, D. C. 1999, ApJ, 523, L29

Bower, G. C., Wright, M. C. H., Backer, D. C., Falcke, H. 1999, ApJ, 527, 851

Bower, G. C., Wright, M. C. H., Falcke, H., Backer, D. C. 2001, ApJ, 555, 103

Bower, G. C., Falcke, H., Sault, R. J., Backer, D. C. 2002, ApJ, 571, 843

Bower, G. C., Wright, M. C. H., Falcke, H., Backer, D. C. 2003, ApJ, 588, 331

Bower, G. C., Falcke, H., Wright, M. C., Backer, Donald C. 2005, ApJ, 618, 29

Broderick, A. 2004, Ph.D. thesis, California Institute of Technology

Broderick, A. E., Fish, V. L., Doeleman, S. S., Loeb, A. 2009, ApJ, 697, 45

Broderick, A. E., Loeb, A., Narayan, R. 2009, ApJ, 701, 1357

Broderick, A. E., Fish, V. L., Doeleman, S. S., Loeb, A. 2010, astro-ph/1011.2770

Broderick, A. E., Narayan, R. 2006, ApJ, 638, L21

Buneman, O. 1993, Computer Space Plasma Physics (Tokyo: Terra Scientific), 67

Buonanno, A., Cook, G. B., Pretorius, F. 2007, Phys. Rev. D, 75, 12401

Campanelli, M., Lousto, C., Zlochower, Y., Merritt, D. 2007, ApJ, 659, L5

Chan, C. K., Liu, S., Fryer, C. L., Psaltis, D., Ozel, F., Rockefeller, G., Melia, F. 2009, ApJ, 701, 521

Chakrabarti, S. K. 1985, ApJ, 288, 1

Chakrabarti, S. K. 1985, ApJ, 294, 383

Chandrasekhar, S. 1943, ApJ, 97, 255

Chandrasekhar, S. 1957, "Introduction to the Study of Stellar Structure" (New York: Dover Publications)

Coker, R.F., Melia, F. 2000, ApJ, 534, 723

Cox, D. P., Reynolds, R. J. 1987, Ann. Rev. A&A, 25, 303

Cuadra, J., Nayakshin, S., Springel, V., Di Matteo, T. 2005, MNRAS, 360, L55

Cuadra, J., Nayakshin, S., Springel, V., Di Matteo, T. 2006, MNRAS, 366, 358

Cuadra, J., Nayakshin, S., Martins, F. 2008, MNRAS, 383, 458

Cowie, L. L., McKee, C. F. 1977, ApJ, 211, 135

De Villiers, J.-P., Hawley, J. F., Krolik, J. H. 2003, ApJ, 599, 1238

Devecchi, B., Volonteri, M. 2009, ApJ, 694, 302

Dexter, J., Agol, E., Fragile, P. C. 2009, ApJ, 703, 142

Dexter, J., Agol, E., Fragile, P. C., McKinney, J. C. 2010, ApJ, 717, 1092

Do, T., Ghez, A. M., Morris, M. R., Yelda, S., Meyer, L., Lu, J. R., Hornstein, S. D., Matthews, K. 2009, ApJ, 691, 1021

Dodds-Eden, K., et al. 2009, ApJ, 698, 676

Dodds-Eden K., Sharma P., Quataert E., Genzel R., Gillessen S., Eisenhauer F., Porquet D. 2010, ApJ, 725, 450

Dodds-Eden K., et al. 2010, ApJ, 728, 37

Doeleman, S. S. et al 2001, AJ, 121, 2610

Doeleman, S. S. et al. 2008, Nature, 455, 78

Dolence, J. C., Gammie, C. F., Moscibrodzka, M., Leung, P. K. 2009, ApJS, 184, 387

Eckart, A., et. al. 2006, A&A, 450, 535

Eckart, A., Schödel, R., Meyer, L., Trippe, S., Ott, T., Genzel, R. 2006, A&A, 455, 1

Eisenstein, D. J., Loeb, A. 1995, ApJ, 443, 11

Ellis, G. F. R., 2009, Rel. Cosmology, 41, 581

Falcke, H., Goss, W. M., Matsuo, H., Teuben, P., Zhao, J.-H., Zylka, R. 1998, ApJ, 499, 731

Falcke, H., Markoff, S. 2000, A&A, 362, 113

Fish, V. L., Broderick, A. E., Doeleman, S. S., Loeb, A. 2009, ApJ, 692, L14

Fish, V. L., et al. 2011, ApJ, 727, 36

Fragile, P. C., Lindner, C. C., Anninos, P., Salmonson, J. D. 2009, ApJ, 691, 482

Fryer, C. L., Woosley, S. E., Heger, A. 2001, ApJ, 550, 372

Fuerst, S. V., Wu, K. 2004, A&A, 424, 733

Gammie, C. F., Popham, R. 1998, ApJ, 498, 313

Gammie, C. F., McKinney, J. C., Toth, G. 2003, ApJ, 589, 444

Gammie, C. F., Shapiro, S. L., McKinney, J. C. 2004, ApJ, 602, 312

Gammie, C. F., Leung, P. K. 2010, MNRAS, submitted

Garcia, M. R., Williams, B. F., Yuan, F., Kong, A. K. H., Primini, F. A., Barmby, P., Kaaret, P., Murray, S. S. 2005, ApJ, 632, 1042

Genzel, R., Eckart, A., Ott, T., Eisenhauer, F. 1997, MNRAS, 291, 219

Genzel, R., Schodel, R., Ott, T., Eckart, A., Alexander, T., Lacombe, F., Rouan, D., Aschenbach B. 2003, Nature, 425, 934

Ghez, A. M., Becklin, E., Duchjne, G., Hornstein, S., Morris, M., Salim, S., Tanner, A. 2003, ANS, 324, 527

Ghez, A. M., et al. 2008, ApJ, 689, 1044

Ghosh, S., Mukhopadhyay, B. 2007, ApJ, 667, 367

Gillessen, S., Eisenhauer, F., Fritz, T. K., Bartko, H., Dodds-Eden, K., Pfuhl, O., Ott, T., Genzel, R. 2009, ApJ, 707, L114

Goldreich, P., Sridhar, S. 1995, ApJ, 438, 763

Goldston, J. E., Quataert, E., Igumenshchev, I. V. 2005, ApJ, 621, 785

Gonzalez, J. A., Sperhake, U., Brugmann, B., Hannam, M., Husa, S. 2007, Phys. Rev. Letters, 98, 091101

Gould, R. J. 1980, ApJ, 238, 1026

Guo, F., Mathews, W. G. 2011, ApJsubmitted, astro-ph/1103.0055

Haehnelt M. G., Rees M. J. 1993, MNRAS, 263, 168

Hamaker, J. P., Bregman, J. D. 1996, A&AS, 117, 161

Hawley, J. F., Balbus, S. A. 2002, ApJ, 573, 738

Hawley, J. F., Krolik, J. H. 2001, ApJ, 548, 348

Hawley, J. F., Guan, X., Krolik, J. H. 2011, astro-ph/1103.5987

Herrnstein, R. M., Zhao, J.-H., Bower, G. C., Goss, W. M. 2004, AJ, 127, 3399

Ho, L. C. 1999, ApJ, 516, 672

Ho, L. C. 2008, Ann. Rev. of Astronomy & Astrophysics, 46, 475

Homan, D. C., Lister, M. L., Aller, H. D., Aller, M. F., Wardle, J. F. C. 2009, ApJ, 696, 328

Hopkins, P. F., Hernquist, L., Cox, T. J., Di Matteo, T., Robertson, B., Springel, V. 2005, ApJ, 630, 716

Hopkins, P. F., Hernquist, L., Cox, T. J., Di Matteo, T., Robertson, B., Springel, V. 2006, ApJS, 163, 1

Howes, G. G., Cowley, S. C., Dorland, W., Hammett, G. W., Quataert, E., Schekochihin, A. A. 2006, ApJ, 651, 590

Huang, L., Liu, S., Shen, Z.-Q., Cai, M. J., Li, H., Fryer, C. L. 2008, ApJ, 676, L119

Huang, L., Liu, S., Shen, Z.-Q., Yuan, Y.-F., Cai, M. J., Li, H., Fryer, C. L. 2009, ApJ, 703, 557

Huang, L., Takahashi, R., Shen, Z.-Q. 2009, ApJ, 706, 960

Igumenshchev, I. V., Narayan, R. 2002, ApJ, 566, 137

Igumenshchev, I. V. 2006, ApJ, 649, 361

Igumenshchev, I. V. 2008, ApJ, 677, 317

Jaynes, E. T., Bretthorst, G. L. 2003, "Probability Theory" (Cambridge: Cambridge University Press)

Jones, T. W., O'dell, S. L. 1977, ApJ, 214, 522

Johnson, B. M., Quataert, E. 2007, ApJ, 660, 1273

Kida, S., Yanase, S., Mizushima, J. 1991, Phys. Fluids A, 3, 457

Komissarov, S. S., McKinney, J. C. 2007, MNRAS, 377, L49

Koyama, K., Maeda, Y., Sonobe, T., Takeshima, T., Tanaka, Y., Yamauchi, S. 1996, PASJ, 48, 249

Krichbaum, T. P., et al. 1998, A&A, 335, L106

Krichbaum, T. P., Graham, D. A., Bremer, M., Alef, W., Witzel, A., Zensus, J. A., Eckart, A. 2006, JPhCS, 54, 328

Krolik, J. H., Hawley, J. F., Hirose, S. 2005, ApJ, 622, 1008

Ladeinde, F., Gaitonde, D. V. 2004, Phys. Fluids, 16, 2097

Lamers, H. J. G. L. M., Cassinelli, J. P. 1999, "Introduction to stellar winds" (New York : Cambridge University Press)

Landau, L. D., Lifshitz, E. M., Pitaevskii, L. P. 1984, "Electrodynamics of Continuous Media" (Oxford: Pergamon Press)

Landau, L. D., Lifshitz, E. M. 1975, "Classical theory of fields" (Oxford: Pergamon Press)

Landau, L. D., Lifshitz, E. M. 1987, "Fluid mechanics" (Oxford: Pergamon Press)

Lazarian, A., Vishniac, E. T. 1999, ApJ, 517, 700

Lazarian, A. 2006, Int. J. Mod. Phys. D, 15, 1099

Legg, M. P. C., Westfold, K. C. 1968, ApJ, 154, 499

Leslie, D. C. 1973, "Developments in the Theory of Turbulence" (Oxford: Oxford University Press)

Leung, P. K., Gammie, C. F., Noble, S. C. 2009, ApJ, submitted

Li, J., Shen, Z.-Q., Miyazaki, A., Huang, L., Sault, R. J., Miyoshi, M., Tsuboi, M., Tsutsumi, T. 2008, JPhCS, 131, 2007

Lifshits, E. M., Pitaevskii, L. P. 1981, "Physical Kinetics" (Oxford: Pergamon Press)

Lo, K. Y., Schilizzi, R. T., Cohen, M. H., Ross, H. N. 1975, ApJ, 202, L63

Lo, K. Y., Shen, Z.-Q., Zhao, J.-H., Ho, P. T. P. 1998, ApJ, 508, L61

Loeb, A. 2004, MNRAS, 350, 725

Loeb A., Rasio F. A. 1994, ApJ, 432, 52

Lu, R.-S., Krichbaum, T. P., Eckart, A., Konig, S., Kunneriath, D., Witzel, G., Witzel, A., Zensus, J. A. 2008, JPhCS, 131, 2059

Lu, J. R., Ghez, A. M., Hornstein, S. D., Morris, M. R., Becklin, E. E., Matthews K. 2009, ApJ, 690, 1463

Macquart, J.-P., Bower, G. C., Wright, M. C. H., Backer, D. C., Falcke, H. 2006, ApJ, 646, L111

Mahadevan, R. 1998, Nature, 394, 651

Maitra, D., Markoff, S., Falcke, H. 2009, A&A, 508, 13

Marichev, O., 2008, Wolfram blog from May 6 http://blog.wolfram.com/2008/05/06/two-hundred-thousand-new-formulas-on-the-web/

Markoff, S., Falcke, H., Yuan, F., Biermann, P. L. 2001, A&A, 379, L13

Marrone, D. P., Moran, J. M., Zhao, J.-H., Rao, R. 2006, JPhCS, 54, 354

Marrone, D. P., Moran, J. M., Zhao, J.-H., Rao, R. 2006, ApJ, 640, 308

Marrone, D. P., Moran, J. M., Zhao, J., Rao R., 2007, ApJ, 654, L57

Marrone, D. P., et al. 2008, ApJ, 682, 373

Martins, F., Genzel, R., Hillier, D. J., Eisenhauer, F., Paumard, T., Gillessen, S., Ott, T., Trippe, S. 2007, A&A, 468, 233

Martins, F., Gillessen, S., Eisenhauer, F., Genzel, R., Ott, T., Trippe, S. 2008, ApJ, 672, L119

Mauerhan, J. C., Morris, M., Walter, F., Baganoff, F. K. 2005, ApJ, 623, 25

McKinney, J. C., Gammie, C. F. 2004, ApJ, 611, 977

McKinney, J. C. 2006, MNRAS, 367, 1797

McKinney, J. C. 2006, MNRAS, 368, 1561

McKinney, J. C., Narayan, R. 2007, MNRAS, 375, 513

McKinney, J. C., Narayan, R. 2007, MNRAS, 375, 531

McKinney, J. C., Blandford, R. D. 2009, MNRAS, 394, L126

Melrose, D. B., 1971, Ap&SS, 12, 172

Melrose, D. B., McPhedran, R. C. 1991, "Electromagnetic Processes in Dispersive Media" (Cambridge University Press: Cambridge)

Melrose, D. B. 1997, J. Plasma Physics, 57, 479

Melrose, D. B. 1997, Phys. Rev. E, 56, 3527

Melrose, D. B. 1997, J. Plasma Physics, 58, 735

Melrose, D. B. 2010, "Quantum Plasmadynamics: Magnetised Plasmas" (New-York: Springer)

Meszaros, P. 1975, Nature, 258, 583

Meyer, L., Schödel, R., Eckart, A., Duschl, W. J., Karas, V., Dovčiak, M. 2007, A&A, 473, 707

Mignone, A., McKinney, J. C. 2007, MNRAS, 378, 1118

Mihalas, D., Mihalas, B. W. 1984, "Foundations of radiation hydrodynamics" (New York: Oxford University Press)

Miller, M. C., Hamilton, D. P. 2002, MNRAS, 330, 232

Misner, C. W., Thorne, K. S., Wheeler, J. A. 1973, "Gravitation" (San-Francisco: Freeman and Company)

Miyazaki, A., Tsutsumi, T., Tsuboi, M. 2004, ApJ, 611, 97

Miyoshi, M., Shen, Z.-Q., Oyama, T., Takahashi, R., Kato, Y. 2010, astro-ph/0906.5511

Mokiem, M. R., de Koter, A., Puls, J., Herrero, A., Najarro, F., Villamariz, M. R. 2005, A&A, 441, 711

Morrison, R., McCammon, D. 1983, ApJ, 270, 119

Moscibrodzka, M., Das, T. K., Czerny, B. 2006, MNRAS, 370, 219

Moscibrodzka, M., Gammie, C. F., Dolence, J. C., Shiokawa, H., Leung, P. K. 2009, ApJ, 706, 497

Muno, M. P., et al. 2008, ApJ, 673, 251

Muno, M. P., et al. 2009, ApJS, 181, 110

Munoz, D., Marrone, D., Moran, J. 2009, Bulletin of the AAS, 41, 761

Najarro, F., Figer, D. F., Hillier, D. J., Kudritzki, R. P. 2004, ApJ, 611, L105

Narayan, R., Medvedev, M. V., ApJ, 562, L129

Narayan, R., Yi, I. 1995, ApJ, 452, 710

Narayan, R., Yi, I., Mahadevan, R. 1995, Nature, 374, 623

Narayan, R., Kato, S., Honma, F. 1997, ApJ, 476, 49

Narayan, R., Mahadevan, R., Grindlay, J. E., Popham, R. G., Gammie, C. 1998, ApJ, 492, 554

Narayan, R., Igumenshchev, I. V., Abramowicz, M. A. 2000, ApJ, 539, 798

Narayan, R., Quataert, E., Igumenshchev, I. V., & Abramowicz, M. A. 2002, ApJ, 577, 295

Noble, S. C., Gammie, C. F., McKinney, J. C., Del Zanna, L. 2006, ApJ, 641, 626

Noble, S. C., Leung, P. K., Gammie, C. F., Book, L. G. 2007, CQGra, 24, 259

Noble, S. C., Krolik, J. H. 2009, ApJ, 703, 964

Noglik, J. B., Walsh, R. W., Ireland, J. 2005, A&A, 441, 353

Ogilvie, G. I. 2003, MNRAS, 340, 969

Özel, F., Psaltis, D., Narayan, R. 2000, ApJ, 541, 234

Pacholczyk, A. G. 1970, "Radio astrophysics. Nonthermal processes in galactic and extragalactic sources" (San Francisco: Freeman)

Paczynski, B., Wiita, P. J. 1980, A&A, 88, 23

Parrish, I. J., Stone, J. M. 2005, ApJ, 633, 334

Paumard T., et al. 2006, ApJ, 643, 1011

Pellegrini, S. 2005, ApJ, 624, 155

Penna, R. F., McKinney, J. C., Narayan, R., Tchekhovskoy, A., Shafee, R., McClintock, J. E. 2010, MNRAS, 408, 752

Phillips, J. A., Wolszczan, A. 1992, ApJ, 385, 273

Quataert, E. 1998, ApJ, 500, 978

Quataert, E., Gruzinov, A. 2000, ApJ, 539, 809

Quataert, E., Gruzinov, A. 2000, ApJ, 545, 842

Quataert, E. 2004, ApJ, 613, 322

Rees, M. J. 1984, Annual Rev. of Astronomy and Astrophysics, 22, 471

Rees, M. J., Volonteri, M. 2007, proceedings to "Black Holes from Stars to Galaxies" (editor: V. Karas), p. 51

Reid, M. J., Broderick, A. E., Loeb, A., Honma, M., Brunthaler, A. 2008, ApJ, 682, 1041

Rochford, K. 2001, book chapter in "Encyclopedia of Physical Science and Technology" (Academic press)

Rockefeller, G., Fryer, C. L., Melia, F., Warren, M. S. 2004, ApJ, 604, 662

Ruffert M., 1994, ApJ, 427, 342

Rybicki, G. B., Lightman, A. P. 1979, "Radiative processes in astrophysics" (New York: Wiley-Interscience)

Sazonov, V. N. 1969, Soviet Astronomy, 13, 396

Sazonov, V. N., Tsytovich, V. N. 1968, Radioph. and Quant. Electr., 11, 731

Scharlemann, E. T. 1983, ApJ, 272, 279

Schekochihin, A. A., Cowley, S. C., Taylor, S. F., Maron, J. L., McWilliams, J. C. 2004, ApJ, 612, 276

Schödel, R., et al. 2002, Nature, 419, 694

Schnittman, J. D., Krolik, J. H., Hawley, J. F. 2006, ApJ, 651, 1031

Schweizer, F. 1998, in "Galaxies: Interactions and Induced Star Formation", ed. R. C. Kennicutt, Jr., et al. (Berlin: Springer), 105

Serabyn, E., Carlstrom, J., Lay, O., Lis, D. C., Hunter, T. R., Lacy, J. H. 1997, ApJ, 490, L77

Shafee, R., McKinney, J. C., Narayan, R., Tchekhovskoy, A., Gammie, C. F., McClintock, J. E. 2008, ApJ, 687, L25

Shakura, N. I., Syunyaev, R. A. 1973, A&A, 24, 337

Sharma, P., Quataert, E., Hammett, G. W., Stone, J. M. 2007, ApJ, 667, 714

Sharma, P., Quataert, E., Stone, J. M. 2007, ApJ, 671, 1696

Sharma, P., Quataert, E., Stone, J. M. 2008, MNRAS, 389, 1815

Shapiro, S. L. 2005, ApJ, 620, 59

Shapiro, S. L., Teukolsky, S. A. 1983, "Black holes, white dwarfs, and neutron stars: The physics of compact objects" (New York: Wiley-Interscience)

Shen, Z.-Q., Lo, K. Y., Liang, M.-C., Ho, P. T. P., Zhao, J.-H. 2005, Nature, 438, 62

Shen, Z.-Q. 2006, J. Phys. Conf. Ser., 54, 377

Shkarofsky, I. P., Johnston, T. W., Bachynski, M. P. 1966, "The particle kinetics of plasma" (London: Addison-Wesley Publishing Company)

Shcherbakov, R. V. 2008, ApJS, 177, 493

Shcherbakov R. V., 2008, ApJ, 688, 695

Shcherbakov, R. V. 2010, Physics of Plasmas, 16, 032104

Shcherbakov, R. V., Baganoff, F. K. 2010, ApJ, 716, 504

Shcherbakov, R. V., Huang, L. 2010, MNRAS, 410, 1052

Shcherbakov, R. V., Penna, R. F., McKinney, J. C. 2010, ApJ, submitted

Shvartsman, V. F. 1971, Soviet Astronomy, 15, 377

Sironi, L., Spitkovsky, A. 2009, ApJ, 707, L92

Soria, R., Fabbiano, G., Graham, A. W., Baldi, A., Elvis, M., Jerjen, H., Pellegrini, S., Siemiginowska, A. 2006, ApJ, 640, 126

Soria, R., Graham, A. W., Fabbiano, G., Baldi, A., Elvis, M., Jerjen, H., Pellegrini, S., Siemiginowska, A. 2006, ApJ, 640, 134

Sreenivasan, K. R. 1995, Phys. Fluids, 7, 2778

Su, M., Slatyer, T. R., Finkbeiner, D. P. 2010, ApJ, 724, 1044

Sutherland, R. S., Dopita, M. A. 1993, ApJS, 88, 253

Swanson, D. G. 2003, "Plasma waves" (Bristol: Institute of Physics Pub.)

Tennekes, H., Lumley, J. L. 1972, "A First Course in Turbulence" (Cambridge, MA: MIT Press)

Tchekhovskoy, A., McKinney, J. C., Narayan, R. 2007, MNRAS, 379, 469

Toomre, A., Toomre, J. 1972, ApJ, 178, 623

Toomre, A. 1977, in Evolution of Galaxies and Stellar Populations, ed. B. M. Tinsley & R. B. Larson (New Haven: Yale Univ. Obs.), 401

Trubnikov, B. A., 1958, "Magnetic emission of high temperature plasma". Thesis, Moscow Institute of Engineering and Physics [English translation in AEC-tr-4073, US Atomic Energy Commission, Oak Ridge, Tennessee, 1960]

Trubnikov, B. A. 1996, "Theory of plasma" (Moscow: Energy Atom Press) (in Russian)

Volonteri, M., Haardt, F., Madau, P. 2003, ApJ, 582, 559

Wardle, J. F. C., Homan, D. C., Ojha, R., Roberts, D. H. 1998, Nature, 395, 457

Wilson, T. L., Rohlfs, K., Huttemeister, S. 2009, "Tools of Radio Astronomy" (Berlin: Springer)

Wolfe, B., Melia, F. 2006, ApJ, 637, 313

Yuan, F. 2001, MNRAS, 324, 119

Yuan, F., Markoff, S., Falcke, H. 2002, A&A, 383, 854

Yuan, F., Quataert, E., & Narayan, R. 2003, ApJ, 598, 301

Yuan, F., Quataert, E., Narayan, R. 2004, ApJ, 606, 894

Yusef-Zadeh, F., Wardle, M., Cotton, W. D., Heinke, C. O., Roberts, D. A. 2007, ApJ, 668, 47

Yusef-Zadeh, F., Wardle, M., Heinke, C., Dowell, C. D., Roberts, D., Baganoff, F. K., Cotton, W. 2008, ApJ, 682, 361

Yusef-Zadeh, F., et al. 2009, ApJ, 706, 348

Yusef-Zadeh, F., Wardle, M., Miller-Jones, J. C. A., Roberts, D. A., Grosso, N., Porquet, D., 2011, ApJ, 729, 44

Zhao, J.-H., Young, K. H., Herrnstein, R. M., Ho, P. T. P., Tsutsumi, T., Lo, K. Y., Goss, W. M., Bower, G. C. 2003, ApJ, 586, 29